THE ^{2}H$(e, e'p)n$ REACTION AT HIGH FOUR-MOMENTUM TRANSFER

by

Hassan F. Ibrahim

B.S., May 1991, Cairo University
M.S., September 1997, Cairo University
M.S., December 2004, Old Dominion University

A Dissertation Submitted to the Faculty of
Old Dominion University in Partial Fulfillment of the
Requirement for the Degree of

DOCTOR OF PHILOSOPHY

PHYSICS

OLD DOMINION UNIVERSITY
December 2006

Approved by:

Paul Ulmer (Director)

Hussein Abdel-Wahab (Member)

Charles I. Sukenik (Member)

J. W. Van Orden (Member)

Lawrence Weinstein (Member)

ABSTRACT

THE ^{2}H$(e, e'p)n$ REACTION AT HIGH FOUR-MOMENTUM TRANSFER

Hassan F. Ibrahim
Old Dominion University, 2006
Director: Dr. Paul Ulmer

This dissertation presents the highest four-momentum transfer, Q^2, quasielastic ($x_{Bj} = 1$) results from Experiment E01-020 which systematically explored the ^{2}H$(e, e'p)n$ reaction ("Electro-disintegration" of the deuteron) at three different four-momentum transfers, $Q^2 = 0.8$, 2.1, and 3.5 GeV^2 and missing momenta, $p_{miss} = 0$, 100, 200, 300, 400, and 500 GeV including separations of the longitudinal-transverse interference response function, R_{LT}, and extraction of the longitudinal-transverse asymmetry, A_{LT}. This systematic approach will help to understand the reaction mechanism and the deuteron structure down to the short range part of the nucleon-nucleon interaction which is one of the fundamental missions of nuclear physics. By studying the very short distance structure of the deuteron, one may also determine whether or to what extent the description of nuclei in terms of nucleon/meson degrees of freedom must be supplemented by inclusion of explicit quark effects.

The unique combination of energy, current, duty factor, and control of systematics for Hall A at Jefferson Lab made Jefferson Lab the only facility in the world where these systematic studies of the deuteron can be undertaken. This is especially true when we want to understand the short range structure of the deuteron where high energies and high luminosity/duty factor are needed. All these features of Jefferson Lab allow us to examine large missing momenta (short range scales) at kinematics where the effects of final state interactions (FSI), meson exchange currents (MEC), and isobar currents (IC) are minimal, making the extraction of the deuteron structure less model-dependent. Jefferson Lab also provides the kinematical flexibility to perform the separation of R_{LT} over a broad range of missing momenta and momentum transfers.

Experiment E01-020 used the standard Hall A equipment in coincidence configuration in addition to the cryogenic target system. The low and middle Q^2 kinematics were completed in June 2002 and the high Q^2 kinematics were completed in November 2002. Before the start of the experiment many preparations were made to assure the quality of

the collected data. Approximately two Terabytes of data were collected by the end of the experiment.

The cross section results in this dissertation show clearly the effect of final state interactions between the two final state nucleons. The cross section ratio to the Laget PWBA+FSI calculation has a wiggle at $p_{miss} \sim 300$ MeV. It is yet to be seen whether this is merely due to the lack of MEC and IC in the present theoretical calculation. However, a similar feature was observed in a previous Hall A experiment. Further, discrepancies at very low p_{miss} cast some doubt on neutron form factor measurements using the deuteron as target.

This study will add to the already growing body of systematic data for the ^{2}H$(e, e'p)n$ reaction to better understand the NN short range and to provide vital input for heavier nuclei.

To my family…

ACKNOWLEDGMENTS

I would like first to thank the chair of my dissertation committee, Paul Ulmer, and the committee members, Hussein Abdel-Wahab, Charles I. Sukenik, J. W. Van Orden, and Lawrence Weinstein, for agreeing to be part of this committee during the several years that I have spent at Old Dominion University as a graduate student. I am very glad and honored to know them and humbled by their kindness. I would like also to thank my research advisor, Paul Ulmer, for making this dissertation possible in the end. Without his continuous guidance and help, none of this analysis would have been done successfully. He was always ready to provide his unlimited support, anytime I needed him, during my graduate years. I want to thank all the spokespersons of Experiment E01-020, Werner Boeglin, Mark Jones, Andi Klein, Paul Ulmer, and Eric Voutier for proposing this experiment, for working hard to run it successfully at Jefferson Lab and for dedicating their precious time to actually do or help the data analysis after the collection of data was completed. My gratitude goes to all the other members of the E01-020 previous and current analysis team: Luminita Coman, Wendy Hinton, Jeff Lachniet and Rikki Roché who cooperated with me during the last five years until we obtained the final results. I am also very appreciative to Lawrence Weinstein for all his valuable and illuminating comments during our weekly analysis meetings at ODU and while writing this dissertation.

Of course I cannot forget to thank the larger Hall A collaboration which performed the actual experiment in Hall A, 24 hours a day for a couple of months in 2002. I would like to thank the Hall A leader, Kees De Jager and all the scientific, postdoctoral and technical staff who participated in the experiment. Special thanks go to all the previous and current ODU and Hall A graduate students who helped me to be optimistic and more enthusiastic during my graduate studies in the United States.

I also want to thank the Chair of the Physics Department at ODU, Gail Dodge, the Operations Manager and Assistant Chair, Walt Hooks, and all the wonderful staff for their help and support over the years.

I conclude with a big thanks to all my teachers in Egypt and the United States who have made me the person I am now.

TABLE OF CONTENTS

Page

LIST OF TABLES xi
LIST OF FIGURES xiii

CHAPTERS

I INTRODUCTION 1
I.1 The Deuteron 1
I.2 Electron Scattering 2
I.3 Experiment E01-020 3
II THEORY OVERVIEW AND EXISTING DATA 5
II.1 One Photon Exchange Approximation 5
II.2 OPEA Cross Section 8
II.3 Plane Wave Impulse Approximation (Factorization) 12
II.4 Plane Wave Born Approximation 12
II.5 Beyond The Plane Wave Impulse Approximation 13
II.5.1 Final State Interactions 14
II.5.2 Meson Exchange Currents and Isobar Configurations 15
II.5.3 Quark-Gluon Degrees of Freedom 15
II.6 Theoretical Calculations 16
II.7 Existing Data 18
II.7.1 Response functions and Asymmetry Data 19
II.7.2 Cross Section Data 19
II.7.3 Remarks 23
III EXPERIMENTAL SETUP 26
III.1 Experiment Overview 26
III.2 Jefferson Lab 26
III.3 Hall A 29
III.4 Beamline 31
III.4.1 Beam Energy Measurements 31
III.4.1.1 Arc Measurement 31
III.4.1.2 eP Measurement 32
III.4.2 Beam Raster 33
III.4.3 Beam Position Monitors (BPMs) 34
III.4.4 Beam Current Monitors (BCMs) 36
III.5 Target System 37
III.5.1 Scattering Chamber 37
III.5.2 Cryotarget 39
III.5.3 Gas Purity 43
III.5.4 Dummy and Solid Target Ladder 43
III.6 Spectrometers 43
III.6.1 Collimators 44

CHAPTERS Page

III.6.2 Magnets . . . 45
III.6.3 Detectors . . . 48
III.6.3.1 Vertical Drift Chambers (VDCs) . . . 48
III.6.3.2 Scintillators . . . 50
III.6.3.3 Gas Čerenkov Detector . . . 51
III.6.3.4 Lead Glass Calorimeter (Pion Rejector) . . . 52
III.7 Coordinate systems . . . 53
III.7.1 Hall Coordinate System . . . 53
III.7.2 Target Coordinate System . . . 54
III.7.3 Focal Plane Coordinate System . . . 55
III.8 Data Acquisition and Electronics . . . 55
III.8.1 Trigger Setup . . . 55
III.8.2 Data Acquisition System . . . 57
III.9 Run Summary . . . 60
IV DATA CALIBRATIONS . . . 62
IV.1 Beam Calibrations . . . 62
IV.1.1 Beam Energy Calibration . . . 62
IV.1.2 Beam Position Calibration . . . 63
IV.1.2.1 Bull's Eye Scan . . . 63
IV.1.2.2 Raster Calibration . . . 66
IV.1.2.3 Beam Position Correction . . . 67
IV.1.3 Beam Current Calibration . . . 69
IV.1.4 Extraction of Stable Current Events . . . 73
IV.2 Target Boiling . . . 77
IV.2.1 Liquid Hydrogen . . . 77
IV.2.2 Deuterium Target . . . 79
IV.3 VDC Calibrations . . . 80
IV.4 Tracking Efficiency . . . 81
IV.5 Trigger Efficiency . . . 83
IV.6 Particle Identification Efficiency . . . 85
IV.6.1 Gas Čerenkov Detector . . . 85
IV.6.2 Pion Rejector (Lead Glass Detector) . . . 85
IV.7 Spectrometer Mispointing . . . 86
IV.8 Optics Calibration . . . 90
IV.8.1 Optimization of the Optics Matrix Elements . . . 90
IV.8.2 Optics Target Positions . . . 93
IV.9 Kinematics Calibration . . . 96
IV.9.1 Reaction Kinematics for ^{1}H$(e, e'p)$ . . . 99
IV.9.2 Fitting Method . . . 103
IV.9.3 Analysis . . . 106
IV.9.4 Fitting Results . . . 108
IV.9.5 Remarks . . . 108
IV.10 Electronic and Computer Deadtime . . . 110

CHAPTERS Page

IV.11 Coincidence Time of Flight . . . 111
IV.12 ESPACE Files . . . 112
V DATA ANALYSIS . . . 114
V.1 Target Energy Loss . . . 114
V.1.1 Target Model . . . 116
V.1.2 Energy Loss . . . 119
V.1.2.1 Mean Energy Loss . . . 119
V.1.2.2 Most Probable Energy Loss . . . 120
V.2 Cuts . . . 123
V.3 Radiative Corrections . . . 129
V.4 Normalization . . . 132
V.5 Binning . . . 133
V.6 Calculation of the Cross Sections . . . 137
V.7 Separation of the R_{LT} Response Function . . . 138
V.8 Extraction of the A_{LT} Asymmetry . . . 138
V.9 Systematic Uncertainties . . . 139
V.10 Simulations . . . 139
V.10.1 Jeschonnek PWBA . . . 143
V.10.2 Laget PWBA and PWBA+FSI . . . 146
VI RESULTS AND CONCLUSIONS . . . 147
VI.1 Single Bin Results . . . 148
VI.1.1 Cross Section . . . 148
VI.1.2 R_{LT} Response Function and A_{LT} Asymmetry . . . 152
VI.2 Multi-Bin Results . . . 159
VI.2.1 Cross Section . . . 159
VI.2.2 R_{LT} Response Function and A_{LT} Asymmetry . . . 160
VI.3 Conclusions . . . 178

REFERENCES . . . 183

APPENDICES

A Analyzed Runs . . . 190
B Optics Matrix Elements . . . 194
C Hall A Survey Sign Conventions . . . 199
C.1 Spectrometer Surveys: . . . 199
C.2 Collimator Surveys: . . . 199
C.3 Target Surveys: . . . 200
D Stable Current Program . . . 201
E Derivatives of Kinematical Offsets . . . 207
F Fitting Files for the Kinematics Calibration . . . 209
F.1 The Input File (kincal.inp) . . . 209
F.2 The Fitting Program (kincal.for) . . . 209

APPENDICES Page
F.3 The Output File (kincal.out) 219

VITA 221

LIST OF TABLES

		Page
I	Properties of the Deuteron.	2
II	Kinematics and motivations of Experiment E01-020.	4
III	Operating Conditions for the LH_2 and LD_2 loops.	40
IV	Target configuration for the Q1 and Q2 Kinematics.	41
V	Target configuration for the Q3 Kinematics.	41
VI	Optics target foil thicknesses.	42
VII	Hall A high resolution spectrometer characteristics.	44
VIII	Collimator configuration for the Q1 and Q2 kinematics.	47
IX	Collimator configuration for the Q3 kinematics.	47
X	Spectrometer magnetic constants.	47
XI	Bjorken variable, x_{Bj}, kinematic labels.	61
XII	Measured beam energy for Experiment E01-020.	63
XIII	Missing energy for the ^{1}H$(e,e'p)$ reaction.	65
XIV	EPICS BCM calibration constants.	74
XV	The V-to-F calibration constants.	74
XVI	PID cut efficiency for the Gas Čerenkov ADC sum (GCSUM) cut, the Pion Rejector two layers ADC sums (PRSUM) cut and the combination of these two cuts.	88
XVII	ESPACE z_{react} for the central foil of the multifoil carbon target.	97
XVIII	Calculated z_{react} from Equation (78) for the central foil of the multifoil carbon target.	97
XIX	ESPACE z_{react} versus calculated z_{react} for the multifoil carbon target.	99
XX	ESPACE z_{react} for the thin carbon target.	100
XXI	Calculated z_{react} from Equation (78) for the thin carbon target.	101
XXII	ESPACE versus calculated z_{react} for the thin carbon target.	102
XXIII	Initial kinematic settings and offsets for the different ^{1}H$(e,e'p)$ runs.	107
XXIV	Minimized kinematical offsets for the different ^{1}H$(e,e'p)$ runs.	108
XXV	Calibration Results for the absolute spectrometer offsets.	108
XXVI	The ^{2}H$(e,e'p)n$ reaction ε_{miss} for the calibrated data versus the simulation.	110
XXVII	ESPACE Databases.	112
XXVIII	ESPACE Detector Maps.	113
XXIX	Spectrometer Settings for the analyzed kinematics.	115
XXX	Beam Settings for the analyzed kinematics.	115
XXXI	Most probable versus Mean energy loss corrections to the ^{1}H$(e,e'p)$ missing energy.	123
XXXII	"Trues" ratio dependence on p_{miss} for all the analyzed kinematics.	128
XXXIII	Corrections and Efficiencies.	129
XXXIV	Normalization yield ratio, f_n, of the data to simulation for ^{1}H$(e,e'p)$, involving different form factor parameterizations.	133
XXXV	Single bin over Q^2 and W.	136

Tables		Page
XXXVI	Multi-bin over Q^2.	136
XXXVII	Multi-bin over W.	136
XXXVIII	Kinematic systematic uncertainties for the beam and the two spectrometers.	141
XXXIX	Estimates of other systematic uncertainties.	141
XL	Kinematics dependent uncertainties for the single bin scheme.	142
XLI	Kinematics dependent uncertainties for the multi-bin schemes.	142
XLII	Results for the single bin scheme.	158
XLIII	Reference for the the multi-bin scheme results.	159
XLIV	Results for the multi-bin scheme over Q^2 at $p_{miss} = 50$ MeV.	174
XLV	Results for the multi-bin scheme over Q^2 at $p_{miss} = 150$ MeV.	174
XLVI	Results for the multi-bin scheme over Q^2 at $p_{miss} = 250$ MeV.	174
XLVII	Results for the multi-bin scheme over Q^2 at $p_{miss} = 350$ MeV.	175
XLVIII	Results for the multi-bin scheme over Q^2 at $p_{miss} = 450$ MeV.	175
XLIX	Results for the multi-bin scheme over Q^2 at $p_{miss} = 550$ MeV.	175
L	Results for the multi-bin scheme over W at $p_{miss} = 50$ MeV.	176
LI	Results for the multi-bin scheme over W at $p_{miss} = 150$ MeV.	176
LII	Results for the multi-bin scheme over W at $p_{miss} = 250$ MeV.	176
LIII	Results for the multi-bin scheme over W at $p_{miss} = 350$ MeV.	177
LIV	Results for the multi-bin scheme over W at $p_{miss} = 450$ MeV.	177
LV	Results for the multi-bin scheme over W at $p_{miss} = 550$ MeV.	177
LVI	Analyzed runs.	190
LVII	Left arm y_{000}, t_{000} and p_{000} offsets.	194
LVIII	Right arm y_{000}, t_{000} and p_{000} offsets.	194
LIX	Left arm Y_{jkl} tensor.	195
LX	Left arm T_{jkl} and P_{jkl} tensors.	196
LXI	Right arm Y_{jkl} tensor.	197
LXII	Right arm T_{jkl} and P_{jkl} tensors.	198
LXIII	Sign of the spectrometer horizontal offset,$h_\circ$.	199

LIST OF FIGURES

		Page
1	Typical inclusive electron scattering cross section from the deuteron versus the energy of the virtual photon for a fixed four-momentum transfer.	3
2	Kinematics of the ^{2}H$(e,e'p)n$ reaction in the OPEA.	6
3	Kinematics conventions used for ^{2}H$(e,e'p)n$.	8
4	Plane Wave Impulse Approximation (PWIA) for the ^{2}H$(e,e'p)n$ reaction.	13
5	Plane Wave Born Approximation (PWBA) for the ^{2}H$(e,e'p)n$ reaction.	13
6	Final state interactions (FSI), meson exchange currents (MEC) and isobar configurations (IC).	14
7	The A_{LT} asymmetry for the ^{2}H$(e,e'p)n$ reaction from different measurements.	20
8	The measured R_{LT} response function (referred to in the plot as f_{LT}) and A_{LT} asymmetry from NIKHEF.	21
9	The A_{LT} asymmetry at $Q^2 = 1.2$ GeV^2 measured at SLAC compared with various nonrelativistic (NR) and relativistic (REL) models.	21
10	Comparison of the measured ^{2}H$(e,e'p)n$ cross section at MAMI to the calculation by Arenhövel with (solid curve) and without (dashed curve) MEC and IC.	22
11	The reduced ^{2}H$(e,e'p)n$ cross section for JLab Experiment E94-004, along with various model calculations.	24
12	Comparison of some previous ^{2}H$(e,e'p)n$ experiments to the highest Q^2 data (Q3 kinematics) from Experiment E01-020.	25
13	The Continuous Electron Beam Accelerator Facility (CEBAF).	28
14	Acceleration of electrons in a typical CEBAF superconducting cavity.	28
15	3D view of Hall A.	30
16	Side view of Hall A.	30
17	Top view of Hall A.	31
18	The Arc section of the beamline consists of eight dipoles and a ninth reference dipole.	32
19	EP Beam energy measurement.	34
20	Rastered electron beam profile.	35
21	Beam Position Monitors.	36
22	Hall A BCM System.	38
23	Cryotarget and solid target ladders.	40
24	Target Configurations.	42
25	6 msr collimators.	46
26	Sieve collimators.	46
27	High resolution spectrometer superconducting magnets (QQDQ).	48
28	Detector packages.	49
29	Vertical Drift Chambers (VDCs).	50
30	Scintillator detector plane (each paddle was coupled to a PMT at either end).	51
31	Gas Čerenkov Detector.	52
32	Lead glass electromagnetic calorimeter (Pion Rejector).	53

Figures Page

33 Hall coordinate system (HCS). 54
34 Target coordinate system (TCS). 55
35 Focal plane coordinate system (FPCS). 56
36 Hall A main triggers. 58
37 Hall A DAQ system. 59
38 Tiefenbach energy for E01-020. 64
39 Missing energy for the ^{1}H$(e,e'p)$ runs in Table XIII. 65
40 Bull's eye scan (Beam positions are in meters). 66
41 Beam raster ADCs and beam positions (in meters) as measured by BPMA and BPMB and the extrapolated position at the target for Run 2831. 68
42 Reaction point z-position in a foil carbon target versus the beam x-position for unrastered beam. 69
43 Reaction point z-position in a foil carbon target versus the beam x-position for a rastered beam. 70
44 Reaction point z-position in a foil carbon target versus the corrected beam x-position for a rastered beam. 70
45 Corrected (dashed lines) and uncorrected (solid lines) beam x-position and y-position (meters). 71
46 Effect of the raster half-cut on the corrected rastered beam. 72
47 Raster size for the highest Q^2 perpendicular kinematics. 73
48 Hall A Unser current (μA) versus time (sec). 74
49 Ratios to the Injector BCM (0L02) current. 75
50 Calibration constants versus the injector BCM current. 76
51 Extraction of the stable current events. 77
52 Beam current for the highest Q^2 perpendicular kinematics. 78
53 LH_2 Target boiling for the 2×2 mm^2 raster for each trigger type. 79
54 The normalized rates for each trigger type as a function of beam current for the LD_2 target (4×4 mm^2 raster case). 80
55 VDC T0 optimization. 82
56 Right fractional momentum deviation versus VDC track position (meters) for the U1 wire plane. 83
57 Tracking efficiencies. 84
58 Čerenkov PID Cut efficiency is 99%. 86
59 Pion Rejector PID 2D Cut efficiency is 99%. 87
60 Gas Čerenkov ADC sum (GCSUM) versus the Pion Rejector two layer ADC sums (PR1SUM and PR2SUMS). 87
61 Hall coordinates and target coordinates for electrons scattering from a thin foil target. 89
62 Event Reconstruction in the multifoil carbon target (in meters). 92
63 Optics optimization steps. 92
64 Coordinate systems used in the optics optimization. 93
65 Right and Left arm reconstruction of the sieve holes. 94

Figures Page

66 Reaction point z-positions, z_{react}, reconstructed from Left and Right arms, versus the focal plane y-position, y_{rot}, for the multifoil carbon target (in meters). 95
67 Determination of the optics target z-position for Run 1052. 98
68 The scattered particle spherical angles, (θ', ϕ'), and geographical angles, (θ, ϕ), in the HCS. 103
69 Some minimized offsets for Run # 2672. 109
70 Fractional momentum deviations for the Left and Right arms of the calibrated data versus the simulation. 111
71 Coincidence time of flight optimization. 112
72 Energy loss in the target for the shown three trajectories have different values. 117
73 Target Model for the "cigar-tube" cells. 117
74 Beam energy loss (MeV) and its dependence on reaction point z-position (m). 121
75 Scattered electron energy loss (MeV) and its dependence on reaction point z-position (m). 121
76 Proton energy loss (MeV) and its dependence on reaction point z-position (m). 122
77 Most probable (dashed lines) and mean (solid lines) energy loss for the electrons and protons. 124
78 Most probable (dashed lines) and mean (solid lines) energy loss corrections to the ^{1}H$(e, e'p)$ missing energy for the data and simulation. 124
79 Difference between the left and right reconstructed reaction point z-position (in meters) for Run 2852. 126
80 Cut on the coincidence time (ns) and subtraction of accidentals. 128
81 Typical representation of the HRS solid angle acceptance boundaries by a contour of 12 lines. 130
82 R-Function cuts for Left and Right arms ($RFn > 0.01$). 130
83 Radiation by real photons (Top) and virtual photons (Bottom) in a typical ^{2}H(e, e). 131
84 Comparisons of the target angles for the data (dashed lines) and the simulation (solid lines). 134
85 Yield ratio of the data to simulation for the ^{1}H$(e, e'p)$ invariant mass, W. . . 135
86 Fractional shifts in the cross section (y-axis) versus the the missing momentum in MeV (x-axis). 140
87 Spectrometer acceptance distributions for Left (top) and Right (bottom) arm solid angles in terms of the target angles (θ_{tg}, ϕ_{tg}). 144
88 Comparisons for the Left (Electron) and Right (Proton) R-Functions for the Q3_f20l ($Q^2 = 3.5$ GeV^2, $p_{miss} = 200$ MeV and $\phi_x = 0$) kinematics. 144
89 Comparisons of the missing energy, E_{miss}, and invariant mass, W for the Q3_f20l ($Q^2 = 3.5$ GeV^2, $p_{miss} = 200$ MeV and $\phi_x = 0$) kinematics. 145
90 Comparisons for the 4-momentum transfer, Q^2, and the missing momentum, p_{miss} for the Q3_f20l ($Q^2 = 3.5$ GeV^2, $p_{miss} = 200$ MeV and $\phi_x = 0$) kinematics. 145

Figures		Page
91	Comparisons of the four-momentum transfer, Q^2, versus the invariant mass, W, for the data (Left) and the radiated simulation (right), before (Top) and after (Bottom) application of the final cuts.	149
92	Comparisons of the out of plane angle, ϕ_x, between the scattering and reaction planes, and the missing momentum, p_{miss}, for the data and simulation.	150
93	The acceptance over the missing momentum, p_{miss}, and the out of plane angle, ϕ_x, after applying the final cuts. For $p_{miss} > 500$ MeV, $\phi_x = 0$ is not populated sufficiently to extract the R_{LT} response function nor the A_{LT} asymmetry.	150
94	Binning schemes.	151
95	Cross Section for the single bin scheme.	153
96	Cross Section Ratio for the single bin scheme.	154
97	Longitudinal-Transverse Response Function , R_{LT}, for the single bin scheme.	155
98	The R_{LT} response function for the single bin scheme (blow-up of Figure 97).	156
99	Longitudinal-Transverse Asymmetry, A_{LT}, for the single bin scheme.	157
100	The dependence of the missing momentum, p_{miss}, on Q^2 and W for the lowest p_{miss} bin ($0 < p_{miss} < 100$ MeV).	162
101	The dependence of the average missing momentum, $\langle p_{miss} \rangle$, on Q^2 and W for the lowest p_{miss} bin ($0 < p_{miss} < 100$ MeV).	162
102	Multi-bin results for the cross section and its ratio at $p_{miss} = 50$ MeV.	163
103	Multi-bin results for the cross section and its ratio at $p_{miss} = 150$ MeV.	164
104	Multi-bin results for the cross section and its ratio at $p_{miss} = 250$ MeV.	165
105	Multi-bin results for the cross section and its ratio at $p_{miss} = 350$ MeV.	166
106	Multi-bin results for the cross section and its ratio at $p_{miss} = 450$ MeV.	167
107	Multi-bin results for the cross section and its ratio at $p_{miss} = 550$ MeV.	168
108	Multi-bin results for the R_{LT} response function and the A_{LT} asymmetry at $p_{miss} = 50$ MeV.	169
109	Multi-bin results for the R_{LT} response function and the A_{LT} asymmetry at $p_{miss} = 150$ MeV.	170
110	Multi-bin results for the R_{LT} response function and the A_{LT} asymmetry at $p_{miss} = 250$ MeV.	171
111	Multi-bin results for the R_{LT} response function and the A_{LT} asymmetry at $p_{miss} = 350$ MeV.	172
112	Multi-bin results for the R_{LT} response function and the A_{LT} asymmetry at $p_{miss} = 450$ MeV.	173
113	Summary of cross section results for the multi-bin schemes.	179
114	Summary of the cross section ratio results for the multi-bin schemes.	180
115	Summary of R_{LT} results for the multi-bin schemes.	181
116	Summary of A_{LT} results for the multi-bin schemes.	182

CHAPTER I

INTRODUCTION

The importance of the deuteron and electron scattering in general as well as the goals of Experiment E01-020 will be discussed in this introductory chapter[1].

I.1 THE DEUTERON

The nucleus of the deuterium atom, the *deuteron* (symbol ^{2}H or d), is a bound system of a proton and a neutron [1]. It is the simplest nucleus, has no excited bound states, and therefore provides a starting point for understanding more complex nuclei. By a suitable choice of reaction and kinematic settings, one can use it to study the short-range correlations (SRC) of the nucleon-nucleon (*NN*) interaction [2], without the additional effects of three body interactions, which is one of the fundamental missions of nuclear physics. The deuteron wave function is a mixture of S ($L = 0$) and D ($L = 2$) momentum states. Accurate knowledge of the high momentum components is essential to understand the short distance structure of the deuteron, and can guide our understanding of the correlation structure of complex nuclei. However, this momentum distribution is not an experimental observable, and can only be extracted in the context of a model. For a summary of the deuteron properties, see Table I.

The deuteron is a valuable tool, not only for what it can tell us about the nuclear force, but also as a source of nearly free neutrons. Lacking pure neutron targets, the deuteron, with its relatively loose binding, is often chosen for studies of the structure of the neutron. Measurements of elastic electron scattering from deuterium have been used extensively in order to extract the neutron electric form factor, G_E^n [3]. Understanding the deuteron is also important for measurements employing deuterium targets to determine the spin structure function of the neutron [4]. Finally, by studying the very short distance structure of the deuteron, one may determine whether or to what extent the description of nuclei in terms of nucleon/meson degrees of freedom must be supplemented by inclusion of explicit quark effects [5].

This dissertation follows the style of the "Physical Review".

[1]The kinematical quantities mentioned in this introductory chapter are defined in Chapter II.

TABLE I: Properties of the Deuteron [1].

Quantity	Value
Mass	1875.612762 (75) MeV
Binding Energy	2.22456612 (48) MeV
Magnetic Dipole Moment	0.857382284 (94) μ_N
Electric Quadrupole Moment	0.2859 (3) fm^2
Asymptotic D/S Ratio	0.0256 (4)
Charge Radius	2.130 (10) fm
Matter Radius	1.975 (3) fm
Electric Polarizability	0.645 (54) fm^3

I.2 ELECTRON SCATTERING

Electron scattering is one of the most powerful tools used in the exploration of nuclei [6]. The main strengths of electron scattering are that the electromagnetic interaction is calculable with well understood Quantum Electrodynamics (QED), and it is relatively weak ($\alpha \approx 1/137$) compared to the hadronic interaction, which implies that the electromagnetic interaction can be described by the one photon exchange approximation (OPEA). There are two classes of unpolarized reactions used to study the high momentum part of the deuteron wave function. They are classified according to how many final particles are detected in the lab[2]:

- Inclusive (single arm) elastic ^{2}H(e,e) and inelastic ^{2}H(e,e') reactions (see e.g. References [7, 8]).
- Exclusive (coincidence) quasielastic ^{2}H$(e,e'p)n$ reaction (see *e.g.*, Reference [9]).

The most direct way of studying the short-range part of the *NN* interaction is to investigate the quasielastic "electro-disintegration" of the deuteron via the ^{2}H$(e,e'p)n$ reaction at high missing momenta, p_{miss}. However, depending on the selected kinematics, these measurements can be overwhelmed by final state interactions (FSI) which involve proton-neutron rescattering and non-nucleonic currents such as meson-exchange currents (MEC) and isobar configurations (IC) [10, 11].

[2]The nuclear reaction $a + A \rightarrow b + c + B$, where a is the incident particle, A is the target nucleus, b and c are the outgoing particles, and B is the product nucleus, is usually represented by the more compact form $A(a,bc)B$. For example, ^{2}H$(e,e'p)n$ represents the reaction $e + d \rightarrow e' + p + n$.

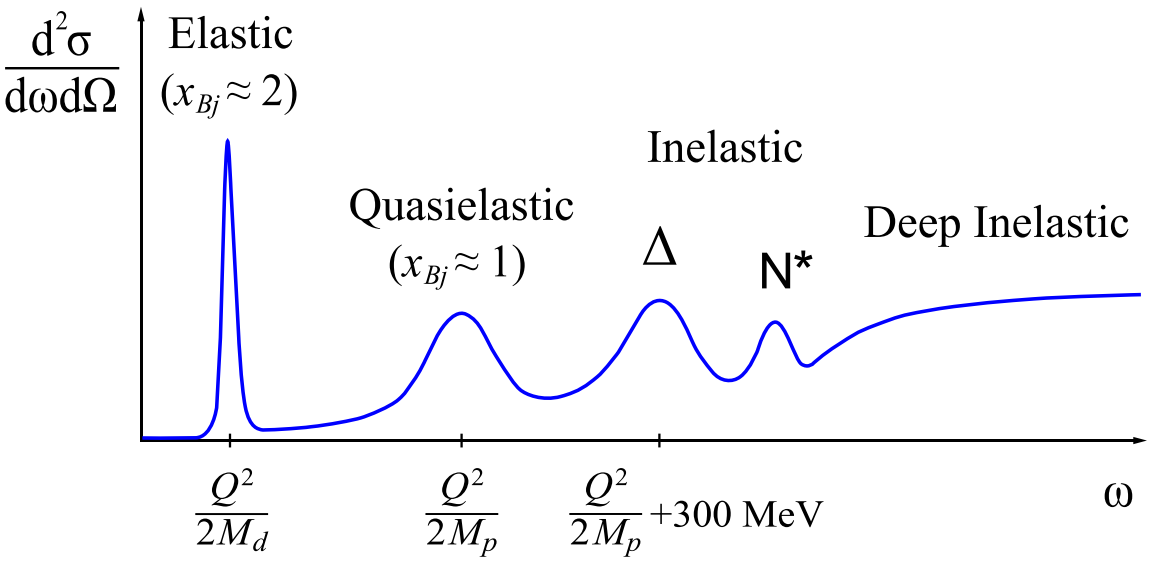

FIG. 1: Typical inclusive electron scattering cross section from the deuteron versus the energy of the virtual photon for a fixed four-momentum transfer.

Figure 1 shows the main features of a typical inclusive electron scattering cross section from the deuteron versus the energy of the virtual photon for a fixed four-momentum transfer. At low photon momentum, the photon wavelength is comparable to or larger than the deuteron size, and the scattering is predominantly *elastic*. As the photon momentum increases, its wavelength decreases and becomes comparable to the nucleon size. In this case, the electron scatters from a nearly free nucleon giving the *quasielastic peak*. The quasielastic peak is broader than the elastic peak because of the Fermi motion of the nucleons inside the deuteron. At sufficiently high energy transfers, we can excite the nucleons to higher states such as Δ and N^* (*inelastic* scattering). Finally, at very high photon momentum, the wavelength of the photon becomes smaller than the size of the nucleon, which contributes to the *deep inelastic* scattering (DIS).

I.3 EXPERIMENT E01-020

The goal of experiment E01-020 [12] is to provide a systematic study of the ^{2}H$(e,e'p)n$ reaction down to very short distance scales. It covers kinematics from below to above the quasielastic peak (see Figure 1) over a wide range of four-momentum transfers, $Q^2 = 0.8$, 2.1, and 3.5 GeV^2 and missing momenta, $p_{miss} = 0$, 100, 200, 300, 400 and 500 MeV (results for only the highest Q^2 perpendicular kinematics are reported in this dissertation).

TABLE II: Kinematics and motivations of Experiment E01-020.

Kinematics[3]	Q^2 (GeV^2)	x_{Bj}	Theoretical Expectations FSI	MEC/IC	Motivations
Parallel	2.1	<1	Minimum	Maximum	Emphasize MEC / IC
Anti-Parallel	2.1	>1	Minimum	Minimum	Study Deuteron Short-range Structure
Perpendicular	0.8	1	Variable	Minimum	Test Relativistic
	2.1				Models (R_{LT})
	3.5				
Neutron	0.8	Variable	Variable	Variable	Study FSI
Angular	2.1				
Distribution	3.5				

These studies will provide important constraints on deuteron structure and reaction models.

Each of the kinematics emphasizes different aspects of the reaction mechanism. For energy transfers below the quasielastic peak ($x_{Bj} > 1$), non-nucleonic effects (virtual nucleonic excitations and meson exchange currents) are expected to be minimized since the energy transfer is relatively low. Thus, the high x_{Bj} parallel kinematics measurements are expected to be mainly sensitive to aspects of the deuteron's short-range structure.

By examining (for fixed Q^2 and p_{miss}) the angular distribution of neutrons in the final hadronic center-of-mass system, one can quantitatively study FSI. The angular distribution is expected to show a large peak near 90° about the $\vec{q}$ direction [12]. The success of theories in predicting this shape will give us confidence in correcting for FSI effects in extracting the deuteron structure. This understanding will also be useful for studies of short-range correlations using $(e, e'p)$ on heavier nuclei.

Finally, a separation of the longitudinal-transverse interference response function, R_{LT}, was performed in quasielastic kinematics ($x_{Bj} = 1$) for p_{miss} up to 0.5 GeV to test the validity of relativistic models. Proper treatment of relativity is essential at kinematics where we probe the deuteron's short-range structure. Table II summarizes the different kinematics and motivations of Experiment E01-020.

CHAPTER II

THEORY OVERVIEW AND EXISTING DATA

In this chapter, an overview of the basic theory used to calculate the cross section of the ^{2}H$(e,e'p)n$ reaction is presented. Examples of actual theoretical calculations will also be discussed and compared with existing data.

II.1 ONE PHOTON EXCHANGE APPROXIMATION

The kinematics[1] for the ^{2}H$(e,e'p)n$ reaction in the One Photon Exchange Approximation (OPEA) [13, 14, 15, 16] are shown in Figure 2. The incident electron four-momentum is denoted by $k^\mu = (E, \vec{k})$ and the scattered electron four-momentum by $k'^\mu = (E', \vec{k}')$. In the extreme relativistic limit (ERL), the electron mass m_e can be neglected so that $k \equiv |\vec{k}| = E$ and $k' \equiv |\vec{k}'| = E'$. The two momenta, $\vec{k}$ and $\vec{k}'$, define the "scattering plane". The virtual photon four-momentum, which is transferred to the target nucleus, is given by

$$q^\mu \equiv k^\mu - k'^\mu = (\omega, \vec{q}), \tag{1}$$

where

$$\omega = E - E', \tag{2}$$

$$\vec{q} = \vec{k} - \vec{k}', \tag{3}$$

and the square of the four-momentum transfer (also called *virtuality*) is given by

$$q_\mu^2 \equiv -Q^2 = \omega^2 - q^2 = 2(\vec{k}\cdot\vec{k}' - EE' + m_e^2); \tag{4}$$

where $q \equiv |\vec{q}|$. Therefore in the ERL

$$Q^2 = 4EE' \sin^2\left(\frac{\theta_e}{2}\right). \tag{5}$$

The deuteron is at rest in the lab frame ($\vec{p}_d = 0$) so that its energy, E_d is equal to its mass, M_d. The final proton has four-momentum $p^\mu = (E_p, \vec{p})$ and the neutron has four

[1] The natural units convention ($\hbar = c = 1$) is used in this dissertation.

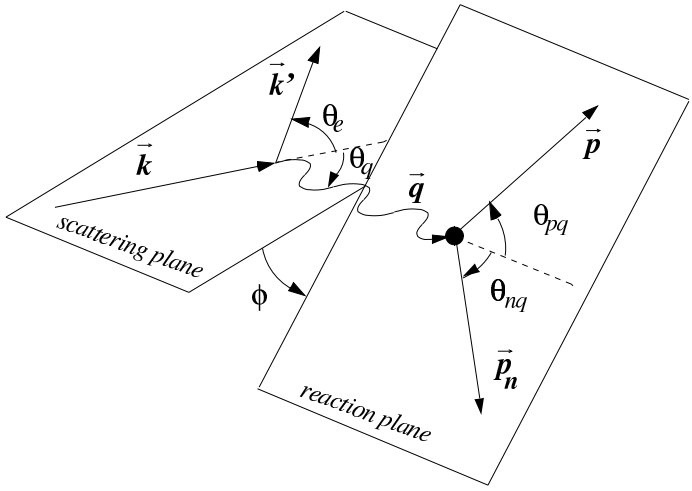

FIG. 2: Kinematics of the ^{2}H$(e,e'p)n$ reaction in the OPEA.

momentum $p_n^\mu = (E_n, \vec{p}_n)$[2]. The square of the reaction invariant mass is given by:

$$W^2 \equiv E_i^2 - P_i^2 = (\omega + M_d)^2 - q^2 = M_d^2 + 2\omega M_d - Q^2, \tag{6}$$

where E_i and P_i are the total initial energy and momentum of the final hadronic system. Conservation of energy and three momentum yields

$$\omega + M_d = E_p + E_n = M_p + T_p + M_n + T_n, \tag{7}$$

$$\vec{q} = \vec{p} + \vec{p}_n, \tag{8}$$

where M_p is the mass of the proton and T_p and T_n are the kinetic energies of the scattered proton and the recoil neutron respectively. The "reaction plane" is defined by the two momenta $\vec{p}$ and $\vec{p}_n$. The azimuthal angle between the electron scattering plane and the hadronic reaction plane is called the out-of-plane angle, ϕ_x. In Hall A, the only possible two values of ϕ_x are 0° and 180° (barring the vertical angle acceptance of the spectrometers) since the spectrometers cannot be elevated out of the horizontal plane. This corresponds to detecting the proton only in the scattering plane (in-plane kinematics). The angle between $\vec{q}$ and $\vec{p}$ is denoted by θ_{pq} and between $\vec{q}$ and $\vec{p}_n$ is denoted by θ_{nq}. The angle θ_{pq} is given by:

[2]The neutron four-momentum is also referred to by the more general term, recoil four-momentum, $p_r^\mu = (E_r, \vec{p}_r)$.

$$\cos\theta_{pq} = \frac{k - k'\cos\theta_e}{q}. \tag{9}$$

In the center-of-mass frame of the final hadronic system, the angle between $\vec{q}$ and $\vec{p}$ is denoted by θ_{cm}. The missing energy (binding energy of the deuteron) and missing momentum[3] for the ^{2}H$(e,e'p)n$ reaction are defined by

$$\varepsilon_{miss} = \omega - T_p - T_n = M_p + M_n - M_d = 2.225\ \text{MeV}, \tag{10}$$

$$\vec{p}_{miss} = \vec{q} - \vec{p}. \tag{11}$$

The angle between the missing momentum and the virtual photon momentum, θ_{miss}, is given by:

$$\cos\theta_{miss} = \frac{q - p\cos\theta_{pq}}{\sqrt{q^2 + p^2 - 2qp\cos\theta_{pq}}}. \tag{12}$$

Figure 3 shows the different kinematics conventions used for ^{2}H$(e,e'p)n$. Detection of the proton along $\vec{q}$ such that $\theta_{pq} = 0°$ corresponds to "parallel kinematics". In this case, $\vec{p}_{miss}$ is parallel to $\vec{q}$ if $q > p$ ($\theta_{miss} = 0°$) and is anti-parallel if $q < p$ ($\theta_{miss} = 180°$). For kinematic settings where $q \approx p$, the detection of the proton on either side of $\vec{q}$ for small values of θ_{pq} yields $\vec{p}_{miss}$ close to being perpendicular to $\vec{q}$ ($\theta_{miss} \approx 90°$). This case is called "perpendicular kinematics". One can also define a Bjorken scaling variable $x_{Bj} = Q^2/(2M_p\omega)$. For electron-proton elastic scattering, $x_{Bj} = 1$. For electron scattering from a nucleus (with mass number, $A > 1$), $x_{Bj} \approx 1$ corresponds to the quasielastic peak which corresponds to scattering off nearly free nucleons (see Figure 1).

[3]For a general reaction, $A(e,e'p)B$, the actual *missing energy*, E_{miss}, which is the energy of the missing (not detected) recoil nucleus B, with a four-momentum, $p_B^\mu = (E_B, \vec{p}_B)$, is always defined as $E_{miss} \equiv E_B = \omega + M_A - E_p = \omega - T_p$, where T_p is the proton kinetic energy. This definition is usually used for *elastic* scatterings and is implemented in ESPACE (see Subsection III.8.2) as the external variable `emiss`. Another definition of the missing energy (also called the missing mass in some literature) is $\varepsilon_{miss} = M_p + M_B - M_A = \omega - T_p - T_B = E_{miss} - T_B$, where T_B is the kinetic energy of nucleus B. ε_{miss} is simply the sum of the proton excitation and separation energies for nucleus A (or the binding energy, in the case of the deuteron). ε_{miss} is a useful variable for *quasielastic* reactions. In ESPACE, ε_{miss} is represented by the external variable `e_miss`. The *missing mass* is defined as $M_{miss} = \sqrt{E_{miss}^2 - p_{miss}^2}$, where $p_{miss} \equiv p_B$. For example, the ^{1}H$(e,e'p)$ reaction has $\varepsilon_{miss} \equiv E_{miss} \equiv 0$ and the ^{2}H$(e,e'p)n$ reaction has $\varepsilon_{miss} = E_{miss} - T_n = 2.225$ MeV.

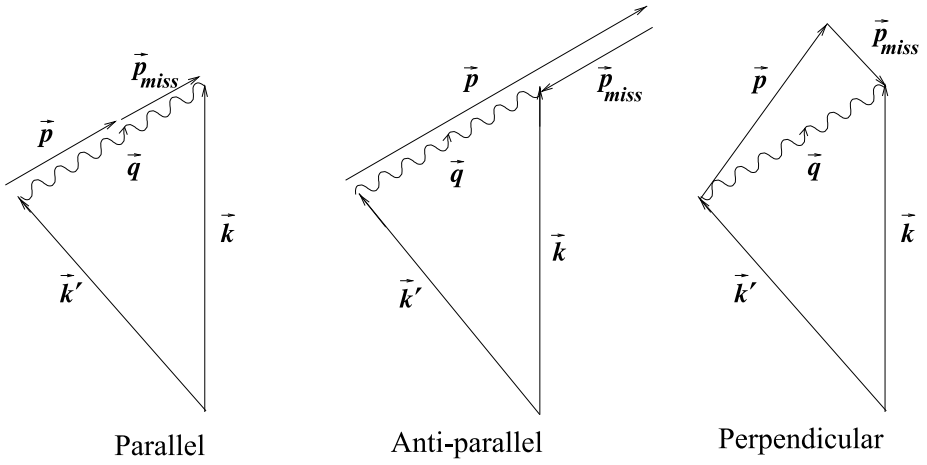

FIG. 3: Kinematics conventions used for ^{2}H$(e, e'p)n$.

II.2 OPEA CROSS SECTION

The unpolarized sixfold differential cross section of this reaction is given by [16, 17, 18, 19]:

$$\frac{d^6\sigma}{dE' d\Omega_e dE_p d\Omega_p} = \frac{pE_p}{(2\pi)^3}\frac{E'}{E}\frac{\alpha^2}{Q^4}\eta_{\mu\nu}\mathcal{W}^{\mu\nu} \tag{13}$$

where $d\Omega_e$ and $d\Omega_p$ are the solid angles of the electron and proton momenta in the lab, α is the fine structure constant, $\mathcal{W}^{\mu\nu}$ is the *nuclear response tensor* and $\eta_{\mu\nu}$ is the *electron response tensor*. The nuclear response tensor is:

$$\mathcal{W}^{\mu\nu} = \left\langle J_\mu J_\nu^\dagger \right\rangle, \tag{14}$$

where the angle brackets denote products of matrix elements averaged over initial states and summed over final states, and $J^\mu = (\rho, \vec{J})$ is the nuclear electromagnetic four-current operator. The electron response tensor is:

$$\eta_{\mu\nu} = K_\mu K_\nu - q_\mu q_\nu - Q^2 g_{\mu\nu}, \tag{15}$$

where $K_\mu = k_\mu + k'_\mu$. Therefore we can write the tensor product in Equation (13) as:

$$\eta_{\mu\nu}\mathcal{W}^{\mu\nu} = \left\langle K \cdot J K \cdot J^\dagger - Q^2 J \cdot J^\dagger \right\rangle \tag{16}$$

In a right handed coordinate system with

$$\hat{z} = \hat{q} \tag{17}$$

$$\hat{y} = \frac{\vec{k} \times \vec{k'}}{|\vec{k} \times \vec{k'}|} \tag{18}$$

$$\hat{x} = \hat{y} \times \hat{z} \tag{19}$$

the continuity equation for the z-component of the current becomes:

$$J_z = \frac{\omega}{q}\rho \tag{20}$$

where ρ is the charge density operator. Using the last equation, we can write Equation (16) as:

$$\eta_{\mu\nu}\mathcal{W}^{\mu\nu} = 4EE' \cos^2\frac{\theta_e}{2} \times [V_{00}\rho\rho^\dagger + V_{xx}J_xJ_x^\dagger + V_{yy}J_yJ_y^\dagger + V_{0x}(\rho J_x^\dagger + J_x\rho^\dagger)] \tag{21}$$

where the coefficients

$$V_{00} = \left(\frac{Q^2}{q^2}\right)^2, \tag{22}$$

$$V_{xx} = \frac{Q^2}{q^2} + \tan^2\frac{\theta_e}{2}, \tag{23}$$

$$V_{yy} = \tan^2\frac{\theta_e}{2}, \tag{24}$$

$$V_{0x} = \frac{Q^2}{q^2}\left[\frac{Q^2}{q^2} + \tan^2\frac{\theta_e}{2}\right]^{\frac{1}{2}}. \tag{25}$$

depend only on the electron kinematics. A more convenient form of Equation (21) is

$$\eta_{\mu\nu}\mathcal{W}^{\mu\nu} = 4EE' \cos^2\frac{\theta_e}{2} \times [v_L R_L + v_T R_T + v_{TT} R_{TT}\cos 2\phi + v_{LT} R_{LT}\cos\phi] \tag{26}$$

where the different leptonic kinematic factors, v, are given by

$$v_L = \left(\frac{Q^2}{q^2}\right)^2, \tag{27}$$

$$v_T = \frac{1}{2}\frac{Q^2}{q^2} + \tan^2\frac{\theta_e}{2}, \tag{28}$$

$$v_{TT} = \frac{1}{2}\frac{Q^2}{q^2}, \tag{29}$$

$$v_{LT} = \frac{Q^2}{q^2}\left[\frac{Q^2}{q^2} + \tan^2\frac{\theta_e}{2}\right]^{\frac{1}{2}}. \tag{30}$$

and the nuclear response functions,

$$R_L = \left\langle \rho\rho^\dagger \right\rangle, \tag{31}$$

$$R_T = \left\langle J_x J_x^\dagger + J_y J_y^\dagger \right\rangle, \tag{32}$$

$$R_{TT}\cos 2\phi = \left\langle J_x J_x^\dagger - J_y J_y^\dagger \right\rangle, \tag{33}$$

$$R_{LT}\cos\phi = -\left\langle \rho J_x^\dagger + J_x \rho^\dagger \right\rangle. \tag{34}$$

are matrix elements of the nuclear charge density operator, ρ, and the nuclear electromagnetic current component operators, J_x and J_y, where J_x lies in the scattering plane and J_y is perpendicular to the scattering plane and both are perpendicular to $\vec{q}$. From Equations (26–34), the sixfold cross section in Equation (13) is simply:

$$\frac{d^6\sigma}{dE' d\Omega_e dE_p d\Omega_p} = \frac{pE_p}{(2\pi)^3}\sigma_{Mott}[v_L R_L + v_T R_T + v_{TT} R_{TT}\cos 2\phi + v_{LT} R_{LT}\cos\phi] \tag{35}$$

where the Mott cross section, σ_{Mott}, of electron scattering on an infinitely massive, spinless point charge is given by

$$\sigma_{Mott} = \left(\frac{2\alpha E'\cos\frac{\theta_e}{2}}{Q^2}\right)^2 \tag{36}$$

By using conservation of energy for the ^{2}H$(e,e'p)n$ reaction, the unpolarized sixfold differential cross section can be integrated over the proton energy to yield a fivefold differential cross section in the lab frame:

$$\frac{d^5\sigma}{d\omega d\Omega_e d\Omega_p} = \frac{M_p M_n p}{(2\pi)^3 M_d}\sigma_{Mott} f_{rec}[v_L R_L + v_T R_T + v_{TT} R_{TT}\cos 2\phi + v_{LT} R_{LT}\cos\phi]. \tag{37}$$

The recoil factor f_{rec} which accounts for the finite mass of the deuteron is defined as

$$f_{rec} = \left(1 + \frac{2E\sin^2\frac{\theta_e}{2}}{M_d}\right)^{-1}. \tag{38}$$

The longitudinal response function, R_L, is due to the charge (longitudinal component of the current). The transverse response function, R_T, is the incoherent sum of the transverse components of the current with respect to the virtual photon. The transverse-transverse response function, R_{TT}, originates from the interference between these two transverse current components. Finally, the longitudinal-transverse response function, R_{LT}, represents the interference between the longitudinal current and the transverse current component in the scattering plane.

The response functions for ^{2}H$(e,e'p)n$ depend on three kinematic variables which may be taken to be Q^2, W and p_{miss}: $R \equiv R(Q^2, W, p_{miss})$. By varying the kinematics (and consequently the kinematic factors weighting each response function) so as to keep the response functions themselves fixed, each may be separately determined from the cross section by solving a set of linear equations. Separation of R_{LT} is accomplished by selecting two kinematics, one with protons forward of $\vec{q}$ ($\phi_x = 0°$) and the other with protons backward of $\vec{q}$ ($\phi_x = 180°$). This changes the $\cos\phi_x$ factor multiplying R_{LT} in Equation (37) from $+1$ to -1, respectively, so that the difference of cross sections gives, to within an overall factor, R_{LT}:

$$R_{LT} \propto \sigma(\phi_x = 0) - \sigma(\phi_x = \pi) \tag{39}$$

The R_{LT} response function is sensitive to the choice of relativistic model. For example, the longitudinal component of the relativistic electromagnetic nuclear current contains an additional spin-orbit term which can interfere with the spin-flip magnetization term in the transverse current component [11]. Non-relativistically, there is no such additional term since L reflects charge only and cannot interfere with the spin-flip part of T. Therefore, we can test relativistic models by separating R_{LT}.

Another important quantity is the Longitudinal-Transverse Asymmetry,A_{LT}, defined as[4]:

$$A_{LT} = \frac{\sigma(\phi_x = 0) - \sigma(\phi_x = \pi)}{\sigma(\phi_x = 0) + \sigma(\phi_x = \pi)}, \tag{40}$$

which is often used in order to minimize the the influence of various systematic uncertainties due to target thickness, beam current and detector efficiencies [20].

[4]Also known as the Left-right asymmetry, A_ϕ, in some literature.

II.3 PLANE WAVE IMPULSE APPROXIMATION (FACTORIZATION)

Figure 4 corresponds to the nonrelativistic Plane Wave Impulse Approximation (PWIA) for the ^{2}H$(e,e'p)n$ reaction. The basic assumptions of the nonrelativistic PWIA for this reaction are

- The total energy and momentum of a single virtual photon is absorbed by the proton.
- The struck proton leaves the nucleus without interacting with the neutron, and the outgoing proton may be represented by a plane wave.
- The ejected proton, not the spectator neutron, is the one detected in the experiment.
- The negative energy states present in a relativistic treatment are neglected.

In the PWIA, the conservation of linear momentum requires that the initial momentum of the struck proton, $\vec{p}'$, is equal to the negative missing momentum:

$$\vec{p}' = \vec{p} - \vec{q} = -\vec{p}_{miss} \equiv -\vec{p}_n. \tag{41}$$

Applying these assumptions allows for the *factorization* of the ^{2}H$(e,e'p)n$ cross section [21, 22]:

$$\frac{d^5\sigma}{d\omega d\Omega_e d\Omega_p} = \frac{M_p M_n p}{M_d}\sigma_{ep} f_{rec} n(\vec{p}'), \tag{42}$$

where σ_{ep} is the electron-proton cross section for a bound proton and $n(\vec{p}')$ is the initial momentum distribution of the proton inside the deuteron.

For a modern covariant description of the relativistic plane wave impulse approximation (RPWIA), see Reference [23]. In RPWIA the differential cross section depends on both positive and negative energy projections of the relativistic bound nucleon wave function. An important difference between the PWIA and RPWIA is that factorization no longer holds in RPWIA.

II.4 PLANE WAVE BORN APPROXIMATION

The Plane Wave Born approximation (PWBA) for the ^{2}H$(e,e'p)n$ reaction contains in addition to the PWIA diagram where the photon couples to the proton (see Figure 4) the diagram where the photon couples to the neutron also as shown in Figure 5. When the magnitude of the missing momentum is much smaller than $\vec{q}$, the difference between PWIA

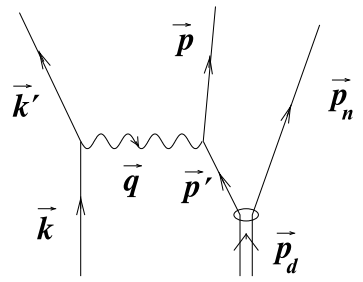

FIG. 4: Plane Wave Impulse Approximation (PWIA) for the ^{2}H$(e,e'p)n$ reaction.

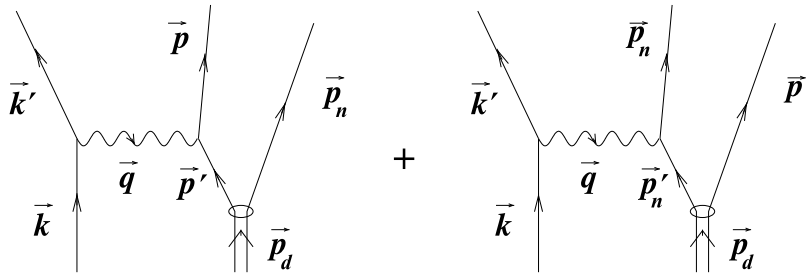

FIG. 5: Plane Wave Born Approximation (PWBA) for the ^{2}H$(e,e'p)n$ reaction.

and PWBA is negligible, since scattering on the neutron would require a very high internal momentum in the deuteron wave-function [24]. However, the PWBA is sufficient to break factorization and to permit the interference of the different wave function components. As for the PWIA, the incident and scattered electrons in the PWBA are described by plane waves and the interaction with the nucleus is mediated by a single virtual photon.

II.5 BEYOND THE PLANE WAVE IMPULSE APPROXIMATION

Within the PWIA, the outgoing proton does not interact with the spectator neutron after the interaction with the virtual photon. However at high p_{miss} one expects a substantial contribution from final state interactions (FSI) between the ejected proton and the spectator neutron (see Figure 6 and Reference [11]). In this case, the logical extension of the PWIA is the Distorted Wave Impulse Approximation (DWIA) which includes FSI between the ejected proton and the spectator neutron while maintaining the other PWIA assumptions. A more general extension is the Distorted Wave Born Approximation (DWBA) where the virtual photon can couple to the neutron also. In the deuteron case, FSI effects can be

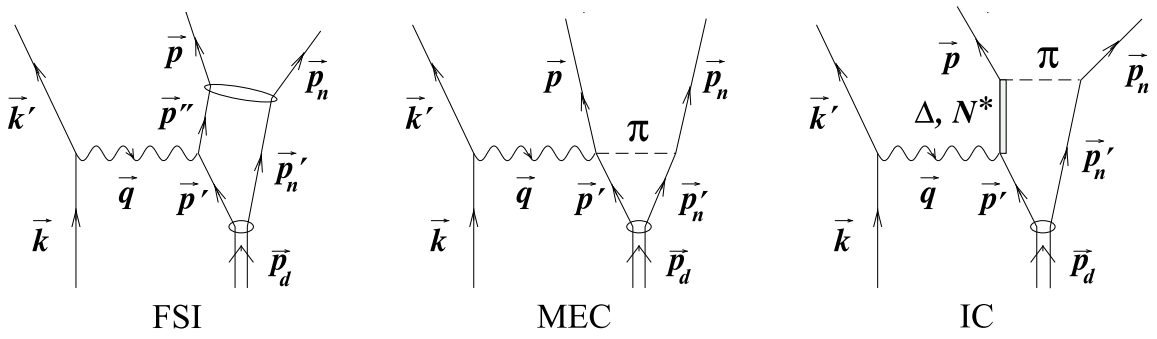

FIG. 6: Final state interactions (FSI), meson exchange currents (MEC) and isobar configurations (IC).

calculated exactly within the Schrödinger approach, or by Glauber approximation [25]. In addition to FSI, other effects should be taken into consideration such as (see Figure 6):

- Meson Exchange Currents (MEC) where the stuck nucleon exchanges a meson such as a pion, at the interaction point.
- Isobar Configurations (IC) where the struck nucleon is excited to a higher state such as Δ or $N*$ and then de-excites by exchanging a meson with the other nucleon.
- Quark-Gluon degrees of freedom which could be important at high momentum transfers.

II.5.1 Final State Interactions

Within PWIA, the outgoing nucleon does not interact with the residual system after the interaction with the virtual photon. However in the kinematic region of high missing momentum where one expects to have an enhanced contribution from the short range correlations (SRC) one may also expect a substantial contribution from FSI between the knock-out and the spectator nucleon. The main effect introduced by FSI is that the initial nucleon momentum carried by the bound nucleon before the interaction with the electron, is not the same as the one measured in the experiment, *i.e.*, $\vec{p}' \neq \vec{p} - \vec{q}$. As a result one cannot be confident that the condition of large p_{miss} automatically guarantees that high momentum components in the ground state wave function of the deuteron are probed. In all previous ^{2}H$(e, e'p)n$ experiments at large p_{miss}, FSI were a major contributor to the overall cross section and therefore substantially overshadowed SRC. With increasing energies,

the situation changes qualitatively. At large angular momenta, FSI are dominated by the *pn* rescattering and then become strongly anisotropic with respect to the direction of $\vec{q}$. The maximal rescattering happens in directions almost transverse to $\vec{q}$. Consequently, FSI contribute much less for parallel and anti-parallel kinematics and can be treated there as a correction. The dominance of large angular momenta allows to apply eikonal approximations in calculating FSI. A well known example of the eikonal approximation of FSI is the Glauber approximation [26]. However the latter was derived for cases where one can neglect the motion of bound nucleons in the nucleus. For the ^{2}H$(e,e'p)n$ reaction at large missing momenta, the eikonal approximation was generalized (GEA) in order to account for finite values of nucleon momenta [8, 27].

II.5.2 Meson Exchange Currents and Isobar Configurations

Experimental ^{2}H$(e,e'p)n$ data at low Q^2 demonstrated that with increasing p_{miss} meson exchange currents (MEC) and isobar configurations (IC) become dominant, making it virtually impossible to extract information on the *NN* SRC. The calculation of MEC and IC at high Q^2 is very complicated since the virtuality of the exchanged mesons greatly exceeds their masses. However it is possible to estimate the Q^2 dependence of these contributions based on the analysis of the corresponding Feynman diagrams. Theoretically one expects that the MEC contribution will decrease with increasing Q^2. Indeed it can be shown that MEC diagrams have an additional $\sim 1/Q^2$ dependence compared to the diagrams where the electron scatters from a nucleon [29]. This suppression comes from two major factors. Firstly, because at the considered kinematics the knocked-out nucleon is fast and takes almost the entire momentum of the virtual photon, $\vec{q}$, the exchanged meson propagator is proportional to $(1 + Q^2/m^2_{meson})$. Secondly, an additional Q^2 dependence comes from the *NN* meson form-factor $(1 + Q^2/\Lambda^2)$ [29]. At low Q^2, MEC and IC contribution is not negligible, as the invariant mass of the *pn* system, W, spans the baryonic resonance regime.

II.5.3 Quark-Gluon Degrees of Freedom

Upon the quantitative understanding of the role of FSI, MEC, and IC in the electrodisintegration of the deuteron, one can start to address the important question of quark-gluon degrees of freedom in the deuteron. Experiments of inclusive Deep Inelastic (DIS) electron scattering from nuclei demonstrated the modification of the nucleon quark-parton

density as compared to that of the free nucleon (the EMC effect [30]). This effect unambiguously demonstrated that nuclei can not be described merely as a collection of unmodified nucleons. Moreover the proportionality of the EMC effect to the nuclear density was an indication that the modification of the quark-parton structure of nucleons depends on how strongly nucleons are bound in a nucleus. Although the effect is observed in the DIS region, one should expect a similar modification for the elastic form-factors of bound nucleons. However, inclusive data alone will not allow one to conclusively check the existence of EMC type phenomena for the elastic form factors. One problem is that with the increase of Q^2 , inelastic channels dominate the inclusive cross section and are thus obscuring elastic contributions [8]. One mechanism of the bound nucleon's form-factor modification is described in the color screening model [31, 32], where at $Q^2 \geq Q_0^2$ ($Q_0^2 \approx 2-3$ GeV^2), the nucleon form-factor becomes sensitive to quark correlations. In this regime the bound nucleon will have suppressed quark correlations as compared to the free nucleon.

II.6 THEORETICAL CALCULATIONS

The electro-disintegration of the deuteron can be described by two different approaches: the Schrödinger equation and the Bethe-Salpeter (B-S) equation. The Schrödinger equation offers a nonrelativistic description, whereas the B-S equation is used to obtain a Lorentz covariant description and is more difficult to solve. Fortunately, it is possible to modify the Schrödinger equation to include relativistic effects, thereby extending the range of its validity.

There are several calculational approaches which include some or all of the effects in the ^{2}H$(e,e'p)n$ reaction. Among these approaches are the calculations of Tjon *et al.* [33, 34, 35], Mosconi *et al.*, [36, 37], Arenhövel *et al.*, [38, 39, 40], Jeschonnek *et al.*, [41, 24], and Laget [42, 43, 44, 45]. These models are mostly based on the nonrelativistic or relativistic PWBA or DWBA (which includes FSI). The deuteron initial and final state wave functions are obtained by solving the wave equation numerically with a realistic *NN* potential such as the Paris, Bonn or Argonne V18 potential [46, 47].

Arenhövel's treatment of the electromagnetic current and the *NN* interaction is based on a one boson exchange model. These calculations were based on the Schrödinger equation. The calculations can be done in conjunction with any standard parametrization of the *NN* interaction such as the Bonn or Paris potentials. The calculations also include

the effects due to final state interactions (FSI), meson exchange currents (MEC), and isobar configurations (IC) and have been extended to include polarization observables and relativistic corrections. Mosconi *et al.*, calculations are very similar in nature to those of Arenhövel while Tjon *et al.*, calculations use a fully covariant approach based on an approximation of the B-S equation for the deuteron.

In contrast to the traditional scheme, where the full relativistic electromagnetic current operator is normally not used, a more recent approach by Jeschonnek *et al.*, uses an improved current operator to incorporate relativistic effects without any approximation in the transferred momentum or transferred energy. It has been shown that the relativistic effects in the current alone are large, and at transferred energies and momenta of a few GeV, the relativistic effect in the current make up the bulk of the total relativistic contributions. In this relativistic approach, the effect on the longitudinal-transverse response function, R_{LT} is large.

Laget uses a diagrammatic expansion approach to calculate the FSI, MEC and IC contributions. In the diagrammatic approach, the plane wave (Figure 5) and FSI (Figure 6a) amplitudes for the ^{2}H$(e,e'p)n$ channel are given by [45]:

$$\begin{aligned} T_{PW} &= \sum_{m_p} \langle m_1 \left| J_p(q^2) \right| m_p \rangle \left\langle \frac{1}{2} m_p \frac{1}{2} m_2 \right| 1 M_J \Big\rangle U_0(\vec{p_2}) \frac{1}{\sqrt{4\pi}} \\ &\quad + \sum_{m_n} \langle m_1 \left| J_n(q^2) \right| m_n \rangle \left\langle \frac{1}{2} m_n \frac{1}{2} m_1 \right| 1 M_J \Big\rangle U_0(\vec{p_1}) \frac{1}{\sqrt{4\pi}} + D \text{ wave,} \quad (43) \end{aligned}$$

$$\begin{aligned} T_{FSI} &= \sum_{\lambda_p \lambda_n m_1 m_s} \int \frac{d^3\vec{n}}{(2\pi)^3} \frac{m}{E_p(p^0 - E_p + i\epsilon)} \\ &\quad \times \left\{ (\lambda_p \left| J_p(q^2) \right| m_s - \lambda_n)(\vec{p_1} m_1 \vec{p_2} m_2 \left| T_{NN} \right| \vec{p} \lambda_p \vec{n} \lambda_n) \right. \\ &\quad \left. + (\lambda_p \left| J_n(q^2) \right| m_s - \lambda_n)(\vec{p_2} m_2 \vec{p_1} m_1 \left| T_{NN} \right| \vec{p} \lambda_p \vec{n} \lambda_n) \right\} \\ &\quad \times \left(\frac{1}{2} \lambda_n \frac{1}{2} (m_s - \lambda_n) \right| 1 m_s \Big) \\ &\quad \times \left\{ \frac{1}{\sqrt{4\pi}} U_0(p_n) \delta_{M_J m_s} \delta_{m_l 0} + U_2(p_n) (2 m_l 1 m_s \left| 1 M_J \right.) Y_2^{m_l}(\hat{n}) \right\}, \quad (44) \end{aligned}$$

where $E_p = \sqrt{m^2 + (\vec{k} - \vec{p_n})^2}$ and $p^0 = M_D + \omega - \sqrt{m^2 - \vec{p_n}^2}$. The momenta and magnetic quantum numbers of the outgoing proton and neutron are, respectively, $\vec{p_1}, \vec{p_2}, m_1$ and m_2, while the magnetic quantum number of the target deuteron is M_J. The S and

D parts of the deuteron wave function are respectively U_0 and U_2 and T_{NN} is the NN scattering amplitude. The relativistic expressions of the proton $J_p(q^2)$ and neutron $J_n(q^2)$ on-shell currents are used in both the PW and FSI amplitudes. The conventional dipole expression is used for the magnetic form factors of the proton and the neutron, while the Galster parametrization [48] is used for the neutron electric form factor and the latest JLab experimental values are used for the proton electric form factor [49]. The FSI integral runs over the momentum $\vec{n}$ of the spectator nucleon. Since the energy is larger than the sum of the masses of the two nucleons, the knocked out nucleon $(\vec{p}, \lambda_P)$ can propagate on-shell. Due to the dominance of the S-wave part of the wave function, the corresponding singular part of the integral is maximum when the scattering of the electron on a nucleon at rest is kinematically possible: this happens in the quasielastic kinematics, x_{Bj} = 1.

II.7 EXISTING DATA

The short range structure of the deuteron is best revealed by measuring very high missing momenta in ^{2}H$(e, e'p)n$. Further, separations of the cross section into the various response functions allow one to exploit the sensitivity inherent in various interferences of components of the nuclear current. The exclusive scattering cross section for ^{2}H$(e, e'p)n$ was first measured by Croissiaux [50] and since then many experiments have examined this reaction which indicates its importance to understand the nuclear electromagnetic current, the short range part of the NN force, and the deuteron structure. Several of these experiments were performed at low four-momentum transfers, $Q^2 \sim 100$ MeV^2 [51, 52], and many other experiments were performed at intermediate or relatively high $Q^2 \sim 1$ GeV^2 under quasielastic conditions [53, 54, 55, 57, 58, 59, 60, 61, 9]. In addition to measuring the unseparated cross section, some of these experiments tried to separate one or more of the electromagnetic response functions [51, 52, 53, 54, 55, 57, 58, 59, 60]. A general review of response function separations in the ^{2}H$(e, e'p)n$ reaction is given in Reference [62]. Another review of experiments which specifically separated the longitudinal-transverse interference response function is given in Reference [20]. The early experiments used this reaction to study the deuteron wave function and also as a benchmark to study the $(e, e'p)$ reaction in general because of the simple nature of the deuteron. This dissertation goes many steps further by studying this reaction at much higher Q^2, up to 3.5 GeV^2.

II.7.1 Response functions and Asymmetry Data

There are several measurements [62] of the longitudinal-transverse interference response function R_{LT} and the asymmetry A_{LT} from NIKHEF [54], Bonn [56], Saclay [55], and Bates [58]. The measured asymmetries are shown in Figure 7. All these measurements were performed in the quasielastic region with Q^2 $\sim$0.2 GeV^2. The asymmetries are compared to the calculations of Arenhövel *et al.*, with and without relativistic corrections. In addition, the NIKHEF data are also compared to the relativistic calculations of Tjon *et al.*, and both the NIKHEF data and Saclay data are compared to the calculations of Mosconi *et al.*, with relativistic corrections. In all cases, the calculations which include relativistic effects reproduce the A_{LT} asymmetries much better than those which do not. Another measurement of R_{LT} and A_{LT} was performed at NIKHEF [59] at Q^2 =0.2 GeV^2 and is shown in Figure 8 together with calculations by Tjon *et al.* and Mosconi *et al.* (with and without relativistic corrections). It demonstrates that the relativistic corrections are needed at Q^2 values as low as 0.2 GeV^2. Finally a measurement of A_{LT} at SLAC [57] for a considerably higher Q^2 $=$ 1.2 GeV^2 but at low missing momentum, is shown in Figure 9. One can see that up to missing momentum of about 120 MeV, these data are described well by the PWIA calculations using the "cc1" offshell description of de Forest [63] (which already incorporates relativity at some level) and the Paris *NN* potential.

II.7.2 Cross Section Data

An example of the ^{2}H$(e,e'p)n$ cross section is shown in Figure 10. This experiment was carried out at the Mainz microtron (MAMI) [61]. In this experiment, the ^{2}H$(e,e'p)n$ reaction cross section was measured for recoil momenta up to 950 MeV and four-momentum transfers in the range 0.13–0.34 GeV^2. At recoil momenta below about 350 MeV, the measured cross sections are well reproduced by Arenhövel calculations which include relativistic corrections. At missing momenta above 350 MeV, the agreement between theory and experiment worsens continuously. At high missing momenta above 400 MeV, the general features of the experimental cross sections can only roughly be reproduced by including MEC and, especially, IC, although the location and magnitude of the calculated structure does not fully agree with the experimental finding.

Figure 11 shows the ^{2}H$(e,e'p)n$ cross section results for a previous JLab experiment (Experiment E94-004 [9]). In this figure, the reduced cross section, σ_{red}, is related to the

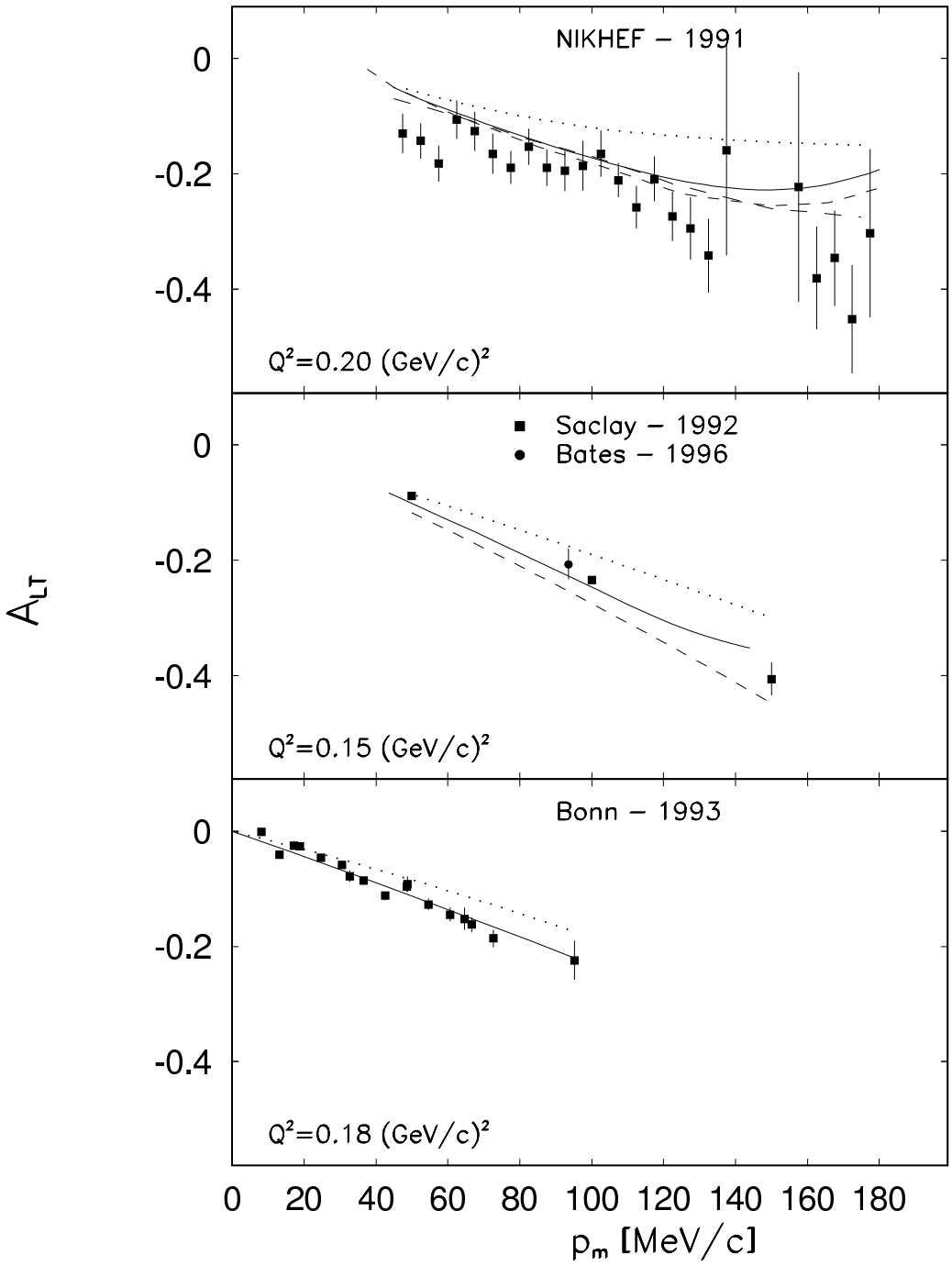

FIG. 7: The A_{LT} asymmetry for the ^{2}H$(e,e'p)n$ reaction from different measurements. Solid curves (dotted curves) are calculations by Arenhövel *et al.*, with (without) relativistic corrections. Also shown are the relativistic calculations of Tjon *et al.*, (long dashed curve) for the NIKHEF data and the calculations of Mosconi *et al.*, with relativistic corrections (short dashed curve) for both NIKHEF and Saclay data.

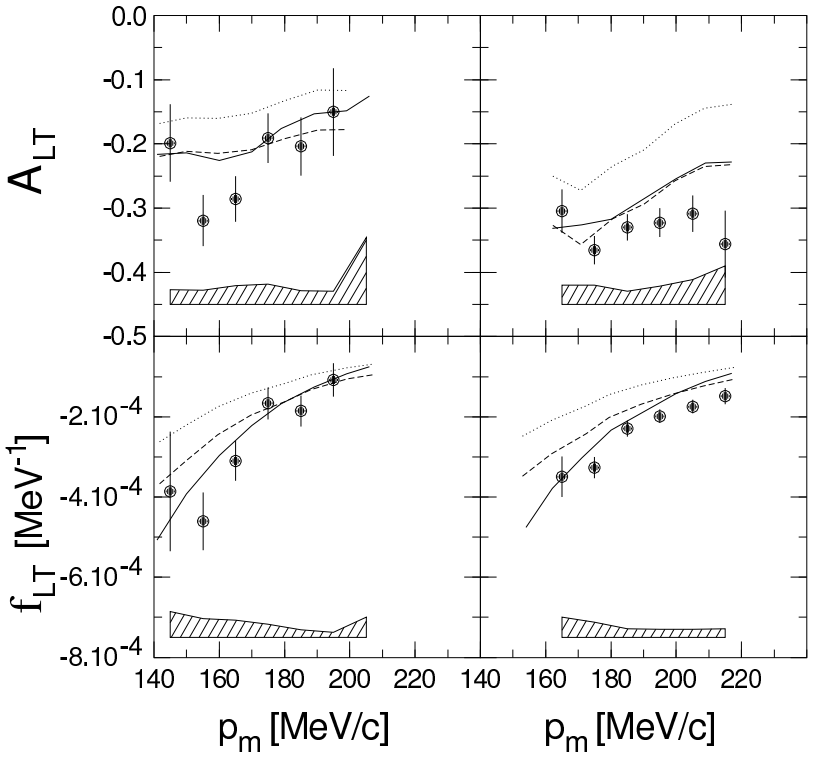

FIG. 8: The measured R_{LT} response function (referred to in the plot as f_{LT}) and A_{LT} asymmetry from NIKHEF [59]. The shaded areas indicate the size of the systematic errors. The solid curve represents the relativistic calculation of Tjon *et al.*, and the dashed (dotted) curves are calculations of Mosconi *et al.*, with (without) relativistic corrections.

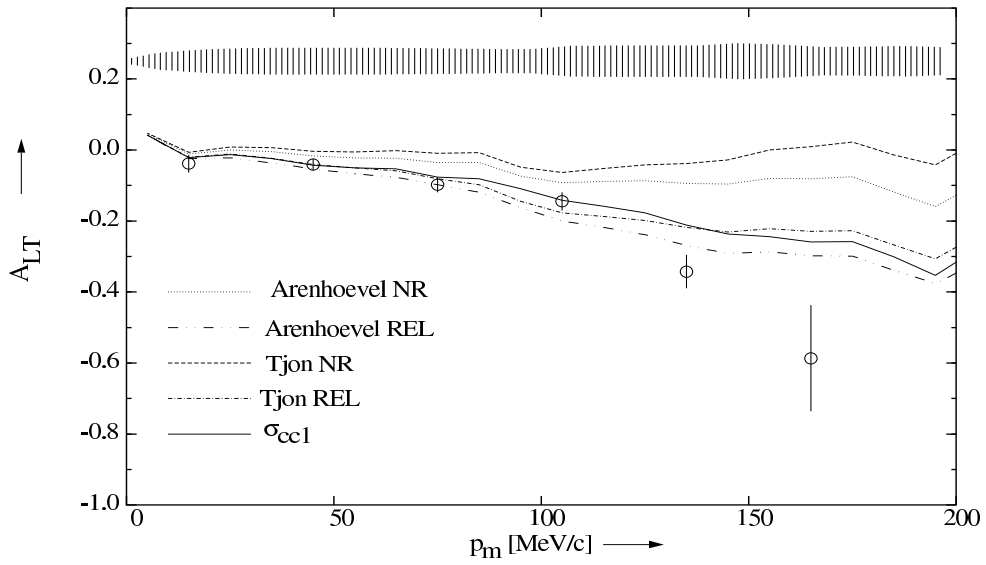

FIG. 9: The A_{LT} asymmetry at $Q^2 = 1.2$ GeV^2 measured at SLAC [57] compared with various nonrelativistic (NR) and relativistic (REL) models.

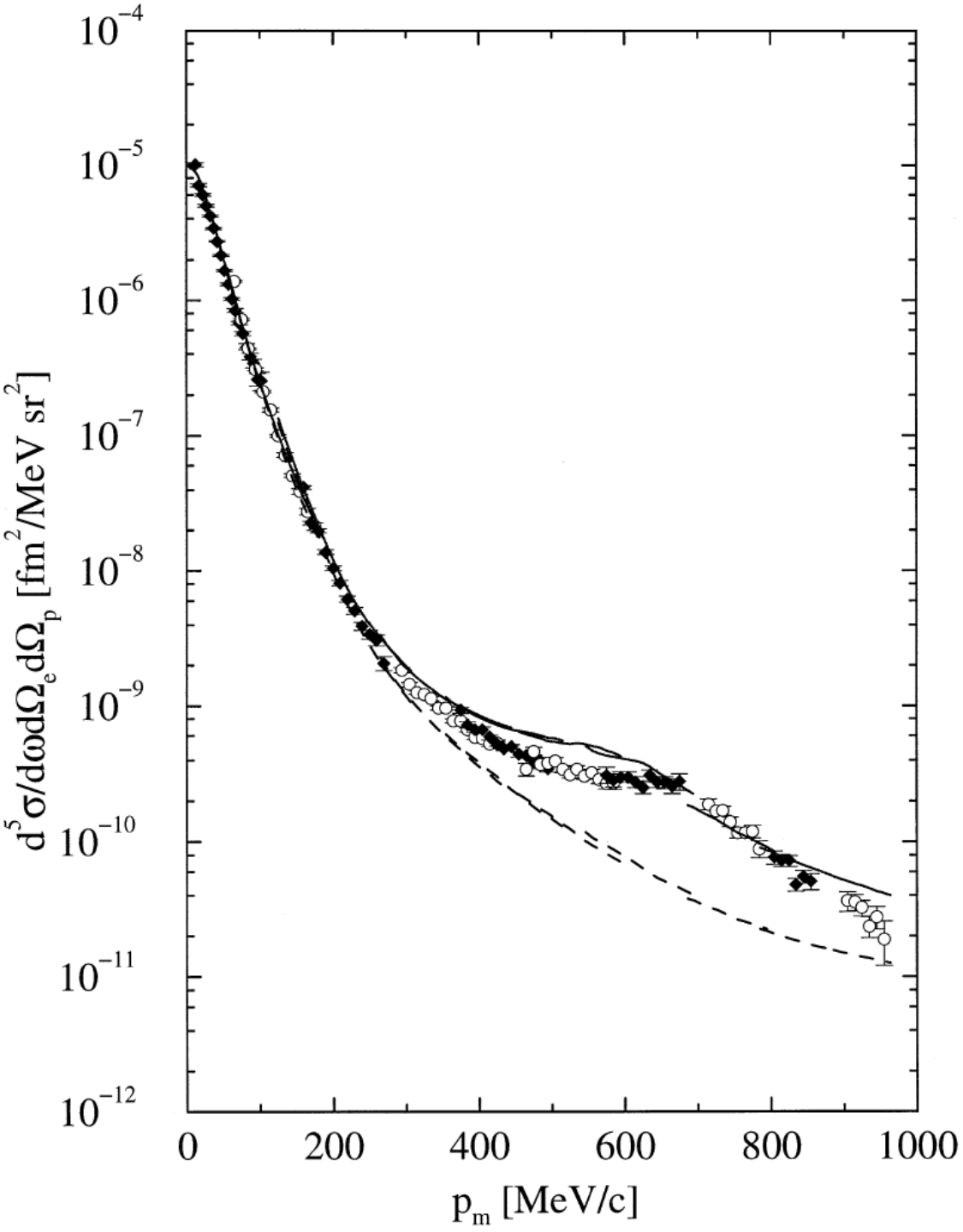

FIG. 10: Comparison of the measured ^{2}H$(e, e'p)n$ cross section at MAMI to the calculation by Arenhövel with (solid curve) and without (dashed curve) MEC and IC. The alternation of open and filled symbols indicates changes in the spectrometer central settings.

cross section given in Equation (42) through

$$\sigma_{red} \equiv \frac{d^5\sigma}{d\omega d\Omega_e d\Omega_p} \times \frac{M_d}{M_p M_n \left|\vec{p}\right| \sigma_{ep} f_{rec}} \tag{45}$$

where σ_{ep} is the half-off-shell electron-proton cross section (initial bound proton is off-shell and final proton is on-shell) [63]. The cross section was measured near the top of the quasielastic peak (Bjorken $x_{Bj} = 0.964$) at $Q^2 = 0.665$ GeV^2 and neutron recoil momentum $p_r \equiv p_n$ up to 550 MeV. At low recoil momentum, there is reasonable agreement between the data and relativistic PWBA calculations but at higher recoil momenta (p_r>300 MeV) the effects of FSI, MEC and IC must be added to maintain a satisfactory agreement with the data, especially FSI.

II.7.3 Remarks

For the cross section measurements, limitations in energy of the various facilities (Bates, Saclay, Bonn, NIKHEF, and Mainz) have frustrated attempts to access the short distance structure of the deuteron. This limitation necessarily forces measurement of very high missing momenta to energy transfers far above the quasielastic peak. Thus, for the high missing momentum Mainz data, the kinematics were in the delta-region where lack of knowledge of the reaction mechanism makes it difficult to deduce aspects of the deuteron structure. Although this limitation is not shared by SLAC data, limitations in current and duty factor restrict the range of missing momenta there as well. Although the Mainz measurement sampled missing momenta up to 928 MeV, the kinematics actually imply that the bulk of the cross section arises from interaction with the neutron, leaving the detected proton as a spectator. Within this proton spectator picture, the actual internal momentum probed in this process is not the recoil momentum, but the momentum of the detected proton (670 MeV). Further, since the kinematics were in the delta-region of the inclusive (e, e') spectrum, the inclusion of virtual nucleon excitations was required to obtain agreement with the data. In contrast, at JLAB one can examine large missing momenta at or even below quasielastic kinematics, making the extraction of the deuteron structure less model-dependent. The ^{2}H$(e, e'p)n$ separation experiments have revealed gaps in our understanding. The R_{LT} response and related A_{LT} asymmetry indicate the need for relativistic treatments but problems still exist in reproducing the data. Again, JLAB provides the kinematic flexibility to perform these separations over a broad range of missing momenta and momentum transfers.

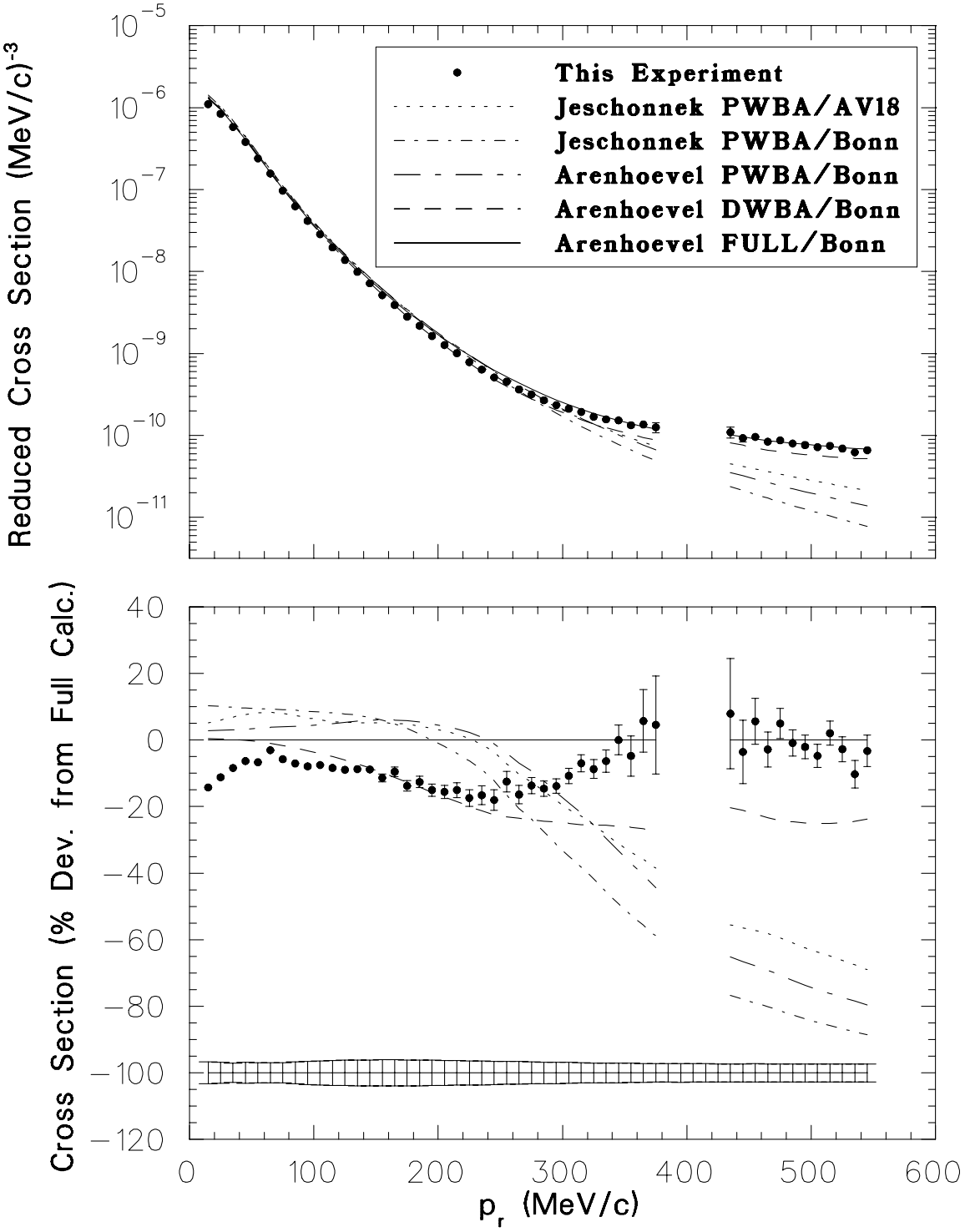

FIG. 11: The reduced ^{2}H$(e,e'p)n$ cross section for JLab Experiment E94-004, along with various model calculations [9].

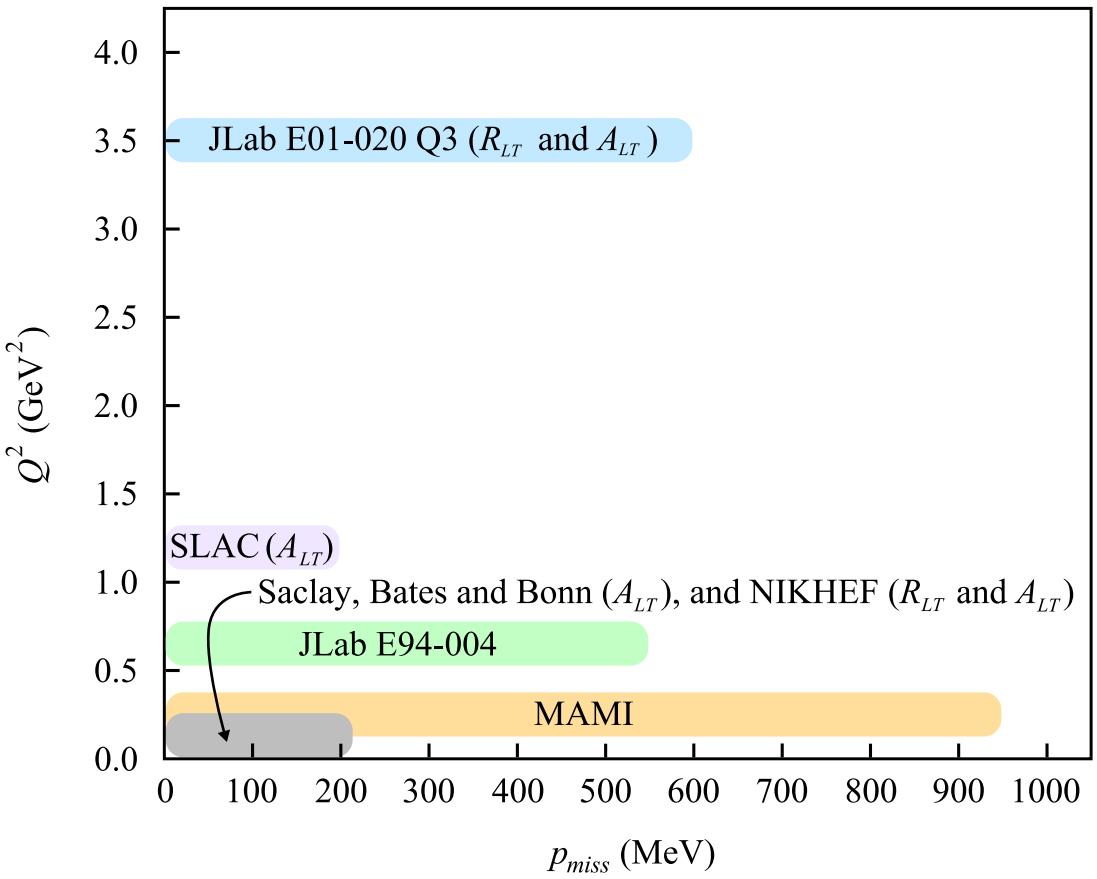

FIG. 12: Comparison of some previous ^{2}H$(e,e'p)n$ experiments to the highest Q^2 data (Q3 kinematics) from Experiment E01-020. It is clear from this graph that Experiment E01-020 was the first experiment to measure the ^{2}H$(e,e'p)n$ reaction at high $Q^2 = 3.5$ GeV^2.

A comparison of the data from some previous ^{2}H$(e,e'p)n$ experiments in addition to Experiment E01-020 is shown in Figure 12. It is very obvious from this graph that Experiment E01-020 was the first experiment of its kind to measure the ^{2}H$(e,e'p)n$ reaction at a high value of the four-momentum transfer, $Q^2 = 3.5$ GeV^2.

CHAPTER III

EXPERIMENTAL SETUP

III.1 EXPERIMENT OVERVIEW

Experiment E01-020 was performed at the world's premier medium energy nuclear physics laboratory, Thomas Jefferson National Accelerator Facility (TJNAF, or Jefferson Lab), located in Newport News, Virginia. The lab includes the Continuous Electron Beam Accelerator Facility (CEBAF) which provides a continuous wave 6 GeV electron beam with maximum currents of 200 μA by recirculating the beam up to five times through two superconducting linacs, each linac producing an energy gain of 600 MeV. Three independent slits (the "chopper") are used to individually control the current to three different experimental Halls (A, B and C). The experiment was run in Hall A. The lower and middle Q^2 kinematics of this experiment were measured in June, 2002, and the highest Q^2 was measured from mid October to mid November of the same year. Prior to the experiment many preparations and surveys were performed such as detector and angular calibrations [64, 65] to ensure the accuracy of the collected data. Also, online analysis programs were written to continuously monitor the status of the apparatus and quality of data during the experiment.

III.2 JEFFERSON LAB

Jefferson Lab [66], consists of a continuous wave electron accelerator, with three experimental halls, A, B and C, which use the electron beam to explore different aspects of nuclear physics, a free electron laser facility (FEL), and an applied research center (ARC). Hall A started taking data during May 1997. It was designed for programs requiring high precision measurements. Hall B has operated since December 1997. Its almost 4π acceptance makes it an ideal device to study multi-particle final states. Hall C has been operational since November 1995 and is used for major set-up experiments, which require complex dedicated apparatus.

The electron accelerator at Jefferson Lab, CEBAF, [67] is capable of delivering high quality continuous electron beams up to 6 GeV. The accelerator was approved for construction in 1987 and became operational in 1994. It was designed to provide the nuclear

physics community with a state-of-the-art laboratory for studying nuclear structure. Its design combined the latest achievements in accelerator technology to produce a continuous, high energy, high current, and high polarization electron beam. Future plans of CEBAF include upgrades to 12 GeV and the addition of a new experimental hall (Hall D). The accelerator site layout is shown in Figure 13.

The electron beam is produced at the "injector" by illuminating a photocathode with a laser beam, then accelerating the electrons to 67 MeV. The resulting electron beam is further accelerated in each of two superconducting "linacs" (North and South Linear Accelerators) located 10 m below ground, through which it can be recirculated up to five times, each pass producing an energy gain of 1.2 GeV. Each linac contains roughly 20 "cryomodules". Each cryomodule contains eight superconducting (SC) five-cell niobium "cavities". Electrons are accelerated by the electric field of 1497 MHz microwaves injected in the cavities and cause the electrons in the niobium metal to concentrate in certain areas (become negatively charged) and depleted from other areas (become positively charged). The electrons in the beam are periodically attracted towards the positively charged areas and are repelled from the negatively charged areas as illustrated in Figure 14. In this figure, the induced microwave signal changes periodically the locations of the positively charged cavity edges to always attract the electrons in the forward direction. The cavities are kept at a temperature of about 2 K by bathing their outside surfaces with superfluid ^{4}He. The superconducting state of the cavities allows the transfer of almost the entire microwave power into the acceleration of the beam[1]. Due to the relatively low electron mass, ≈ 0.5 MeV, electrons with different energies move through the linacs with essentially identical velocities close to the speed of light ($c \approx 3 \times 10^8$ m/s), and are accelerated together in the same electron packets. The distance between the moving packets is $3{\times}10^8$ m/s / 1497 MHz $\approx$ 20 cm, which is equal to the longitudinal periodicity of the cavity shape. The length of each electron packet is about 0.5 mm.

The beam can be delivered "simultaneously" to each of the three experimental halls, A, B and C. The beam current for each hall can be controlled independently. The design maximum current is 200 μA, which can be split arbitrarily between three interleaved bunch trains. One such bunch train can be delivered after any linac pass to any one of the Halls using Radio-Frequency (RF) separators and septa. All Halls can simultaneously receive the maximum energy beam. Hall B with its CEBAF Large Acceptance Spectrometer (CLAS)

[1]At room temperature, the electric currents in the cavities would produce large amount of heat which eventually could damage the cavities unless the accelerator shuts down periodically to allow the cavities to cool down. In this case, the duty factor of the accelerator would be reduced significantly.

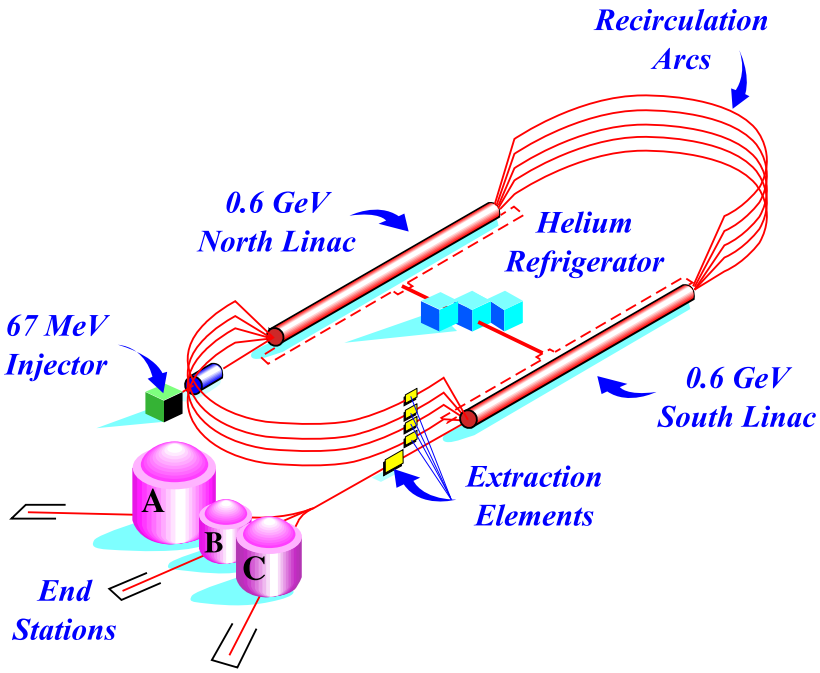

FIG. 13: The Continuous Electron Beam Accelerator Facility (CEBAF).

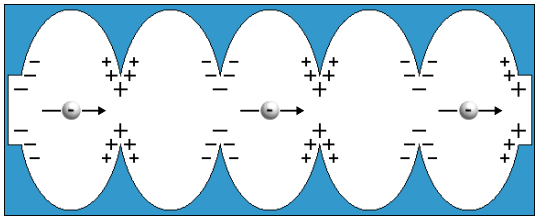

(a) Positive cell boundries attract the electrons.

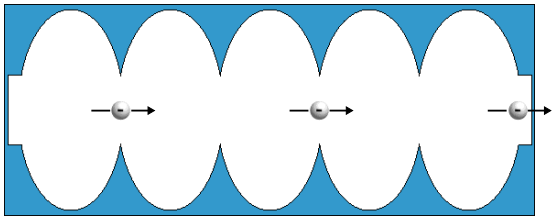

(b) Electrons are freely crossing the cell boundries.

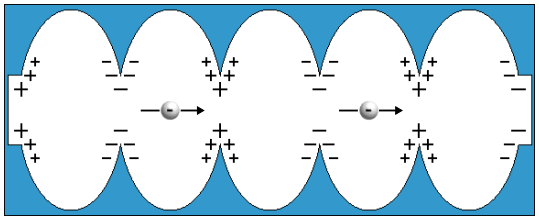

(c) The new positive cell boundries attract the electrons again and so on.

FIG. 14: Acceleration of electrons in a typical CEBAF superconducting cavity.

[68] requires currents as low as 1 nA, while up to 120 μA currents are typically delivered to one or even both of the other two Halls.

III.3 HALL A

The present base instrumentation in Hall A [69, 70] has been used with great success for experiments which require high luminosity and high resolution in momentum and/or angle for at least one of the reaction products. Figures 15, 16 and 17 show different views of the Hall A layout. The hall is circular in shape and has a diameter of 53 m and a height of about 20 m. The bulk of the volume of the hall is underground, well shielded to contain radiation with concrete and a thick layer of earth. The electron beam enters the hall via a vacuum pipe, and passes through several quadrupole magnets and through systems for beam rastering and measurement of beam current, position and energy. Just before reaching the center of the hall, the electron beam enters a cylindrical aluminum scattering chamber. The scattering chamber contains a vertical assembly of targets. The whole assembly inside the chamber can be remotely moved in the vertical direction, exposing the desired target to the beam.

The majority of electrons in the beam do not substantially interact with the material in the scattering chamber and pass through to a shielded beam dump. Some of the scattered electrons and knocked-out protons enter either of the two 4 GeV high resolution magnetic spectrometers, labeled left high resolution spectrometer (HRS-L or Left Arm) and right high resolution spectrometer (HRS-R or Right Arm). The spectrometers are used for measurement of particle trajectories, momenta, relative timing, and particle identification. Each spectrometer consists of three quadrupole and one dipole superconducting magnets which use liquid helium at 4.5 K as coolant. The QQDQ magnet configuration was selected to achieve a momentum resolution of about 2×10^{-4} and horizontal angular resolution of about 2 mrad at the design maximum central momentum of 4 GeV. The main part of the detector package in the two spectrometers, trigger scintillators and vertical drift chambers (VDC), are identical, whereas the arrangement of particle identification (PID) detectors differs slightly. The tracking information (position and direction) is provided by a pair of VDCs. The triggering and timing information are provided by the scintillators. The PID information is obtained from a variety of Čerenkov detectors (silica aerogel and atmospheric pressure CO_2 gas) and a lead glass electromagnetic calorimeter. The following sections will provide more details about the Hall A instrumentation.

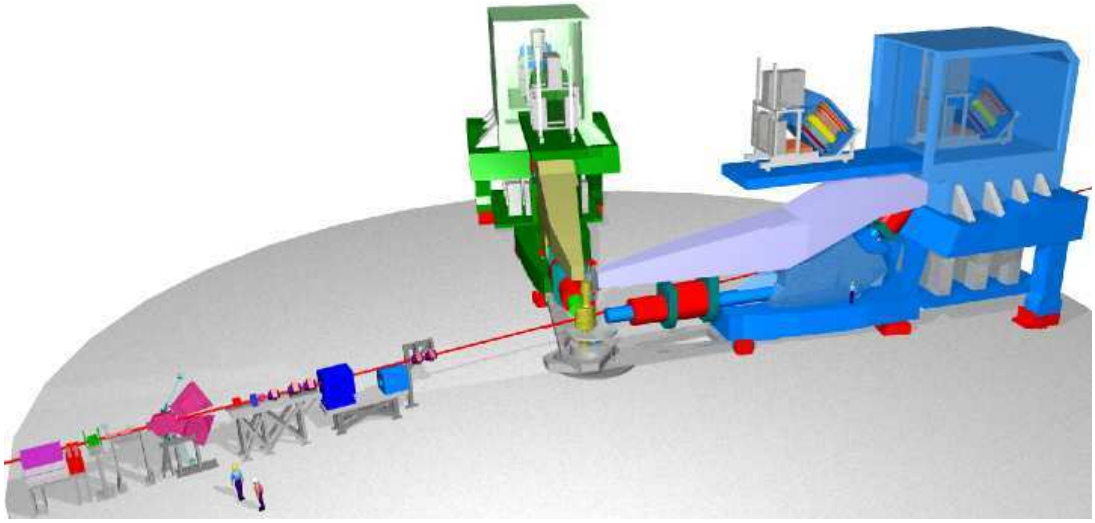

FIG. 15: 3D view of Hall A.

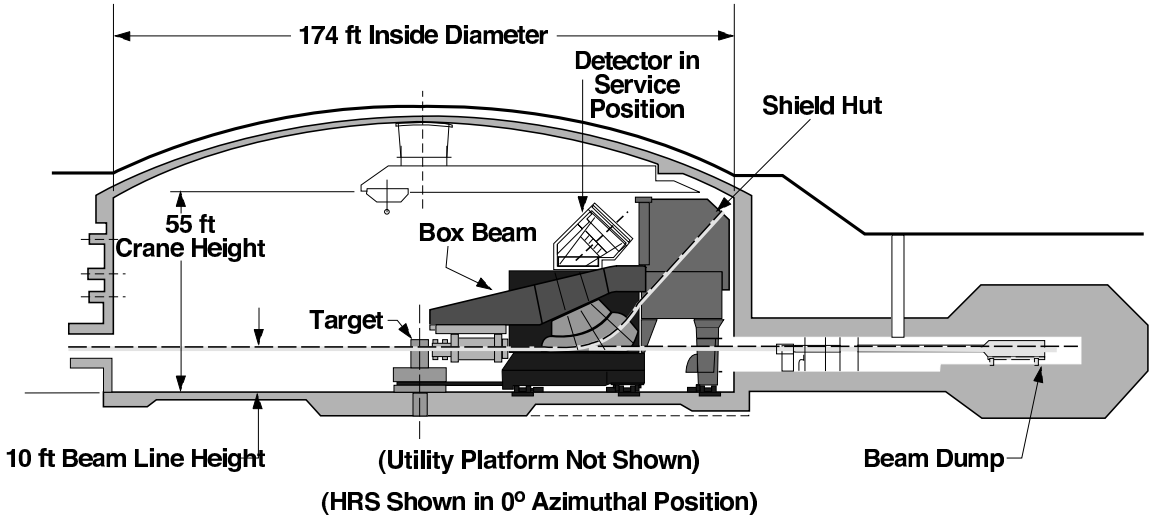

FIG. 16: Side view of Hall A.

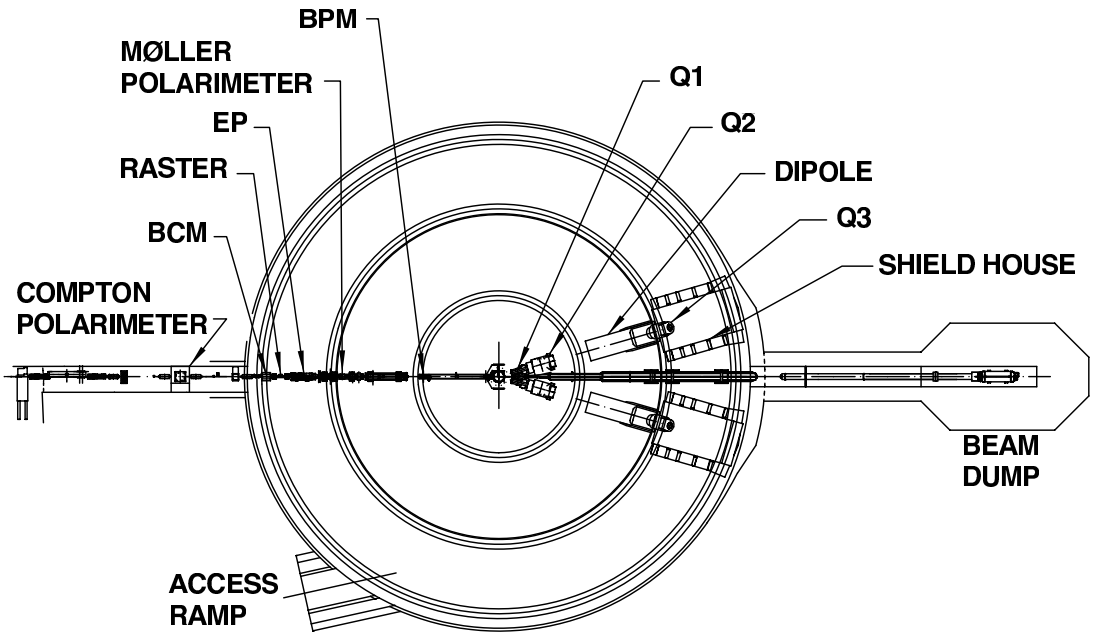

FIG. 17: Top view of Hall A.

III.4 BEAMLINE

III.4.1 Beam Energy Measurements

The absolute beam energy for Hall A is measured by two independent methods: the "Arc" method based on the deflection of the beam in a known magnetic field in the arc section of the beam line just prior to the entrance of the Hall A, and the "eP" method, based on elastic electron-proton scattering in a special device inside Hall A [71]. Each method can provide an accuracy of $\Delta E_{Beam}/E_{Beam} \sim 2 \times 10^{-4}$.

III.4.1.1 Arc Measurement

The Arc measurement is based on the principle that an electron in a constant magnetic field has a circular trajectory with a radius which depends on the magnitude of the magnetic field and the electron's momentum. This method measures the deflection of the beam in the section of the beam line between the beam switch-yard and the hall entrance known as the "Arc" section.

Figure 18 shows the setup used for the Arc measurement. A measurement of the magnetic field integral, $\int Bdl$, is made at the ninth reference dipole which is not part of the

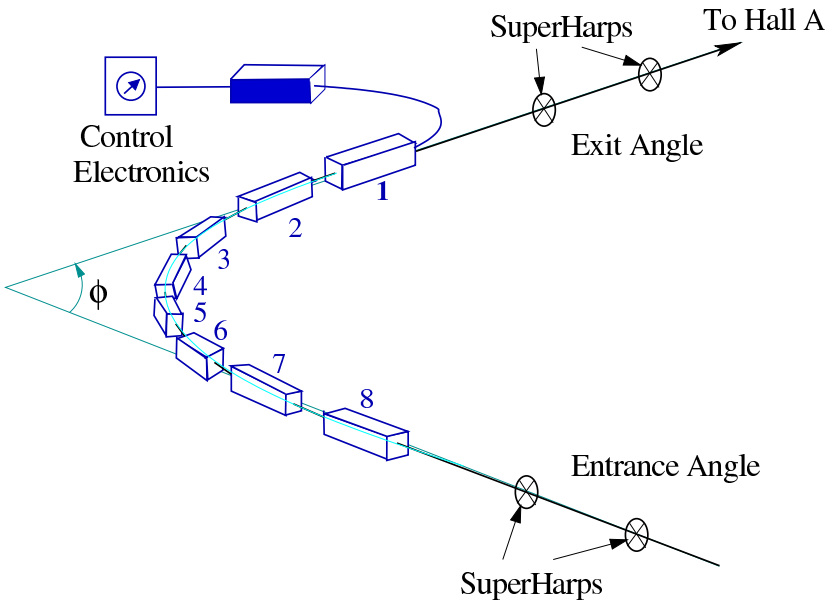

FIG. 18: The Arc section of the beamline consists of eight dipoles and a ninth reference dipole.

beamline, but is powered in series with the eight dipoles used to bend the beam into Hall A. Measurements are also made of the bend angle, θ, of the beam by using a set of invasive wire scanners called "superharps". The superharps are moved across the beam path. When the beam strikes a wire, the particles scattering off the wire are collected by a simple ion chamber; hence a current is generated and the beam position is recorded.

The electron momentum, and therefore its energy, can be calculated in this case by:

$$p = \frac{c \int_0^l B dl}{\theta} \tag{46}$$

where c is the speed of light, θ is the deflection angle, B is the component of magnetic field perpendicular to the particle's trajectory and dl is the path length of the electron.

III.4.1.2 eP Measurement

The eP method utilizes a device along the beamline located 17 m upstream of the target. The device measures the resulting angles of the ejected electron, θ_e, and the recoil proton, θ_p, during the elastic scattering of the beam on protons in a thin polyethylene (CH_2) target. A schematic diagram of the eP energy measurement system is shown in Figure 19. The

beam energy is calculated by:

$$E_{Beam} = M_p \frac{\cos\theta_e + \sin\theta_e/\tan\theta_p - 1}{1 - \cos\theta_p} + O(m_e^2/E'^2) \tag{47}$$

where M_p is the proton mass and m_e and E' are the electron mass and scattered energy, respectively. Terms of order m_e^2/E'^2 are neglected (the error due to this approximation is one part in 10^8). The proton angle is always fixed at values near 60°, while the electron angle is in the range from 9° to 41° depending on the beam energy, which can range from 0.5 to 6 GeV. The respective particles are detected in a vertical plane using silicon micro-strip detectors (SSD). Seven electron detectors with dimensions 12.8×12.8 mm^2 are located in each arm. Each detector is equipped with an associated scintillator and Čerenkov counter. In addition there is a proton detector with dimensions of 51.2×25.6 mm^2 placed at precisely 60° in the vertical plane of each arm. Each proton detector has two scintillators for triggering and time-of-flight measurement purposes. Furthermore, each SSD is equipped with an additional detector oriented perpendicularly to it. This detector is used to make measurements in the transverse plane, which is needed to improve the accuracy as well as to distinguish between background and elastic events.

The eP beam energy measurements were not used in the final analysis of this dissertation (see Subsection IV.1.1).

III.4.2 Beam Raster

In an effort to reduce beam-induced target density changes and prevent damage from depositing too much beam power in a very small area, the beam is rastered before it hits the target. The hardware for this "fast" rastering system is located 23 m upstream of the target, between the beam current monitors and the eP energy measurement system. The fast rastering system consists of two sets of steering magnets. The first set has its magnetic field oriented so as to deflect the beam horizontally and the second set has its magnetic field oriented to deflect the beam vertically. The magnetic fields of the deflecting coils were varied sinusoidally, at 25.3 kHz in the horizontal direction and 17.7 kHz in the vertical direction. The ratio of the oscillation frequencies of the two coils was chosen so that the resulting raster pattern would sweep out a rectangular pattern at the target. The beam position on an event by event basis is shown in Figure 20. Since the beam rastering was sinusoidal, the beam spent more time around the edges of the raster pattern than at the center.

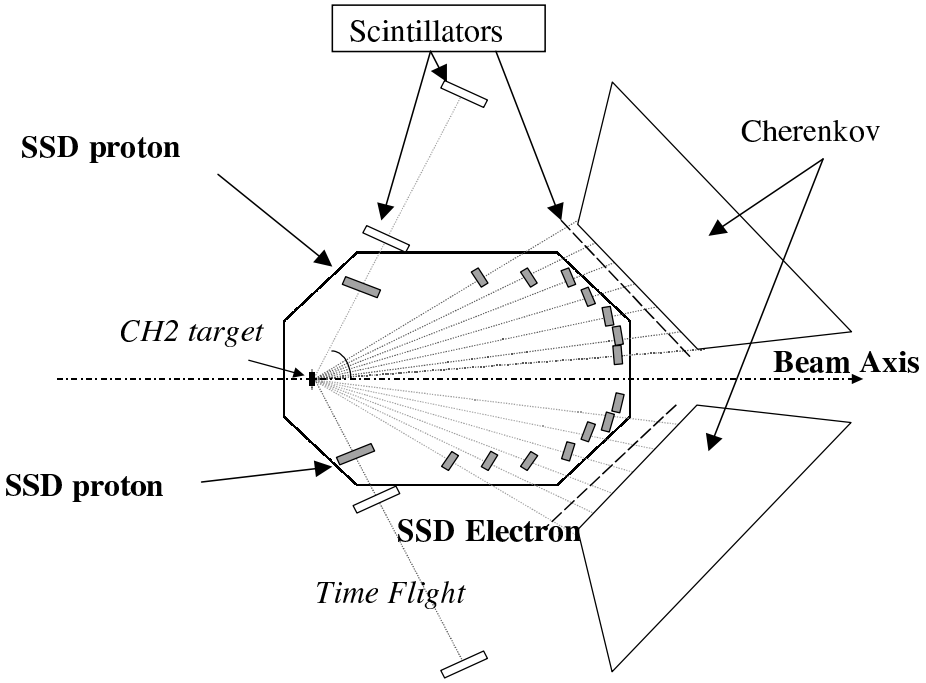

FIG. 19: EP Beam energy measurement.

III.4.3 Beam Position Monitors (BPMs)

The beam position monitor (BPM) is a device for non-invasive continuous measurement of the position of the beam. Each of the employed BPMs has a cavity with four antennae as shown in Figure 21, each oriented parallel to the nominal beam direction and located symmetrically around the nominal beam position. The electron beam passing through the cavity induces signals in the antennae, with amplitudes inversely proportional to the distance from the beam to each of the antennae. The Analog-to-Digital Converter (ADC) readouts from pairs of antennae are combined with calibration coefficients to yield the beam position in each of the two directions.

The position and direction of the beam at the target for each scattering event was measured by the last two BPMs, located 7.524 m and 1.286 m upstream from the nominal

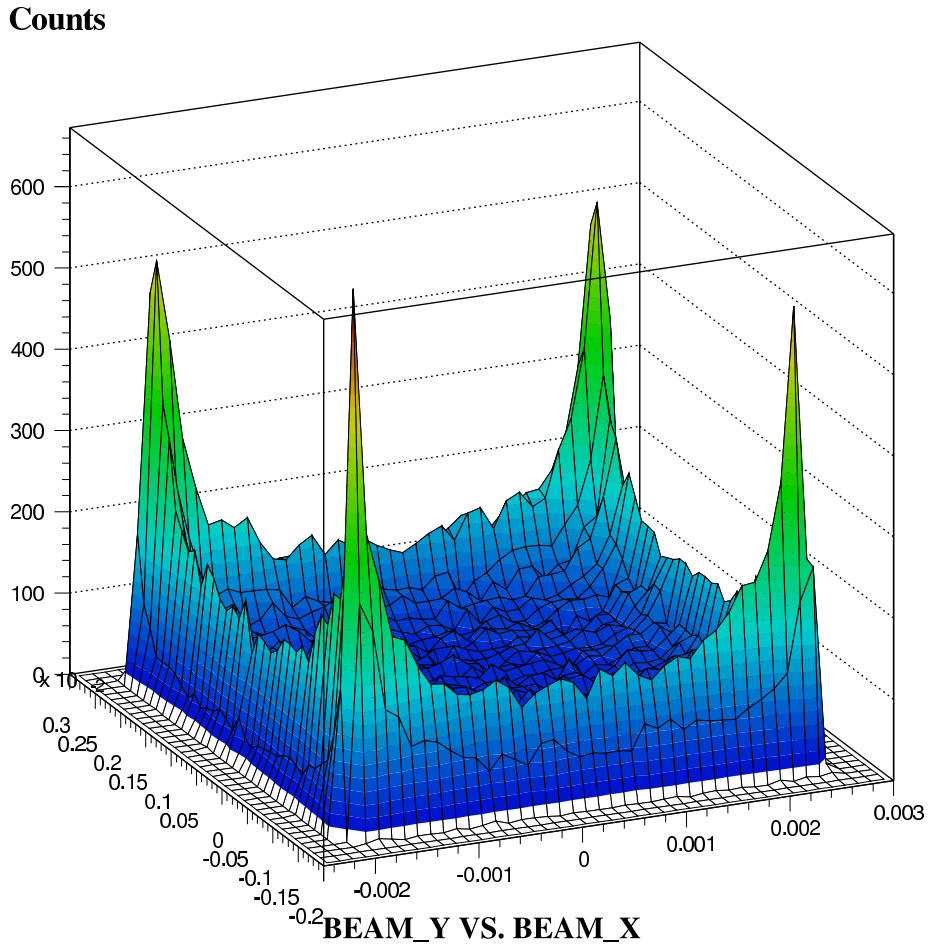

FIG. 20: Rastered electron beam profile. Beam positions are in meters.

target center (BPMA and BPMB). The "Burst Mode" readout of the BPMs[2] allows to precisely track the motion of the beam due to rastering for each event. In burst mode, the beam position is sampled six times per event, with intervals of 4 μs. For each event, amplitude, offset and phase of the beam position is fitted and the corrected beam position can be calculated correctly. The advantage of the Burst mode BPM readings is that this calibration is independent of the beam tune, thus also of beam energies. After the necessary corrections, the beam positions at the two BPMs are extrapolated linearly to the interaction point in the target during event reconstruction. The precision of the measurement of both the vertical and horizontal angles of the beam at the target is about 0.3 mrad.

[2]This mode was not used for the Q3 kinematics because of a hardware problem in the associated "readout controller" (ROC 14). This controller is located in a high radiation area in Hall A and tends to crash quite often. In this case, a two-pass analysis is necessary to determine the actual beam positions for each run (see Subsection IV.1.2.2).

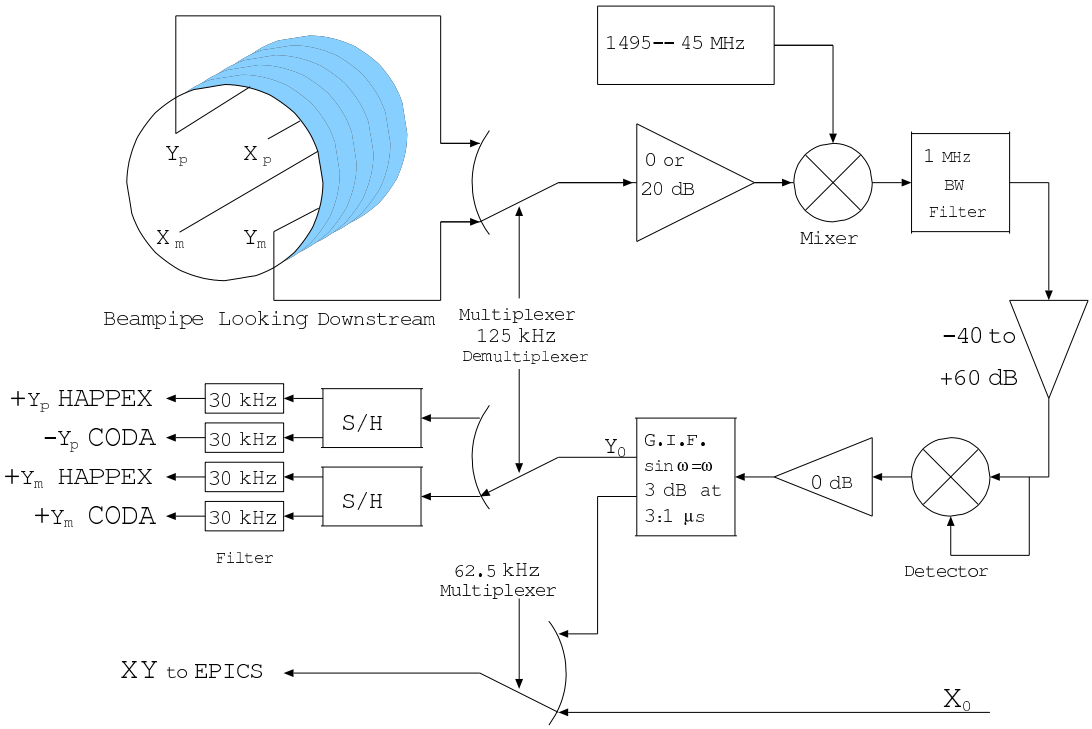

FIG. 21: Beam Position Monitors.

Another invasive method to measure the beam position and profile is via wire ("harp") scanners. The method involves moving differently oriented wires across a low current beam (< 5 μA) along with readout of induced wire signals. The adjacent harp scanners to BPMA and BPMB (Harp5 and Harp6), are surveyed relative to the Hall Coordinate System (see Subsection III.7.1), and are used for calibration of the BPMs in the so-called "bull's eye scan" procedure. During the analysis of this dissertation, we found that the measured rastered beam position needs to be corrected by using two different scale factors for the horizontal and vertical directions respectively (see Subsection IV.1.2.3).

III.4.4 Beam Current Monitors (BCMs)

There are two identical beam current monitor (BCM) cavities and, between them, one "Unser" current monitor located about 25 m upstream from the target center in Hall A (see Figure 22). The Unser monitor (named after CERN scientist Klaus Unser) is a parametric current transformer (PCT) which is simply a toroidal transformer designed for non-invasive beam current measurement. The Unser current monitor is calibrated by passing a precisely known current in a wire running along the inside of the PCT. The Unser monitor

is used to calibrate the two Hall A BCMs at high beam currents (see Subsection IV.1.3).

The BCM is also a device for non-invasive continuous measurement of the beam current. It consists of a stainless steel cylindrical cavity, 15.48 cm in diameter, and 15.24 cm in length, with the cylinder axis coinciding with the nominal beam position. Resonant frequencies of the cavities are tuned to the frequency of the beam. Inside each cavity there are two loop antennae, one of which provides an output signal proportional to the beam current. The RF output signal from the cavity is converted to a 10 kHz signal by a down-converter and fed to an RMStoDC converter board with a 50 KHz bandpass filter. After this conversion, two output signals are produced:

1. One is sent to a high precision digital AC voltmeter which produces a digital output as the RMS value of the input signal averaged over a one second period. The conversion of the voltage to current for each cavity has to be determined in a calibration procedure.

2. The other is split into three signals; each sent to an amplifier with relative gains of of $1\times$, $3\times$ and $10\times$. The $1\times$ signal should not be used below 10 μA. The $3\times$ gain can be used for beam currents up to 100 μA. The $10\times$ amplified signal is used to measure currents up to about 35 μA. Each amplified signal is then sent to an RMStoDC converter and the resulting DC voltage level is sent to a voltage-to-frequency converter (V-to-F). The output from the V-to-F is sent to a scaler. The number of counts measured by the scaler is proportional to the integrated charge. The constant of proportionality between the V-to-F frequency and current has to be determined (see Subsection IV.1.3).

III.5 TARGET SYSTEM

III.5.1 Scattering Chamber

The scattering chamber used in this experiment consisted of three sections. The bottom section was fixed to the spectrometer pivot in Hall A. This section contained several viewports through which the targets could be visually inspected and several ports for vacuum pumps. The middle section, where the beam interacted with the target, was an aluminum cylinder with an inner diameter of 104 cm, a height of 91 cm and a wall thickness of 5 cm. The beam entrance and exit pipes were coupled directly to this central section, so the beam passed through no material before interacting with the target. Scattered particles exited the

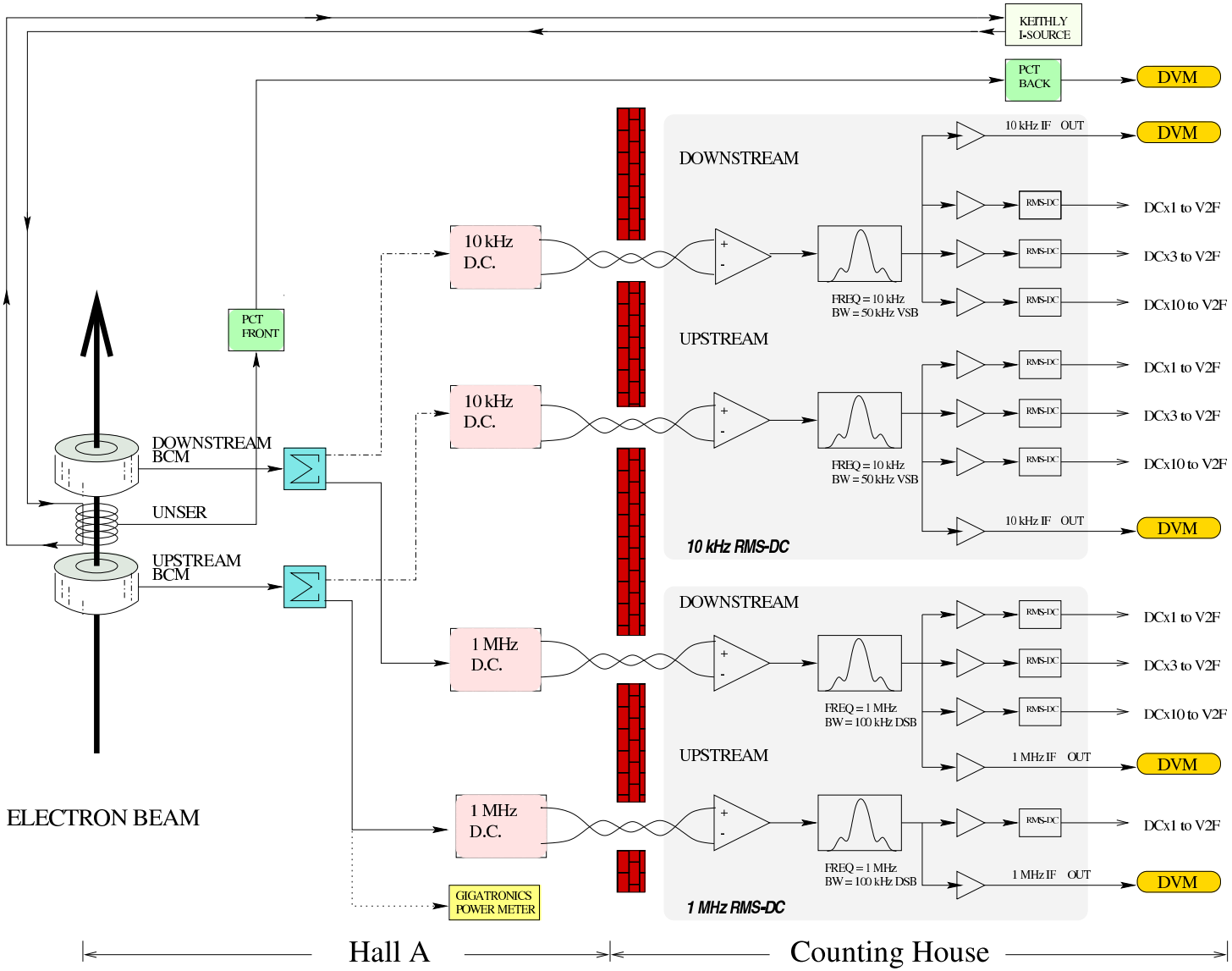

FIG. 22: Hall A BCM System.

scattering chamber to the spectrometers through aluminum windows. Both exit windows were 18 cm tall and together these windows span about 93% of the scattering chamber's circumference, interrupted only by supports for the beam entrance and exit and four additional smaller support rods spaced around the circumference. The scattering chamber exit windows for both the electron and hadron spectrometer were made of 0.016 inch thick aluminum sheet (5052-H34 alloy, density: 2.68 g/cm^3). The third and uppermost section of the scattering chamber contained space for the cryogenic target plumbing and instrumentation related to its coolant. All three sections of the scattering chamber were maintained under vacuum. Besides reducing multiple scattering, the chamber vacuum served as an insulator which helped keep the cryogenic target cold. The vacuum level was carefully maintained at the 10^{-6} Torr level. Any degradation in the scatting chamber vacuum was quickly noted, as it led to an increase in temperature of the cryogenic target.

III.5.2 Cryotarget

The cryogenic target system is mounted inside an evacuated scattering chamber along with sub-systems for cooling, gas handling, temperature and pressure monitoring, target control and target motion (to change the target remotely), and an attached "dummy", optics and solid target ladder. Figure 23 shows the target ladder used in this experiment [72]. Shown in this figure are the three cryogenic target loops, the two aluminum "dummy" targets that were used to estimate the contribution from the target cell windows and the several solid targets that were used for various calibration purposes. Two of the cryotarget loops were filled with liquid hydrogen (LH_2) and liquid deuterium (LD_2). Each loop has two horizontal cylindrical target aluminum cells (cigar-shaped tubes), 15 cm and 4 cm long, with their axes along the beam direction where the interactions happen. The liquid targets are cooled by 15 K helium. Table III lists the operating conditions for the liquid targets. The cell material is Al 7075 T6 for each of the loops and Al 6061 T6 for the dummy targets. The nominal side thickness of each cell is 0.005 inches. The variation in thickness is < 10% over the length of the tube. The nominal diameter of each cell is 4.066 cm. The target system components were slightly different for the two run periods of Experiment E01-020. Tables IV, V and VI list the two target configurations for E01-020. Figure 24 shows the corresponding ladder diagrams.

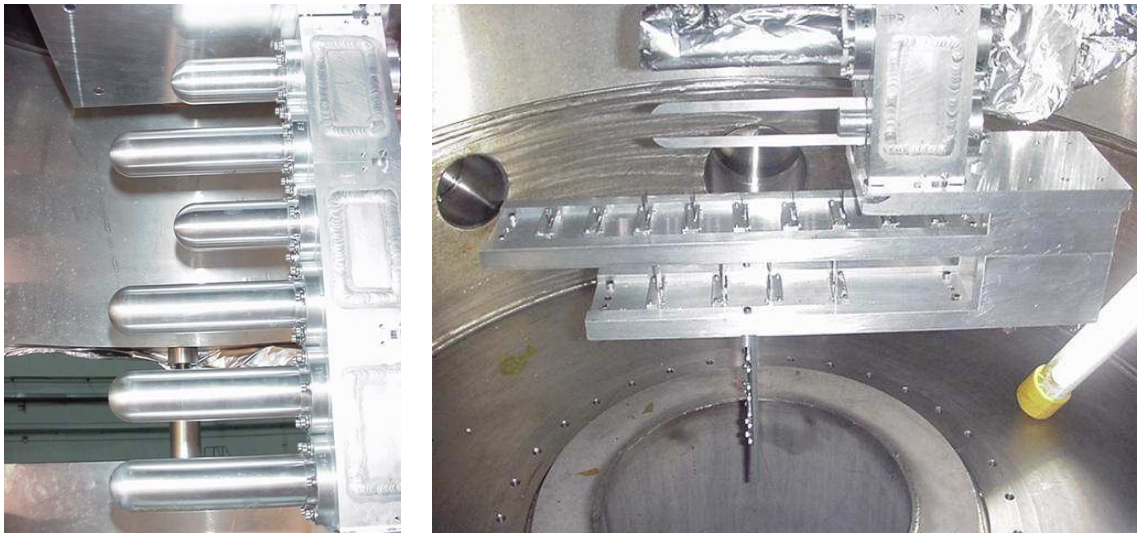

(a) Three liquid target cells. (b) Flow diverters, two dummy, and several solid targets.

FIG. 23: Cryotarget and solid target ladders.

TABLE III: Operating Conditions for the LH_2 and LD_2 loops.

Target Type	Temperature (K)	Pressure (psi)	Density g/cm^3
LH_2	19	25	0.0723
LD_2	22	22	0.1670

TABLE IV: Target configuration for the Q1 and Q2 Kinematics.

Target Type	Encoder Position	Material	Length or Thickness	Front Window Thickness	Back Window Thickness
Loop 1 Top Cell	7026466	LD_2	4 cm	0.142±0.003 mm	0.150±0.003 mm
Loop 1 Bottom Cell	6270242	LD_2	15 cm	0.124±0.003 mm	0.127±0.003 mm
Loop 2 Top Cell	5554978	LH_2	4 cm	0.114±0.003 mm	0.130±0.003 mm
Loop 2 Bottom Cell	4839714	LH_2	15 cm	0.114±0.003 mm	0.140±0.003 mm
Optics Carbon	2658338	Pyrolitic Graphite	32 cm	-	-
Top Dummy	2269320	-	15 cm	269.94±0.5 mg/cm^2	271.46±0.5 mg/cm^2
Bottom Dummy	2139272	-	4 cm	205.24±0.8 mg/cm^2	206.20±0.8 mg/cm^2
Thin Carbon	1505288	Pyrolitic Graphite	110.9±0.8 mg/cm^2	-	-
Thick Carbon	1180168	Pyrolitic Graphite	594.3±0.8 mg/cm^2	-	-
BeO	529898	BeO (99.99% pure)	369.2±0.5 mg/cm^2	-	-

TABLE V: Target configuration for the Q3 Kinematics.

Target Type	Encoder Position	Material	Length or Thickness	Front Window Thickness	Back Window Thickness
Loop 1 Top Cell	6969289	LH_2	15 cm	0.126 mm	0.128 mm
Loop 1 Bottom Cell	6251977	LH_2	4 cm	0.136 mm	0.138 mm
Loop 2 Top Cell	5536717	LD_2	15 cm	0.126 mm	0.128 mm
Loop 2 Bottom Cell	4821450	LD_2	4 cm	0.136 mm	0.138 mm
Optics Carbon	2708170	Pyrolitic Graphite	32 cm	-	-
Top Dummy	2185032	-	15 cm	269.94±0.5 mg/cm^2	271.46±0.5 mg/cm^2
Bottom Dummy	2055984	-	4 cm	205.24±0.8 mg/cm^2	206.20±0.8 mg/cm^2
Thin Carbon	1422000	Pyrolitic Graphite	110.9±0.8 mg/cm^2	-	-
Thick Carbon	1096880	Pyrolitic Graphite	594.3±0.8 mg/cm^2	-	-
BeO	446640	BeO (99.99% pure)	369.2±0.5 mg/cm^2	-	-

TABLE VI: Optics target foil thicknesses. Foil number 1 is the most upstream foil and foil number 9 is the most downstream foil.

	Kinematics	
Foil Number	Q1 and Q2 Thickness (mg/cm^2)	Q3 Thickness (mg/cm^2)
1	50.94±0.7	86.18±0.7
2	51.19±0.7	50.60±0.7
3	51.59±0.7	52.93±0.7
4	50.72±0.7	52.55±0.7
5	49.38±0.7	53.64±0.7
6	50.22±0.7	51.93±0.7
7	51.59±0.7	52.50±0.7
8	53.08±0.7	50.46±0.7
9	49.03±0.7	52.03±0.7

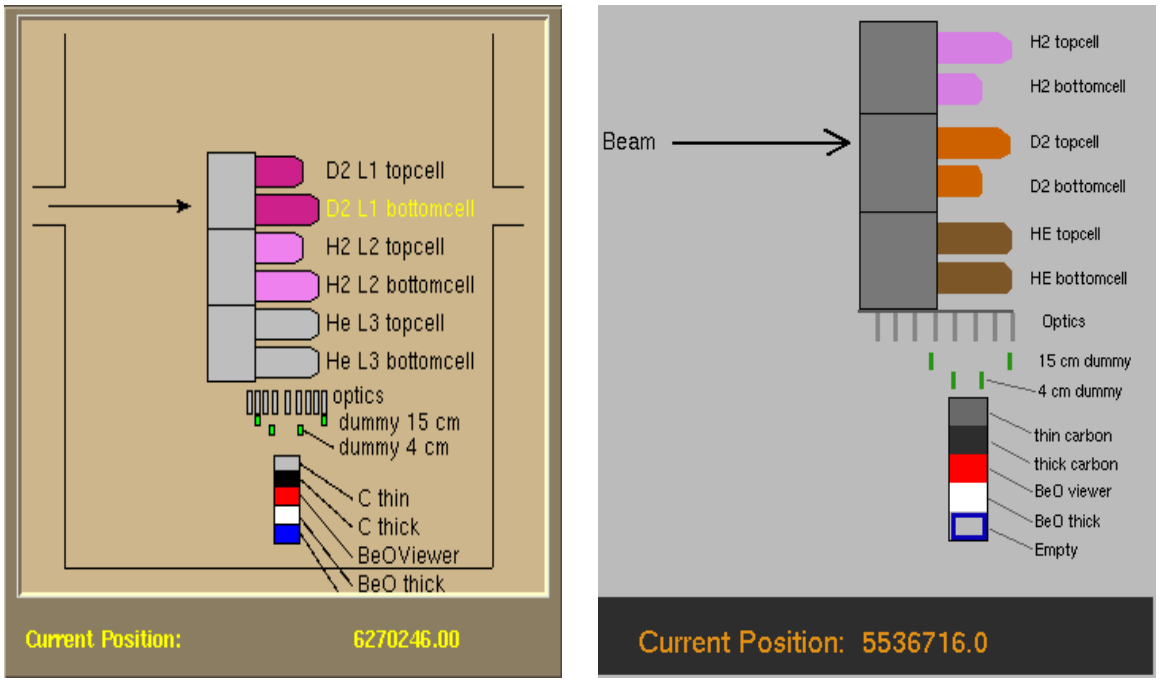

(a) Q1 and Q2 Kinematics.

(b) Q3 Kinematics.

FIG. 24: Target Configurations.

III.5.3 Gas Purity

A Gas Chromatography analysis of the deuterium target gas (used in the target loops after liquefaction) was performed by Merlin Microscienc, Inc. [73]. The purity of the deuterium gas was found to be 99.8% where the largest contamination were HD (deuterium hydride) at 0.19%, and hydrogen at less than 100 ppm (part-per-million). Therefore it is assumed that the contamination in the target cell is negligible and no correction to density was applied in the analysis. Another deuterium sample was analyzed by Mass Spectrometry at Atlantic Analytical Laboratory [74]. For this sample, deuterium molecules and atoms were found to be more than 99.6% of the sample with HD the largest contamination at 0.3% and water vapor at about 400 ppm.

III.5.4 Dummy and Solid Target Ladder

Attached to the bottom of the cryotarget ladder was a solid target ladder. A multifoil carbon target was used along with the thin and thick carbon targets for the optics optimization. The two dummy targets (aluminum flat plates, separated by 15 cm and 4 cm respectively), could be used to estimate the contribution of the target aluminum windows to the cross sections for other Hall A experiments (In this experiment, a target length cut was used to exclude the contributions of the cell windows to the cross section). Next on the solid target ladder was the beryllium-oxide target (BeO). When the beam is incident on a BeO target, it causes the target to glow brilliantly. This target is used for a visual check that the beam is present and in the correct position. At the bottom of the solid target ladder is the empty target, which is essentially an aluminum foil with a circular hole cut in it through which the beam goes straight through the scattering chamber to the beam dump.

III.6 SPECTROMETERS

The core of the Hall A equipment is a pair of identical 4 GeV high resolution spectrometers (HRSs) and use the QQDQ configuration of superconducting magnets to deflect charged particles into their focal planes. The vertical bending design includes a pair of superconducting Quadrupoles followed by a 6.6 m long Dipole magnet with focusing entrance and exit pole faces, including additional focusing from a field gradient in the dipole. Following the dipole is a third superconducting Quadrupole. The second and third quadrupoles of each spectrometer are identical in design since they have similar field and size requirements. The main design characteristics of the HRSs are shown in Table VII.

The two high resolution spectrometers (HRS) are nominally identical. At the focal planes the particles, dispersed vertically in momentum, are detected in the detector packages. The optical length of each spectrometer is 23.4 m and the nominal bend angle of the central ray is 45°. Each of the spectrometers can operate in either polarity to deflect positively or negatively charged particles, with a nominal central momentum range of 0.3–4 GeV. The scattering angle of the detected particles was varied via rotation of the spectrometers around the hall center, with a central scattering angle range of 12.5–150°. The nominal acceptance of the spectrometers is ± 28 mrad in the horizontal direction, ± 60 mrad in the vertical direction, with $\pm 4.5\%$ momentum bite, and ± 5 cm target length acceptance.

During the collection of the quasielastic data, the spectrometer located left from the beamline (labeled "electron spectrometer"), was in negative polarity and detected negatively charged particles, while the spectrometer right from the beamline (labeled "proton spectrometer") was in positive polarity and detected positively charged particles[3].

TABLE VII: Hall A high resolution spectrometer characteristics.

Quantity	Value
Deflection angle	45°
Optical length	23.4 m
Momentum coverage	0.3 - 4.0 GeV
Momentum acceptance	± 4.5%
Momentum resolution	2.5×10^{-4}
Left HRS Angular coverage	12.5 - 150°
Right HRS Angular coverage	12.5 - 130°
Horizontal angular acceptance	± 30 mrad
Horizontal angular resolution (FWHM)	0.5 mrad
Vertical angular acceptance	± 60 mrad
Vertical angular resolution (FWHM)	1.0 mrad

III.6.1 Collimators

Each spectrometer is equipped with a set of collimators, positioned about 1 m from the target. Experiment E01-020 used three collimator settings for each spectrometer and each collimator can be selected remotely via a vertical actuator (linear motor). Each arm has a collimator box including (from top to bottom):

[3]Except for run 1052 when electrons were detected in both spectrometers to calibrate the optics matrix elements (see Section IV.8).

- "Open" collimator (or no front-end collimator). All production data were collected with this setting.

- "6 msr" collimator, made of 80 mm thick tungsten, used for acceptance studies. The tolerance in the dimensions of the 6 msr collimator is $\pm$0.5 mm in each direction. The dimensions of the 6 msr collimators for the electron (left) and hadron (right) arms are shown in Figure 25.

- "Sieve" slit collimator, used to study optical proprieties of the spectrometers. The sieve slit is a 5 mm thick tungsten plate with dimensions of approximately 200×300 mm^2. A regular pattern of 49 (7$\times$7) circular holes was drilled through the sieve slit surface. Most of the holes are 2 mm in diameter, except for two, one in the center and one displaced two rows vertically and one row horizontally, which are 4 mm in diameter. The tolerance in the position of each of the sieve-slit holes is $\pm$0.1 mm in each direction. The dimensions of the sieve collimators for the left and right spectrometers are shown in Figure 26. The origin of the "Sieve Coordinate System" for each spectrometer is located at the central sieve hole and the positive directions of the x_{sieve} and y_{sieve} coordinates are illustrated in the figure.

Tables VIII and IX list the collimator configurations for the Q1, Q2 and Q3 kinematics (Hall A surveys A629, A753, A779, A812, and A820 [70]). The coordinate system in these tables is relative to the ideal target center. A positive ΔX is to the beam left, positive ΔY is upward, and a positive ΔZ is downstream. The sign convention in these tables is explained in Appendix C. The reproducibility of collimator positions after moving the ladder was better than 0.1 mm in the horizontal and vertical directions. The distance between the hall center and the collimators has an uncertainty of $\pm$2 mm. The encoder positions for the open collimators are averages for all runs.

III.6.2 Magnets

Each HRS has three quadrupole magnets and one dipole magnet forming a QQDQ configuration as shown in Figure 27. In this configuration, Q1 focuses the scattered particles in the dispersive direction while Q2 and Q3 focus them in the transverse direction [75]. The quadrupole fields are regulated by monitoring the current in the magnets. The central momentum of each arm is measured and regulated with an NMR measurement of the dipole magnetic field. The field of the dipole is stable at the 10^{-5} level. The focal plane of this

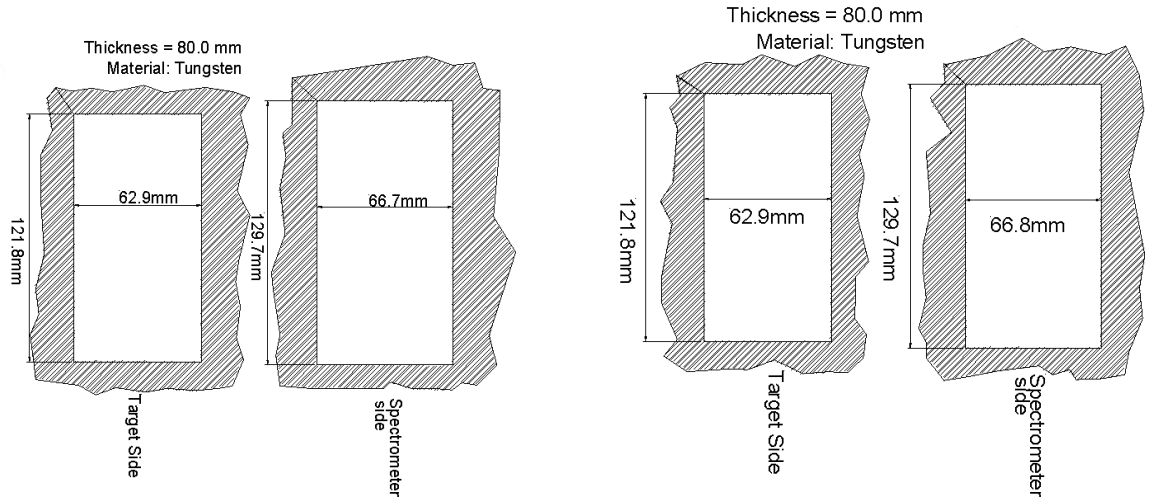

(a) Left Arm (b) Right Arm

FIG. 25: 6 msr collimators.

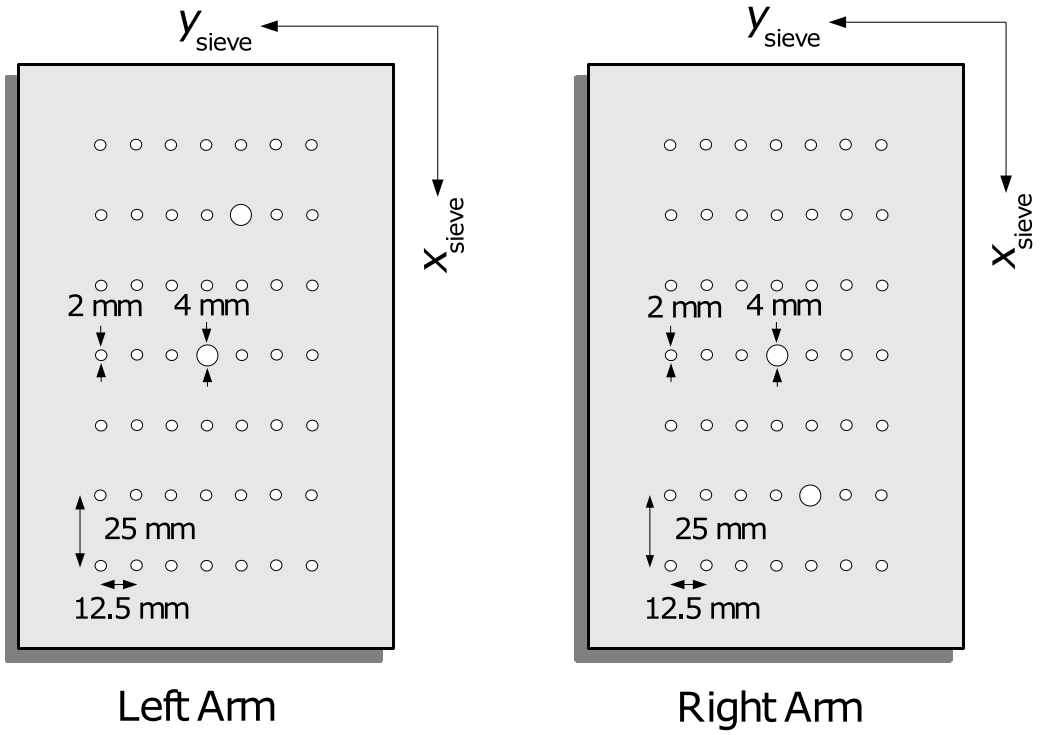

FIG. 26: Sieve collimators.

TABLE VIII: Collimator configuration for the Q1 and Q2 kinematics.

Arm		Left			Right	
Collimator	Sieve	6 msr	Open	Sieve	6 msr	Open
ΔX (mm)	-0.50	-1.81	-	+1.06	+2.72	-
ΔY (mm)	+0.01	+0.07	-	-0.07	+0.11	-
ΔZ (mm)	1184.3	1109.9	-	1175.5	1101.0	-
Encoder	3682	6193	8705	3605	6119	8622

TABLE IX: Collimator configuration for the Q3 kinematics.

Arm		Left			Right	
Collimator	Sieve	6 msr	Open	Sieve	6 msr	Open
ΔX (mm)	-0.89	-2.21	-	-0.03	+1.45	-
ΔY (mm)	+0.05	+0.01	-	-0.05	-0.03	-
ΔZ (mm)	1182.9	1108.6	-	1175.2	1100.8	-
Encoder	3694	6201	8715	3610	6129	8630

TABLE X: Spectrometer magnetic constants.

Arm	γ_1 (MeV/kG)	γ_3 (MeV/kG^3)
Left	270.2	-0.00157
Right	269.8	-0.00157

configuration was designed to be at 45° with respect to the central ray, and coincides with the first wire plane.

The central momentum, P, is calculated from the measured dipole magnetic field, B, by:

$$P = \gamma_1 B + \gamma_3 B^3 \tag{48}$$

where γ_1 and γ_3 are constants [76]. The values of γ_1 and γ_3 for the two arms are given in Table X.

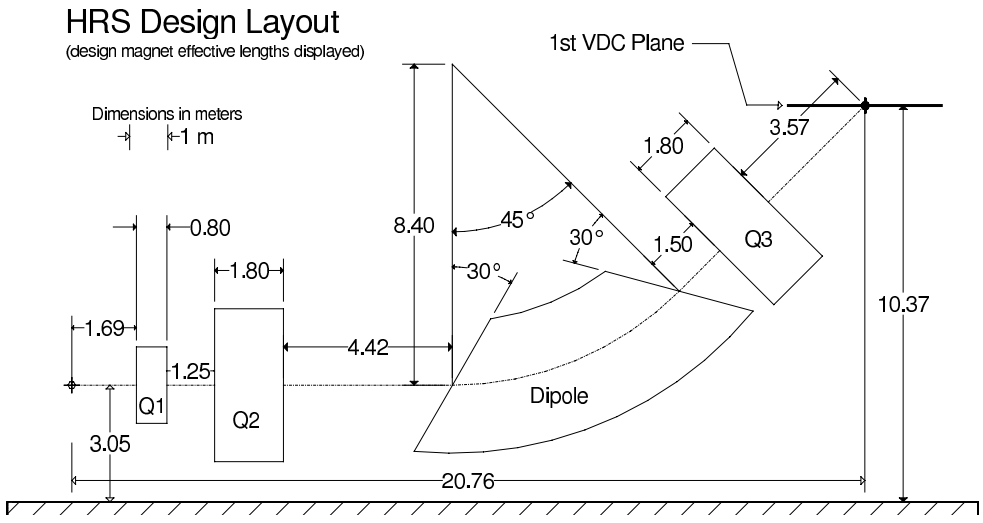

FIG. 27: High resolution spectrometer superconducting magnets (QQDQ).

III.6.3 Detectors

Figure 28 shows schematic diagrams of the detectors employed in the experiment, and their arrangement at the spectrometer focal planes. Each spectrometer detector package contained two planes of scintillators used for triggering, and two vertical drift chambers used for tracking of particles. A Gas Čerenkov detector, located in the electron spectrometer detector package, was employed for separation of electrons from negative pions. The silica aerogel Čerenkov detector [77, 78] in the right arm detector package was not needed in the final analysis to identify the protons after applying all the other optimized cuts. Auxiliary triggers were generated by the S0 scintillator paddle, and used for the measurement of efficiency of main trigger types.

During the collection of data for Experiment E01-020, the detector packages and the data acquisition (DAQ) electronics were located inside a shielded "detector hut" to protect them from most radiation. The detectors and the DAQ were mounted on a retractable steel frame, and were moved out of the hut for maintenance or reconfiguration. In the following, each detector is briefly described.

III.6.3.1 Vertical Drift Chambers (VDCs)

Two Vertical Drift Chambers (VDCs), located at the focal planes of each of the two spectrometers, were used for tracking of particles [79]. All four VDCs are nominally identical,

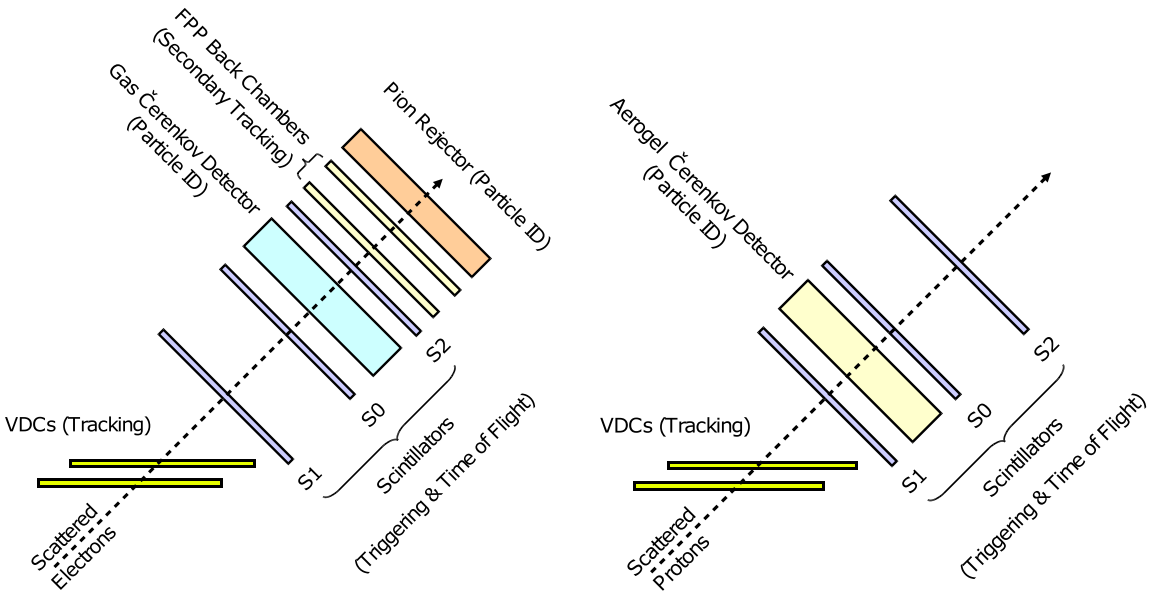

(a) Left Arm. (b) Right Arm.

FIG. 28: Detector packages.

with an active area of 240×40 cm^2. The VDC located near the spectrometer nominal focal surface is labeled "VDC1". The other VDC, labeled "VDC2", was offset 50 cm along the spectrometer nominal central ray. Both VDCs are parallel to each other and to a horizontal plane, and intersect the spectrometer central ray at an angle of 45°(see Figure 29).

Each VDC contains two planes of parallel 20 μm-diameter gold-coated tungsten wires (386 wires in each plane), sandwiched between gold-coated mylar planes. The wires in the two wire planes are perpendicular to each other, and each wire plane was oriented at 45° to the projection of the nominal central ray on the VDC surface. A gas mixture of Argon (62%) and Ethane (38%) was supplied in between the mylar planes at a rate of 5 liters per hour. During the operation, the mylar planes were kept at a voltage of –4 kV, while the tungsten (sense) wires were grounded. A charged particle crossing a VDC ionizes atoms in the gas mixture, creating a trace of released electrons. The electrons are accelerated by the electric field created by the high voltage, and drift along the field lines toward the wires. In the close vicinity of the sense wires (where the electric field is the strongest) the drifting electrons initiate electron avalanches. The electron avalanches hit the wires and induce wire signals, which are amplified, discriminated, and sent to multihit TDCs. The TDCs, which are stopped by the event trigger, are used to infer the elapsed time between the initial

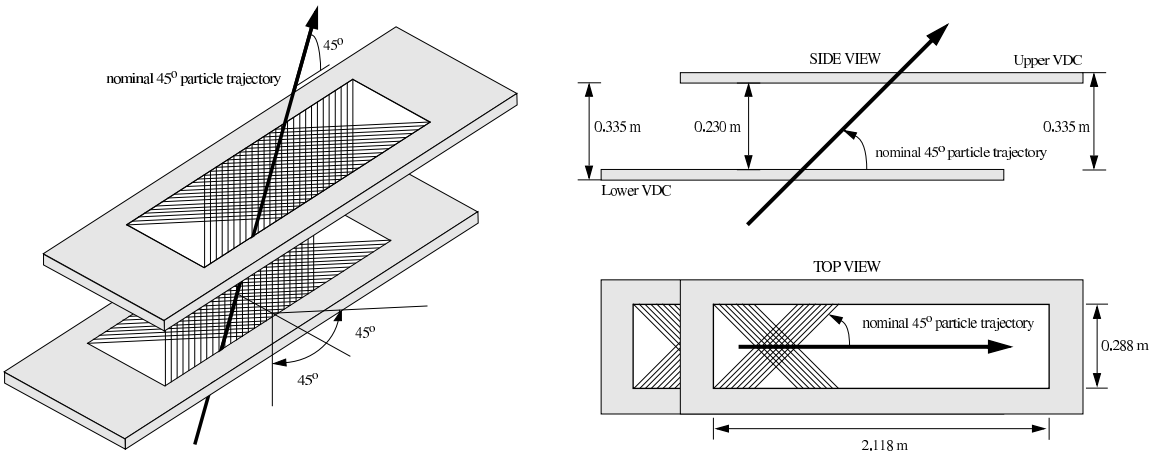

(a) Tilted view. (b) Side and top views

FIG. 29: Vertical Drift Chambers (VDCs).

ionization and the common stop signal. This drift time, combined with the electron drift velocity, yields the drift distance.

The lower (upper) wire plane of the lower VDC is denoted "U1" ("V1") and the lower (upper) wire plane of the upper VDC is denoted "U2" ("V2"). TDC readouts from wires hit in any "U" and "V" planes allow one to fully reconstruct the particle trajectory. However, the resolution can be substantially improved by combining the TDC information from wires hit in all four wire planes. The overall position resolution of the two wire chambers is about 100 μm and the angular resolution is about 0.5 mrad.

III.6.3.2 Scintillators

Triggering of single arm and coincidence events was provided by the scintillators, arranged in two planes for each spectrometer. The two planes are parallel to each other and perpendicular to the spectrometer nominal central ray. The distance between them is about 2 m. Figure 30 shows a typical scintillator plane. The lower scintillator plane is labeled "S1" and the upper scintillator plane is labeled "S2". Each plane is formed by 6 identical overlapping horizontal scintillator "paddles". The paddles are 5 mm thick plastic, with a photomultiplier tube (PMT) at each end (Left and Right). The active area of the S1 scintillator plane is about 170×35 cm^2, and that of the S2 scintillator plane is about 220×54 cm^2.

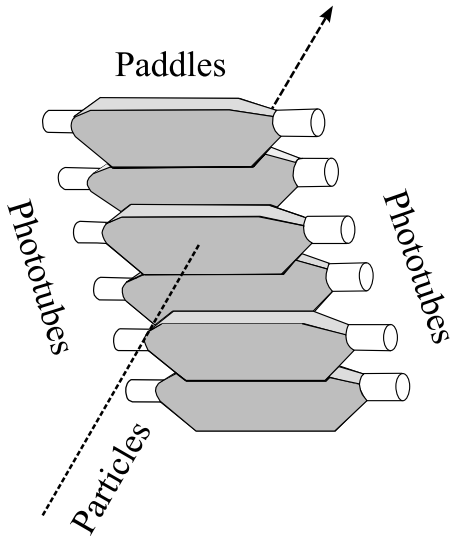

FIG. 30: Scintillator detector plane (each paddle was coupled to a PMT at either end).

An additional vertical scintillator paddle S0 was located between the two planes and was used to form secondary triggers for trigger efficiency measurements. The S0 paddle was 10 mm thick with an active area of 190×40cm^2 and was viewed by 2 PMTs (Top and Bottom).

III.6.3.3 Gas Čerenkov Detector

The Gas Čerenkov detector (see Figure 31) was mounted between the S1 and S2 scintillator planes in the electron spectrometer detector package [80]. The Gas Čerenkov detector is a rectangular chamber filled with carbon dioxide (CO_2) gas. Charged particles traversing the chamber at relative velocities ($\beta = v/c$) larger than $1/n$, where n is the refractive index of the gas, emit Čerenkov radiation. Ten spherical mirrors located at the chamber walls focus the radiation on ten PMT photo cathodes.

The Čerenkov light is emitted about the particle's trajectory in a forward pointing cone with an angle, θ_c defined by:

$$\cos\theta_c = 1/n\beta. \tag{49}$$

The CO_2 gas was at atmospheric pressure, leading to an index of n=1.00041. With this index of refraction, the minimum particle momentum for the production of Čerenkov light is 0.017 GeV/c for electrons and 4.8 GeV/c for pions. Note that the threshold momentum

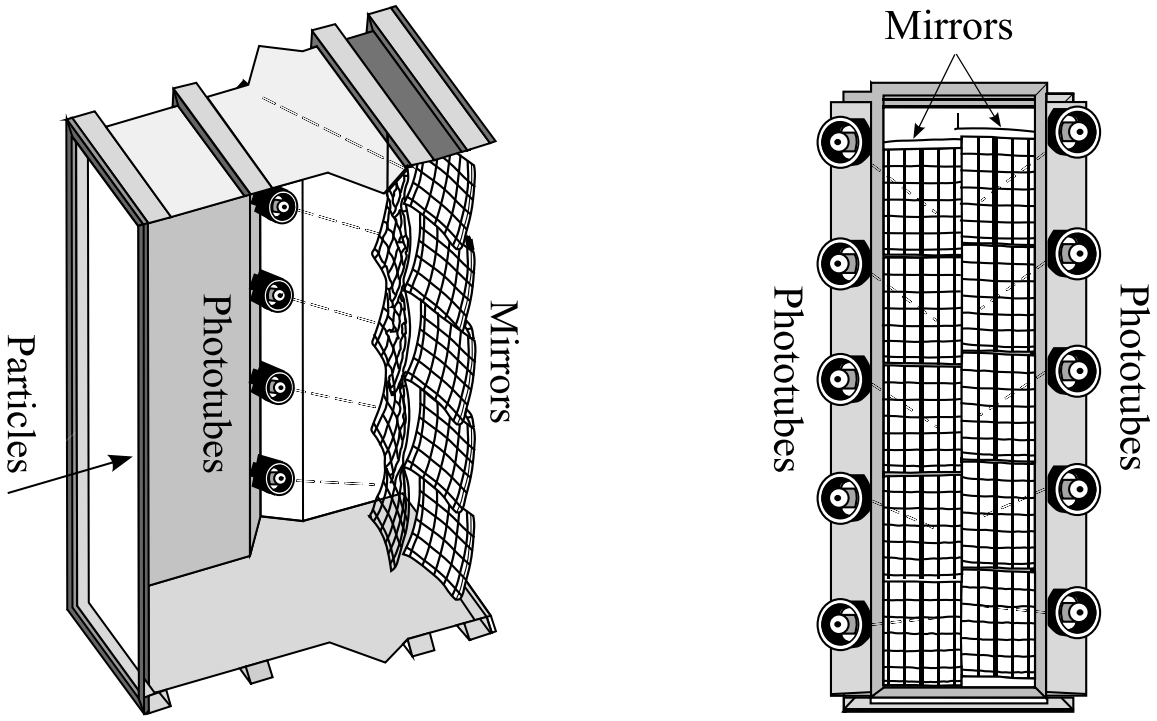

(a) 3D view (b) Front view

FIG. 31: Gas Čerenkov Detector.

of pions is above the maximum momentum for the spectrometer so pions could only give a Čerenkov signal through the production of knock-on electrons (known as δ-ray electrons). The Gas Čerenkov detector provided very efficient separation of electrons from π^- in the electron spectrometer.

III.6.3.4 Lead Glass Calorimeter (Pion Rejector)

A lead glass detector (called "Pion Rejector") provided a redundant separation of scattered electrons from π^-. High-energy charged particles create bremsstrahlung radiation when traveling through the lead glass. The bremsstrahlung in turn creates e^-/e^+ pairs which will also produce bremsstrahlung radiation and create more new e^-/e^+ pairs. The photomultiplier tubes detect the Čerenkov light from the created e^-/e^+ pairs. This process is known as an electromagnetic shower and the energy of the original particle is proportional to the intensity of the collected Čerenkov light if the particle was completely stopped in the calorimeter. Bremsstrahlung radiation intensity decreases with increased particle mass

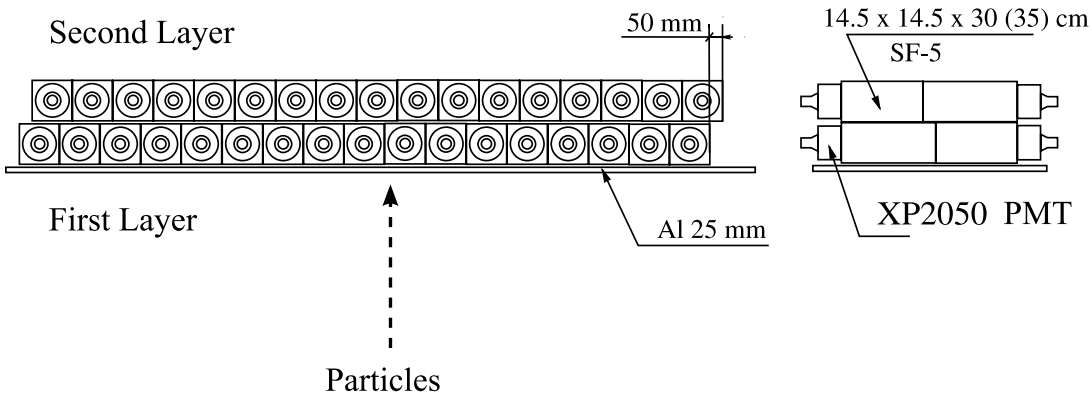

FIG. 32: Lead glass electromagnetic calorimeter (Pion Rejector).

as $1/m^2$. Therefore, the intensity of the light created by pions and heavier particles will be significantly less than electrons.

The detector consisted of rectangular blocks of lead-glass with a photo-multiplier tube glued to each end. There were 17 long blocks and 17 short blocks assembled into two layers as shown in Figure 32. The gaps between the first layer blocks were covered by the second layer blocks, and vice versa. The photo-multipliers were perpendicular to the spectrometer central ray.

The photo-multiplier tubes were connected to ADCs and the intensity of light corresponding to each event was recorded. The signal detected by lead glass counters is linearly proportional to the energy deposited by the particle. Typical pion rejection with a lead glass detector is of the order of 100-1000:1 in the 1 to 10 GeV region. The Hall A pion rejector is meant to offer rejection ratios better than 100:1 (see Subsection IV.6.2).

III.7 COORDINATE SYSTEMS

There are several coordinate systems used in the context of Hall A experiments. All these coordinate systems are related and can be transformed from one to another [84, 81].

III.7.1 Hall Coordinate System

The origin of the Hall Coordinate System (HCS) is at the center of Hall A which is defined by the intersection of the electron unrastered beam, centered in the last two BPMs, and a vertical axis at the target center as defined by gravity. A top view of the Hall A coordinate

system is shown in Figure 33. The z axis is along the beam line and points in the direction of the beam dump, the y axis is vertically upward, and $\hat{x} = \hat{y} \times \hat{z}$.

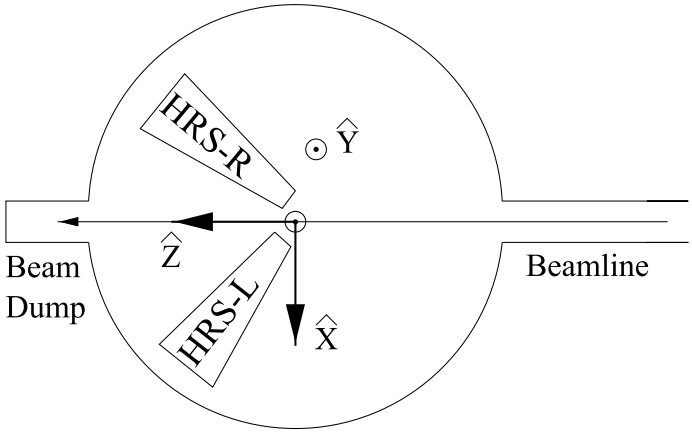

FIG. 33: Hall coordinate system (HCS).

III.7.2 Target Coordinate System

Each spectrometer has its own Target Coordinate System (TCS). A line perpendicular to the sieve slit surface of each spectrometer and going through the mid-point of the central sieve slit hole defines the z axis of the TCS for a given spectrometer (see Figure 34). The x axis is the line crossing the center of the sieve slit and pointing downward. Optimally, this origin should coincide with the origin of Hall A coordinate system and the center of rotation of the spectrometer. The $x - z$ plane contains the y axis of the hall coordinate system, and $\hat{x} = \hat{y} \times \hat{z}$. Variables referring to the coordinates at the target are designated by the subscript “tg". Variables x_{tg} and y_{tg} are defined as the x and y coordinates of the point of intersection of a particle trajectory with the z_{tg} = 0 plane. The variables θ_{tg} and ϕ_{tg} are defined as:

$$\tan\theta_{tg} = \frac{dx}{dz} \tag{50}$$

$$\tan\phi_{tg} = \frac{dy}{dz} \tag{51}$$

The relative momentum δ_{tg} is defined by $\delta_{tg} = (p - p_0)/p_0$, where p is the particle momentum and p_0 is the spectrometer central momentum.

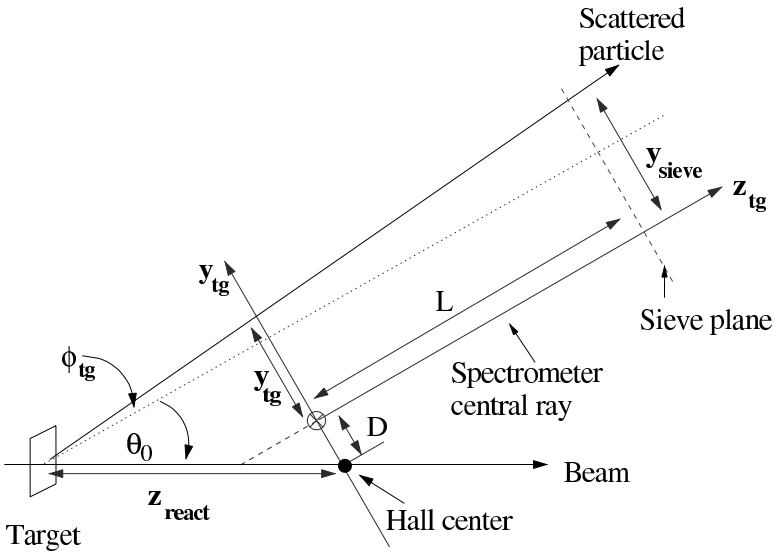

FIG. 34: Target coordinate system (TCS).

III.7.3 Focal Plane Coordinate System

The origin of the focal plane coordinate system (FPCS) is defined as the point of intersection of wire 184 of the U1 VDC wire plane with the projection of wire 184 of the V1 wire plane on the U1 wire plane (see Figure 35). The $\hat{y}$ axis lies in the U1 wire plane and is parallel to the short symmetry axis of the VDC1, the $\hat{z}$ axis points in the direction of the projection of the local central ray ($x_{tg} = y_{tg} = \theta_{tg} = \phi_{tg} = 0$) on a plane perpendicular to the $\hat{y}$ axis. Variables referring to the focal plane coordinate system are designated by the subscript “fp".

III.8 DATA ACQUISITION AND ELECTRONICS

III.8.1 Trigger Setup

For Experiment E01-020, the main trigger types were: a proton spectrometer singles trigger, T1, an electron spectrometer singles trigger, T3, and a coincidence trigger, T5. Auxiliary triggers, used for efficiency measurements of the main triggers, were a proton spectrometer trigger, T2, and an electron spectrometer trigger, T4.

Figure 36 shows a schematic diagram of the setup of the main triggers. The main triggers were generated using scintillator signals. The scintillators were arranged in two

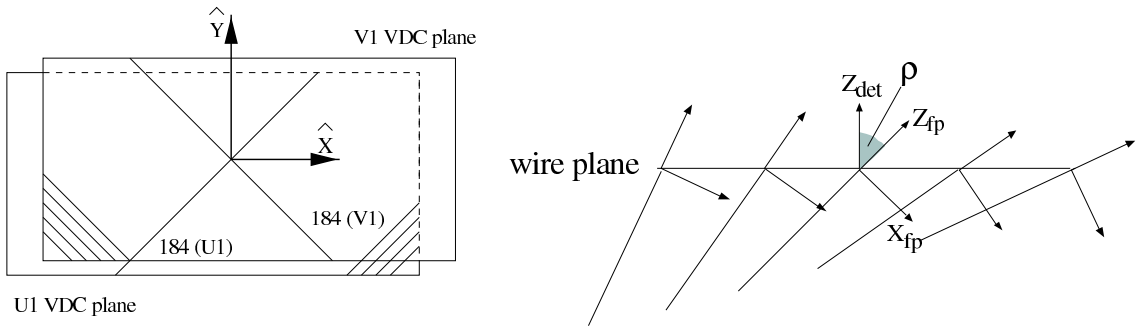

(a) Top view. (b) Side view.

FIG. 35: Focal plane coordinate system (FPCS).

planes in each of the two detector packages, with six scintillator paddles in each plane, and two photomultiplier tubes (PMTs) viewing each paddle. Therefore, the PMTs of the two scintillator planes provided $2 \times 2 \times 6 = 24$ signals for each spectrometer. In Figure 36, S1 (S2) denotes signals from the lower (upper) scintillator plane. S1-L (S1-R) denotes scintillator signals from the left (right) PMT of the lower scintillator plane. S2-L (S2-R) denotes scintillator signals from the left (right) PMT of the upper scintillator plane.

Analog signals from the scintillator PMTs were sent to Analog-to-Digital Converters (ADCs). In addition, the analog signals were sent to discriminators and split three ways: one signal was sent to Time-to-Digital Converters (TDCs), another signal was sent to scalers gated by the start and the end of each run, and the third signal was sent to a logical AND unit making a coincidence between pairs of PMTs viewing the same paddle. For each spectrometer, 12 outputs of the logical AND unit were fed into a Memory Look-up Unit (MLU). The MLU is a programmable device that, given a combination of logical signals at its inputs, provides a corresponding combination of logical signals at its outputs. In the experiment, the electron and the proton spectrometer MLUs were programmed to issue a logical output signal when three conditions were satisfied:

- Coincident hits were present in both PMTs of a scintillator paddle in the S1 scintillator plane.
- Coincident hits were present in both PMTs of a scintillator paddle in the S2 scintillator plane.
- The relative positions of these two paddles were either adjacent or the same in the

two planes[4].

The coincidence between the MLU outputs from the two spectrometers within about 100 ns time window formed the coincidence trigger T5. The absence of a coincidence, but the presence of an MLU output, formed either the proton spectrometer singles trigger T1 or the electron spectrometer singles trigger T3.

The auxiliary trigger T2 (T4) for the proton (electron) spectrometer was generated when the proton (electron) MLU output was not present and any two of the three following "events" occurred:

- A coincidence between both PMTs of a scintillator paddle in the S1 scintillator plane.
- A coincidence between both PMTs of a scintillator paddle in the S2 scintillator plane.
- A coincidence between both PMTs of the S0 scintillator paddle.

From the above description, it can be concluded that the five trigger types are exclusive. This means any given trigger can have only a single type, T1, T2, T3, T4, or T5.

Generated trigger signals were fed into the "Trigger Supervisor" (TS), which prescaled the triggers. Trigger prescale factors were downloaded into the TS at the start of runs. In the Hall A TS setup, the prescale factor n for the trigger type i means that the TS attempts to read out every nth event of type i.

III.8.2 Data Acquisition System

Data acquisition (DAQ) is the sampling of electronic signals to generate data that can be analyzed by computers. Experiment E01-020 used the CEBAF Online Data Acquisition system (CODA) [82]. CODA is specially designed for nuclear physics experiments at Jefferson Lab. It consists of a set of software and hardware systems from which the event data can be constructed. The recorded data file starts with a header which gives the run size and the run number. The data file also contains:

- CODA events from the detectors.

[4]The S1 and S2 paddles which fire must be in a good geometrical configuration. It is required that if paddle i (i = 1,...,6) fires in plane S1, either paddle i or $i+1$, when i is not equal to 6, or $i-1$, when i is not equal to 1, fires in the S2 scintillator array.

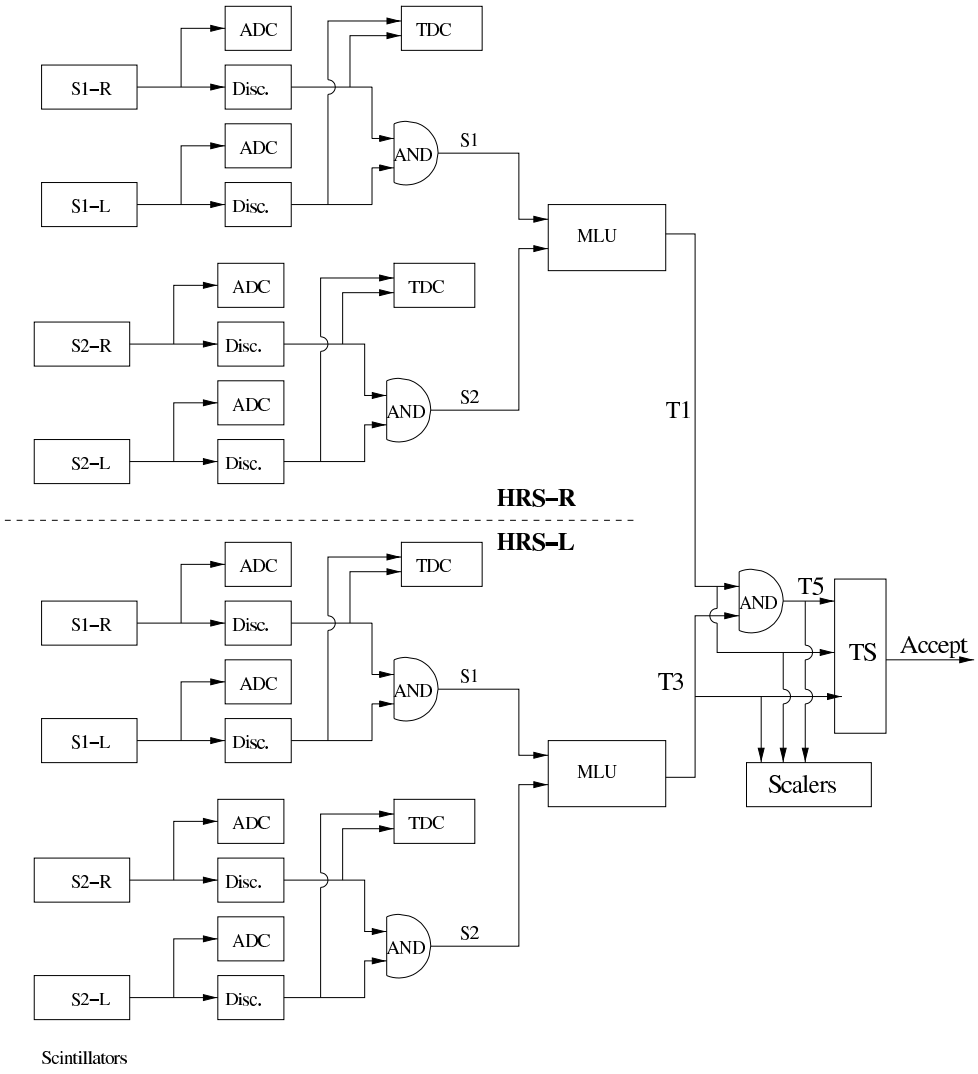

FIG. 36: Hall A main triggers.

- EPICS [83] data from the slow control software used at JLAB. The sampled beam current and beam position information as well as the magnet information and target temperature and pressure are fed to EPICS and recorded.

- CODA scaler events: the DAQ reads the scaler values every few seconds and feeds them to the main data stream. The scalers are not affected by the DAQ deadtime. Therefore, one can use scaler readings to correct for DAQ deadtime.

The data were first written to local disks and then transferred to the Mass Storage System (MSS) which uses high capacity tapes. The total space of recorded data for Experiment

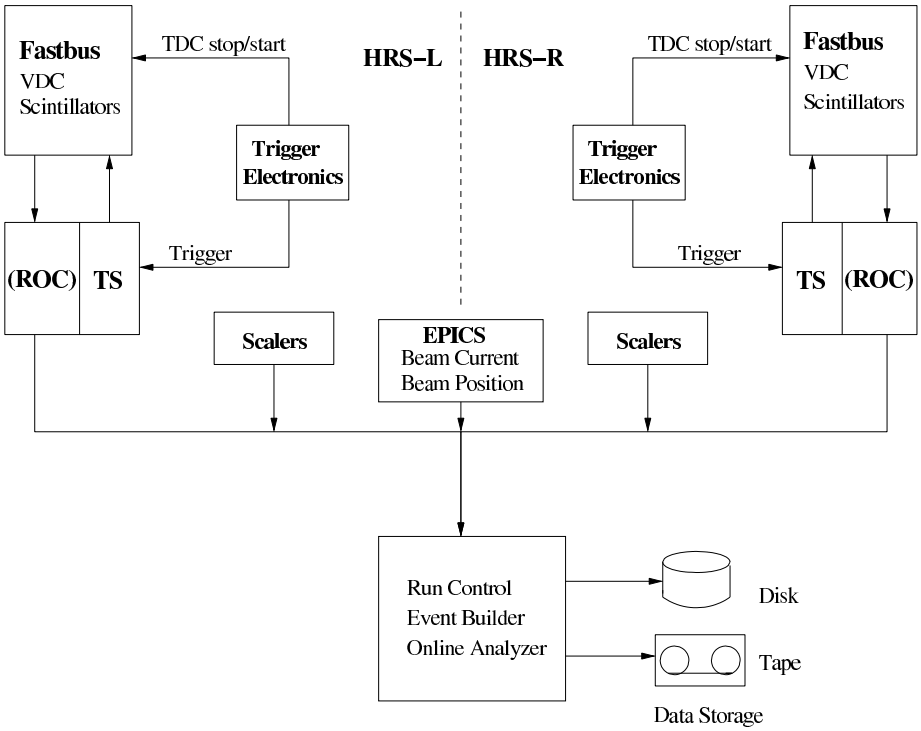

FIG. 37: Hall A DAQ system.

E01-020 was about two Terabytes (TB). The data were analyzed using the Event Scanning Program for Hall A Collaboration Experiments (ESPACE) [84]. Capabilities of ESPACE include:

- Reading, decoding and scaling raw event data.
- Reconstruction of wire chamber tracks, computation of spectrometer focal-plane coordinates and target quantities.
- Computation of basic physics quantities like particle angles and four vectors.
- Dynamic definition of histograms and ntuples in the HBOOK format [85].
- Fitting of analysis parameters to experimental data, including the spectrometer mis-pointing offsets and optics matrix elements.
- Analysis control via the Kit for a User Interface Package (KUIP) [85].

The physics analysis was done mostly by the Physics Analysis Workstation (PAW) [86] which is part of the CERN Library Programs [85] and to a lesser degree by the newer ROOT System [87].

III.9 RUN SUMMARY

Many different configurations were used during the experiment to obtain full information about the apparatus and physics of the ^{2}H$(e,e'p)n$ reaction. The main types were:

- Spectrometer optics and acceptance studies, detector calibrations, and target boiling effects.
- Measurement of the electron-proton elastic ^{1}H$(e,e'p)$ scattering cross section for calibrations and optimizations.
- Measurement of the electron-deuteron quasielastic ^{2}H$(e,e'p)n$ reaction cross section to separate R_{LT} and extract A_{LT}.

The ^{2}H$(e,e'p)n$ cross section was measured for a range of missing momentum, $p_{miss} = 0.1$, 0.2, 0.3, 0.4 and 0.5 GeV at three different values of $Q^2 = 0.8$, 2.1 and 3.5 GeV^2 and labeled later by Q1, Q2, and Q3 (not to be confused with the symbols used for Quadrupole magnets). For each different value of Q^2 and p_{miss}, perpendicular kinematics measurements with $\phi_x = 0°$ and $180°$ were performed to separate the R_{LT} response function. For the middle Q^2, parallel and anti-parallel kinematics measurements were performed at each different value of p_{miss} to minimize the effects of FSI. Further, at $p_{miss} = 0.2$, 0.4 and 0.5 GeV the neutron angular distribution was measured by induction through the other known or detected charged particles. Keeping p_{miss} constant at 0.2 and 0.4 GeV, the angle of the recoiling neutron with respect to $\vec{q}$, θ_{nq}, was varied in the domains 20°–150° and 20°–110° respectively. This corresponds to a variation in Bjorken x_{Bj} between typically 0.7 and 1.5. This variation of the neutron angle allows us to study in detail the various reaction mechanisms such as final state interactions, meson exchange currents and isobar configurations in addition to the dynamics of the deuteron. Results for only the highest Q^2 perpendicular kinematics ($x_{Bj} = 1$) are reported in this dissertation.

The ^{2}H$(e,e'p)n$ kinematics that were measured during the experiment are labeled according to the following rules [88]:

TABLE XI: Bjorken variable, x_{Bj}, kinematic labels.

x_{Bj}	Label
0.448	a
0.519	b
0.668	c
0.827	d
0.900	e
1.000	f
1.172	g
1.293	h
1.351	i
1.525	j
1.684	k
1.819	l

- Q#_*i*## : labels a cross section measurement of the ^{2}H$(e,e'p)n$ quasielastic reaction at a given Q^2, referenced by #, a given Bjorken value, x_{Bj}, referenced by the alphanumeric label *i* (see Table XI), and a given recoil momentum, indicated by ## in hundredth of MeV,

- Q#_f##*k*: labels a cross section measurement of the ^{2}H$(e,e'p)n$ quasielastic reaction at x_{Bj}= 1 where the meanings of # and ## are similar to the Q#_i## kinematics, and where the alphanumeric label k = l, r indicates the detection of the knocked-out proton on the left (l) or the right (r) side of the virtual photon. The cross section and the longitudinal-transverse response function, R_{LT}, and the A_{LT} asymmetry in this dissertation are extracted from these kinematic settings for the highest Q^2 value.

CHAPTER IV

DATA CALIBRATIONS

The analysis phase started right after the end of the experiment. There were several analysis tasks which had to be performed to achieve the objectives of this experiment. These analysis tasks could be divided into four primary categories:

- Beam and Luminosity studies: Calibration of beam current and position. Target density and boiling effects. Luminosity monitoring.
- Kinematics studies: Target model and energy loss corrections. Optics optimization. Vertical drift chambers calibration. Absolute angular and momentum offsets. Spectrometer pointing offsets. ^{1}H$(e,e'p)$ kinematics calibration.
- Normalization studies: Detectors gain matching and efficiency determination. Tracking efficiency. Computer and electronic deadtimes. Absolute normalizations.
- Physics studies: Cut definitions. Radiative corrections. Phase space determination. Cross sections calculation. Separation of the longitudinal-transverse response function, R_{LT}. Extraction of the longitudinal-transverse asymmetry, A_{LT}.

This chapter describes the several optimizations and calibrations of the E01-020 data which were necessary to extract the cross section and the R_{LT} response function.

IV.1 BEAM CALIBRATIONS

The beamline for Hall A includes several elements which need to be calibrated in order to extract precise cross sections. The major parameters of the electron beam that need to be calibrated are the beam energy, beam position, and beam current.

IV.1.1 Beam Energy Calibration

The value of the beam energy is crucial in determination the reaction kinematics. During the data collection of E01-020, several measurements of the beam energy were made by using the Arc and eP methods. Table XII summarizes the beam energy measured during Experiment E01-020 using these methods. In this table, the "Tiefenbach" energy measurement (named after CEBAF physicist Michael Tiefenbach) is calculated by using the

TABLE XII: Measured beam energy for Experiment E01-020.

Date	Arc Method (MeV)	eP Method (MeV)	Tiefenbach Energy (MeV)	Set Energy (MeV)
06/06/02	2843.6±0.6	2840.4±0.9	2843.50	2842.3
06/24/02	4703.1±1.6	4704.0±1.5	4703.20	4702.3
10/24/02	5008.5±1.4	—	5009.02	5005.69

Hall A Arc $\int Bdl$ value, determined from the ninth reference dipole, and the Hall A Arc non-invasive beam position monitors. This measurement is continuously recorded in the data stream and is ultimately calibrated against the Arc energy measurement. The "Set Energy" is the nominal beam energy the accelerator is setup to run.

Comparison between the measured Arc and eP beam energies indicated problems with the eP results giving rise to unacceptable shifts in the physics analysis results (e.g., few MeV for E_{miss}). Therefore, it was decided to ignore the eP energy measurement and consider only the Arc energy measurement. The Arc measurement was done only when the beam energy changed because it is an invasive measurement. The Tiefenbach energy was recorded continuously in the collected data allowing us to correct for any drifts in the beam energy over time (see Figure 38).

Table XIII and Figure 39 show a comparison of the missing energy for the ^{1}H$(e,e'p)$ reaction, by using both the Arc energy measurement and the continuously measured Tiefenbach energy. From this, we can see that the variations in the Tiefenbach beam energy represent actual variations in the beam energy (better missing energy agreement in this case). In this case, it is adequate to calculate the actual calibrated beam energy for each run as:

$$E_{Beam} = \frac{E_{Arc}}{E^{\circ}_{Tief}} \times E_{Tief} \tag{52}$$

where E°_{Tief} is the Tiefenbach beam energy measurement taken at the same time as the Arc beam energy measurement, E_{Arc}, and both are given in Table XII.

IV.1.2 Beam Position Calibration

IV.1.2.1 Bull's Eye Scan

Two "Bull's eye" scans were performed just before the first run period and during the second run period [89]. During a bull's eye scan, unrastered beam was steered away from

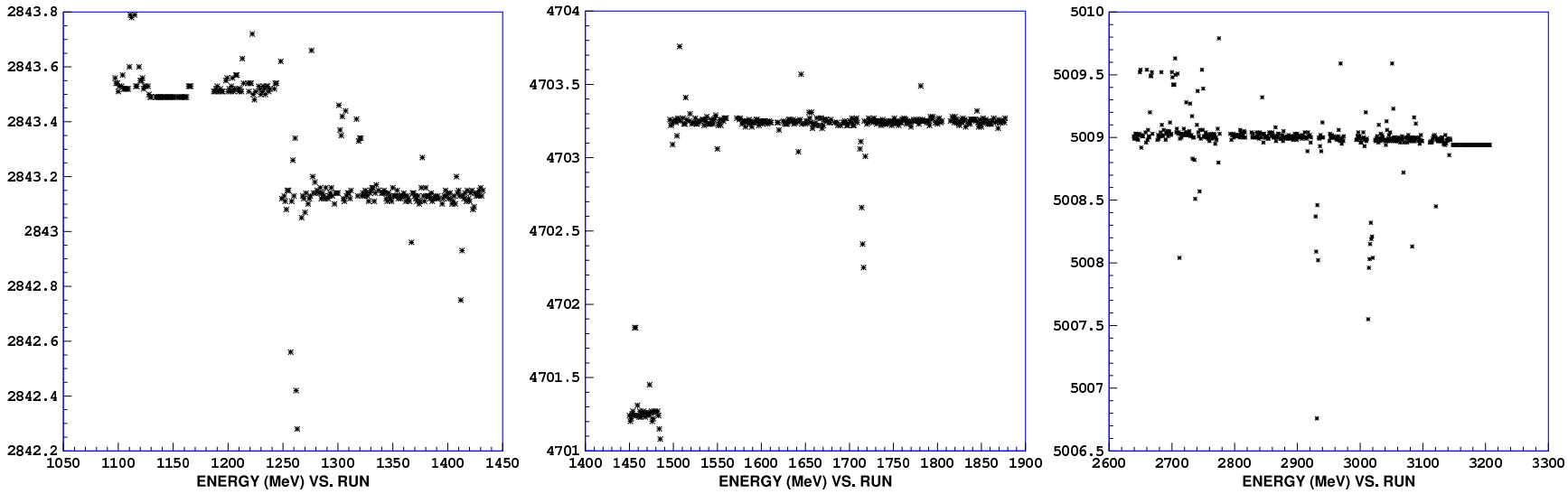

(a) Q1 Kinematics. (b) Q2 Kinematics. (c) Q3 Kinematics.

FIG. 38: Tiefenbach energy for E01-020.

TABLE XIII: Missing energy for the ^{1}H$(e, e'p)$ reaction. The difference between the Arc and Tiefenbach beam energy and the corresponding missing energy generally agree.

Run	E_{Beam} (MeV)			E_{miss} (MeV)		
Number	Arc	Tiefenbach	Difference	Arc	Tiefenbach	Difference
1436	2843.6	2843.12	$+0.48$	-0.41	-0.93	$+0.52$
1439	2843.6	2843.12	$+0.48$	-0.04	-0.55	$+0.51$
1442	2843.6	2843.12	$+0.48$	$+0.51$	-0.03	$+0.54$
1444	2843.6	2843.47	$+0.13$	-1.06	-1.29	$+0.23$

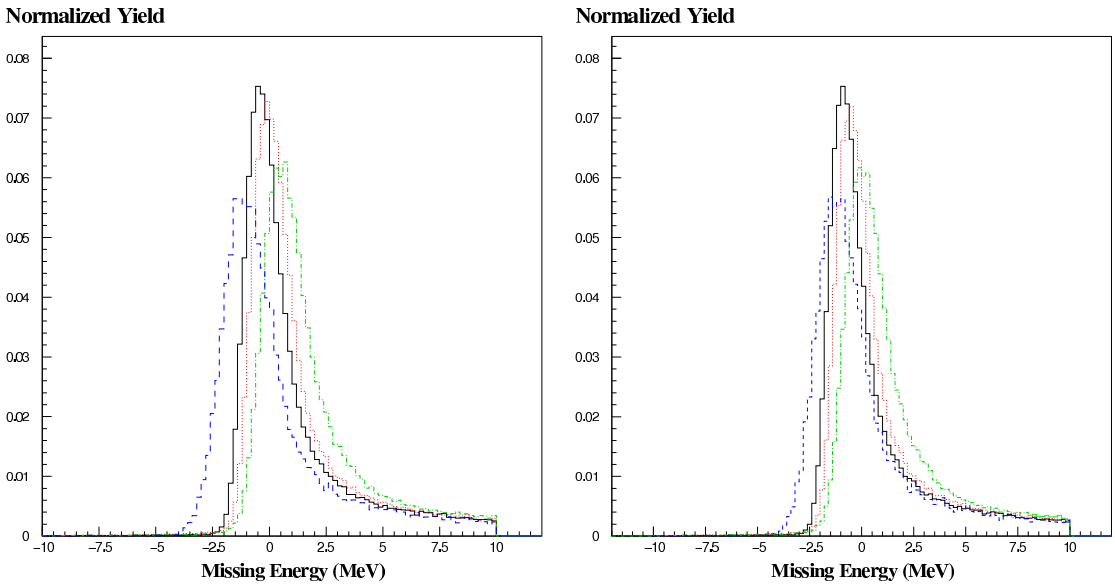

(a) Using the Arc beam energy

(b) Using the Tiefenbach beam energy

FIG. 39: Missing energy for the ^{1}H$(e, e'p)$ runs in Table XIII. Run 1436 is solid lines, Run 1439 is dotted lines, Run 1442 is dashed-dotted lines, and Run 1444 is dashed lines.

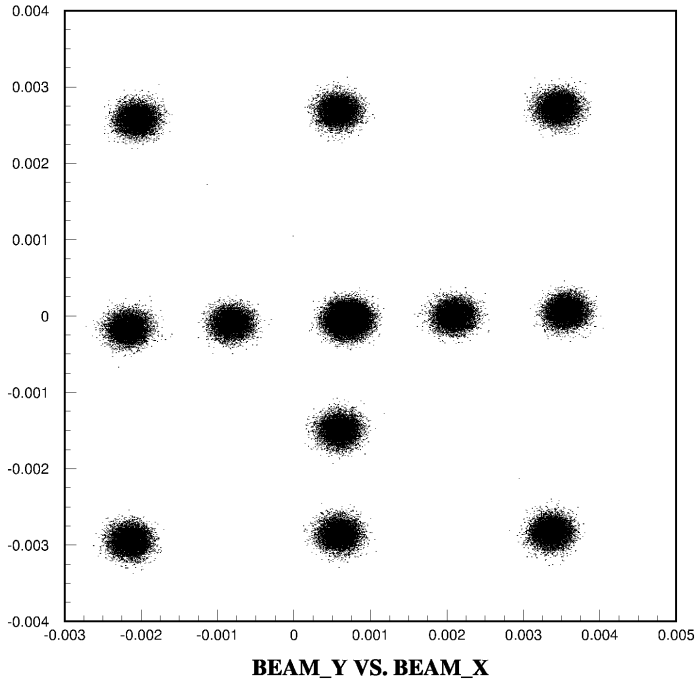

FIG. 40: Bull's eye scan (Beam positions are in meters).

its nominal position to various different positions, and data were recorded simultaneously with the Harps (Harp runs) and with the BPMs (standard CODA runs). Since the Harps have been surveyed, those runs give the absolute beam position in the Hall A coordinate system and the BPMs can be calibrated against the Harps. Figure 40 shows all the BPM data from the first Bull's eye scan. After the analysis of the harp runs and the coda runs, the offsets and slopes for the BPM data versus the harp data are determined and put into ESPACE's database. This method allows the beam position to be analyzed on an event by event basis only if the "Burst" mode was used for the BPM ADCs. In this case, no two-pass analysis is necessary.

IV.1.2.2 Raster Calibration

Unfortunately, the "Burst" mode was not used for the highest Q^2 kinematics. Therefore, we performed a two-pass analysis [89] to calibrate the beam position for each Q3 run separately. In the first pass a run is analyzed to obtain the average beam position ($\langle x_{BPM} \rangle$ and $\langle y_{BPM} \rangle$) and the associated raster size (σ^x_{BPM} and σ^y_{BPM}) as determined from BPMA and BPMB (see Figure 41). At the same time one also gets the average raster ADC channel ($\langle x_{Raster} \rangle$ and $\langle y_{Raster} \rangle$) and the distribution of this quantity (σ^x_{Raster} and σ^y_{Raster}). This

information is put into individual files for each run. These files are then read by ESPACE in a second pass to do the actual calibrated beam position analysis. In the actual analysis, the phase corrected beam position from the BPMA and BPMB is calculated in terms of the raster ADC values (x_{Raster} and y_{Raster}) as:

$$x_{BPM} = \langle x_{BPM} \rangle + \frac{\sigma^x_{BPM}}{\sigma^x_{Raster}} (x_{Raster} - \langle x_{Raster} \rangle) \tag{53}$$

$$y_{BPM} = \langle y_{BPM} \rangle + \frac{\sigma^y_{Beam}}{\sigma^y_{Raster}} (y_{Raster} - \langle y_{Raster} \rangle) \tag{54}$$

and then the resulting beam positions at the two BPMs are extrapolated linearly to the interaction point in the target to determine the beam position at the target (x_{Beam} and y_{Beam}).

IV.1.2.3 Beam Position Correction

The reconstructed average reaction point z-position, z_{react}, should be independent of the beam x-position, x_{Beam}, for the thin carbon target since it is perpendicular to the electron beam. This is valid for an unrastered beam as shown in Figure 42. However for the rastered beam, there was a linear correlation between z_{react} (reconstructed from both the left and right spectrometers) and x_{Beam} as shown in Figure 43. Similar correlations were encountered before for another Hall A experiment [90]. Further analysis of this correlation indicated that multiplying x_{Beam} by roughly 1.3 removes these correlations for both the Left and Right z_{react} simultaneously [91] as shown in Figure 44.

After further studies of these correlations, we reached the conclusion that x_{Beam} should be corrected by a factor of 1.35 to remove any remaining correlations between z_{react} and x_{Beam}. A similar study of E_{miss}versus y_{Beam} revealed that y_{Beam} should be corrected by a factor of 1.15 to remove any observed correlations between them. Figure 45 shows the final corrected and uncorrected x_{Beam} and y_{Beam}. A good way to check the final rastered beam position corrections is to simply make sure that there is no dependence of the z_{react} and E_{miss} peak positions on the left or right raster half-cut (one peak cut) as shown in Figure 46.

The corrected and calibrated beam position and raster size for all the $Q^2 = 3.5$ GeV and $x_{Bj} = 1$ runs are shown in Figure 47.

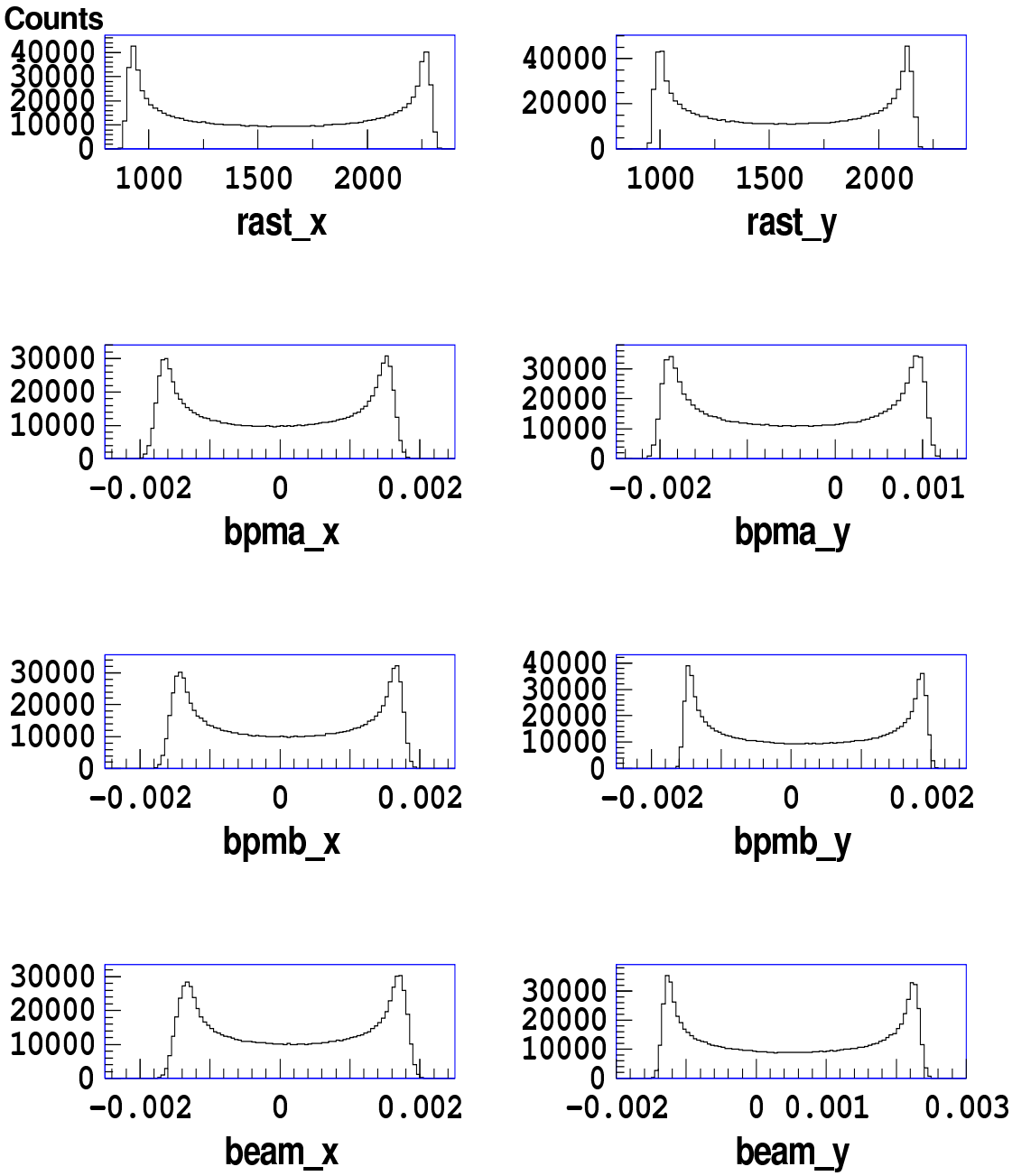

FIG. 41: Beam raster ADCs and beam positions (in meters) as measured by BPMA and BPMB and the extrapolated position at the target for Run 2831.

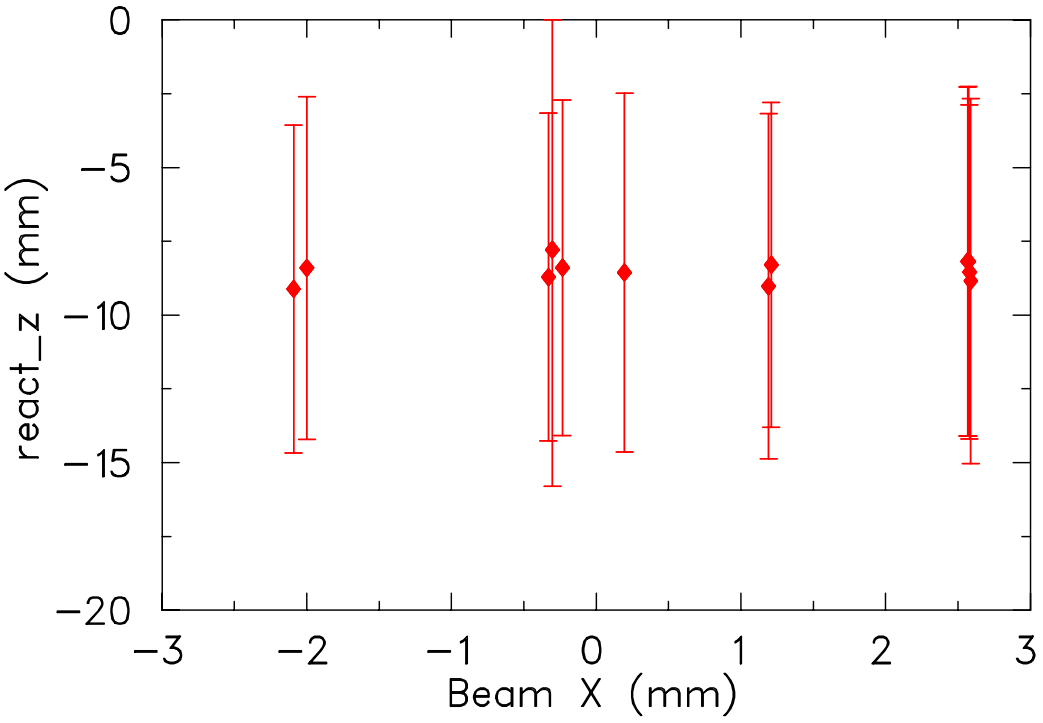

(a)

FIG. 42: Reaction point z-position in a foil carbon target versus the beam x-position for unrastered beam. The error bars represent the standard deviation ($\pm\sigma$) of the z_{react} distribution.

IV.1.3 Beam Current Calibration

The Hall A upstream and downstream beam current monitors (BCMs) are calibrated by normalizing to the injector BCM cavity (0L02 BCM) [92]. Measurements were done during the two run periods of E01-020 for this purpose. During the measurements, the beam was only delivered to Hall A and was interrupted frequently by the insertion of a Faraday Cup[1] (located after the injector BCM) so that the zero offsets for the Hall A BCMs and Unser could be determined. The procedure was to set the beam current at one setting for one minute and then insert the Faraday cup for one minute and then step down to the next current. This is shown in Figure 48 in which the current measured by the Unser is plotted as a function of time. While the beam was being stepped through various currents,

[1] A current measuring device that when inserted in the beam, intercepts all beam current and dissipates the beam power. The cup is designed for maximum efficiency at a given energy. A Faraday Cup is electrically isolated so that all intercepted beam current can be measured using standard instrumentation.

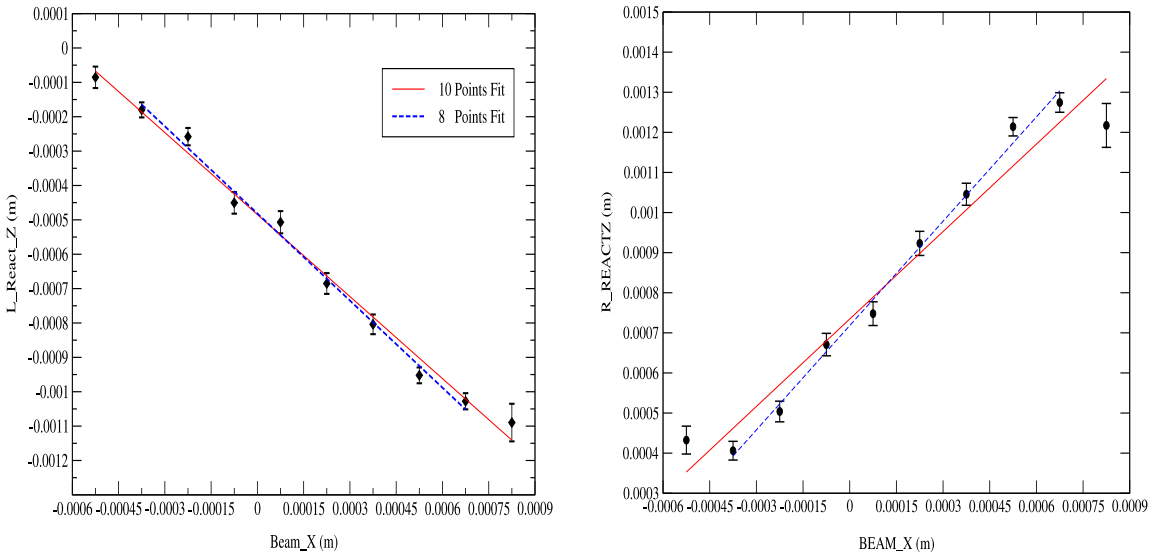

(a) Left Arm. (b) Right Arm.

FIG. 43: Reaction point z-position in a foil carbon target versus the beam x-position for a rastered beam.

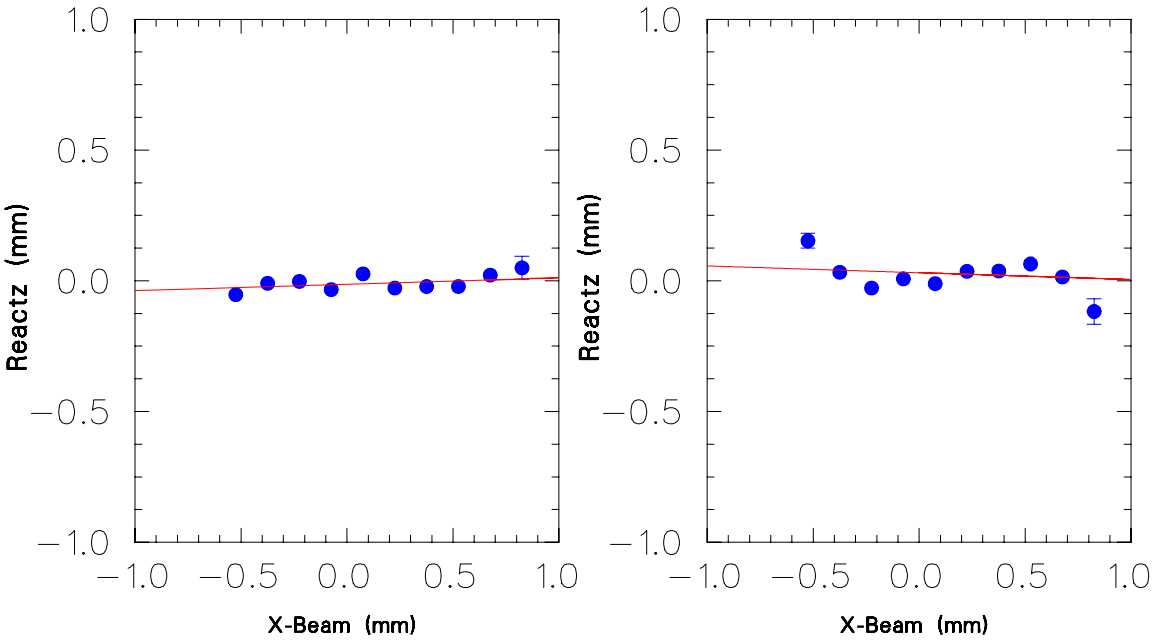

(a) Left Arm. (b) Right Arm.

FIG. 44: Reaction point z-position in a foil carbon target versus the corrected beam x-position for a rastered beam.

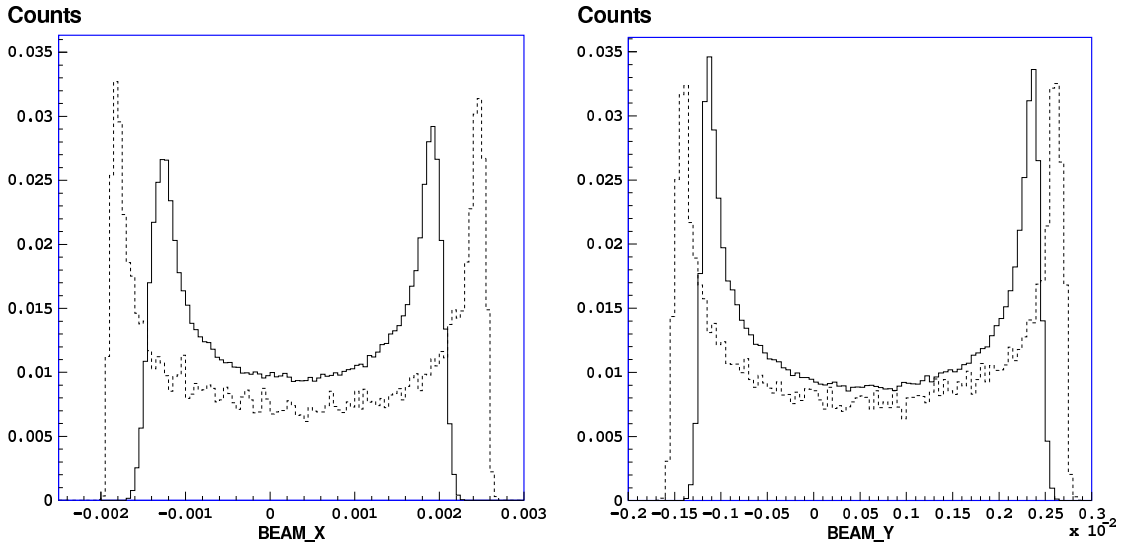

FIG. 45: Corrected (dashed lines) and uncorrected (solid lines) beam x-position and y-position (meters).

the EPICS values for the upstream and downstream BCM voltages, Unser current, Faraday cup current and injector BCM current were recorded once per second. One can determine the zero offsets for Hall A BCM cavities and Unser from the beam off periods when the Faraday cup was inserted. The EPICS constant is then:

$$\text{EPICS Constant} = \frac{\text{Injector BCM Current}}{\text{Hall A BCM Voltage} - \text{Zero Offset}} \tag{55}$$

The ratio of the Unser current to the injector BCM current is plotted in Figure 49 for all kinematics and the average value was found to be 0.995 ± 0.003 for the first run period. Also shown in Figure 49, are the ratios of the injector BCM current to the downstream and upstream Hall A BCMs as a function of the injector BCM current. The average values are given in Table XIV for the two run periods. The calibration constants have been stable for this period of time. The calibration constants for converting the V-to-F scalers to charge were later determined. During the data taking, the scalers were written to a regular data file and subsequently were extracted from the data file to determine the calibration constants. The scaler data were divided into time intervals and the average value of the V-to-F rate and the corresponding zero offsets were determined for each interval. The calibration constants are plotted versus the injector BCM current in Figure 50 and the average values are given in Table XV.

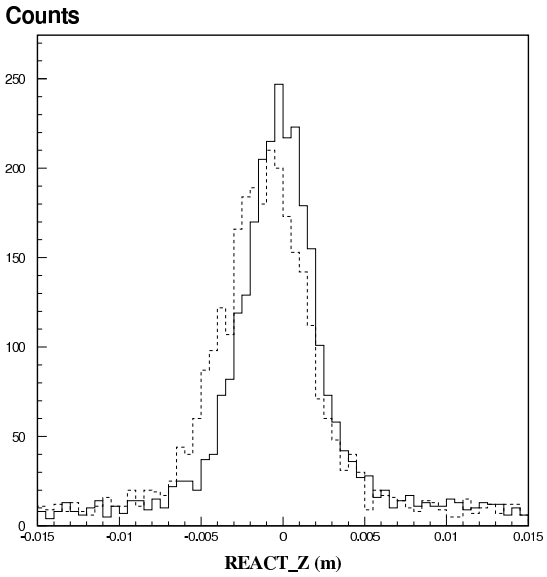

(a) z_{react} for the carbon foil target before correcting x_{beam}.

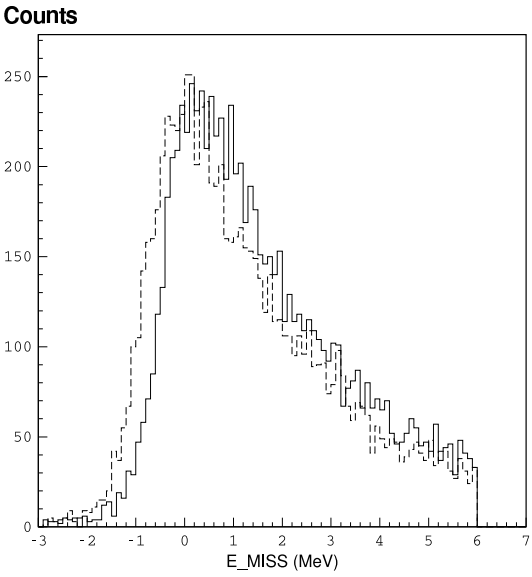

(b) E_{miss} for ^{1}H$(e,e'p)$ before correcting y_{beam}.

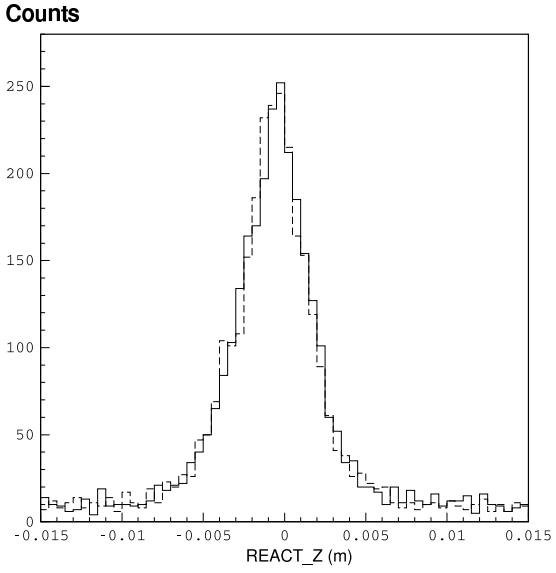

(c) z_{react} for the carbon foil target after correcting x_{beam}.

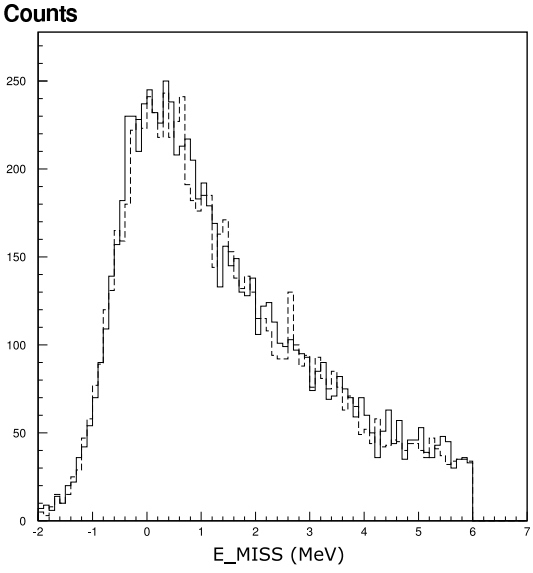

(d) E_{miss} for ^{1}H$(e,e'p)$ after correcting y_{beam}.

FIG. 46: Effect of the raster half-cut on the corrected rastered beam. Left beam x-position and y-position peak cuts are solid lines, and right beam x-position and y-position peak cuts are dashed lines.

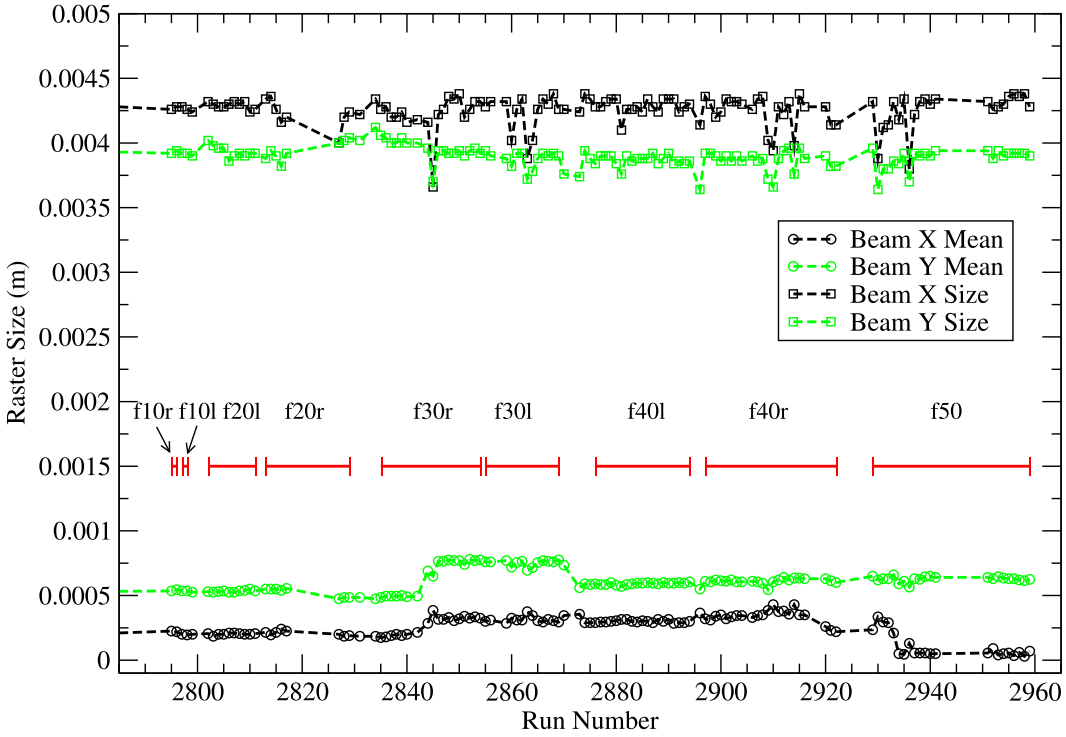

FIG. 47: Raster size for the highest Q^2 perpendicular kinematics. The different kinematics are indicated by the solid segmented lines.

The formula for using these calibration constants and offsets to determine the beam current is

$$\text{Average Current} = \frac{\text{EPICS BCM Scaler/EPICS Time Scaler} - \text{Calibration Offset}}{\text{Calibration Constant}} \quad (56)$$

This equation is used in this dissertation to calculate the average beam current from the $3\times$ upstream and downstream BCMs scalers. The beam current is required to determine the integrated charge and also to correct for beam related target boiling effects (see Section IV.2).

IV.1.4 Extraction of Stable Current Events

Due to the instability of the beam current during Experiment E01-020, we needed to discard all the unstable beam periods. This was needed to calculate the target boiling effects accurately as a function of the current, since the boiling effect can only be characterized

TABLE XIV: EPICS BCM calibration constants. They are the ratios of cavity output voltage to the injector BCM current.

EPICS	Kinematics		Difference
Constant	Q1 and Q2	Q3	(%)
Downstream BCM	79.06±0.04	79.66±0.20	+0.75
Upstream BCM	77.42±0.04	77.37±0.20	−0.06

TABLE XV: The V-to-F calibration constants.

Calibration	Offset	Kinematics		Difference
Constant	(Hz)	Q1 and Q2	Q3	(%)
V-to-F U1x	152.8	1330.4 ± 0.7	1333.3 ± 0.3	+0.22
V-to-F U3x	163.8	4092.4 ± 2.0	4101.6 ± 0.9	+0.22
V-to-F U10x	360.7	12446.6 ± 7.8	12474.3 ± 2.9	+0.22
V-to-F D1x	34.6	1352.7 ± 0.7	1345.1 ± 0.3	−0.56
V-to-F D3x	110.0	4188.5 ± 2.1	4165.7 ± 0.9	−0.55
V-to-F D10x	307.8	13190.3 ± 10.2	13122.2 ± 3.7	−0.52

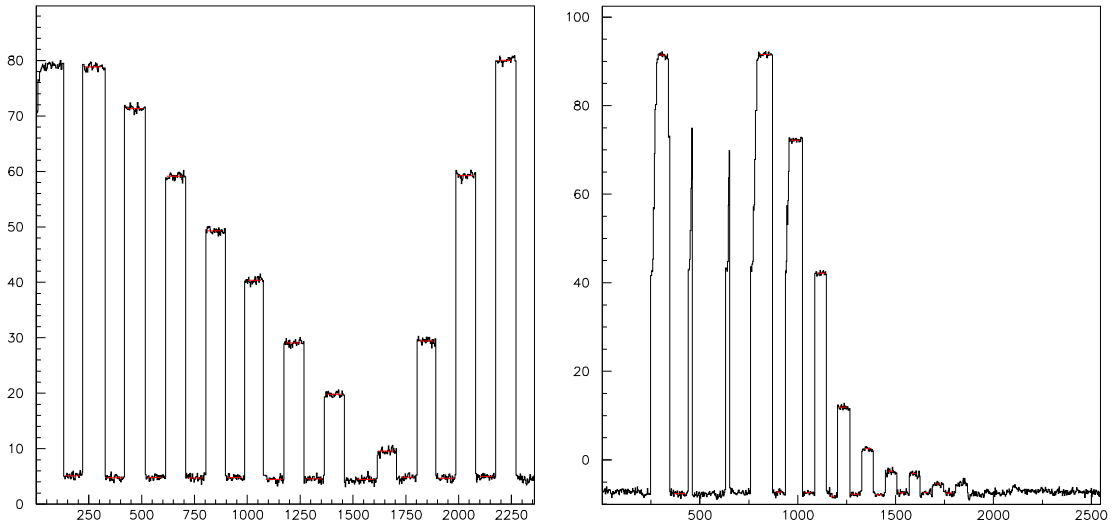

(a) Q1 and Q2 Kinematics.

(b) Q3 Kinematics.

FIG. 48: Hall A Unser current (μA) versus time (sec).

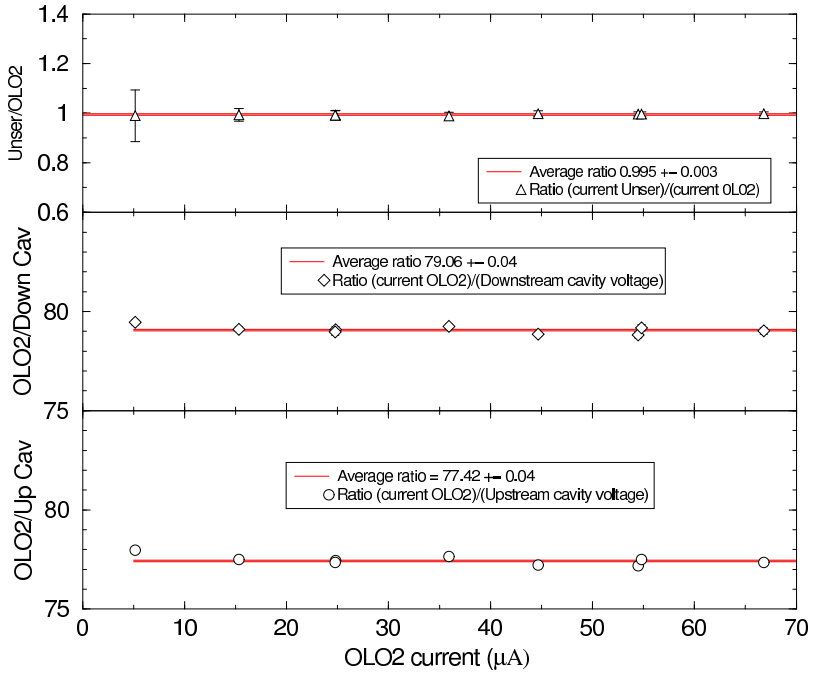

(a) Q1 and Q2 Kinematics

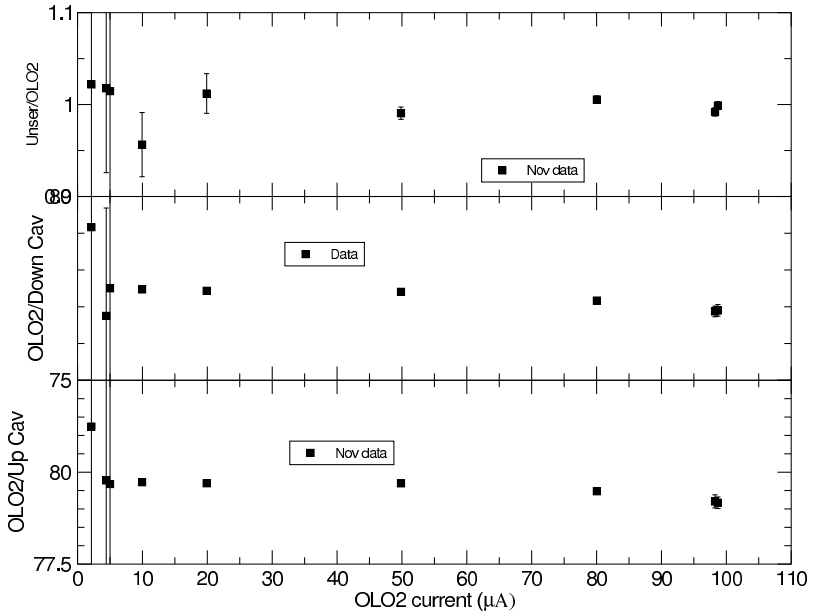

(b) Q3 Kinematics

FIG. 49: Ratios to the Injector BCM (0L02) current.

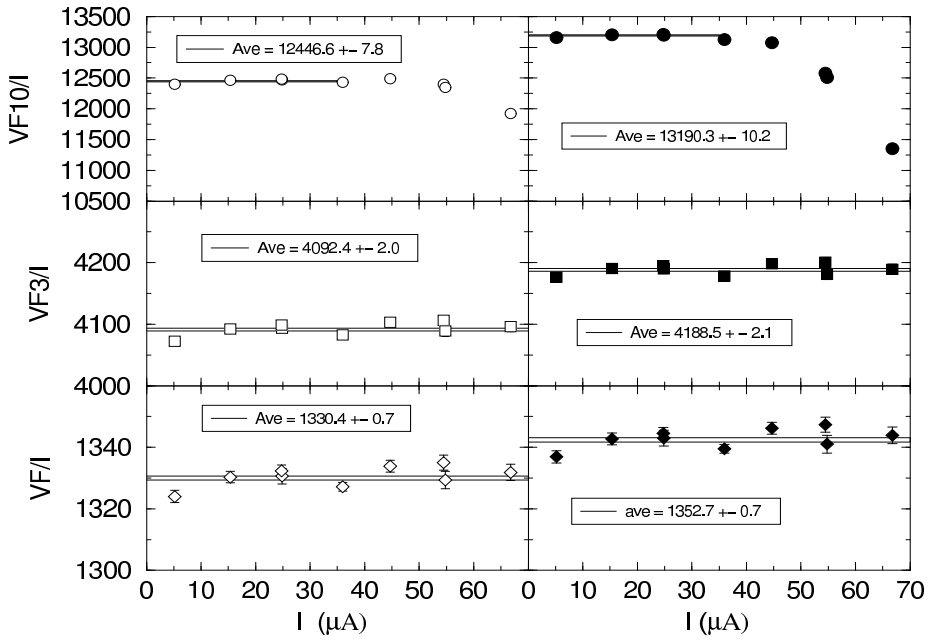

(a) Q1 and Q2 Kinematics.

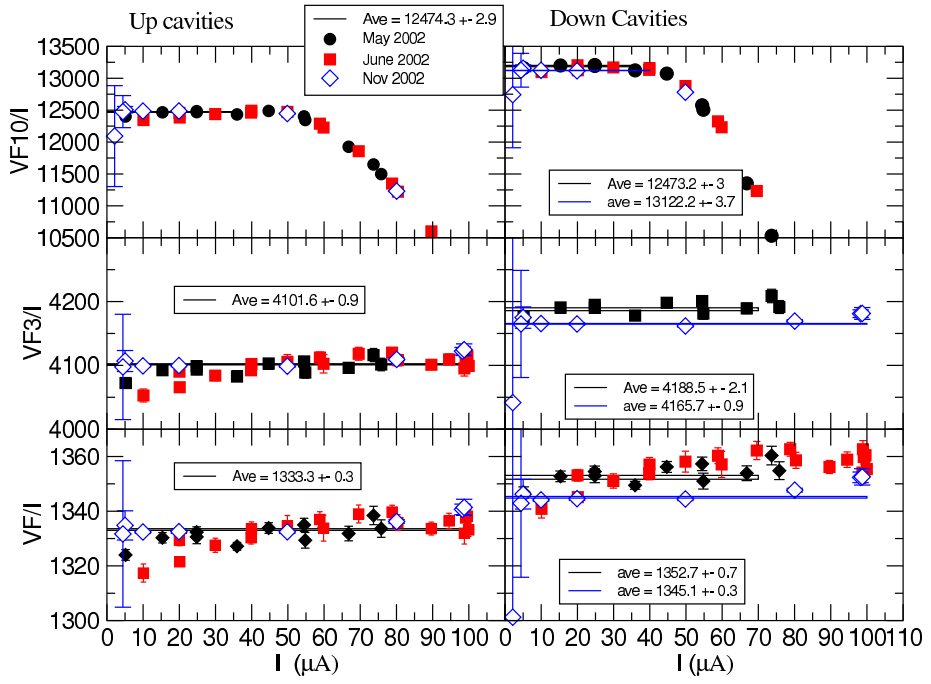

(b) Q3 Kinematics.

FIG. 50: Calibration constants versus the injector BCM current. Left panels are for the Downstream BCM and right panels are for the Upstream BCM. The VF1, VF3, and VF10 are the V-to-F values corresponding to the BCM 1x, 3x, and 10x amplified signals.

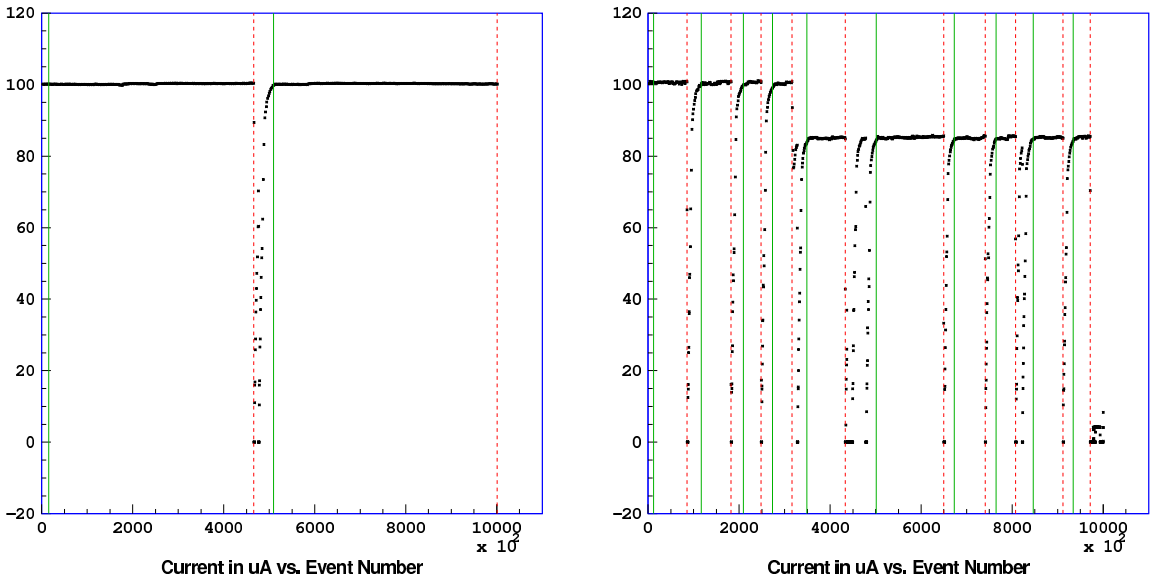

(a) Almost stable current (Run 2849). (b) Unstable current (Run 2934).

FIG. 51: Extraction of the stable current events. A dotted (dashed) vertical line indicates the start (end) of a stable current period.

during stable beam conditions. To extract only the stable beam events, a new code was written (see Section V.2 and Appendix D) and applied to all the ^{2}H$(e,e'p)n$ runs (see Figures 51 and 52).

IV.2 TARGET BOILING

Beam-induced target density fluctuations ("Target Boiling") were observed for the "cigar-tube" liquid targets used in Experiment E01-020. We corrected for this to ensure the validity of the extracted cross section. This section discusses the boiling corrections done for the LH_2 and LD_2 targets.

IV.2.1 Liquid Hydrogen

In order to check the hydrogen normalization we studied the dependence of the liquid hydrogen, LH_2, density on beam current for fixed kinematics [93]. During this study the beam was rastered over a nominally 2×2 mm^2 spot, the same raster size used for the production data on deuterium. The target fan speed was fixed at 60 Hz. The analyzed hydrogen run numbers were 2615–2625.

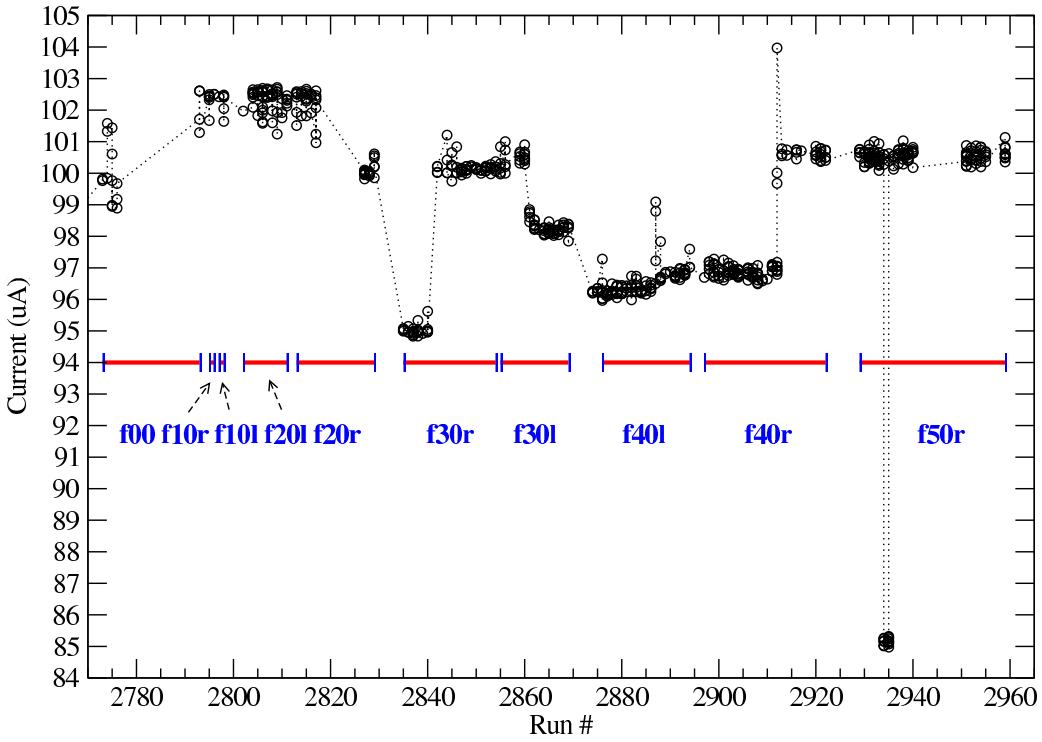

FIG. 52: Beam current for the highest Q^2 perpendicular kinematics. The different kinematics are indicated by the solid segmented lines.

The normalized rates for each trigger type as a function of beam current are shown in Figure 53a along with linear fits for the high current (> 40 μA) runs. The rates for runs with currents below 40 μA are consistent with a constant, indicating no significant density reduction at low current. (This qualitative behavior was also found from another study performed immediately following our experiment using "lumi" monitors [94]). Extractions from all three trigger types (T1, T3 and T5) are reasonably consistent with one another. The extraction of the target density dependence is quite sensitive to the cut on z_{react} (there is no apriori reason to expect the target density to be independent of the z-position). Therefore the z_{react} dependence of the yield was examined in detail for different beam currents. The slopes of the normalized yield versus z_{react} for each beam current were calculated by assuming that the yield linearly depends on z_{react}. Figure 53b shows these slopes as a function of beam current. The magnitude of the slopes increases with increasing current. The density reduction becomes small and consistent with zero as the beam current drops below about 40 μA.

For beam currents $\geq$ 40 μA, we can parametrize the density of the LH_2 target liquid

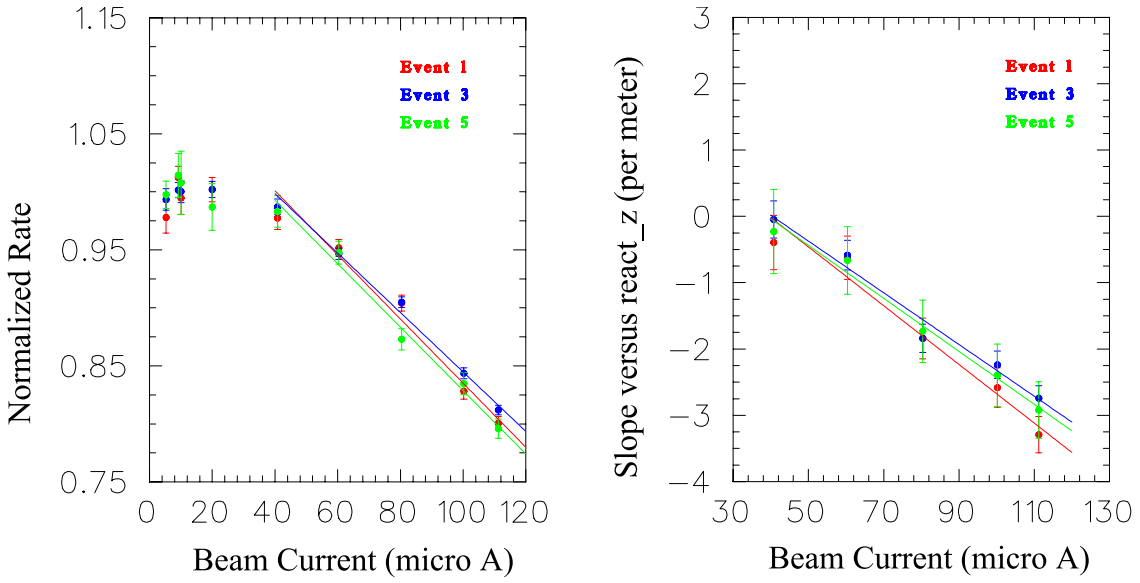

(a) The normalized rates as a function of beam current.

(b) The slopes vs. reaction z-position as a function of beam current.

FIG. 53: LH_2 Target boiling for the 2×2 mm^2 raster for each trigger type.

as:

$$\rho(z, I) = \rho_0[1 + \alpha(z - z_0)(I - I_0)], \qquad (I \geq 40\mu\text{A}), \tag{57}$$

and as a constant (ρ_0) for currents below 40 μA. Here, ρ_0 is the density of the target liquid in the absence of beam, z is the value of the reaction point z-position in meters, $z_0 = -0.05$ m, I is the beam current in μA and I_0 = 40 μA. The weighted average of α for the three trigger types is

$$\alpha = -0.0406 \pm 0.0031 \tag{58}$$

From this relation we can estimate, for example, the density reduction at the center of the target (z = 0) which is equal to the overall reduction for any distribution symmetric about the target center. For a beam current of 100 μA this amounts to ρ = 0.878 ρ_0 with an uncertainty of 0.9%.

IV.2.2 Deuterium Target

A similar study was carried out for the LD_2 target [95] (see Figure 54) . The data were taken at a fixed target fan speed of 60 Hz. The analyzed runs were 2641–2652 for raster

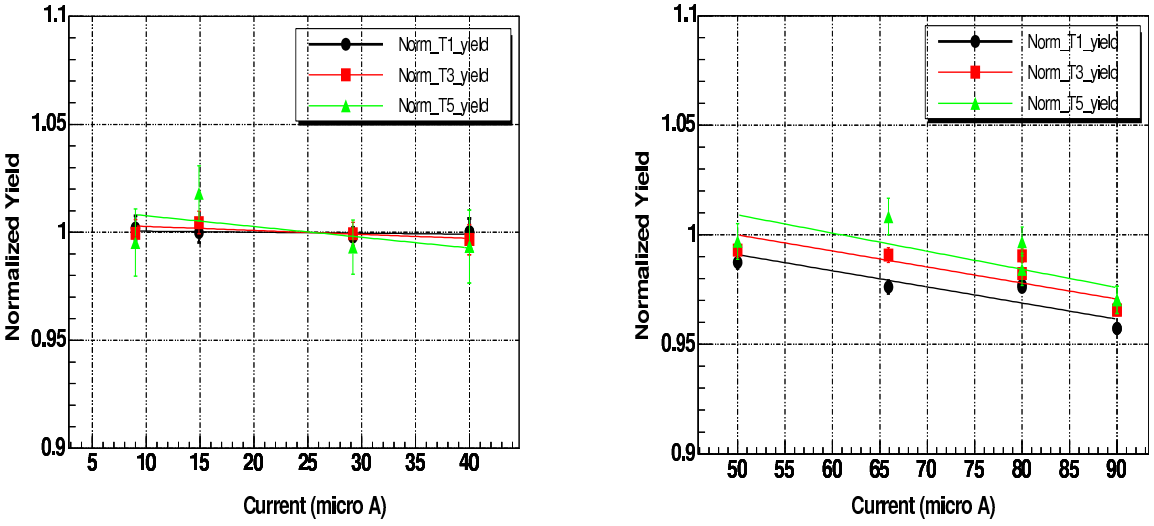

(a) Low current

(b) High current

FIG. 54: The normalized rates for each trigger type as a function of beam current for the LD_2 target (4×4 mm^2 raster case).

size 4×4 mm^2 and 2660–2669 for raster size 2×2 mm^2. The beam current ranged from 10 μA up to 90 μA. For the 2×2 mm^2 raster, the average α value was found to be

$$\alpha = -0.0173 \pm 0.0047 \tag{59}$$

which gives $\rho = 0.945\ \rho_0$ at the target center for a beam current of I =100 μA.

The ratio

$$f_\rho = \rho(z, I)/\rho_0 \tag{60}$$

is called the boiling factor and is used to correct the data yield before extracting the cross section.

IV.3 VDC CALIBRATIONS

The VDC time offsets for each signal wire (T0) are needed to determine the drift distances and thus the particle track through the VDC planes. Figure 55a shows the reduced chi-square, χ^2, of the fit to the drift times in the VDC wire planes for each cluster before optimizing T0. An optimization for T0 lowers the values of χ^2 as shown in 55b. Figure 55c shows the reconstructed slope differences (or angle differences) as determined from

the drift times in one plane versus two planes before T0 optimization. After the T0 optimization, the mean values of these slope differences become close to zero as shown in Figure 55d.

In addition to T0 optimization, the electron drift velocities, v_{drift}, and drift time difference look-up table (tdc_diff) were optimized and the results used to update ESPACE's database. Figure 56a shows the correlation between the fractional momentum deviation, δ_p, versus the track position along the U1 plane. The odd feature around the lower group of wires was discovered during the analysis and was deduced to be caused by an inverted cable connection during the experiment. This problem was fixed as shown in 56b by correctly modifying the detector map of ESPACE.

IV.4 TRACKING EFFICIENCY

A reasonable assumption, involving only the VDC detectors, assumes that any real particle traversing the VDCs should produce three-or-more hits in each of the four wire planes. A multiplicity cut of at least three wire hits in each of the 4 wire planes was applied. Also applied was a "one track at least" cut for each arm. The tracking efficiency ϵ_i for events of type i was then calculated as

$$\epsilon_i = \frac{T_i'}{T_i}, \qquad\qquad i = 1, 3, 5 \tag{61}$$

where T_i' is the number of coincidence events of type i passing the tracking cuts, and T_i is the total number of recorded events of type i. The above cuts were applied to the data in the highest Q^2 kinematics. Figure 57a shows the tracking efficiency for a VDC multiplicity cut of three to 10 hits. Figure 57b shows the tracking efficiency for a VDC multiplicity cut of three to 20 hits. By increasing the multiplicity upper limit from 10 to 20, the tracking efficiencies increase. During the final analysis of this dissertation, it was decided not to set any upper limit for the multiplicity cut (only require the multiplicity to be at least three hits per plane). In this case, the left and right tracking efficiency averages were found to be about 99% (see Table XXXIII in Section V.2).

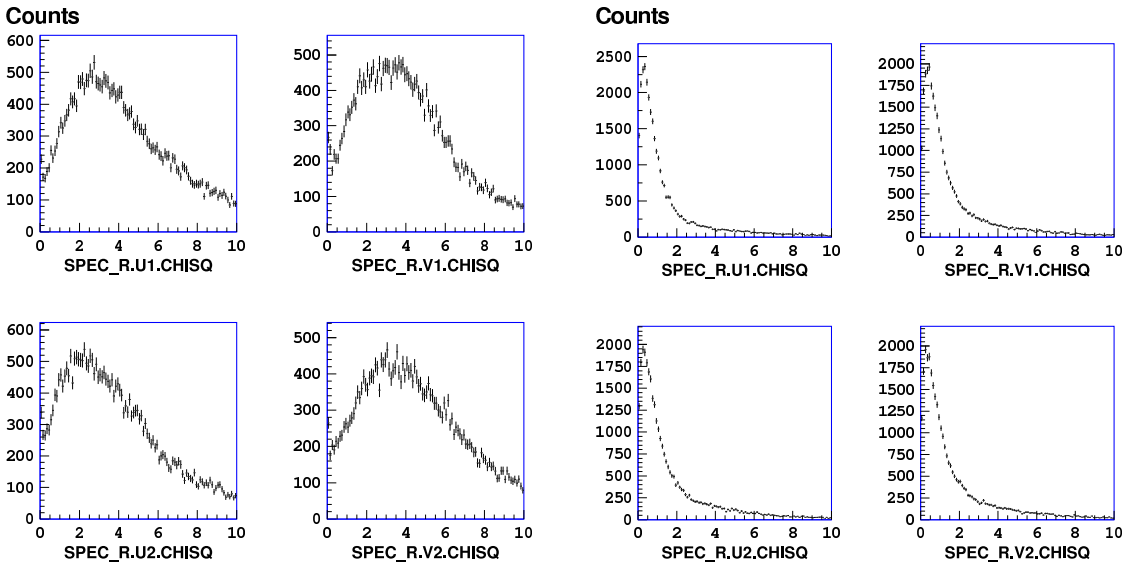

(a) Unoptimized Chi-Square. (b) Optimized Chi-Square.

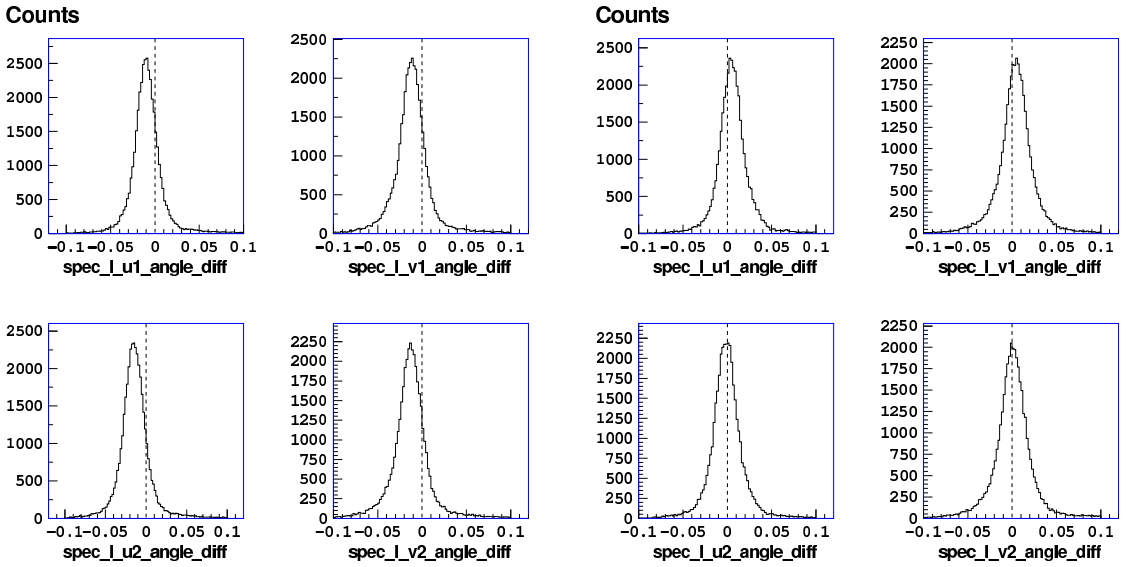

(c) Unoptimized Angle Difference. (d) Optimized Angle Difference.

FIG. 55: VDC T0 optimization.

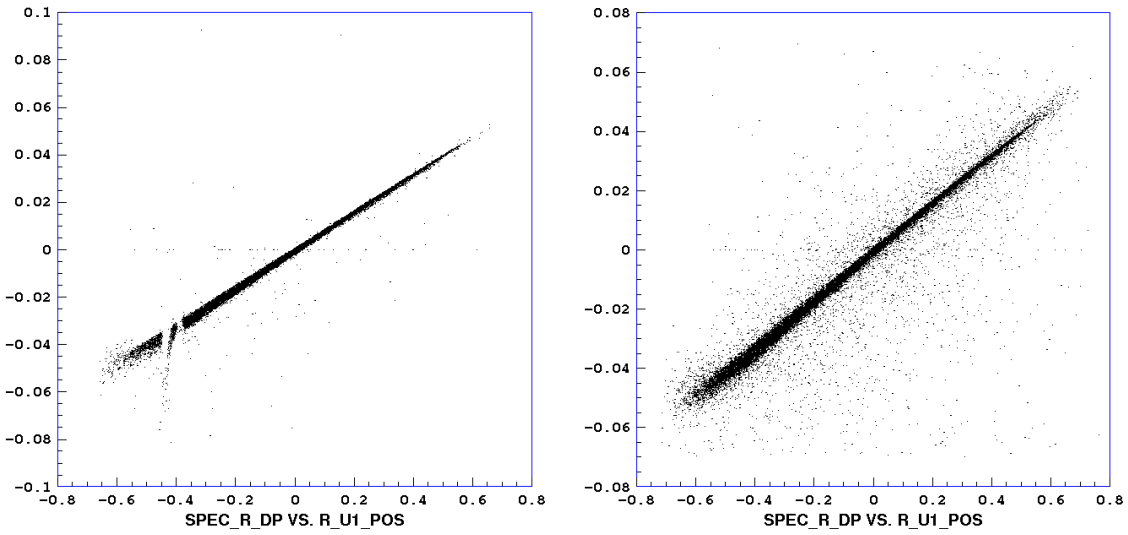

(a) Original ESPACE detector map

(b) Modified ESPACE detector map

FIG. 56: Right fractional momentum deviation versus VDC track position (meters) for the U1 wire plane.

IV.5 TRIGGER EFFICIENCY

Triggers are generated from scintillator signals and therefore trigger inefficiency is directly caused by scintillator inefficiency and the trigger electronics. This arises due to statistical fluctuations in the small amount of energy deposited by the charged particles in the scintillator paddles. It could be also due imperfect transmission of light emitted by the particles in the paddles to the photomultiplier tubes (PMTs), or simply inefficiencies of the PMTs themselves. Events missed by the main trigger types (T1, T3 and T5) due to the trigger inefficiency normally cause a T2 trigger in the proton spectrometer or T4 trigger in the electron spectrometer. The T2 and T4 triggers therefore allow us to calculate the trigger efficiencies. To determine the trigger efficiency, good VDC tracks were required and electrons were separated from π^- by a PID cut on the Gas Čerenkov ADC sum signal (ADCSUM > 150). A "good track" cut implies multiplicity of three hits or more and at least one track. The trigger efficiencies ϵ_p and ϵ_e for detection of electrons and protons, respectively, can be calculated from the trigger counts as

$$\epsilon_p = \frac{T_1 + T_5}{T_1 + T_5 + T_2}. \tag{62}$$

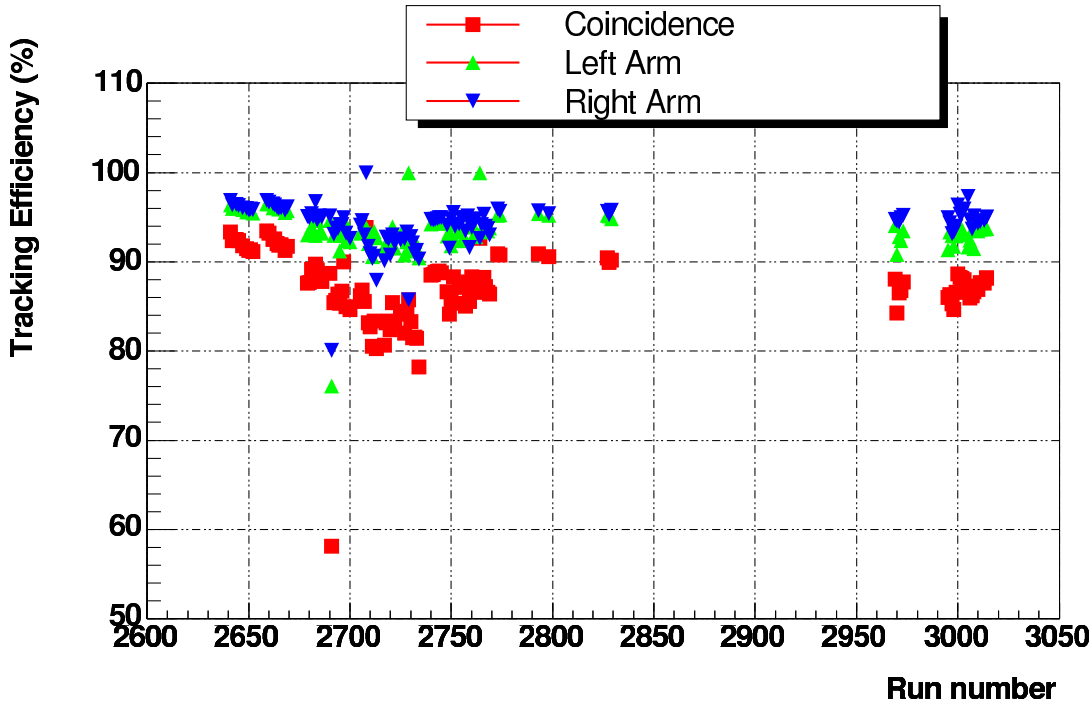

(a) VDC multiplicity between 3 and 10.

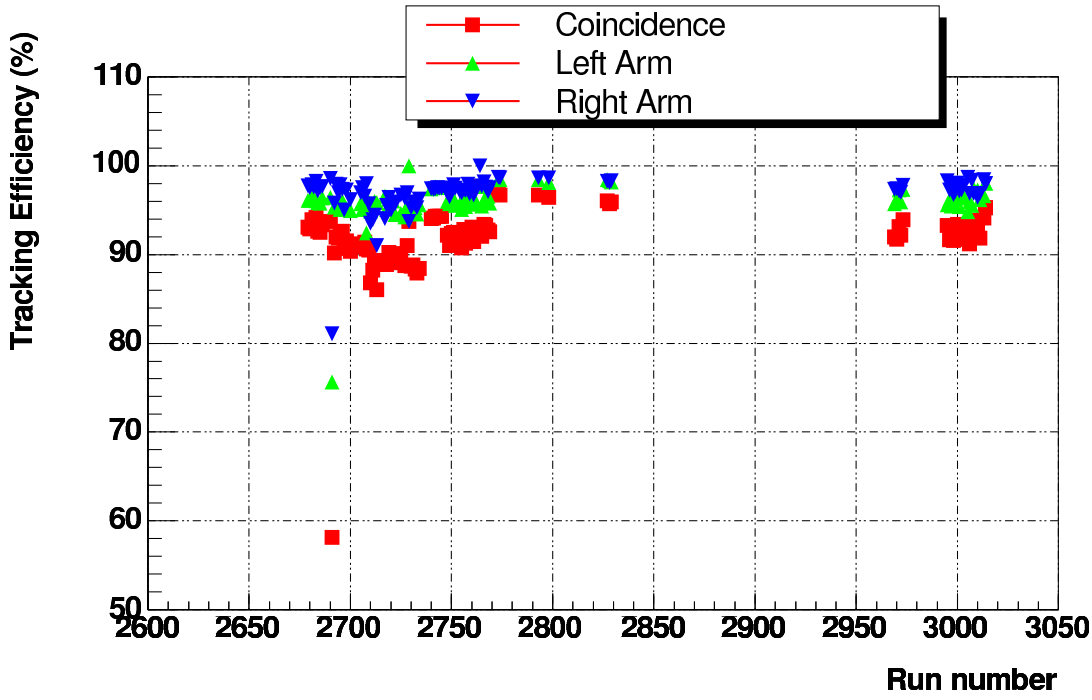

(b) VDC multiplicity between 3 and 20.

FIG. 57: Tracking efficiencies.

and

$$\epsilon_e = \frac{T_3 + T_5}{T_3 + T_5 + T_4}, \tag{63}$$

The trigger efficiency determined for the analyzed Q3 kinematics was 99% for detection of electrons and protons (see Table XXXIII in Section V.2). Statistical errors of the measurements were less than 0.5%.

IV.6 PARTICLE IDENTIFICATION EFFICIENCY

In this section, we discuss how we distinguished between the electrons and pions, π^-, detected in the left spectrometer by using the "particle identification" (PID) detectors.

IV.6.1 Gas Čerenkov Detector

The Čerenkov detector ten ADC pedestals and gains were calibrated by using data from run 2793. The Gas Čerenkov part of ESPACE database was updated to include the new calibration parameters.

To calculate the Gas Čerenkov detection efficiency for electrons in the left arm, coincidence events (T5 trigger type) from a ^{1}H$(e, e'p)$ elastic run (2792) were chosen to form a clean electron sample. Then, the Gas Čerenkov efficiency was calculated by:

$$\epsilon_{GC} = \frac{N_{cut}}{N_{tot}}, \tag{64}$$

where N_{tot} is the total number of events in the sample and N_{cut} is the number of events in the sample after the application of the one dimensional cut GCSUM > 150.0 on the corrected Gas Čerenkov ADC sum for all mirrors (see Figure 58). This cut was found to have a detection efficiency of more than 99% as shown in Table XVI. This table also shows the same cut efficiency calculated by applying a tight missing energy cut for the ^{2}H$(e, e'p)n$ quasielastic runs (2793 and 2955) which indicates the "stability" of the Čerenkov calibration for the full range of the highest Q^2 perpendicular kinematics (Q3_f00 - Q3_f50).

IV.6.2 Pion Rejector (Lead Glass Detector)

The Pion Rejector ADC pedestals and gains for the two layers were also calibrated by using data from run 2793. A pion rejector calibration file which includes all the new calibration offsets and coefficients was created and read by ESPACE.

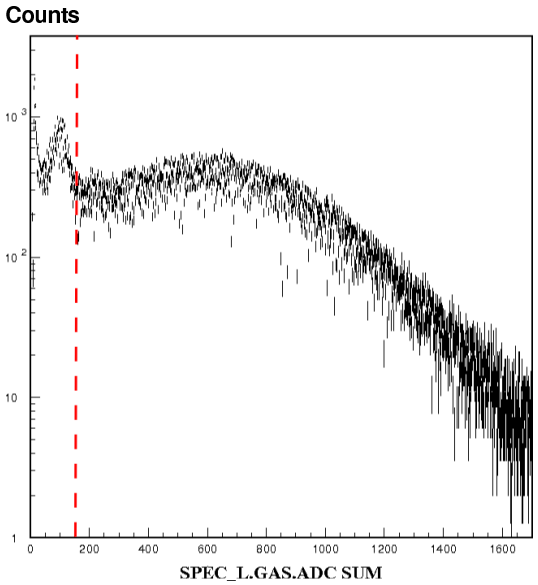

(a) Cerenkov ADC sum cut.

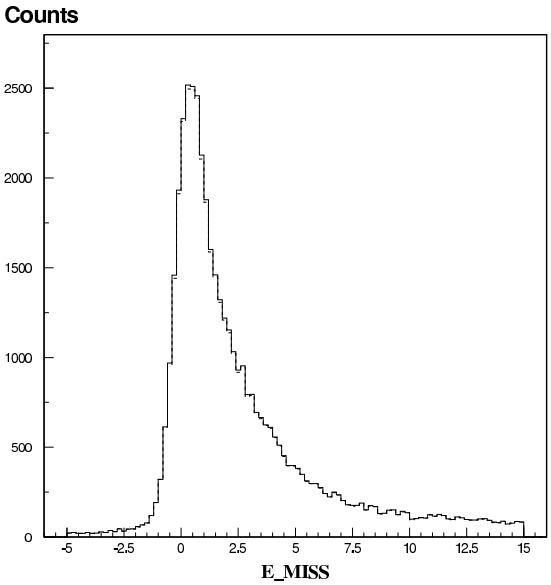

(b) Missing energy (MeV) for ^{1}H$(e,e'p)$ before (solid line) and after (dashed line) the Gas Čerenkov ADC sum cut.

FIG. 58: Čerenkov PID Cut efficiency is 99%.

To calculate the Pion Rejector detection efficiency for electrons in the left arm, coincidence (T5 trigger type) events from a ^{1}H$(e,e'p)$ elastic run (2792) were chosen to form a clean electron sample. A two-dimensional (2D) graphical cut (see Figure 59) on the corrected Pion Rejector ADC sums for the two layers (PR1SUM and PR2SUM), to exclude the dashed band, was found to have a detection efficiency of more than 99% as shown in Table XVI. Also listed in this table, is the cut efficiency for the ^{2}H$(e,e'p)n$ quasielastic runs (2793 and 2955), after applying a tight missing energy cut, which show the "stability" of the Pion Rejector calibration for the analyzed kinematics. The combination of the two PID cuts (GCSUM and the PRSUMs) is shown in Figure 60. In this figure, the electrons are simply represented by the irregular spheroid at the center of the cube.

IV.7 SPECTROMETER MISPOINTING

The method for correcting the mispointing of the Hall A High Resolution Spectrometers (HRS-L and HRS-R) is presented in this section [95]. This method uses runs taken with carbon targets, either single foil or multifoil targets, and the target position survey data. From the analysis of these data we determined the mispointing offset between the centers

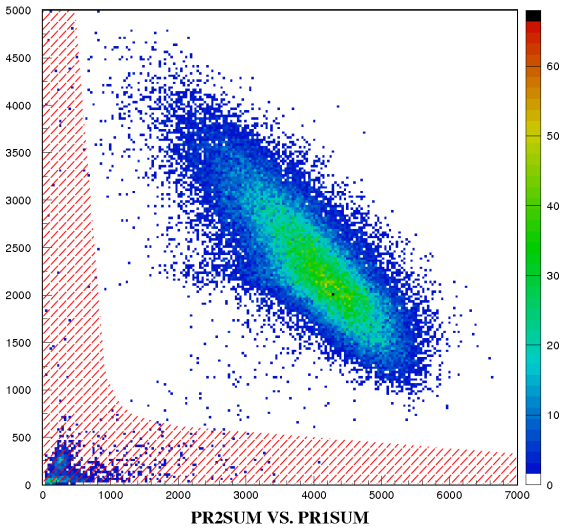

(a) Pion Rejector ADC sum 2D cut.

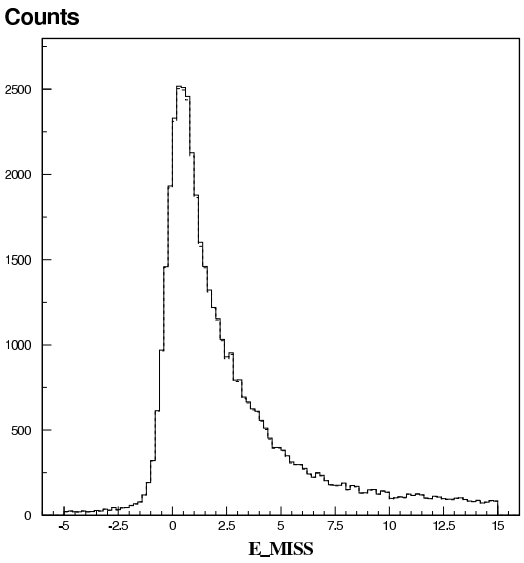

(b) Missing energy (MeV) for ^{1}H$(e,e'p)$ before (solid line) and after (dashed line) the Pion Rejector ADC sum 2D cut.

FIG. 59: Pion Rejector PID 2D Cut efficiency is 99%.

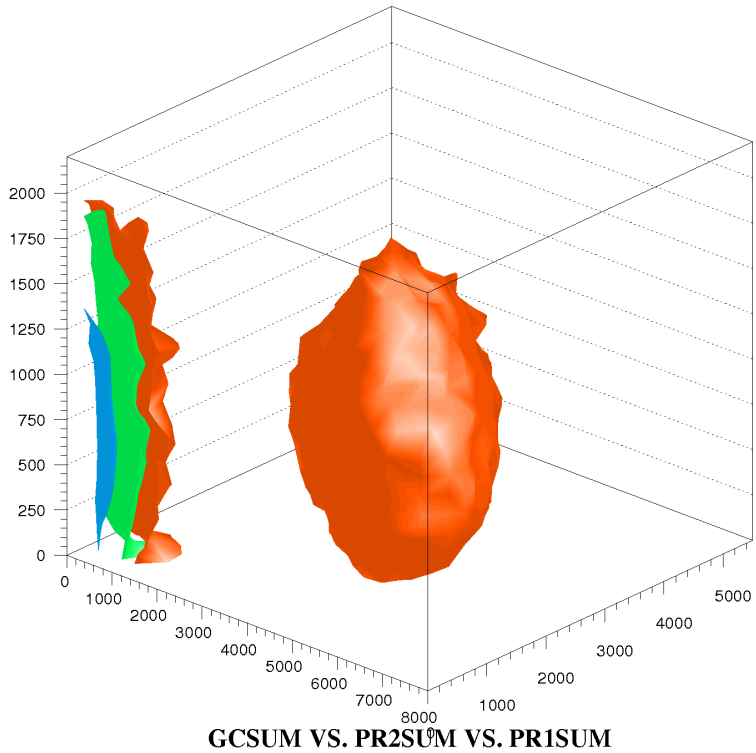

FIG. 60: Gas Čerenkov ADC sum (GCSUM) versus the Pion Rejector two layer ADC sums (PR1SUM and PR2SUMS).

TABLE XVI: PID cut efficiency for the Gas Čerenkov ADC sum (GCSUM) cut, the Pion Rejector two layers ADC sums (PRSUM) cut and the combination of these two cuts.

Run Number	Target Type	p_{miss} (MeV)	Cut Efficiency GCSUM Cut	PRSUM Cut	GCSUM+PRSUM Cuts
2792	LH_2	0	99.2	99.2	98.4
2793	LD_2	0	99.0	98.9	98.0
2955	LD_2	500	99.4	97.8	97.2

of two coordinate systems, the Hall Coordinate System (HCS) and the Target Coordinate System (TCS) (see Section III.7). In the ideal case the origin of the TCS coincides with the origin of the HCS. The mispointing offset is approximated by a horizontal displacement of the spectrometer, $\vec{r}_\circ$, with components in the HCS as $x_\circ$ and $z_\circ$. The target z-position, z_{tg}, as given in the survey, the reconstructed target variables y_{tg}, ϕ_{tg}, the spectrometer central angle $\theta_\circ$ (positive value for the left arm and negative value for the right arm) and the beam x-position, x_{Beam}, are used to calculate the spectrometer horizontal offset, $h_\circ$.

The vertex (or the reaction point) is defined as the intersection of the incoming electron trajectory (beam) and the scattered particle (electron or proton) trajectory as shown in Figure 61. The incoming electron trajectory in HCS is given by:

$$x_{Beam} = x_{0B} + z \tan\theta_{Beam}, \tag{65}$$

where x_{0B} is the point where the beam intersects the x-axis in the HCS, and θ_{Beam} is the angle that the beam makes with the z-axis in the HCS. The scattered particle trajectory in HCS is given by:

$$x_{traj} = x_{0t} + z \tan\beta, \tag{66}$$

where x_{0t} is the point where the scattered particle (electron or hadron) intersects with the x-axis in the HCS, and $\beta = \theta_\circ + \phi_{tg}$ is the angle that the particle trajectory makes with the z-axis in the HCS:

$$\tan\beta = \frac{p_x}{p_z}. \tag{67}$$

Here, p_x and p_z are the components of the scattered particle momentum, $\vec{p}$, in the HCS. The vertex horizontal location is where these two trajectories in Equations (65) and (66) intersect:

$$x_{traj} = x_{Beam}. \tag{68}$$

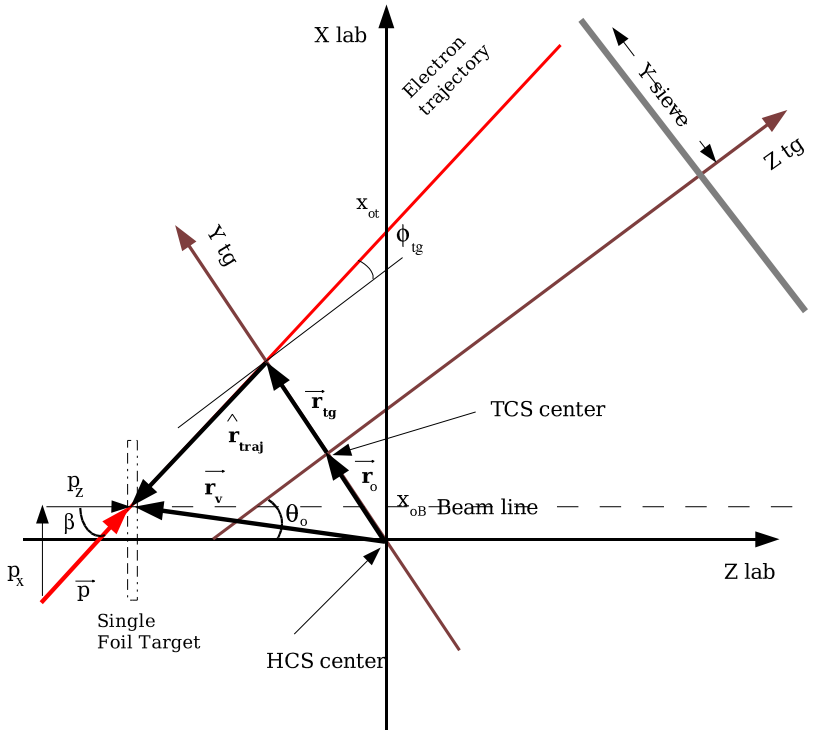

FIG. 61: Hall coordinates and target coordinates for electrons scattering from a thin foil target. Distances are not to scale. $\theta_\circ$ is the spectrometer central angle. Note that the x_{tg}-axis is vertically down and the y-axis in the HCS (or Lab) is vertically up.

The vector diagram in Figure 61 allows the calculation of the spectrometer offsets by using the following vector equation (see Figure 61):

$$\vec{r}_\circ + \vec{r}_{tg} + \alpha \hat{r}_{traj} = \vec{r}_v, \tag{69}$$

where α is the distance between the vertex and the intersection of the scattered particle trajectory with the y_{tg}-axis. Using Equations (68) and (69), the expression for the horizontal offset, $h_\circ \equiv |\vec{r}_\circ|$, can be found to be:

$$h_\circ = -y_{tg} + x_{Beam}(\cos\theta_\circ - \sin\theta_\circ \tan\phi_{tg}) - z_{tg}(\sin\theta_\circ + \cos\theta_\circ \tan\phi_{tg}), \tag{70}$$

or in terms of the angle β as:

$$h_\circ = -y_{tg} + \frac{x_{Beam}\cos\beta - z_{tg}\sin\beta}{\cos\phi_{tg}}. \tag{71}$$

The components of the horizontal offset vector can now be obtained from:

$$x_\circ = h_\circ \cos\theta_\circ, \tag{72}$$

$$z_\circ = -h_\circ \sin\theta_\circ. \tag{73}$$

Table XXIX in Chapter V lists the results for the Left and Right arm mispointing offsets, $x_\circ$ and $z_\circ$, for all the highest Q^2 perpendicular kinematics of Experiment E01-020.

IV.8 OPTICS CALIBRATION

The Hall A optimizer program was used to optimize the optics part of the ESPACE database for Experiments E01-020 and then the optimized database was used to determine the optics target z-positions.

IV.8.1 Optimization of the Optics Matrix Elements

The target coordinates are related to the focal plane coordinates through the optics (or reconstruction) matrix elements (Y_{jkl}, T_{jkl}, P_{jkl}, D_{jkl}):

$$y_{tg} = \sum_{j,k,l=0}^{n} Y_{jkl}\theta_{fp}^{j} y_{fp}^{k} \phi_{fp}^{l}, \tag{74}$$

$$\theta_{tg} = \sum_{j,k,l=0}^{n} T_{jkl}\theta_{fp}^{j} y_{fp}^{k} \phi_{fp}^{l}, \tag{75}$$

$$\phi_{tg} = \sum_{j,k,l=0}^{n} P_{jkl}\theta_{fp}^{j} y_{fp}^{k} \phi_{fp}^{l}, \tag{76}$$

$$\delta_{tg} = \sum_{j,k,l=0}^{n} D_{jkl}\theta_{fp}^{j} y_{fp}^{k} \phi_{fp}^{l}. \tag{77}$$

Each one of the Y_{000}, T_{000} and P_{000} offsets (or y_{000}, t_{000} and p_{000} as defined in the ESPACE database) is represented by a polynomial in x_{fp} as $\sum_i c_i x_{fp}^i$. Similarly, each element of the Y_{jkl}, T_{jkl}, P_{jkl} and D_{jkl} tensors is represented by a polynomial in x_{fp} as $\sum_i C_i x_{fp}^i$. In practice, the expansion of the focal plane coordinates is done up to the forth order ($n = 4$). In order to optimize the optics matrix elements efficiently, we started by testing the best available ESPACE database which was optimized for a recent experiment [96] and then optimizing it for experiments E01-020. The Hall A optimizer computer program [97] was

used to test and optimize the database. The data (Run 1052) was collected for the multifoil carbon target (see Figure 62) by detecting electrons in the Left and Right arms with sieve slits placed on both of them. Many Hall A surveys were used in the optimization process [70], in particular, spectrometer survey # A776, collimator surveys # A753 and # A779 and target surveys # A770 and # A805 [70]. For a summary of the different sign conventions used in the surveys see Appendix C.

Figure 63 shows a flow chart of the necessary steps needed to complete the optics optimization. The database was optimized first for the offsets, y_{000}, t_{000} and p_{000} (y000, t000 and p000 database matrix elements). These offsets are expressed as polynomials in the focal plane x-coordinate, x_{fp}, and are used in the transformation from the detector to the focal plane coordinate systems. In the next stage the database was optimized for the Y_{jkl} tensor (Yxxx matrix elements). Finally, the database was optimized for the T_{jkl} and P_{jkl} tensors (Txxx and Pxxx database matrix elements). No optimization was done for the D_{jkl} tensor (Dxxx database matrix elements). The Y_{jkl}, T_{jkl}, P_{jkl} and D_{jkl} tensors are also polynomials in x_{fp} and are used to link the focal plane coordinates, y_{fp}, θ_{fp} and ϕ_{fp} to the target coordinates, y_{tg}, θ_{tg} and ϕ_{tg} in addition to the relative momentum, δ, (see Figure 64). Tables LVII-LXII in Appendix B list the numerical values of the c_i and C_i coefficients before and after the optimization for both the left and right arms[2].

Some modifications were necessary to complete the optimization process. The most important modification was to allow ESPACE to analyze the large number of peaks needed to optimize the database for the angles (the previous maximum was only 50 peaks) [92]. All the ESPACE and PAW scripts and Fortran codes associated with the optimizer program were entirely rewritten to achieve the best optimization. Careful attention was paid to the format of the resulting database after each optimization stage so that the resulting database would be compatible with the read routine within ESPACE. Manual corrections of the optimized databases were necessary in some cases.

Comparisons between Hall A surveys and the data for Run # 1052 are shown in Figures 65 and 66. When the initial database was tested, the sieve hole positions were off by about 0.5 cm compared with the corresponding sieve survey, and the reaction point z-positions, z_{react}, were initially correlated with the rotated (or focal plane) y-coordinate, y_{rot}. The optimized database removed all these offsets and correlations as can be seen from the figures.

[2]In Reference [97], c_i's are referred to as y_{i000}, t_{i000} and p_{i000} and C_i's are referred to as $C_i^{Y_{jkl}}$, $C_i^{T_{jkl}}$, $C_i^{P_{jkl}}$ and $C_i^{D_{jkl}}$.

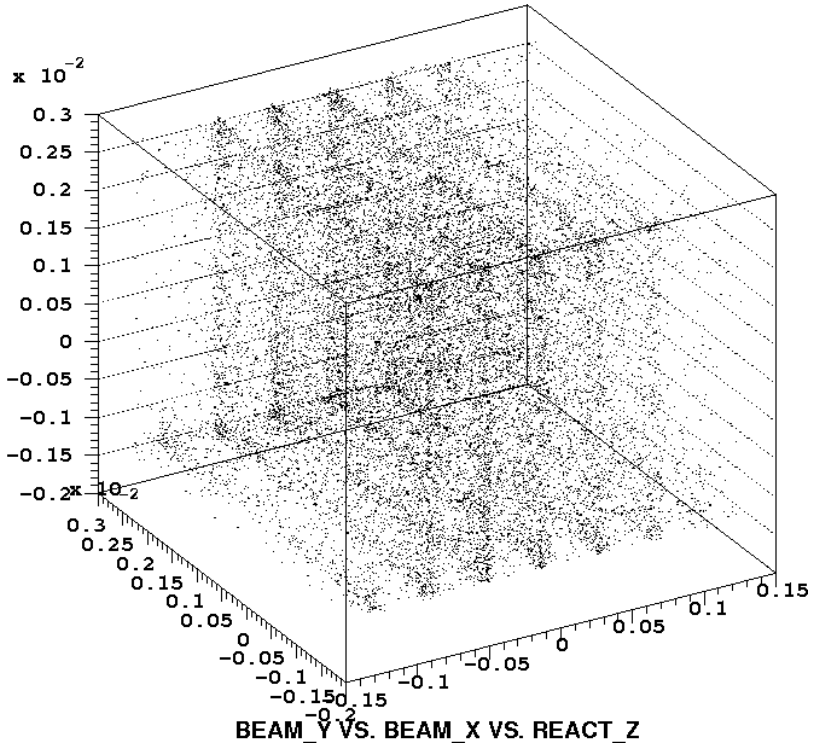

FIG. 62: Event Reconstruction in the multifoil carbon target (in meters).

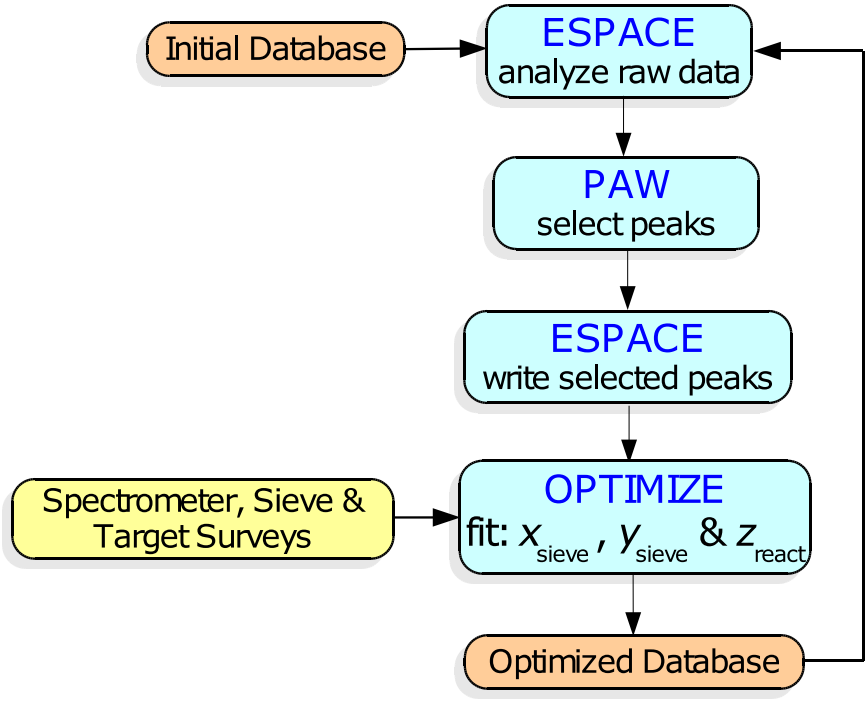

FIG. 63: Optics optimization steps.

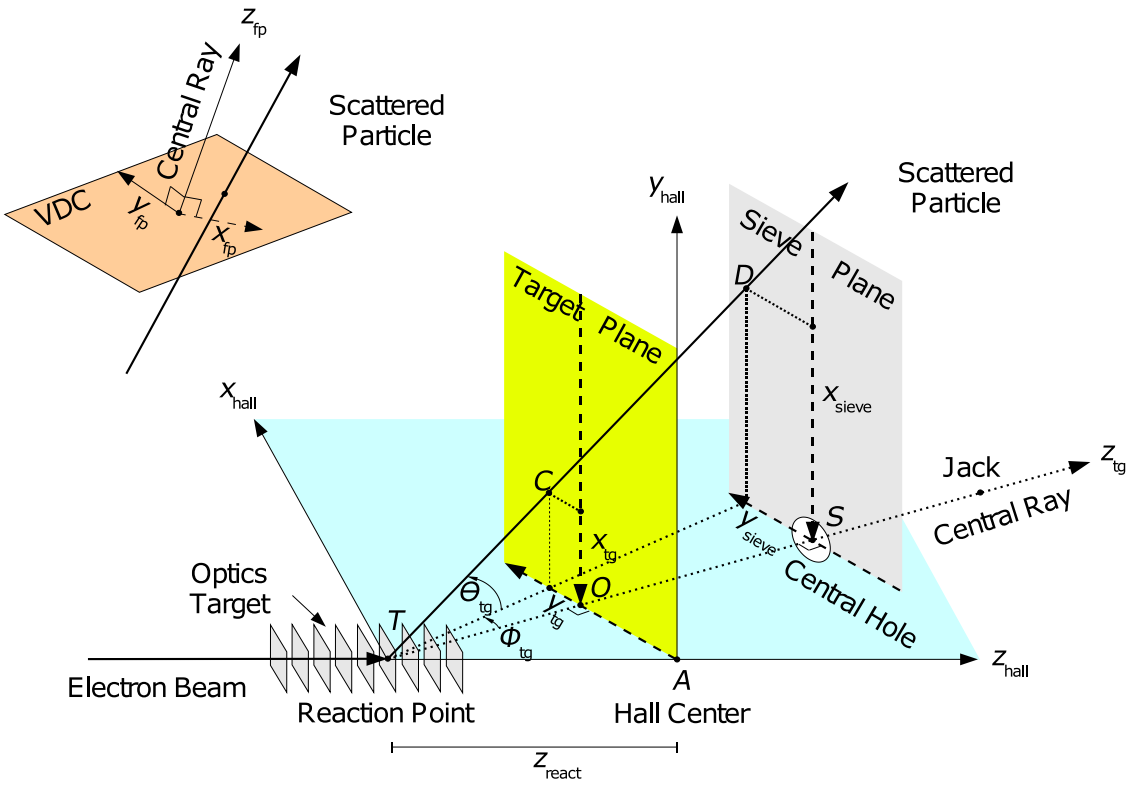

FIG. 64: Coordinate systems used in the optics optimization.

IV.8.2 Optics Target Positions

The optimized database was then used to determine the optics target z-positions. The available target survey during the run period (survey #A770) indicated the z-position of the multifoil carbon target central foil to be at about -1 mm relative to the Hall A origin. Unfortunately, the thin carbon target z-position was not surveyed. The reaction point z-positions, z_{react}, for the central foil calculated directly by ESPACE versus those calculated from y_{tg}, ϕ_{tg} and x_{Beam} are shown in Tables XVII and XVIII respectively, while a comparison is given in Table XIX. Similar results are shown in Tables XX-XXII for the thin carbon target. The calculation of z_{react} was introduced as a way to check the method used by ESPACE to calculate z_{react} after observing some dependence on the x_{Beam} cuts (double rows in the tables). The following equation was used to calculate z_{react} (see Equation (70)):

$$z_{react} = \frac{-h_\circ - y_{tg} + x_{Beam}(\cos\theta_\circ - \sin\theta_\circ \tan\phi_{tg})}{(\sin\theta_\circ + \cos\theta_\circ \tan\phi_{tg})}, \tag{78}$$

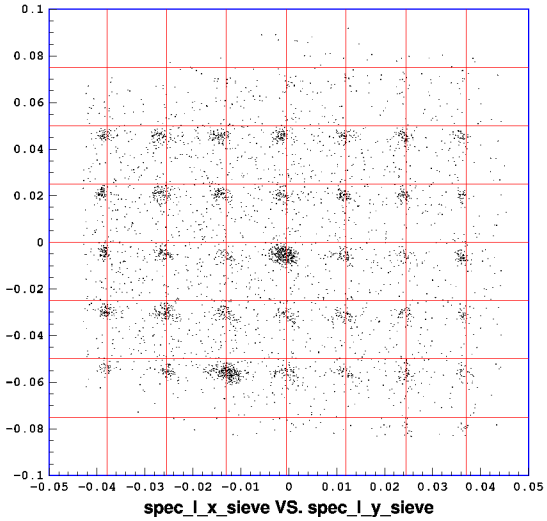

(a) Left sieve holes before optics optimization.

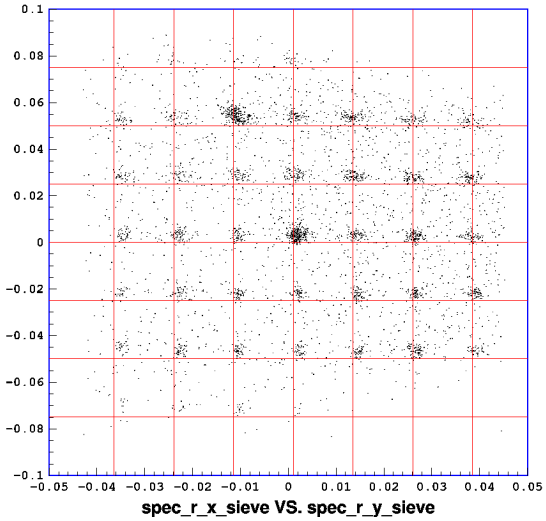

(b) Right sieve holes before optics optimization.

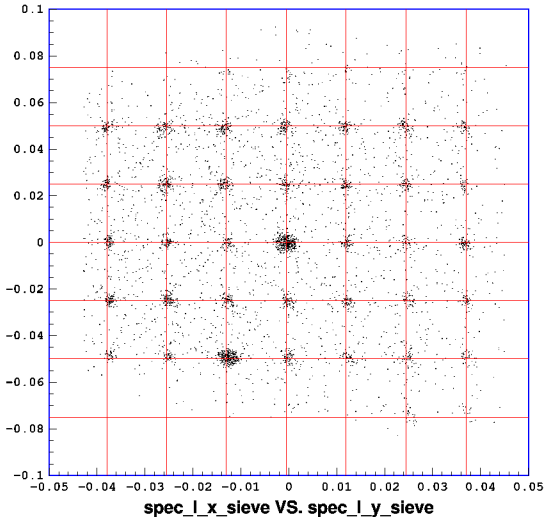

(c) Left sieve holes after optics optimization.

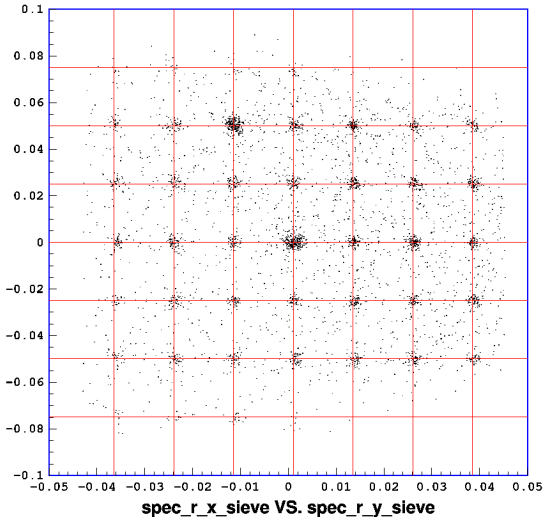

(d) Right sieve holes after optics optimization.

FIG. 65: Right and Left arm reconstruction of the sieve holes. The grid lines represent the surveyed positions (in meters).

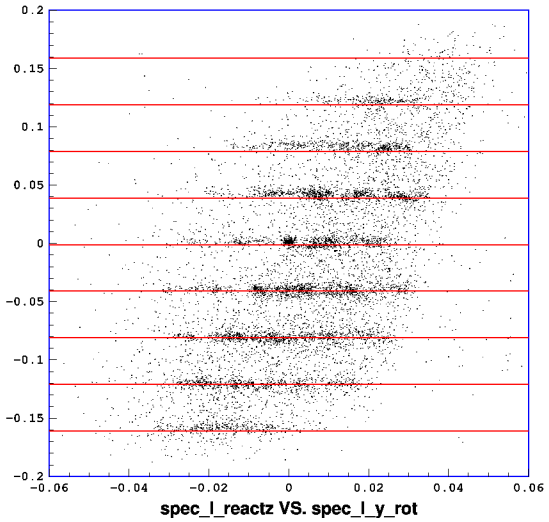

(a) Left z_{react} before optics optimization.

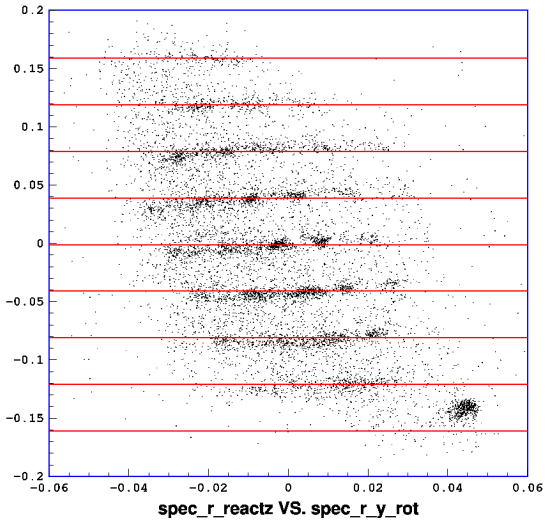

(b) Right z_{react} before optics optimization.

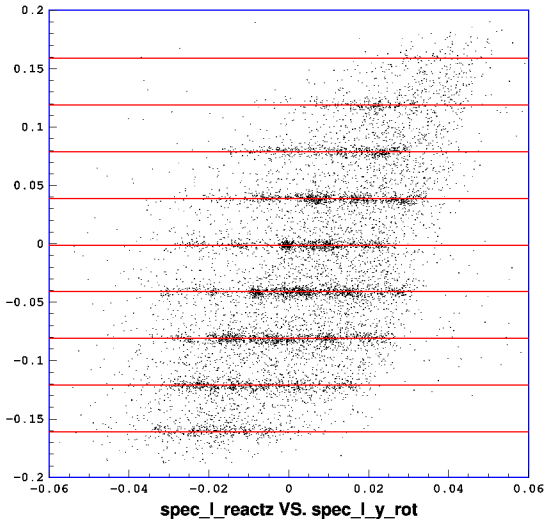

(c) Left z_{react} after optics optimization.

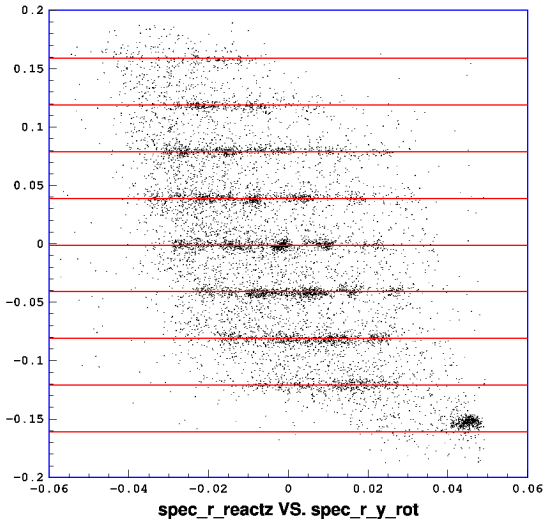

(d) Right z_{react} after optics optimization.

FIG. 66: Reaction point z-positions, z_{react}, reconstructed from Left and Right arms, versus the focal plane y-position, y_{rot}, for the multifoil carbon target (in meters). The horizontal lines represent the surveyed foil positions (in meters).

where $\theta_\circ$ is the spectrometer central angle and $h_\circ$ is the spectrometer horizontal offset from the survey (see Appendix C). Tight cuts were applied on x_{Beam}, y_{sieve} and y_{tg} to choose the beam x-position, the central sieve hole and the central target foil respectively (for example see Figure 67). The cut on x_{Beam} was necessary when the beam raster was turned on or the beam position was not stable. The uncertainty for z_{react} in Equation (78) was calculated by ignoring the $\tan\phi_{tg}$ terms and the uncertainty in $\theta_\circ$ and assuming a typical uncertainty of 0.3 mm for $h_\circ$ and x_{Beam}.

In general, we see that the measured central foil z-position is within the approximate range -1.0 ± 1.0 mm. This ± 1.0 mm range is consistent with variations seen in the past due to target warm-up and cool-down [98] and also the movement of the target ladder. The weighted averages of z_{react} for the central foil are -1.28 ± 0.29 mm and -0.53 ± 0.31 mm for the Left and Right arms respectively and the overall weighted average of both arms is -0.93 ± 0.21 mm which agrees with the surveyed position of -1.0 mm. Similar results are shown in Tables XX-XXII for the thin carbon target position which was not surveyed during the experiment. From these tables we see that the measured z-position of the thin carbon target is within the approximate range 0.5 ± 0.5 mm. Again, this is consistent with the variations in the target position seen in the past. The weighted averages of z_{react} for the thin carbon target are 0.34 ± 0.24 mm and 0.73 ± 0.11 mm for the left and right arms respectively and the overall weighted average for both arms is 0.66 ± 0.10 mm.

IV.9 KINEMATICS CALIBRATION

The calibration of the Hall A Left and Right High Resolution Spectrometers (HRS) central kinematics is an important task, especially for absolute measurements of the cross sections. Several methods were applied earlier to calibrate only the spectrometer in-plane angles (see References [64, 65]) but no efforts were done before to globally calibrate also the momentum and the out-of-plane angles for the two Hall A HRS. In this section, a general method is developed to calibrate the Hall A HRS central kinematics for Experiment E01-020 [91]. This method uses the kinematical constraints on the invariant mass, W, the missing energy, E_{miss}, and the missing momentum components, p_{missx}, p_{missy}, and p_{missz}, for ^{1}H$(e,e'p)$ elastic scattering in a χ^2 minimization fitting procedure to determine the global absolute spectrometer momentum and angular offsets [99].

TABLE XVII: ESPACE z_{react} for the central foil of the multifoil carbon target.

Date	Survey #	Exp #	Run #	Raster	x_{Beam} (mm)	Left Arm $\theta_\circ$ (°)	Left Arm z_{react} (mm)	Right Arm $\theta_\circ$ (°)	Right Arm z_{react} (mm)
May 2	A764	E01-001	1170	on	-0.78	22.155	-1.09	-22.184	-1.66
					$+0.17$		-2.30		-0.12
June 1	A776	E01-020	1052	off	$+0.45$	19.612	-1.04	-19.670	-0.54
June 25	A790	E01-020	1809	off	$+0.42$	74.979	-1.22	-66.270	-0.46

TABLE XVIII: Calculated z_{react} from Equation (78) for the central foil of the multifoil carbon target.

Run #	Left Arm x_{Beam} (mm)	Left Arm $h_\circ$ (mm)	Left Arm y_{tg} (mm)	Left Arm z_{react} (mm)	Right Arm $h_\circ$ (mm)	Right Arm y_{tg} (mm)	Right Arm z_{react} (mm)	Difference z_{react} (mm)
1170	-0.78	1.51	-1.81	-1.14 ± 1.08	$+3.20$	-4.58	-1.74 ± 1.08	0.60 ± 1.85
	$+0.17$		-0.47	-2.33 ± 1.08		-3.05	-0.03 ± 1.08	-2.30 ± 1.85
1052	$+0.45$	1.92	-1.13	-1.08 ± 1.23	$+3.33$	-3.10	-0.58 ± 1.22	-0.50 ± 2.10
1809	$+0.42$	3.10	-1.82	-1.21 ± 0.32	-0.12	-0.12	-0.45 ± 0.35	-0.76 ± 0.50

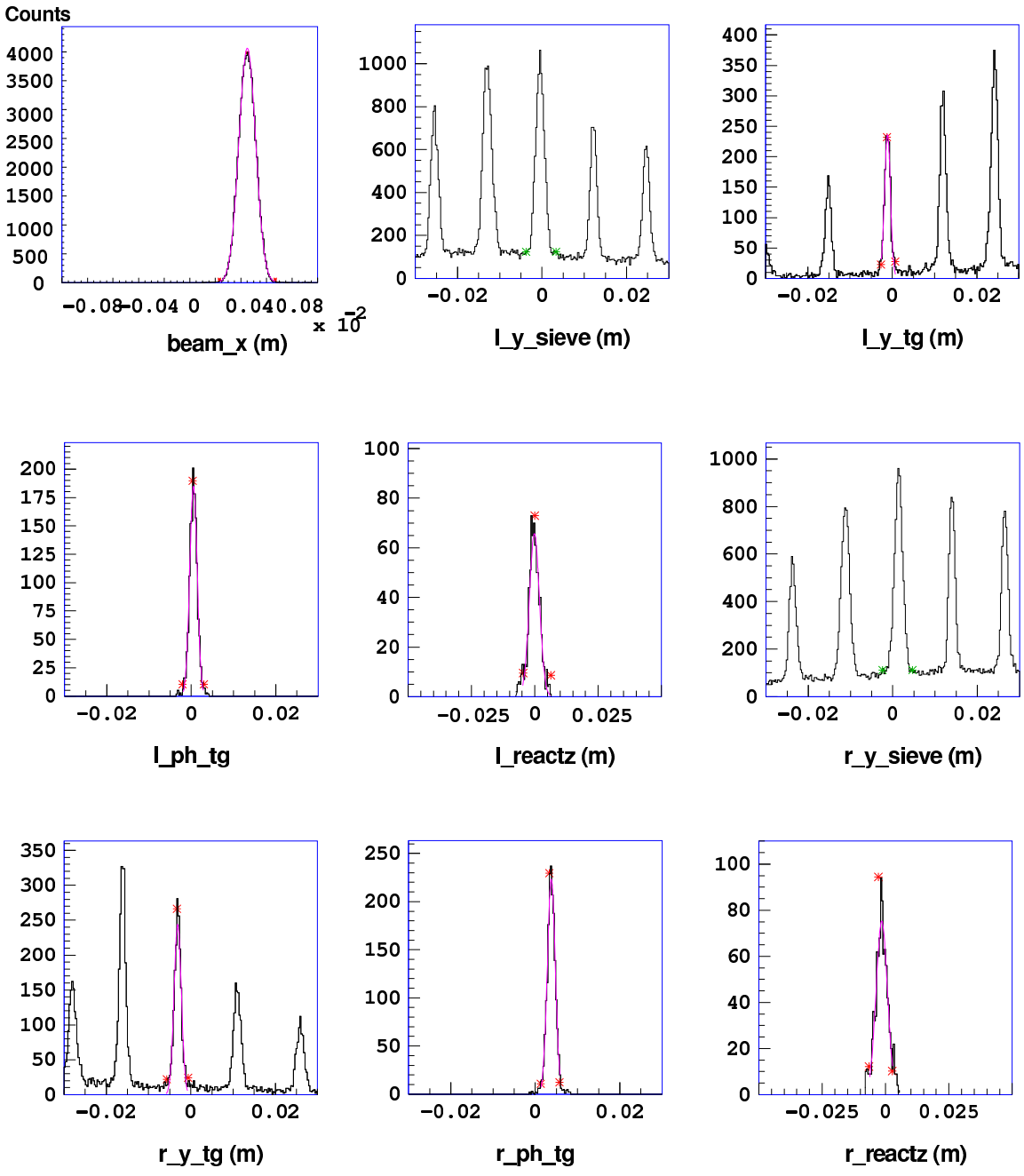

FIG. 67: Determination of the optics target z-position for Run 1052.

TABLE XIX: ESPACE z_{react} versus calculated z_{react} for the multifoil carbon target.

	Left Arm		Right Arm	
Run #	ESPACE (mm)	Equation (78) (mm)	ESPACE (mm)	Equation (78) (mm)
1170	-1.09	-1.14	-1.66	-1.74
	-2.30	-2.33	-0.12	-0.03
1052	-1.04	-1.08	-0.54	-0.58
1809	-1.22	-1.21	-0.46	-0.45

IV.9.1 Reaction Kinematics for ^{1}H$(e,e'p)$

The incident and scattered electron four-momenta are defined as $k^\mu = (e, \vec{k})$ and $k'^\mu = (e', \vec{k}')$ where E and E' are the incident and scattered electron energies and $\vec{k}$ and $\vec{k}'$ are the incident and scattered electron momenta. In the *extreme relativistic limit*, the electron mass m_e can be neglected so that $k \approx E$ and $k' \approx E'$. The four-momentum transfer $q^\mu = (\omega, \vec{q})$, is the difference between the incident and scattered electron four-momenta, where, $\omega = E - E'$ and $\vec{q} = \vec{k} - \vec{k}'$ are the energy and momentum transfer respectively. The proton four-momentum is given by $p^\mu = (E_p, \vec{p})$, where $E_p = \sqrt{p^2 + M_p^2}$ and $\vec{p}$ are the proton energy and momentum respectively. Finally, the missing four-momentum, $p^\mu_{miss} = (E_{miss}, \vec{p}_{miss})$, is the difference between the *observed* initial and final total four-momenta of the system, where $E_{miss} = \omega + M_p - E_p$ and $\vec{p}_{miss} = \vec{q} - \vec{p}$ are the missing energy and momentum respectively.

In the Hall Coordinate System (HCS) shown in Figure 68, the momentum vectors are given by:

$$\vec{k} = (0, 0, E) \tag{79}$$

$$\vec{k}' = (E' \sin\theta'_e \cos\phi'_e, E' \sin\theta'_e \sin\phi'_e, e' \cos\theta'_e), \tag{80}$$

$$\vec{q} = (-E' \sin\theta'_e \cos\phi'_e, -E' \sin\theta'_e \sin\phi'_e, E - E' \cos\theta'_e), \tag{81}$$

$$\vec{p} = (p \sin\theta'_p \cos\phi'_p, p \sin\theta'_p \sin\phi'_p, p \cos\theta'_p), \tag{82}$$

where θ' and ϕ' are the spherical in-plane and out-of-plane angles. It is desirable to do the calibration in terms of the geographical angles rather than the spherical angles[3]. The

[3]The standard ESPACE header files requires the values of the geographical angles.

TABLE XX: ESPACE z_{react} for the thin carbon target.

Date	Survey #	Exp #	Run #	Raster	x_{Beam} (mm)	Left Arm $\theta_\circ$ (°)	Left Arm z_{react} (mm)	Right Arm $\theta_\circ$ (°)	Right Arm z_{react} (mm)
May 3	A764	E01-001	1181	on	−0.37	22.155	−0.11	−22.184	−0.02
					0.60		−1.16		0.81
May 6	A765/A772	E01-001	1318	off	0.13	12.528	0.43	−60.070	0.39
May 9	A765/A768	E01-001	1386	off	0.14	40.070	0.35	−65.684	0.76
May 10	A765/A769	E01-001	1407	off	0.11	30.984	0.11	−65.663	0.76
May 10	A769	E01-001	1436	off	0.08	33.150	0.95	−63.202	0.13
May 17	A772/A773	E01-001	1596	on	−0.16	29.462	0.66	−62.038	0.74
					1.03		0.02		1.22
May 21	A773	E01-001	1739	off	0.15	28.368	0.64	−64.981	0.91
May 22	A775	E01-001	1782	off	0.41	12.624	1.08	−58.309	0.86
May 24	A776	E01-001	1864	on	0.07	23.652	0.74	−63.871	1.11
					0.58		0.86		1.17
May 31	A776	E01-020	1040	off	−0.79	19.612	0.04	−19.670	0.16
					0.35		−0.15		0.29
					0.57		−0.17		0.28

TABLE XXI: Calculated z_{react} from Equation (78) for the thin carbon target. The difference between Left and Right z_{react} is given in the last column.

	Left Arm				Right Arm			Difference
Run #	x_{Beam} (mm)	$h_\circ$ (mm)	y_{tg} (mm)	z_{react} (mm)	$h_\circ$ (mm)	y_{tg} (mm)	z_{react} (mm)	z_{react} (mm)
1181	-0.37	1.51	-1.78	-0.17 ± 1.08	3.20	-3.54	-0.01 ± 1.08	-0.16 ± 1.85
	0.60		-0.53	-1.13 ± 1.08		-2.38	0.69 ± 1.08	-1.82 ± 1.85
1318	0.13	1.78	-1.78	0.57 ± 1.93	-0.63	1.05	0.41 ± 0.39	0.16 ± 2.09
1386	0.14	2.15	-2.27	0.36 ± 0.59	3.43	-2.80	0.62 ± 0.36	-0.26 ± 0.75
1407	0.11	1.53	-1.52	0.16 ± 0.77	3.43	-2.78	0.66 ± 0.36	-0.50 ± 0.92
1436	0.08	1.53	-1.97	0.91 ± 0.72	3.11	-2.91	0.19 ± 0.37	0.82 ± 0.89
1596	-0.16	1.70	-2.15	0.64 ± 0.81	2.42	-1.82	0.76 ± 0.38	-0.12 ± 0.98
	1.03		-0.75	-0.12 ± 0.81		-0.88	1.20 ± 0.38	-1.32 ± 0.98
1739	0.15	1.70	-1.91	0.72 ± 0.84	0.51	0.41	0.94 ± 0.36	-0.22 ± 1.00
1782	0.41	1.78	-1.63	1.11 ± 1.92	3.24	-2.47	0.66 ± 0.40	0.45 ± 2.08
1864	0.07	1.25	-1.48	0.73 ± 1.01	0.62	0.39	1.08 ± 0.37	-0.35 ± 1.17
	0.58			1.01 ± 1.01		0.49	0.95 ± 0.37	0.06 ± 1.17
1040[a]	-0.79	1.92	-2.69	0.06 ± 1.23	3.33	-4.06	0.06 ± 1.22	0.00 ± 2.10
	0.35		-1.54	-0.12 ± 1.23		-2.91	0.27 ± 1.22	-0.39 ± 2.10
	0.57		-1.35	-0.11 ± 1.23		-2.70	0.29 ± 1.22	-0.40 ± 2.10

[a]The beam position was not stable during Run # 1040.

TABLE XXII: ESPACE versus calculated z_{react} for the thin carbon target.

	Left Arm		Right Arm	
Run #	ESPACE (mm)	Equation (78) (mm)	ESPACE (mm)	Equation (78) (mm)
1181	−0.11	−0.17	−0.02	−0.01
	−1.16	−1.13	0.81	0.69
1318	0.43	0.57	0.39	0.41
1386	0.35	0.36	0.76	0.62
1407	0.11	0.16	0.76	0.66
1436	0.95	0.91	0.13	0.19
1596	0.66	0.64	0.74	0.76
	0.02	−0.12	1.22	1.20
1739	0.64	0.72	0.91	0.94
1782	1.08	1.11	0.86	0.66
1864	0.74	0.73	1.11	1.08
	0.86	1.01	1.17	0.95
1040	0.04	0.06	0.16	0.06
	−0.15	−0.12	0.29	0.27
	−0.17	−0.11	0.28	0.29

relations between the spherical angles (θ', ϕ') and the geographical angles (θ, ϕ) are:

$$\cos\theta' = \cos\theta\cos\phi, \tag{83}$$

$$\sin\theta'\cos\phi' = \sin\theta\cos\phi, \tag{84}$$

$$\sin\theta'\sin\phi' = \sin\phi. \tag{85}$$

The square of the four-momentum transfer is given by

$$q_\mu^2 = q^\mu q_\mu = \omega^2 - q^2 = 2(\vec{k}\cdot\vec{k}' - EE' + m_e^2). \tag{86}$$

The variable $Q^2 = -q_\mu^2$ is approximately given by:

$$Q^2 \approx 2EE'(1-\cos\theta_e') = 2EE'(1-\cos\theta_e\cos\phi_e). \tag{87}$$

The square of the invariant mass for ^{1}H$(e,e'p)$ elastic scattering is given by:

$$W^2 \equiv E_i^2 - P_i^2 = (\omega + M_p)^2 - q^2 = M_p^2 + 2\omega M_p - Q^2, \tag{88}$$

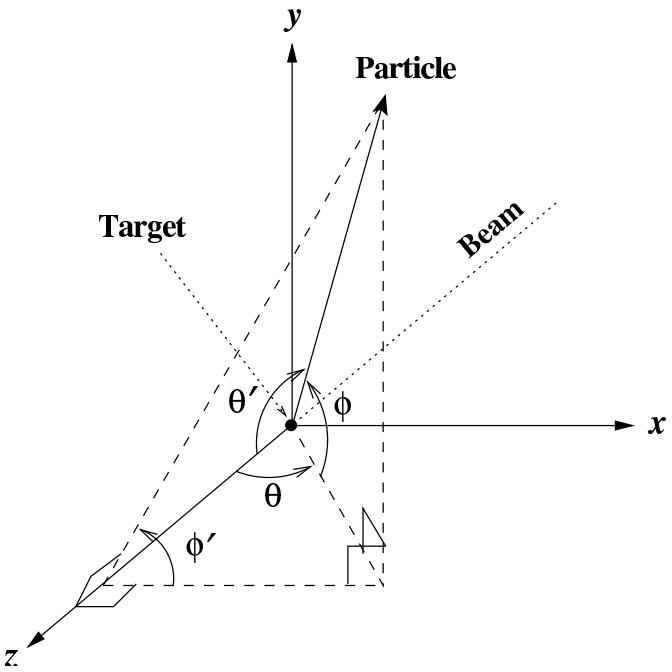

FIG. 68: The scattered particle spherical angles, (θ', ϕ'), and geographical angles, (θ, ϕ), in the HCS.

where E_i and P_i are the total initial energy and momentum of the final hadronic system. Using Equations (81) and (82), we can rewrite the missing momentum components as:

$$p_{missx} = q_x - p_x = -E' \sin\theta_e \cos\phi_e - p \sin\theta_p \cos\phi_p, \tag{89}$$

$$p_{missy} = q_y - p_y = -E' \sin\phi_e - p \sin\phi_p, \tag{90}$$

$$p_{missz} = q_z - p_z = E - E' \cos\theta_e \cos\phi_e - p \cos\theta_p \cos\phi_p. \tag{91}$$

IV.9.2 Fitting Method

The objective of this method is to determine the spectrometer absolute fractional momentum and geographical angular offsets (from here on called the *spectrometer offsets*) by using a wide range of ^{1}H$(e, e'p)$ scattering kinematic settings at fixed and known beam energy. To achieve this purpose, the offsets between the data mean values (analyzed by ESPACE [84]) and the simulation mean values (created by MCEEP [100]) for the invariant mass, W, the missing energy, E_{miss} and the missing momentum components p_{missx},

p_{missy} and p_{missz} (from here on called the *kinematical offsets*) have to be determined first for each kinematic setting separately:

$$\delta W = W(data) - W(sim), \tag{92}$$

$$\delta E_{miss} = E_{miss}(data) - E_{miss}(sim), \tag{93}$$

$$\delta \vec{p}_{miss} = \vec{p}_{miss}(data) - \vec{p}_{miss}(sim). \tag{94}$$

The spectrometer offsets which will be determined, namely, the electron and proton fractional momentum offsets, δ_e and δ_p, the electron and proton in-plane geographical angular offsets, $\delta\theta_e$ and $\delta\theta_p$ and the electron and proton out-of-plane geographical angular offsets, $\delta\phi_e$ and $\delta\phi_p$ are defined by:

$$\delta_e = \frac{\delta k'}{k'_\circ} = \frac{k' - k'_\circ}{k'_\circ},\ \delta_p = \frac{\delta p}{p_\circ} = \frac{p - p_\circ}{p_\circ}, \tag{95}$$

$$\delta\theta_e = \theta_e - \theta_e^\circ,\ \delta\theta_p = \theta_p - \theta_p^\circ, \tag{96}$$

$$\delta\phi_e = \phi_e - \phi_e^\circ,\ \delta\phi_p = \phi_p - \phi_p^\circ, \tag{97}$$

where $k'_\circ$ and $p_\circ$ are the electron and proton central momenta, θ_e° and θ_p° are the electron and proton in-plane geographical central angles and ϕ_e° and ϕ_p° are the electron and proton out-of-plane geographical central angles (these are nominally zero). To simplify the notation, we rename these offsets to a more convenient form. Assume that for each kinematic setting, k, the kinematical offsets, in Equations (92)-(94), will be denoted by δy_{jk}, where $j = (1, ..., 5)$. Also assume that the spectrometer offsets, in Equations (95)-(97), will be denoted by δx_i, where $i = (1, ..., 6)$. Using this new notation, we can now express each of the kinematical offsets, δy_{jk}, in terms of the spectrometer offsets, δx_i, for each kinematic setting, k, as:

$$\delta y_{jk} = \sum_i \frac{\partial y_{jk}}{\partial x_i} \delta x_i. \tag{98}$$

The initial chi-square, χ^2, of the kinematical offsets, δy_{jk}, for no spectrometer offsets ($\delta x_i = 0$) is given by

$$\chi^2 = \sum_{jk} \frac{(\delta y_{jk})^2}{\sigma_{jk}^2}, \tag{99}$$

where σ_{jk} is the uncertainty of δy_{jk}:

$$\sigma_{jk} = \sqrt{\sum_i \left(\frac{\partial y_{jk}}{\partial x_i}\right)^2 \sigma_i^2}, \tag{100}$$

and σ_i is the nominal uncertainty of δx_i. To fit for the optimum spectrometer offsets, δx_i, responsible for the initial kinematical offsets, δy_{jk}, we need to minimize the chi-square, χ^2, of δy_{jk} defined by:

$$\chi^2 = \sum_{jk} \left[\left(\delta y_{jk} - \sum_i \frac{\partial y_{jk}}{\partial x_i} \delta x_i \right)^2 / \sigma_{jk}^2 \right]. \tag{101}$$

All the variable derivatives in Equations (98)-(100) are given in Appendix E. The derivative of χ^2 with respect to δx_l gives:

$$\frac{\partial \chi^2}{\partial \delta x_l} = 2 \sum_{jk} \left\{ \left[\left(\delta y_{jk} - \sum_i \frac{\partial y_{jk}}{\partial x_i} \delta x_i \right) / \sigma_{jk}^2 \right] \frac{\partial}{\partial \delta x_l} \sum_i \frac{\partial y_{jk}}{\partial x_i} \delta x_i \right\}, \quad l = (1, ..., 6), \tag{102}$$

$$\frac{\partial \chi^2}{\partial \delta x_l} = 2 \sum_{jk} \left\{ \left[\left(\delta y_{jk} - \sum_i \frac{\partial y_{jk}}{\partial x_i} \delta x_i \right) / \sigma_{jk}^2 \right] \frac{\partial y_{jk}}{\partial x_l} \right\}. \tag{103}$$

Setting this derivative to zero to minimize χ^2:

$$\sum_{jk} \left\{ \left[\left(\delta y_{jk} - \sum_i \frac{\partial y_{jk}}{\partial x_i} \delta x_i \right) / \sigma_{jk}^2 \right] \frac{\partial y_{jk}}{\partial x_l} \right\} = 0, \tag{104}$$

$$\sum_{jk} \frac{\delta y_{jk}}{\sigma_{jk}^2} \frac{\partial y_{jk}}{\partial x_l} - \sum_{ijk} \left[\left(\frac{\partial y_{jk}}{\partial x_i} \frac{\partial y_{jk}}{\partial x_l} \delta x_i \right) / \sigma_{jk}^2 \right] = 0. \tag{105}$$

Let us rename the terms on the left hand side as

$$A_l - \sum_i B_{il} \delta x_i = 0, \tag{106}$$

where

$$A_l = \sum_{jk} \frac{\delta y_{jk}}{\sigma_{jk}^2} \frac{\partial y_{jk}}{\partial x_l}, \tag{107}$$

and

$$B_{il} = \sum_{jk} \left[\left(\frac{\partial y_{jk}}{\partial x_i} \frac{\partial y_{jk}}{\partial x_l} \right) / \sigma_{jk}^2 \right], \tag{108}$$

therefore

$$\sum_i B_{il} \delta x_i = A_l. \tag{109}$$

The last equation is equivalent to the following matrix equation:

$$B \delta x = A, \tag{110}$$

where B is 6×6 matrix and A and δx are six-dimensional vectors. Multiplying both sides by B^{-1} gives:

$$\delta x = B^{-1} A. \tag{111}$$

which is the global absolute spectrometer offsets that caused the initial kinematical offsets. In this case, the absolute spectrometer offsets uncertainty is simply given by the square root of the covariance matrix B^{-1} diagonal elements:

$$\sigma_i = \sqrt{B_{ii}^{-1}}. \tag{112}$$

Finally, to test the validity of this approach, we used the absolute spectrometer offsets δx_i to correct the spectrometer central kinematics, x_i, and reanalyzed the data.

IV.9.3 Analysis

Data from experiment E01-020 were used to find the absolute spectrometer offsets. The calibration was done for elastic ^{1}H$(e, e'p)$ runs from the $Q^2 = 3.5$ GeV^2 run period (October, 2002). Table XXIII shows the different kinematic settings and the initial kinematical offsets between the data and simulation mean values for the invariant mass, W, the missing energy, E_{miss}, and the missing momentum components p_{missx}, p_{missy}, and p_{missz}. The initial chi-square, χ^2, per degree of freedom for the initial kinematical offsets was 96.889. A necessary modification to the data analysis software, ESPACE, was done to ensure that the missing momentum components are calculated along the fixed hall coordinates (Figure 68). Also attention was paid to tune the simulation to match the data distributions as much as possible to minimize resolution effects when extracting the kinematical offsets.

TABLE XXIII: Initial kinematic settings and offsets for the different ^{1}H$(e, e'p)$ runs.

	Beam	Electron Arm		Proton Arm		Kinematical Offsets				
Run	Energy	k'	θ_e	p	θ_p	$\triangle W$	$\triangle E_{miss}$	$\triangle p_{missx}$	$\triangle p_{missy}$	$\triangle p_{missz}$
#	(MeV)	(MeV)	(°)	(MeV)	(°)	(MeV)	(MeV)	(MeV)	(MeV)	(MeV)
2594	5008.46	2918.58	30.48	2877.32	−30.48	+09.97	+2.24	+3.22	+0.85	+0.86
2596	5008.48	3159.31	26.98	2617.49	−33.30	+10.86	+2.35	+4.01	+0.84	+1.00
2599	5008.48	3425.23	23.98	2338.96	−36.58	+10.77	+2.56	+4.21	−0.39	+1.36
2600	5008.48	3695.41	20.98	2044.66	−40.40	+08.80	+1.84	+3.94	−0.98	+0.70
2632	5008.49	3140.31	27.26	2648.08	−32.91	+09.84	+2.32	+3.60	+0.61	+1.29
2672	5008.51	3140.33	27.26	2648.08	−32.91	+09.90	+2.06	+3.83	+0.35	+0.96
2792	5008.52	3140.25	27.26	2648.08	−32.93	+11.06	+2.53	+4.10	+0.55	+1.30

TABLE XXIV: Minimized kinematical offsets for the different ^{1}H$(e,e'p)$ runs.

	Kinematical Offsets				
Run #	$\triangle W$ (MeV)	$\triangle E_{miss}$ (MeV)	$\triangle p_{missx}$ (MeV)	$\triangle p_{missy}$ (MeV)	$\triangle p_{missz}$ (MeV)
2594	-0.53	-0.17	-0.36	-0.22	-0.24
2596	$+0.65$	$+0.03$	$+0.22$	$+0.40$	-0.06
2599	$+0.82$	$+0.34$	$+0.19$	-0.15	$+0.35$
2600	-0.73	-0.29	-0.33	-0.03	-0.27
2632	-0.40	-0.01	-0.18	$+0.10$	$+0.22$
2672	-0.34	-0.28	$+0.05$	-0.16	-0.11
2792	$+0.82$	$+0.19$	$+0.32$	$+0.05$	$+0.23$
Average	$+0.04$	-0.03	-0.01	$+0.00$	$+0.02$

TABLE XXV: Calibration Results for the absolute spectrometer offsets.

δ_e ($\times 10^{-3}$)	δ_p ($\times 10^{-3}$)	$\delta\theta_e$ (mrad)	$\delta\theta_p$ (mrad)	$\delta\phi_e$ (mrad)	$\delta\phi_p$ (mrad)
-0.29 ± 0.17	-0.57 ± 0.23	-1.15 ± 0.12	-0.45 ± 0.13	-1.05 ± 0.23	-1.44 ± 0.29

IV.9.4 Fitting Results

Using the following nominal spectrometer uncertainties:

$$\sigma_\delta = 0.0001, \tag{113}$$

$$\sigma_\theta = \sigma_\phi = 0.08 \text{ mrad}, \tag{114}$$

along with the initial kinematical offsets as inputs to a special fitting program (see Appendix F) gives the minimized kinematical offsets shown in Table XXIV. The chi-square, χ^2, per degree of freedom for these minimized offsets is 0.736. The results of the calibration for the absolute spectrometer offsets is given in Table XXV. The results after correcting for the absolute spectrometer offsets are shown in Figure 69.

IV.9.5 Remarks

This is the first time this spectrometer calibration method was employed in Hall A. The method succeeded in extracting the optimum spectrometer offsets. The extracted in-plane

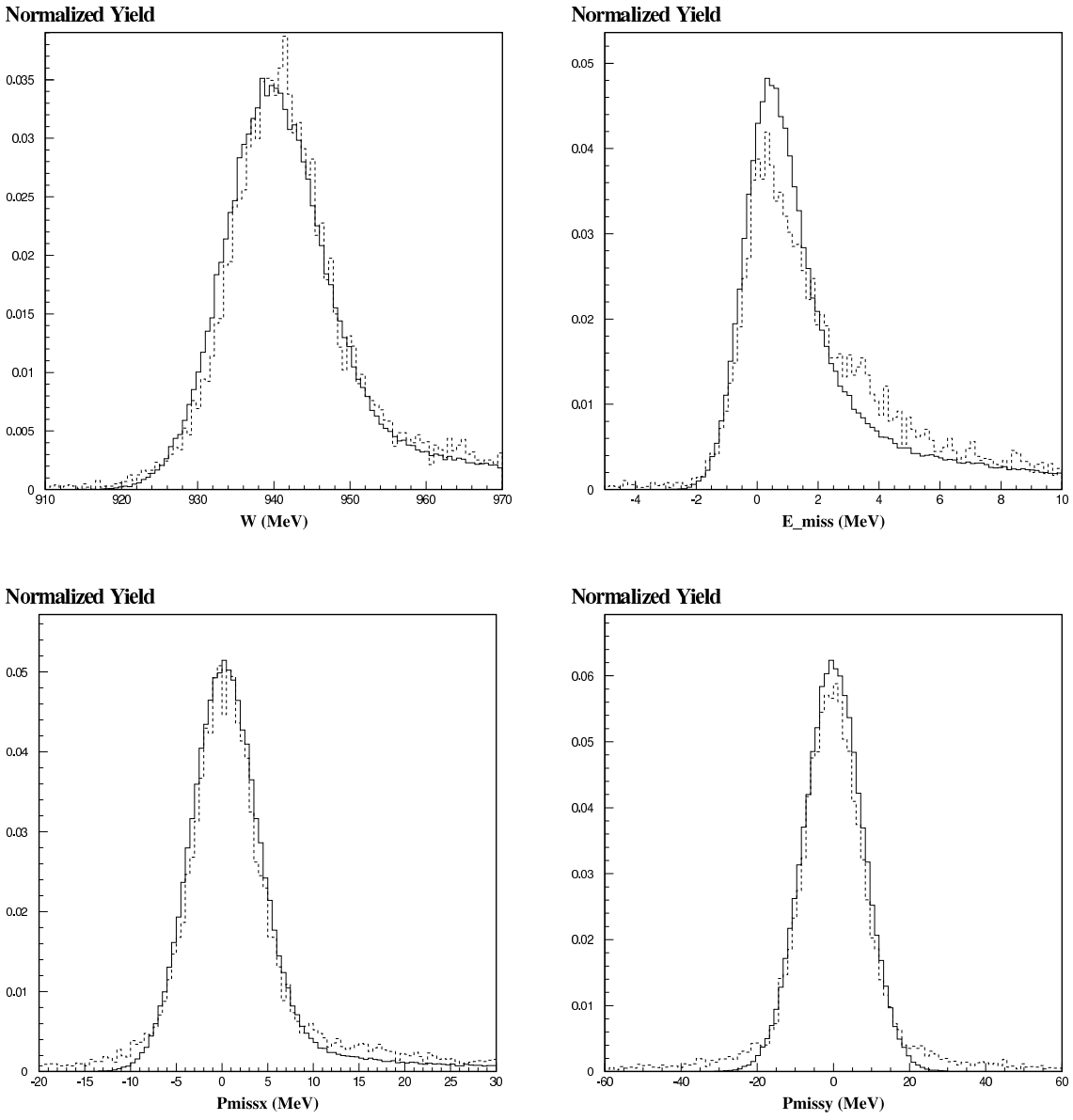

FIG. 69: Some minimized offsets for Run # 2672. Data is dashed and simulation is solid. The minimized offsets between the data and simulation mean values for each plot are given in Table XXIV.

TABLE XXVI: The ^{2}H$(e,e'p)n$ reaction ε_{miss} for the calibrated data versus the simulation.

p_{miss}	Data (MeV)		Simulation (MeV)		Difference (MeV)	
(MeV)	$\phi=0$	$\phi=\pi$	$\phi=0$	$\phi=\pi$	$\phi=0$	$\phi=\pi$
0	2.58		2.90		0.31	
100	2.46	3.03	2.94	2.87	0.47	−0.16
200	2.60	3.46	3.08	2.93	0.48	−0.52
300	2.67	3.41	3.25	3.01	0.58	−0.40
400	2.85	3.26	3.34	3.06	0.49	−0.19
500	-	3.07	-	3.09	-	0.02

angular offsets agree with previously extracted similar offsets [64, 65] for Hall A spectrometers but the absolute spectrometer momentum and out-of-plane angular offsets were also determined simultaneously for the first time for Hall A in this global calibration scheme. The newly extracted spectrometer offsets were checked carefully by reanalyzing the calibrated data and comparing again with the simulation. Table XXVI compares the deuterium missing energy for calibrated data and simulation. Data and simulation values agree within 0.5 MeV. Another comparison is shown for the fractional momentum deviation in Figure 70. Again very good agreement is found between the calibrated data and the simulation.

IV.10 ELECTRONIC AND COMPUTER DEADTIME

There are two different types of deadtime for Experiment E01-020, Electronic Dead Time (EDT) and Computer Dead Time (CDT). These deadtimes occur when the electronics or the DAQ (computer) systems are not able to keep up with the data rate. Electronic deadtime is caused when triggers are missed because the hardware is busy when an event that should generate a trigger arrives. When a logic gate in the trigger is activated, the output signal stays high for a fixed time. If another event tries to activate the gate in that time, it is ignored. The data analyzed in this dissertation were mostly at low rate (less than 2 kHz). For this reason, the EDT was considered negligible.

A more significant source of deadtime is the computer deadtime. In this case, events are lost because a hardware trigger is formed when the data acquisition system is busy processing the previous event. The computer deadtime is measured by counting the number of triggers that were formed and the number of triggers that were processed by the Trigger Supervisor. The number processed over the number generated is the computer live time

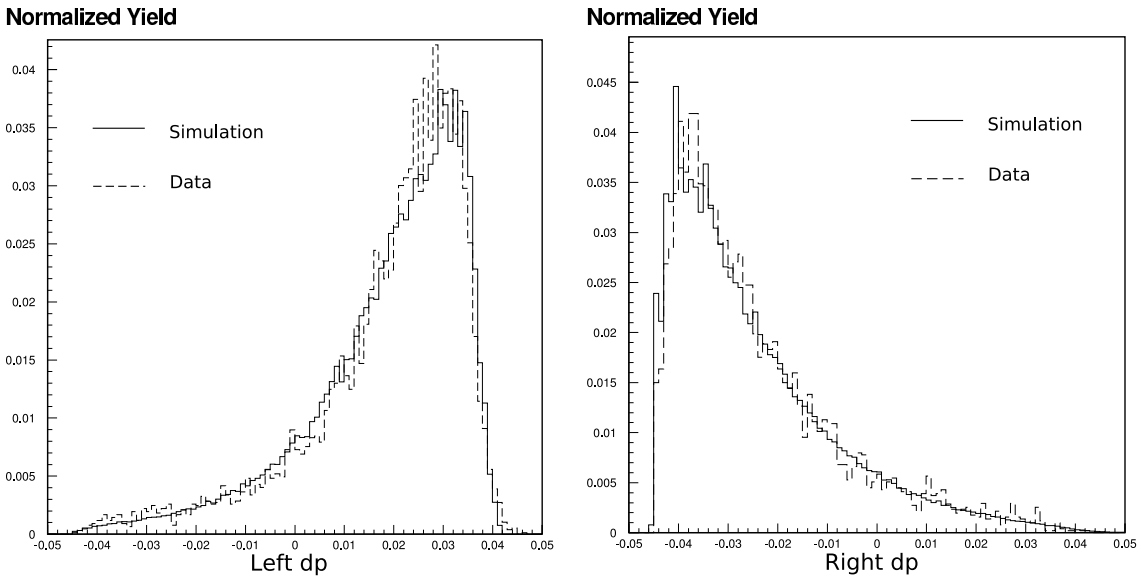

FIG. 70: Fractional momentum deviations for the Left and Right arms of the calibrated data versus the simulation.

(CLT) of the data acquisition system. The deadtime was calculated for each run, and the cross section was corrected for the lost triggers. For the data analyzed in this dissertation, the CDT was found to be about 1–2%.

The total deadtime is calculated from the electronic and the computer deadtimes as:

$$DT = 1 - (1 - CDT)(1 - EDT) \tag{115}$$

The total deadtime correction applied to the data is expressed in terms of the total live time:

$$LT = 1 - DT \tag{116}$$

IV.11 COINCIDENCE TIME OF FLIGHT

A check of the corrected time of flight distributions revealed the need to recalibrate the original time of flight (TOF) offsets which were optimized previously for E01-020 [101]. The recalibration was performed by aligning the fractional momentum deviation, δ, for each scintillator paddle. Figure 71a shows the distribution of the corrected time of flight before the recalibration. A cut on the missing energy (-5 MeV$< \varepsilon_{miss} < 15$ MeV) had an undesirable effect on the TOF. Figure 71b shows the TOF after the recalibration as a

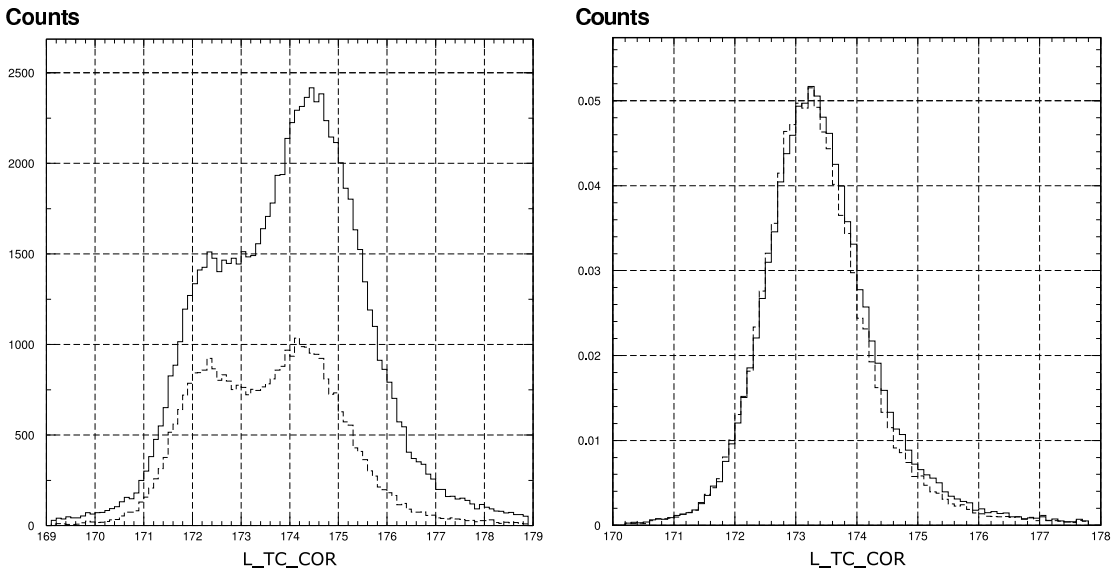

(a) Before the calibration (b) After the calibration

FIG. 71: Coincidence time of flight optimization. The dashed line shows the effect of a typical ^{2}H$(e, e'p)n$ reaction ε_{miss} cut.

single peak with a much better symmetrical effect of the missing energy cut.

IV.12 ESPACE FILES

Many of the calibration results and detector wiring corrections discussed in this chapter ended up in the ESPACE database and detector map files [102]. Table XXVII lists the optimized databases of this experiment. Three different databases were optimized for the three main Q^2 values. The different detector maps for E01-020 are date stamped as listed in Table XXVIII.

TABLE XXVII: ESPACE Databases.

Q^2	Dates (All in 2002)		Runs		Database
(GeV^2)	From	To	From	To	File
0.8	May 28	June 11	1002	1446	`db_E01-020_q1`
2.1	June 11	June 28	1447	1878	`db_E01-020_q2`
3.5	October 16	November 16	2501	3207	`db_E01-020_q3`

TABLE XXVIII: ESPACE Detector Maps.

Q^2	Dates (All in 2002)		Runs		Detector Map
(GeV^2)	From	To	From	To	File
0.8, 2.1	May 31	Jun 28	1001	1878	`detmap_E01-020_may31`
3.5	October 19	October 21	2501	2612	`detmap_E01-020_oct19`
	October 21	October 28	2613	2820	`detmap_E01-020_oct21`
	October 28	October 29	2821	2839	`detmap_E01-020_oct28`
	October 29	November16	2840	3207	`detmap_E01-020_oct29`

CHAPTER V

DATA ANALYSIS

The main objective of this dissertation is to separate the longitudinal-transverse response function at Q^2=3.5 GeV^2. To achieve this purpose, several measurements were performed at several kinematics as shown in Tables XXIX and XXX. For each spectrometer, $\theta_\circ$ is the central angle, B is the dipole magnetic field, and $x_\circ$and $z_\circ$ are the spectrometer mispointing offsets. For the rastered beam, $x_\circ$ and $y_\circ$ are the mean values of the position, and Δx and Δy are the spot size. For a full list of runs see Appendix A. Many of the operations that required the processing of several quantities for a large number of runs were made feasible by the creation of an online run database[1].

Several steps were taken to obtain the final results:

1. Calibrations and optimizations of the collected data.
2. Events were reconstructed with ESPACE and a set of initial cuts were applied to select coincidence events and stable current periods, etc.
3. Full MCEEP simulations (including energy losses, internal and external radiation and multiple scattering in the target, and spectrometer resolutions) were made.
4. A set of final cuts were applied to ensure the match between data and simulation.
5. Several "binning schemes" were applied to the data and simulation yields to study the dependence on p_{miss}, Q^2, and W.
6. Finally, the cross section, R_{LT}, and A_{LT} were extracted from the yields for each bin.

V.1 TARGET ENERGY LOSS

Experiment E01-020 used the new target cells (tubular or "Cigar Tube" shaped cells) which were introduced in Hall A for the first time in 2002. These new target cells have smaller diameter than the older cell type (cylindrical or "Beer Can" shaped cells). This required

[1]A full MySQL [103] database with a PHP web interface of all E01-020 runs was created for this experiment [104]. For each run, the database includes about 60 variables, such as the beam energy and the spectrometer momenta and angles. This database was a valuable tool to do collective calculations over all runs, search for runs which have specific properties, and to troubleshoot data problems. It was also used extensively in the preparation of the final analysis files such as ESPACE "header files".

TABLE XXIX: Spectrometer Settings for the analyzed kinematics.

		Left Arm				Right Arm			
ID	Kinematics	$\theta_\circ$ (°)	B (Tesla)	$x_\circ$ (mm)	$z_\circ$ (mm)	$\theta_\circ$ (°)	B (Tesla)	$x_\circ$ (mm)	$z_\circ$ (mm)
0	f00	27.2893	11.6312	3.800	-1.972	-32.9218	9.8205	0.709	0.459
1	f10l	27.2893	11.6312	3.800	-1.972	-30.8711	9.7733	0.737	0.440
2	f10r	27.2893	11.6312	3.800	-1.972	-35.1999	9.7733	-2.371	-1.670
3	f20l	27.2893	11.6312	3.800	-1.972	-28.7091	9.7114	1.113	0.609
4	f20r	27.2893	11.6312	3.800	-1.972	-37.3613	9.7114	-2.727	-2.078
5	f30l	27.2893	11.6312	3.800	-1.972	-26.5601	9.6101	1.128	0.563
6	f30r	27.2893	11.6312	3.800	-1.972	-39.5088	9.6101	-2.849	-2.345
7	f40l	27.2893	11.6312	3.800	-1.972	-24.4206	9.4724	1.129	0.512
8	f40r	27.2893	11.6312	3.800	-1.972	-41.6394	9.4724	-2.921	-2.592
9	f50r	27.2893	11.6312	3.800	-1.972	-43.7719	9.3017	-2.923	-2.795

TABLE XXX: Beam Settings for the analyzed kinematics.

		Energy	Time	Current	Raster			
ID	Kinematics	(MeV)	(sec)	(μA)	$x_\circ$ (mm)	$y_\circ$ (mm)	Δx (mm)	Δy (mm)
0	f00	5008.93	2099.372	101.616	0.209	0.539	4.300	3.917
1	f10l	5009.02	2195.122	102.214	0.195	0.535	4.260	3.920
2	f10r	5009.00	1566.086	102.334	0.225	0.535	4.260	3.920
3	f20l	5009.02	20421.267	102.319	0.204	0.535	4.286	3.919
4	f20r	5009.02	18327.280	101.442	0.206	0.525	4.236	3.945
5	f30l	5009.02	28857.965	99.065	0.308	0.757	4.264	3.892
6	f30r	5009.02	31020.640	98.301	0.269	0.655	4.253	3.966
7	f40l	5009.00	41381.539	96.567	0.297	0.592	4.298	3.876
8	f40r	5009.00	35293.809	97.824	0.331	0.613	4.271	3.879
9	f50r	5008.76	37845.033	98.980	0.106	0.631	4.262	3.889

the creation of a new target model in both the data analysis and the simulation programs (ESPACE and MCEEP) to calculate the energy loss. Besides having a new target model in ESPACE, the entire calculation of the average expected energy loss was integrated in ESPACE instead of using additional standalone code. In this way, the energy loss can be calculated on an event by event basis instead of using only a fixed value for each kinematics.

V.1.1 Target Model

Figure 72 shows the geometry of the scattering chamber and the target cell. Based on the location of the reaction point in the target and the scattering angle, each scattered particle will have a different material thicknesses to cross before entering the spectrometer. At the reaction point the actual incident energy is "less" than the initial beam energy before entering the target cell. On the contrary, the scattered particles have "more" energy at the reaction point than the final detected energy in the spectrometer:

$$E_{inc} = E_{Beam} - E_{loss}(\text{Cell}) - E_{loss}(\text{Liquid}) \tag{117}$$

$$E_{scat} = E_{spec} + E_{loss}(\text{Kapton}) + E_{loss}(\text{Air}) + E_{loss}(\text{Chamber}) + E_{loss}(\text{Cell}) + E_{loss}(\text{Liquid}) \tag{118}$$

In order to calculate the energy loss for the incident and scattered particles, we first need to know the path lengths in the encountered materials. For the incident electrons, the path length in the cell is simply the thickness of the cell "Entrance Window". In the liquid, the path length is given by (see Figure 73):

$$d_{liquid} = z_{front} - z_{vertex} \tag{119}$$

where z_{front} is the z-position of the front (entrance) window and z_{vertex} is the z-position of the vertex (reaction point) on the HCS z-axis (zero is at the target center and the positive direction points downstream towards the beam dump).

For the scattered particles, we need to know the path length in the target liquid and the cell material. Based on the relation between the z-position of the reaction point, z_{vertex}, and the "End Cap" base z-position, z_{base}, the path length, d, can be calculated according to the following cases (see Figure 73):

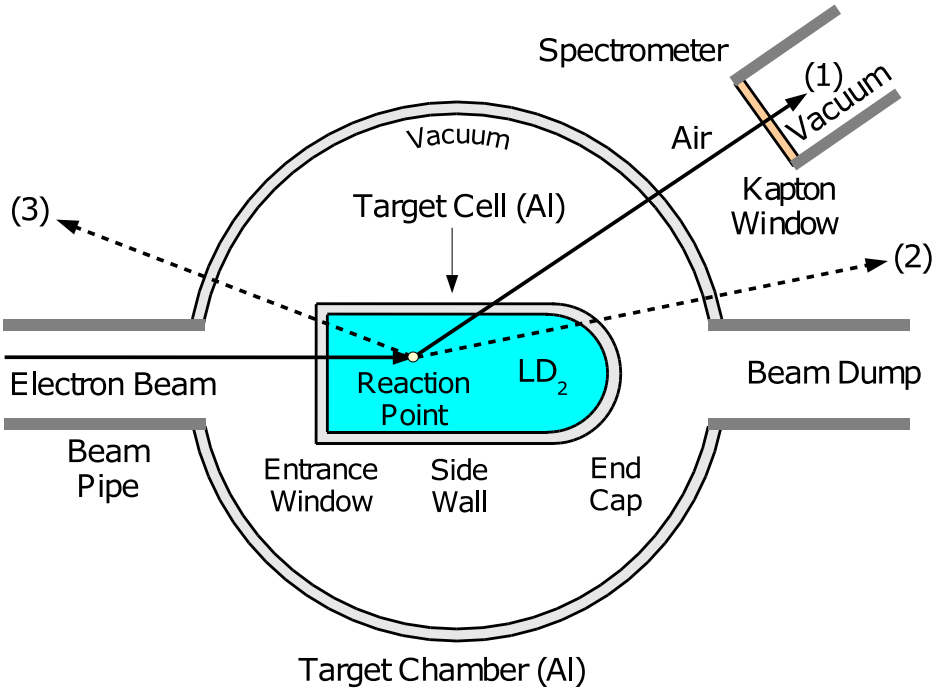

FIG. 72: Energy loss in the target for the shown three trajectories have different values.

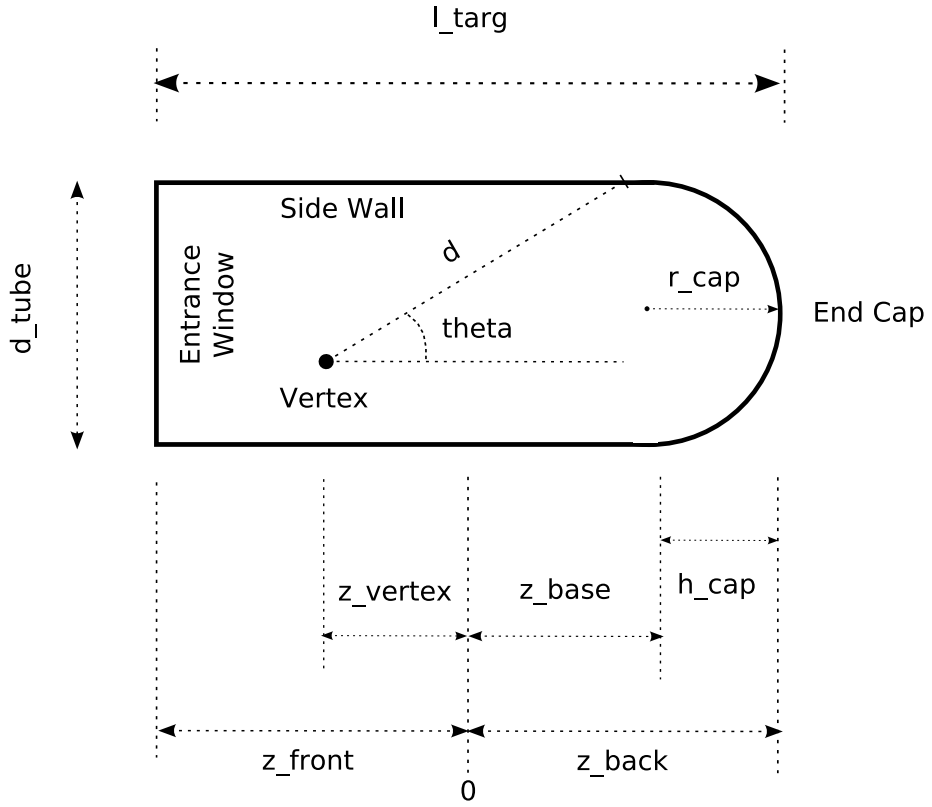

FIG. 73: Target Model for the "cigar-tube" cells.

- Case A: $z_{vertex} < z_{base}$

  1. if $\theta = 0$ then $d = d_{cap}$
  2. if $0 < \theta < 90°$ then $\begin{cases} d = d_{side}, & \text{if } d_{side} \leq d_{base} \\ d = d_{cap}, & \text{if } d_{side} > d_{base} \end{cases}$
  3. if $\theta = 90°$ then $d = d_{side}$
  4. if $\theta > 90°$ then $d = \min(d_{side}, d_{front})$

- Case B: $z_{vertex} = z_{base}$

  1. if $0 \leq \theta < 90°$ then $d = d_{cap}$
  2. if $\theta = 90°$ then $d = d_{side}$
  3. if $\theta > 90°$ then $d = \min(d_{side}, d_{front})$

- Case C: $z_{vertex} > z_{base}$

  1. if $0 \leq \theta \leq 90°$ then $d = d_{cap}$
  2. if $\theta > 90°$ then $\begin{cases} d = d_{cap}, & \text{if } d_{side} < d_{base} \\ d = d_{side}, & \text{if } d_{side} = d_{base} \\ d = \min(d_{side}, d_{front}), & \text{if } d_{side} > d_{base} \end{cases}$

where

$$d_{front} = \frac{-l_{targ}/2 - z_{vertex}}{\cos\theta}, \tag{120}$$

$$d_{base} = \frac{z_{base} - z_{vertex}}{\cos\theta}, \tag{121}$$

$$d_{side} = \frac{-x_{vertex}\cos\phi - y_{vertex}\sin\phi \pm \sqrt{r_{tube}^2 - (x_{vertex}\sin\phi - y_{vertex}\cos\phi)^2}}{\sin\theta}, \tag{122}$$

$$d_{cap} = \frac{-b \pm \sqrt{b^2 - 4ac}}{2a}, \tag{123}$$

and a, b, and c are defined by

$$a = 1 \tag{124}$$

$$b = 2\left[(x_{vertex}\cos\phi + y_{vertex}\sin\phi)\sin\theta + (z_{vertex} - z_{base})\cos\theta\right], \tag{125}$$

$$c = x_{vertex}^2 + y_{vertex}^2 + z_{vertex}^2 - 2z_{vertex}z_{center} + z_{center}^2 - r_{cap}^2, \tag{126}$$

The different variables used above are defined here (see Figure 73):

- $z_{center} = l_{targ}/2 - r_{cap}$ is the end cap spherical center z-position,
- $z_{base} = l_{targ}/2 - h_{cap}$ is the end cap base z-position,
- h_{cap} is the end cap height ($h_{cap} \leq r_{cap}$),
- l_{targ} is the target cell length,
- $r_{tube} = d_{tube}/2$ is the tube cylindrical radius,
- r_{cap} is the end cap spherical radius.

The path length is calculated twice for the inner and outer surfaces of the target cell to determine the path lengths in the liquid and in the cell material as follows:

$$d_{liquid} = d_{inner} \tag{127}$$

$$d_{cell} = d_{outer} - d_{inner} \tag{128}$$

In addition to that, we assume that the scattered particles have the same path length in the "Kapton Window", the "Air" and the scattering chamber material which is the nominal thickness of the scattering chamber exit aluminum window.

V.1.2 Energy Loss

Energy loss corrections for the beam and the scattered particles are necessary before extracting the cross section. Since the energy loss is a statistical process, we can only use the "mean" or the "most probable" energy loss to correct for the reaction kinematics.

V.1.2.1 Mean Energy Loss

The mean energy loss is calculated by using the Bethe-Bloch formula for protons [105]:

$$-\frac{1}{\rho}\frac{dE}{dx} = \frac{4\pi N r_e^2 m_e c^2}{\beta^2}\frac{Z}{A}\left[\ln\left(\frac{2m_e c^2(\beta\gamma)^2}{I_{ex}}\right) - \beta^2 - \frac{\delta}{2} - \frac{C_z}{Z}\right], \tag{129}$$

while for electrons:

$$-\frac{1}{\rho}\frac{dE}{dx} = \frac{2\pi N r_e^2 m_e c^2}{\beta^2}\frac{Z}{A}\left[\ln\left(\frac{T^2}{I_{ex}}\right) + \ln(1+\frac{\tau}{2}) + F(\tau) - \delta\right], \tag{130}$$

where

$$F(\tau) = (1 - \beta^2)\left[1 + \frac{\tau^2}{8} - (2\tau + 1)\ln 2\right] \tag{131}$$

and

- N is Avogadro's number,
- m_e and r_e are the electron mass and electron classical radius respectively,
- β is the particle relative velocity v/c and $\gamma = 1/\sqrt{1-\beta^2}$,
- T is the particle kinetic energy and $\tau = T/m_e c^2$,
- Z, A and ρ are the atomic number, atomic weight and density of the medium,
- I_{ex} is the mean excitation energy of the medium,
- δ is the density effect correction,
- C_z is the shell correction.

Figures 74, 75 and 76 show the calculated mean energy loss which is done on an event by event basis. For the scattered electrons and protons, the 2D plots of p_{loss} versus z_{react} show that the energy loss is broken into two distinct regions based on the geometrical shape of the target cell. The p_{loss} peak is due to particles coming from the tubular side wall while the lower continuous distribution is due to particles coming out of the hemispherical end-cap. The exact transition between the two regions is controlled by the spectrometer angle (For forward angles, the transition is at low z_{react} and for larger angles, the transition is at high z_{react}).

V.1.2.2 Most Probable Energy Loss

The energy loss calculated by Equations (129) and (130) refers to the mean energy loss. To correct for energy loss in our analysis, we need to calculate the most probable energy loss from the following equations (Landau's theory) [105]:

$$\Delta_{mp} = \xi(\ln\kappa + \beta^2 - C + 1) \tag{132}$$

where C is Euler's constant$\simeq$0.577215, and

$$\kappa = \xi/W_{max}. \tag{133}$$

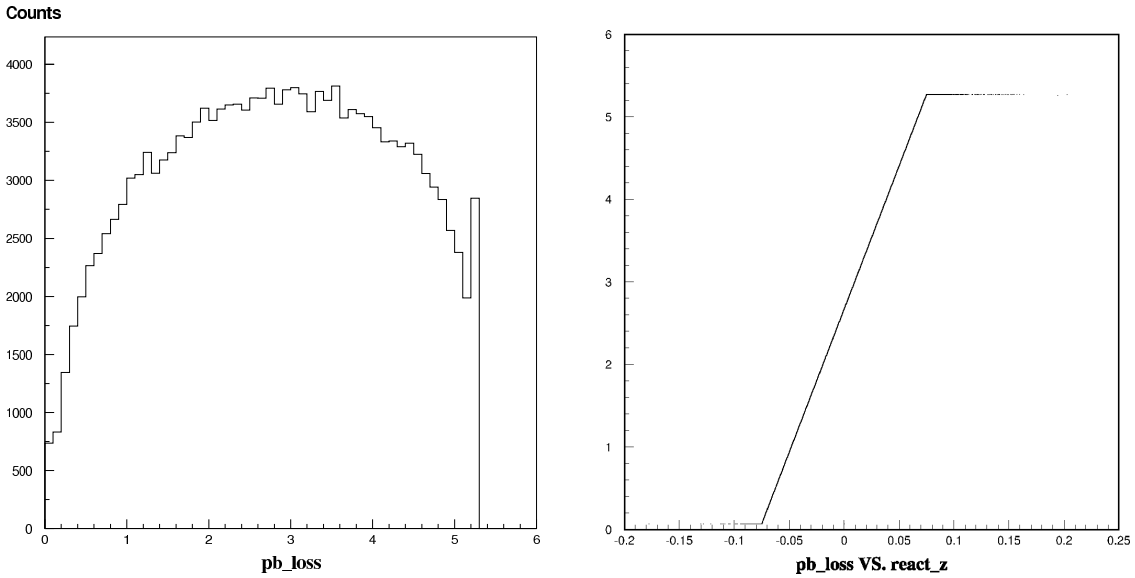

FIG. 74: Beam energy loss (MeV) and its dependence on reaction point z-position (m).

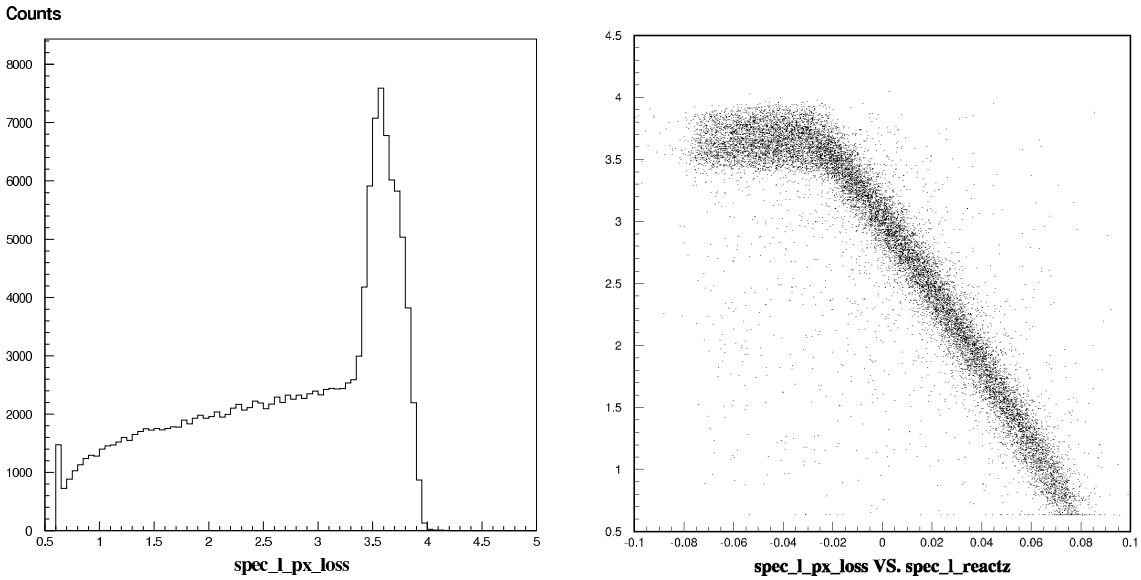

FIG. 75: Scattered electron energy loss (MeV) and its dependence on reaction point z-position (m).

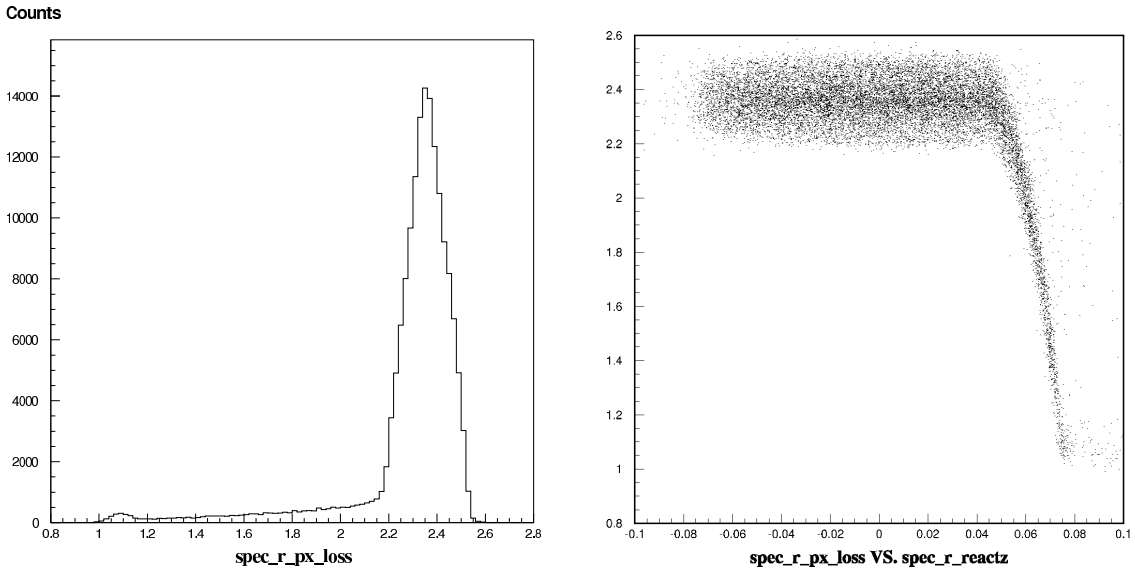

FIG. 76: Proton energy loss (MeV) and its dependence on reaction point z-position (m).

Here, ξ is the mean energy loss after ignoring the logarithmic term in the Bethe-Bloch formula, and W_{max} is the maximum energy transferred in a single collision:

$$\xi = 2\pi N r_e^2 m_e c^2 \frac{1}{\beta^2} \rho \frac{Z}{A} x, \tag{134}$$

$$W_{max} = \frac{2m_e c^2 \eta^2}{1 + 2s\sqrt{1+\eta^2} + s^2}, \tag{135}$$

where

$$s = \frac{m_e}{M}, \tag{136}$$

$$\eta = \beta\gamma, \tag{137}$$

and M is the particle mass. For protons ($M_P \gg m_e$), the maximum energy transfer per collision, W_{max}, is reduced to:

$$W_{max} \simeq 2m_e c^2 \eta^2. \tag{138}$$

Table XXXI shows the difference between the calculated missing energy, E_{miss}, by using the mean energy and most probable energy loss. From this table we can see that the most probable energy loss gives more realistic positive values of the E_{miss}. Figure 77 shows a comparison of the most probable versus mean energy loss for the Left and Right arms and Figure 78 shows a comparison of the most probable versus mean energy loss corrections

TABLE XXXI: Most probable versus Mean energy loss corrections to the ^{1}H$(e, e'p)$ missing energy.

Run Number	E_{miss} (MeV) Most Probable	Mean Value	Difference
1436	0.66	-0.93	1.59
1439	1.01	-0.55	1.56
1442	1.44	-0.02	1.46
1444	0.16	-1.29	1.45

to E_{miss} for both the data and the simulation.

V.2 CUTS

Several cuts were applied during the initial data analysis and the final physics analysis:

- Event cut to select coincidence events,
- Beam current cuts to exclude unstable beam periods,
- VDC tracking cuts, to eliminate badly reconstructed events,
- Cut on the difference between the reaction points along the beam reconstructed by the two spectrometers (vertex cut), to remove some of the accidental coincidences,
- Cuts on the reconstructed reaction point along the beam, to remove contributions from the aluminum target walls,
- Cuts on the corrected coincidence time between the spectrometers to discard more accidental coincidences,
- Cut on the corrected missing energy to reduce radiative effects,
- Cut on the sum of the Gas Čerenkov ADC channels, to remove the contribution from the π^- real coincidences,
- R-function acceptance cuts, to limit events to the acceptable regions of Left and Right spectrometers.

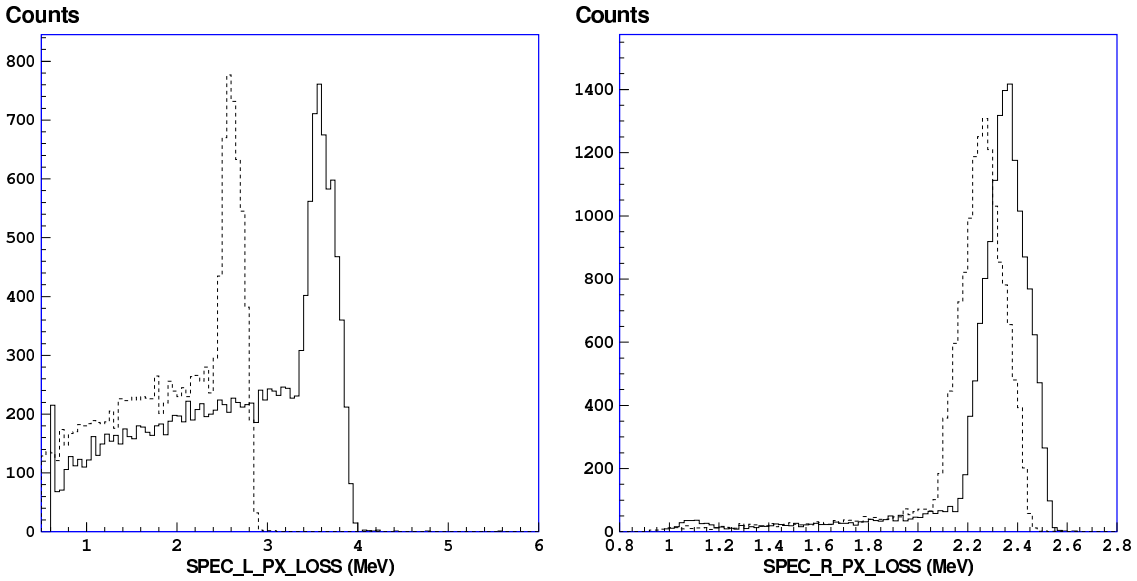

(a) Electrons. (b) Protons.

FIG. 77: Most probable (dashed lines) and mean (solid lines) energy loss for the electrons and protons.

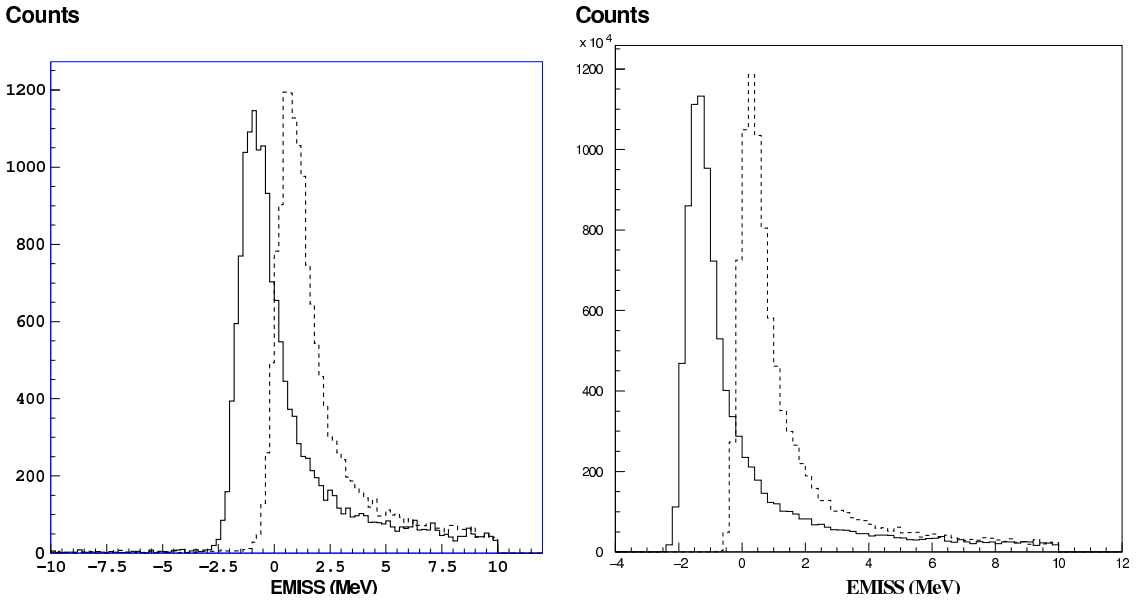

(a) Data. (b) Simulation.

FIG. 78: Most probable (dashed lines) and mean (solid lines) energy loss corrections to the ^{1}H$(e, e'p)$ missing energy for the data and simulation.

Cuts identical to those imposed on the data were applied to the simulation (except for cuts on Gas Čerenkov, coincidence time between spectrometers and VDC tracking cuts). More details about the applied cuts are given below:

Event Cut The coincidence events were selected from the data by simply selecting the T5 trigger type events because the prescale factor for trigger type 5 was unity (PS5 = 1) for the quasielastic runs. Coincidence events can also be selected by using the ESPACE "Trigger Supervisor Pattern" variable, ts_patt,

$$\text{ts\_patt} = \sum_i 2^{i-1}, \tag{139}$$

where i runs over all the "available" trigger types, i.e. $i \in (1, ..., 5)$, at the trigger supervisor input for a specific event. In this case coincidence events are selected if any of the following conditions is true.

- 15.5 < ts_patt < 16.5
- 16.5 < ts_patt < 17.5
- 19.5 < ts_patt < 20.5
- 20.5 < ts_patt < 21.5

Beam Current Cuts Only the stable beam current periods of each run were selected for the final analysis. The following conditions were applied:

- Beam was stable for at least 30 sec before the start of the selected period (to stabilize the target density).
- Beam has been stable for at least 30 sec since the start of the selected period.
- Beam current is larger than 5 μA for the selected period.
- Beam current does not fluctuate larger than $\pm$5 μA for the selected period.

VDC Tracking Cuts The applied VDC tracking cuts in the final analysis are listed below:

- All multiplicities for all VDC planes of the two spectrometers must be ≥ 3,
- There must be at least one track in both spectrometer's VDCs.

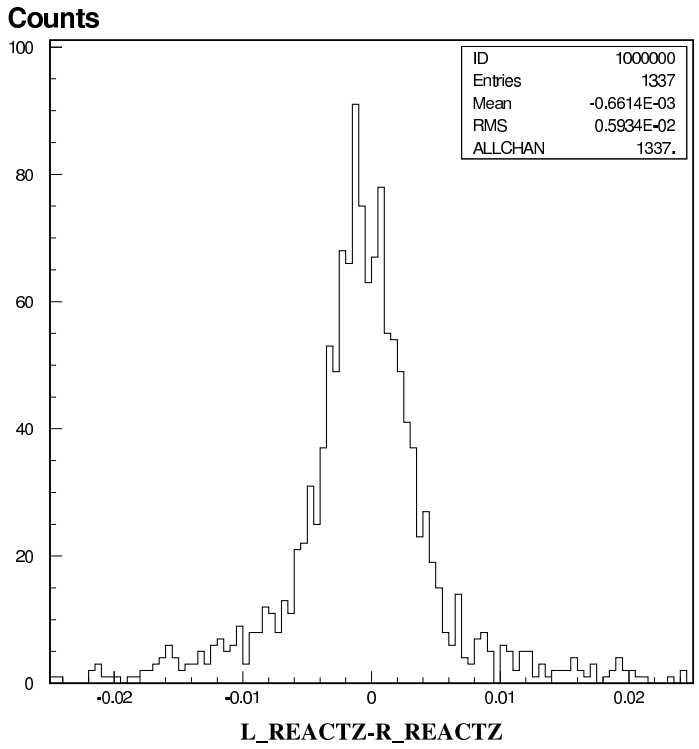

FIG. 79: Difference between the left and right reconstructed reaction point z-position (in meters) for Run 2852.

Target Length Cut The contributions from the aluminum target cell entrance window and end cap were removed by the cut $|z_{react}| < 5.0$ cm, on the reaction point z-position.

Vertex Cut Figure 79 shows the typical difference between Left and Right reconstructed reaction points z-positions for the analyzed kinematics. A cut on the absolute difference, $|z_{lreactz} - z_{rreactz}| < 2.0$ cm, was used to exclude most of the accidental coincidences.

Corrected Coincidence Time Cut Figure 80 shows the distribution of the coincidence time between particles detected in the electron and proton spectrometers corrected for time of flight to the focal planes. Vertical dashed lines in the figure indicate the edges of the real and accidental coincidence windows. A corrected coincidence time cut between r_1 and r_2 (reals window) was applied to remove accidentals. This reals window was practically equal for all kinematics analyzed as part of this dissertation with $r_1 = 168$ ns and $r_2 = 180$ ns. The number of true coincidence events N_t in the reals window was determined from the following equation:

$$N_t = N_r - N_a \tag{140}$$

where N_r and N_a are the number of the real and accidental coincidence events in the reals window, r,

$$r = r_2 - r_1. \tag{141}$$

N_a can be estimated from:

$$N_a = \langle N_a \rangle \, r. \tag{142}$$

The average of accidental coincidence events per unit coincidence time is given by

$$\langle N_a \rangle = \frac{N'_a + N''_a}{a' + a''} \tag{143}$$

where N'_a and N''_a are the number of the accidentals in the accidental windows, a' and a'',

$$a' = a'_2 - a'_1 = 160 - 110 = 50 \text{ ns}, \tag{144}$$

$$a'' = a''_2 - a''_1 = 210 - 190 = 30 \text{ ns}. \tag{145}$$

The ratio N_t/N_r is called the "trues" ratio, $f_t(p_{miss})$, and is listed in Table XXXII. This ratio is used to correct the data for accidental coincidence events after applying the coincidence time cut.

Corrected Missing Energy Cut Even with the kinematics and other calibrations applied, the peaks of the missing energy, ε_{miss}, for the data were found to be slightly different than the almost constant simulation ε_{miss} peak at 2.25 MeV. A correction of the missing energy was necessary before applying the same ε_{miss} cut of -0.5 MeV $< \varepsilon_{miss} <$ 15.0 MeV on the data and simulation. This cut was required to remove any remaining pions in the data and to limit the contribution of the radiative tail. Table XXXIII lists the missing energy shifts that were added to the data along with the trigger and tracking efficiencies for the two arms and the computer livetime for the perpendicular highest Q^2 kinematics.

PID Cut We required the Gas Čerenkov ADC sum to be larger than 150 to exclude π^- in the Left arm.

TABLE XXXII: "Trues" ratio dependence on p_{miss} for all the analyzed kinematics. All the other cuts in this section were applied to obtain these ratios.

p_{miss}	Kinematics									
(MeV)	f00	f10l	f10r	f20l	f20r	f30l	f30r	f40l	f40r	f50r
20	1.00	1.00	1.00	1.00	1.00	1.00	1.00	1.00	1.00	1.00
60	1.00	1.00	1.00	1.00	0.99	1.00	1.00	1.00	1.00	1.00
100	1.00	1.00	1.00	1.00	1.00	1.00	1.00	1.00	1.00	1.00
140	0.99	1.00	1.00	1.00	1.00	1.00	1.00	1.00	1.00	1.00
180	1.00	0.99	0.99	1.00	1.00	1.00	0.99	1.00	1.00	1.00
220	1.00	0.99	1.00	0.99	0.99	0.99	1.00	1.00	1.00	1.00
260	1.00	1.00	0.99	0.99	0.99	0.99	1.00	1.00	1.00	1.00
300	1.00	1.00	1.00	0.99	1.00	0.99	1.00	0.99	1.00	1.00
340	1.00	1.00	1.00	1.00	0.99	0.99	1.00	0.98	0.99	1.00
380	1.00	1.00	1.00	1.00	0.99	0.98	0.99	0.98	0.99	1.00
420	1.00	1.00	1.00	1.00	1.00	0.99	1.00	0.96	0.99	1.00
460	1.00	1.00	1.00	1.00	1.00	1.00	1.00	0.97	1.00	1.00
500	1.00	1.00	1.00	1.00	1.00	1.00	1.00	0.94	1.00	0.99
540	1.00	1.00	1.00	1.00	1.00	1.00	1.00	0.95	1.00	0.99
580	1.00	1.00	1.00	1.00	1.00	1.00	1.00	1.00	1.00	1.00

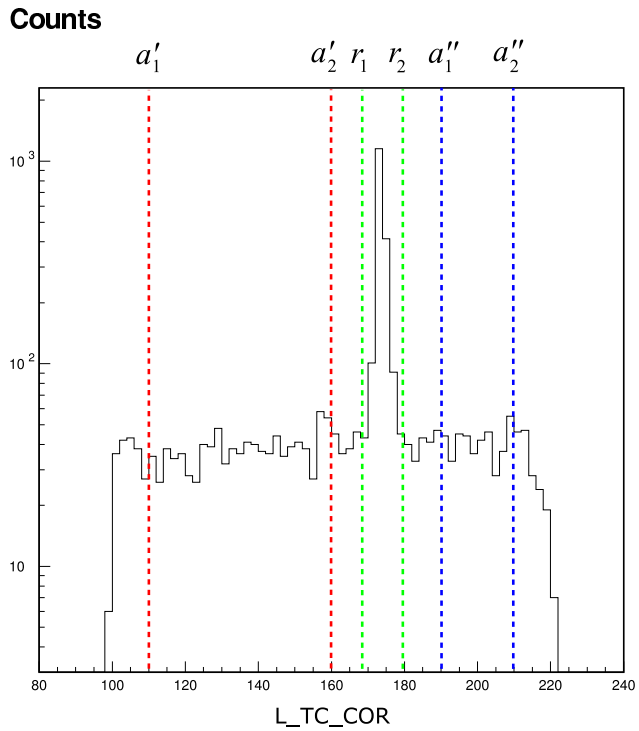

FIG. 80: Cut on the coincidence time (ns) and subtraction of accidentals. No other cuts (such as the vertex cut) were applied to reduce the accidentals in this plot.

TABLE XXXIII: Corrections and Efficiencies.

ID	Kinematics	$\Delta\varepsilon_{miss}$ (MeV)	Trigger Efficiency Left	Trigger Efficiency Right	Tracking Efficiency Left	Tracking Efficiency Right	Computer Livetime
0	f00	0.31	0.99	0.99	0.99	1.00	0.96
1	f10l	0.47	0.99	0.99	0.98	1.00	0.98
2	f10r	−0.16	0.99	0.99	0.98	0.99	0.92
3	f20l	0.48	0.99	0.99	0.98	1.00	0.99
4	f20r	−0.52	0.99	0.98	0.99	0.99	0.97
5	f30l	0.58	0.99	0.99	0.98	1.00	0.99
6	f30r	−0.40	0.99	0.97	0.99	0.99	0.98
7	f40l	0.49	0.99	0.99	0.98	0.99	1.00
8	f40r	−0.19	0.99	0.97	0.99	0.99	0.98
9	f50r	0.02	0.99	0.97	0.98	0.99	0.99

R-Function Cut The solid angle acceptance boundary of the HRS is a complicated function of y_{tg} and δ. The R-function, RFn, is a function of the target coordinates $(\theta_{tg}, \phi_{tg}, y_{tg}, \delta)$ for each HRS, which determines where a given value of θ_{tg} and ϕ_{tg} is located with respect to the the solid angle acceptance boundaries corresponding to y_{tg} and δ. The RFn uses a "look-up table" approach to determine the boundaries of the solid angle for each (y_{tg}, δ) value [106]. These boundaries take the form of 12 straight lines as shown in Figure 81. The RFn evaluates the distance between a given point (θ_{tg}, ϕ_{tg}) and each of the boundary lines. The minimum of those distances is then returned as the RFn value. Typically, $RFn = 0$ at the boundaries of the HRS acceptance, $RFn > 0$ inside the HRS acceptance, and $RFn < 0$ outside the HRS acceptance.

By comparing the data and the simulation for the analyzed kinematics, we found that the two R-function distributions start to match if we require that the Left and Right $RFn \geq 0.01$ (see Figure 82).

V.3 RADIATIVE CORRECTIONS

The ^{2}H$(e, e'p)n$ reaction is more complicated than the simple one photon exchange diagram shown in Figure 2. Electrons can radiate real or virtual photons during the scattering. The radiation of real photons add tails to the peaks (radiative tails). This changes the electron momentum and the observed cross section for the reaction. Furthermore, while these radiative effects constitute an important correction to the ^{2}H$(e, e'p)n$ cross section, theoretical calculations do not include them. Therefore, it was necessary to correct the measured

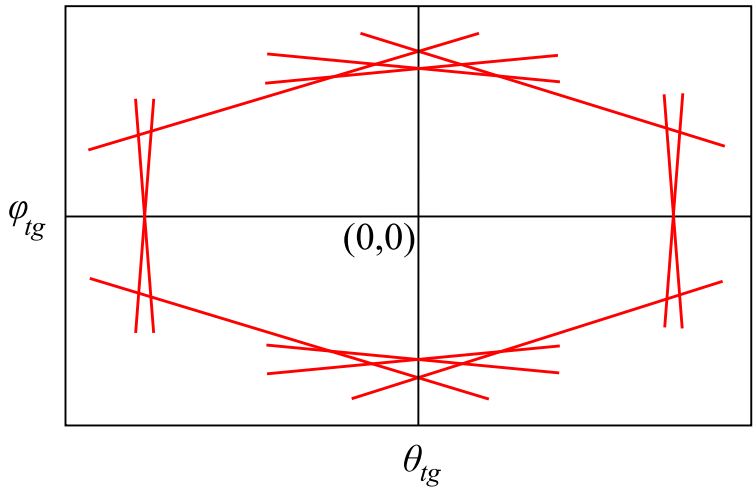

FIG. 81: Typical representation of the HRS solid angle acceptance boundaries by a contour of 12 lines.

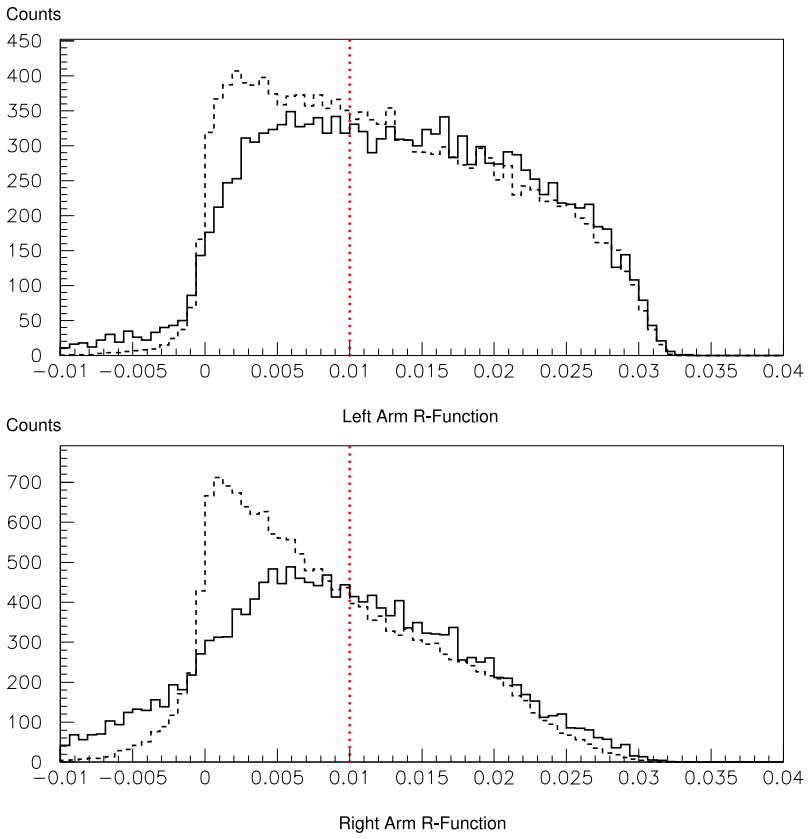

FIG. 82: R-Function cuts for Left and Right arms ($RFn > 0.01$). The data (dashed lines) and simulation (solid lines) are plotted for Run 2811 ($Q^2 = 3.5$ GeV^2, $p_{miss} = 200$ MeV and $\phi_x = 0$).

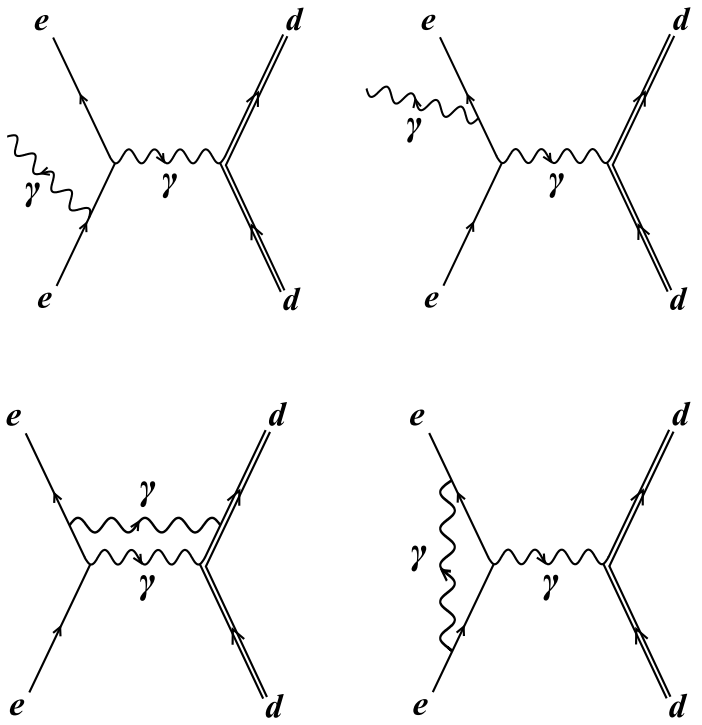

FIG. 83: Radiation by real photons (Top) and virtual photons (Bottom) in a typical ^{2}H(e,e).

cross sections for radiative effects in order to perform a meaningful comparison between the experimental results and the theoretical calculations.

There are two main types of radiative effects: internal radiation and external radiation.

1. Internal Radiation: The electron radiates real and virtual photons (see Figure 83) in the presence of the Coulomb field of the specific target nucleus involved in the reaction. The radiation of soft photons (real photons with energies below the photon "cutoff energy") and virtual photons contribute to the "Schwinger" correction to the cross section. The hard photons (real photons with energy above the cutoff energy) emission lead to the radiative tail and affect the kinematics of the reaction. The peaking approximation was used, wherein the photon is assumed to be radiated either along the incident or the scattered electron directions.

2. External Radiation: The electron radiates real and virtual photons in the presence of the Coulomb fields of other nuclei. This was described in Section V.1.

In this dissertation, the radiative corrections of the data were done in the following

way:

1. For each (ϕ_x, p_{miss}) bin (see Section V.5) of the simulation, the ratio of the unradiated to the radiated yields, $f_r(\phi_x, p_{miss})$, calculated using the Laget PWBA+FSI formalism is determined.

2. Yields for each corresponding bin of the data are then multiplied by these ratios to correct the data for radiative effects.

The average value of the radiative correction, $\langle f_r \rangle$, was found to be 1.38.

V.4 NORMALIZATION

The yields of the ^{1}H$(e, e'p)$ elastic data for different Q^2 values from Experiment E01-020 were compared to previous data from Hall A and other world data by using different proton electromagnetic form factor (EMFF) parameterizations [108, 109] in MCEEP. To do these comparisons, sensible cuts were applied to both the data and the simulation, such as E_{miss}, vertex, target length, and R-function cuts, for Left and Right arms [107]. Also different resolution factors were adjusted in MCEEP to properly simulate the shapes of the data distributions (see *e.g.*, Figure 84). Figure 85 shows some of the data to simulation yield ratios, f_n, for the invariant mass, W, and Table XXXIV lists all the obtained ratios. In this table, the elastic $Q^2 = 3.438$ GeV^2 value is very close to the quasielastic $Q^2 = 3.5$ GeV^2 value in this dissertation. Different proton EMFF were used to calculate the normalization ratios:

- MMD parameterization [110] is more suitable for low Q^2 data because it did not incorporate any high Q^2data.

- Hall A parameterization [111, 112] (MCEEP's default) uses an alternate MMD parameterization for G_M^p in addition to the G_E^p/G_M^p ratio from Hall A polarization transfer data to get G_E^p.

- Lomon's parameterization [113, 114] is an extended Gari-Krümpelmann (GK) parametrization [115, 116] which can be used for high momentum transfer data.

- Kelly's parameterization [117] is a simple function of Q^2 with only few parameters.

TABLE XXXIV: Normalization yield ratio, f_n, of the data to simulation for ^{1}H$(e, e'p)$, involving different form factor parameterizations. Three different Hydrogen kinematics were analyzed.

Form Factor	Q^2 (GeV^2)		
	2.451	3.438	4.348
MMD	0.79	0.76	0.76
Hall A	0.82	0.80	0.79
Lomon	0.83	0.80	0.79
Kelly	0.80	0.76	0.76
Arrington	0.79	0.75	0.75

- Finally, Arrington's parameterization [118] is a global reanalysis of previous Rosenbluth cross section measurements [119] to extract the proton EMFF. At the present time, Arrington's parameterization seems to be the most satisfactory among all the other EMFF parameterizations.

The obtained normalization ratios indicated that the elastic ^{1}H$(e, e'p)$ data yield from Experiment E01-020 was about 20–25% less than almost all previous data. Based on this discrepancy, it was decided to normalize the ^{2}H$(e, e'p)n$ cross section by using the normalization ratio $f_n = 0.75$, obtained by using the Arrington's parameterization for $Q^2 = 3.438$ GeV^2.

This discrepancy was studied extensively [91] and the results indicated a problem at the trigger level (much lower trigger rates than expected). There are also indications of the same discrepancy from other Hall A experiments, though these other results are not final yet. For example, some efforts were made to compare Hall A Experiment E01-015 data to simulations by using both MCEEP and the SIMC program [120]. The preliminary normalization results from this experiment were found to be similar to Experiment E01-020 results under different analysis conditions [121].

V.5 BINNING

The binning of the data and the simulation was done over the out-of-plane angle, ϕ_x, the magnitude of the missing momentum, p_{miss}, the square of the four-momentum transfer, Q^2, and the invariant mass, W (four-dimensional bins). Tables XXXV, XXXVI, and XXXVII list the three binning schemes used in the analysis. The binning scheme selections

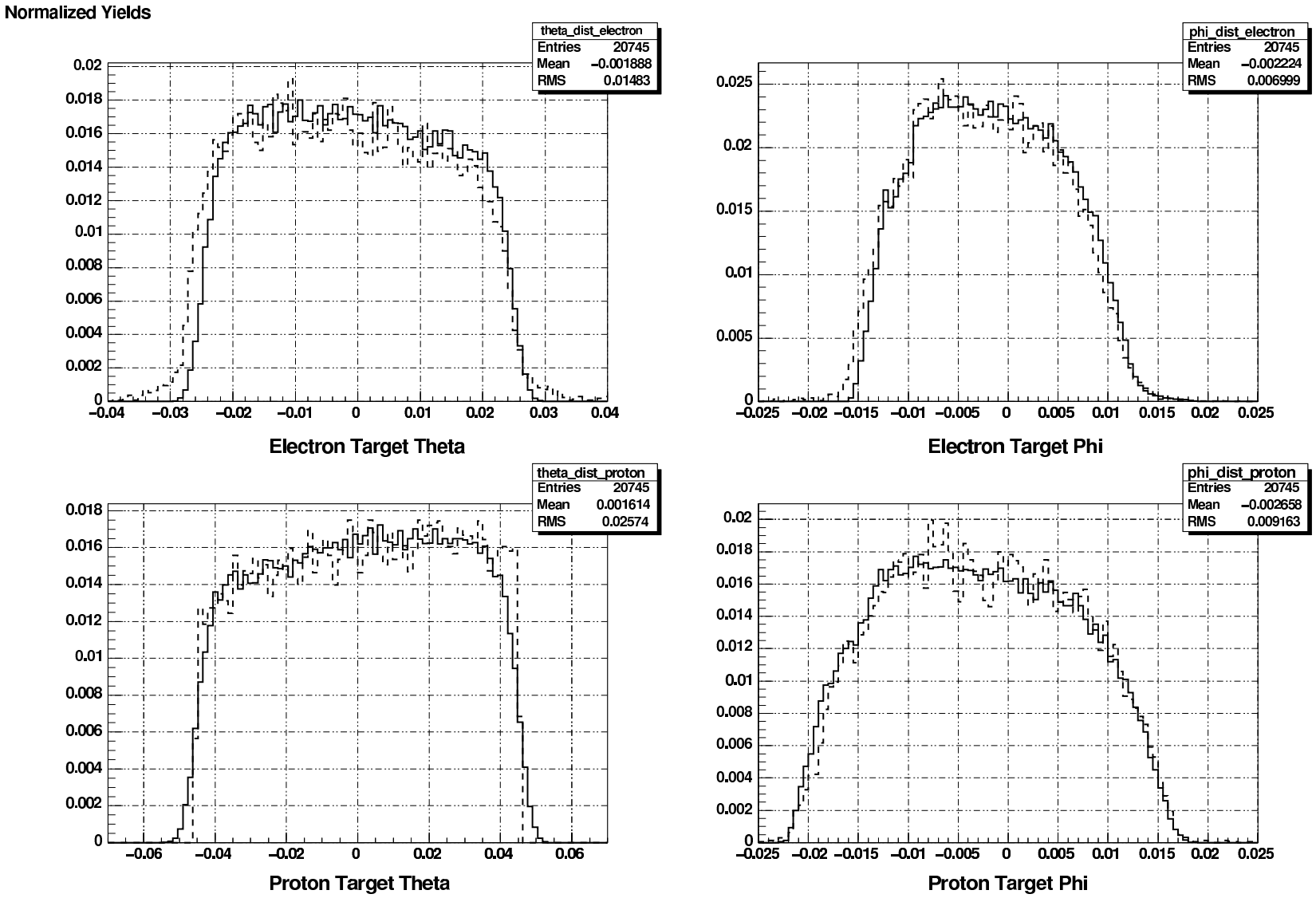

FIG. 84: Comparisons of the target angles for the data (dashed lines) and the simulation (solid lines). The yields are arbitrarily normalized.

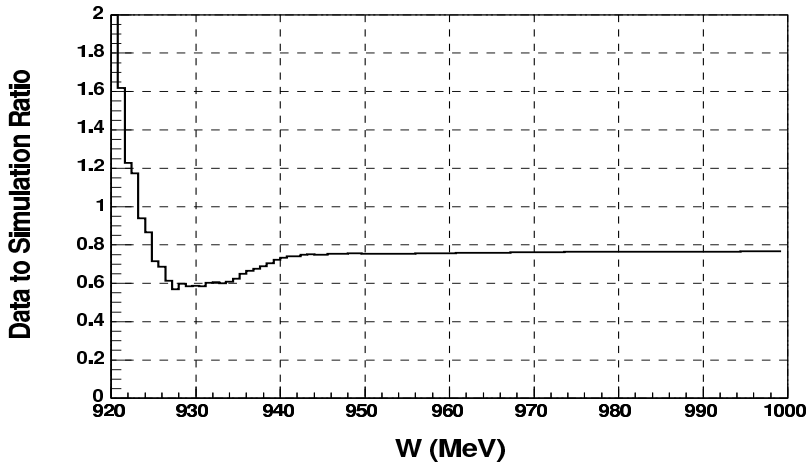

(a) $Q^2 = 2.451$ GeV^2 (Kelly parameterization).

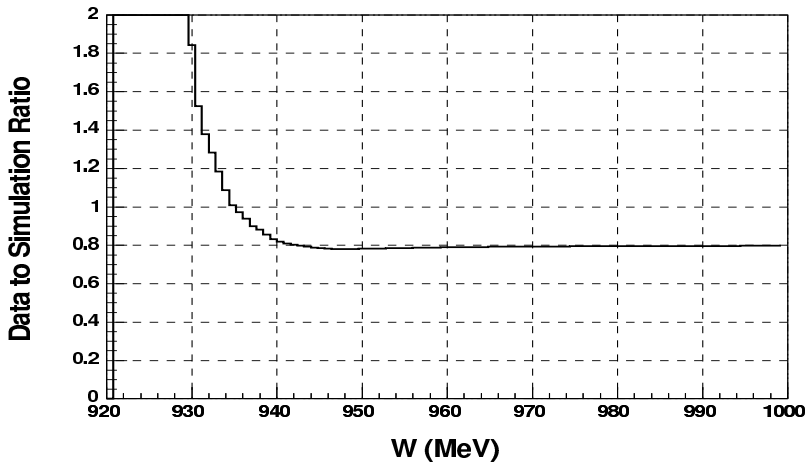

(b) $Q^2 = 3.438$ GeV^2 (Kelly parameterization).

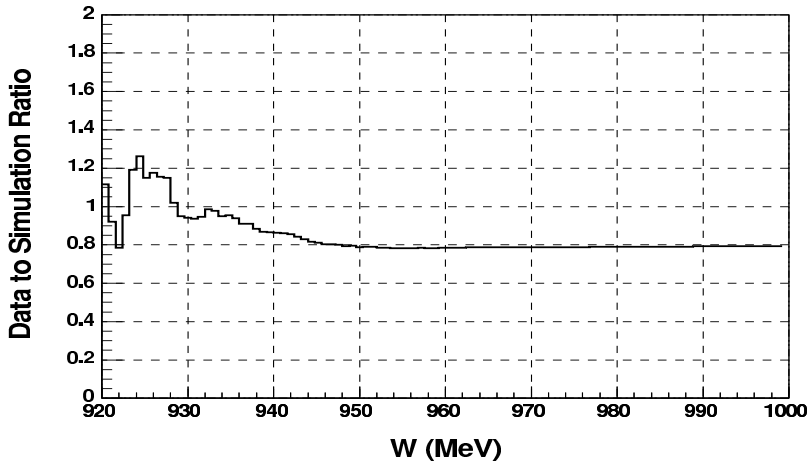

(c) $Q^2 = 4.348$ GeV^2 (Hall A parameterization).

FIG. 85: Yield ratio of the data to simulation for the ^{1}H$(e, e'p)$ invariant mass, W.

TABLE XXXV: Single bin over Q^2 and W.

Variable	ϕ_x (°)	p_{miss} (MeV)	Q^2 (GeV^2)	W (MeV)
Lower limit	0	0	3.15	2500
Upper limit	360	600	3.85	2800
Bin width	2	40	0.7	300
Number of bins	180	15	1	1

TABLE XXXVI: Multi-bin over Q^2.

Variable	ϕ_x (°)	p_{miss} (MeV)	Q^2 (GeV^2)	W (MeV)
Lower limit	0	0	3.15	2500
Upper limit	360	600	3.85	2800
Bin width	2	100	0.1	300
Number of bins	180	6	7	1

were optimized to represent the major features in the cross section and the R_{LT} response function, and at the same time making sure that all the different bins are sufficiently populated in all four dimensions (except for the ϕ_x bin at high p_{miss}). The ϕ_x bins are used in this analysis to extract R_{LT} and A_{LT} and their width was selected to be the same for all the binning schemes. The multi-bin schemes were used in order to study the gross dependence of the cross section over the coverage of Q^2 and W in this dissertation.

TABLE XXXVII: Multi-bin over W.

Variable	ϕ_x (°)	p_{miss} (MeV)	Q^2 (GeV^2)	W (MeV)
Lower limit	0	0	3.15	2500
Upper limit	360	600	3.85	2800
Bin width	2	100	0.7	50
Number of bins	180	6	1	6

V.6 CALCULATION OF THE CROSS SECTIONS

The five-fold cross section per four-dimensional bin is defined as

$$\frac{d^5\sigma}{d\omega d\Omega_e d\Omega_p}(\phi_x, p_{miss}, Q^2, W) = \frac{N'(\phi_x, p_{miss}, Q^2, W)}{\Phi(\phi_x, p_{miss}, Q^2, W)} \tag{146}$$

where $N'(\phi_x, p_{miss}, Q^2, W)$ is the corrected data yield and $\Phi(\phi_x, p_{miss}, Q^2, W)$ is the phase space (or acceptance) volume per bin. We can write:

$$N'(\phi_x, p_{miss}, Q^2, W) = \frac{f_t(p_{miss}) \cdot f_r(\phi_x, p_{miss})}{f_\rho(z_{react}, I) \cdot f_n \cdot \epsilon_{track} \cdot \epsilon_{trig} \cdot CLT} N(\phi_x, p_{miss}, Q^2, W) \tag{147}$$

where:

- $f_t(p_{miss})$ is the trues ratio,
- $f_r(\phi_x, p_{miss})$ is the radiative correction factor,
- $f_\rho(z_{react}, I)$ is the boiling factor.
- f_n is the normalization correction ratio,
- ϵ_{track} is the tracking efficiency,
- ϵ_{trig} is the trigger efficiency,
- CLT is the computer live time,
- $N(\phi_x, p_{miss}, Q^2, W)$ is the uncorrected data yield per bin.

The five-fold phase space volume per bin for ^{2}H$(e, e'p)n$ was calculated by MCEEP as:

$$\Phi(\phi_x, p_{miss}, Q^2, W) = \frac{N_{sim}(\phi_x, p_{miss}, Q^2, W)}{N_{total}} \Delta\omega \Delta\Omega_e \Delta\Omega_p \tag{148}$$

where $N_{sim}(\phi_x, p_{miss}, Q^2, W)$ is the number of sampled events in this bin, N_{total} is the total number of sampled events, and $\Delta\omega$, $\Delta\Omega_e$, and $\Delta\Omega_p$ are the sampled ω, Ω_e, and Ω_p ranges respectively.

V.7 SEPARATION OF THE R_{LT} RESPONSE FUNCTION

The reduced cross section is defined as:

$$\left(\frac{d^5\sigma}{d\omega d\Omega_e d\Omega_p}\right)_{red}(\phi_x, p_{miss}, Q^2, W) = \frac{d^5\sigma}{d\omega d\Omega_e d\Omega_p}(\phi_x, p_{miss}, Q^2, W)/f_\sigma(\phi_x, p_{miss}, Q^2, W) \tag{149}$$

where

$$f_\sigma(\phi_x, p_{miss}, Q^2, W) = \frac{M_p M_n \left|\vec{p}\right|}{(2\pi)^3 M_d}\frac{\sigma_{Mott} f_{rec}}{v_{LT}}. \tag{150}$$

Therefore

$$\left(\frac{d^5\sigma}{d\omega d\Omega_e d\Omega_p}\right)_{red}(\phi_x, p_{miss}, Q^2, W) = \frac{v_L}{v_{LT}}R_L + \frac{v_T}{v_{LT}}R_T + R_{LT}\cos\phi_x + \frac{v_{TT}}{v_{LT}}R_{TT}\cos 2\phi_x. \tag{151}$$

Rewriting this equation in the form

$$\left(\frac{d^5\sigma}{d\omega d\Omega_e d\Omega_p}\right)_{red}(\phi_x, p_{miss}, Q^2, W) = A + B\cos\phi_x + C\cos 2\phi_x \tag{152}$$

and doing a χ^2 minimization to find the values of A, B, and C over the angle ϕ_x directly gives the R_{LT} response function:

$$R_{LT} = B. \tag{153}$$

The uncertainty in the extracted R_{LT} is given by:

$$\delta R_{LT} = \frac{1}{2}\sqrt{[\delta\sigma(\phi_x = 0)]^2 + [\delta\sigma(\phi_x = \pi)]^2}, \tag{154}$$

where $\delta\sigma(0)$ and $\delta\sigma(\pi)$ are the uncertainties of $\sigma(0)$ and $\sigma(\pi)$. In this expression, $\delta\sigma(0)$ and $\delta\sigma(\pi)$ are assumed to be uncorrelated.

V.8 EXTRACTION OF THE A_{LT} ASYMMETRY

The A_{LT} asymmetry can be written in terms of the reduced cross section as:

$$A_{LT} = \frac{\sigma_{red}(0) - \sigma_{red}(\pi)}{\sigma_{red}(0) + \sigma_{red}(\pi)}. \tag{155}$$

Therefore

$$A_{LT} = \frac{R_{LT}}{\frac{v_L}{v_{LT}}R_L + \frac{v_T}{v_{LT}}R_T + \frac{v_{TT}}{v_{LT}}R_{TT}}, \tag{156}$$

or simply

$$A_{LT} = \frac{B}{A+C}, \tag{157}$$

where A, B, and C are the same extracted values from the χ^2 minimization in the previous section.

The uncertainty in the extracted A_{LT} is obtained from:

$$\delta A_{TL} = \frac{2\sqrt{[\sigma(0)\delta\sigma(\pi)]^2 + [\sigma(\pi)\delta\sigma(0)]^2}}{[\sigma(0)+\sigma(\pi)]^2}, \tag{158}$$

where $\delta\sigma(0)$ and $\delta\sigma(\pi)$ are the uncertainties of $\sigma(0)$ and $\sigma(\pi)$. In this expression, $\delta\sigma(0)$ and $\delta\sigma(\pi)$ are assumed to be uncorrelated.

V.9 SYSTEMATIC UNCERTAINTIES

The kinematic systematic uncertainties for the beam and the two spectrometers (nine uncertainties) are listed in Table XXXVIII. They are used to calculate the "kinematics dependent systematic uncertainties" or "kinematic sensitivities" of the reaction cross section. The kinematics dependent systematic uncertainties are p_{miss} dependent and were determined with the code "systerr" which is part of the simulation program MCEEP [100]. This code does not deal with radiative effects but assumes the errors can be calculated from the unradiated cross sections. It calculates the nominal cross section and uses the uncertainties given in Table XXXVIII to calculate nine other cross sections for shifts equal to each of the kinematic uncertainties in turn (with all others at nominal values). The fractional shifts of the nine cross sections from the nominal cross section are shown in Figure 86. The total (quadrature sum) of these fractional shifts (kinematics dependent systematic uncertainties) for each p_{miss} bin are listed in Table XL for the single bin scheme and Table XLI for the multi-bin schemes. Estimates of the other systematic uncertainties that mostly do not vary on a point-to-point basis (kinematics independent or global) but still contribute to the kinematics dependent systematic uncertainty slightly are listed in Table XXXIX. The listed values were estimated based on previous Hall A experiments.

V.10 SIMULATIONS

The ^{2}H$(e,e'p)n$ reaction was simulated with the "Monte Carlo for $(e,e'p)$ experiments" program (MCEEP) [100]. MCEEP calculates the mean energy losses of electrons and

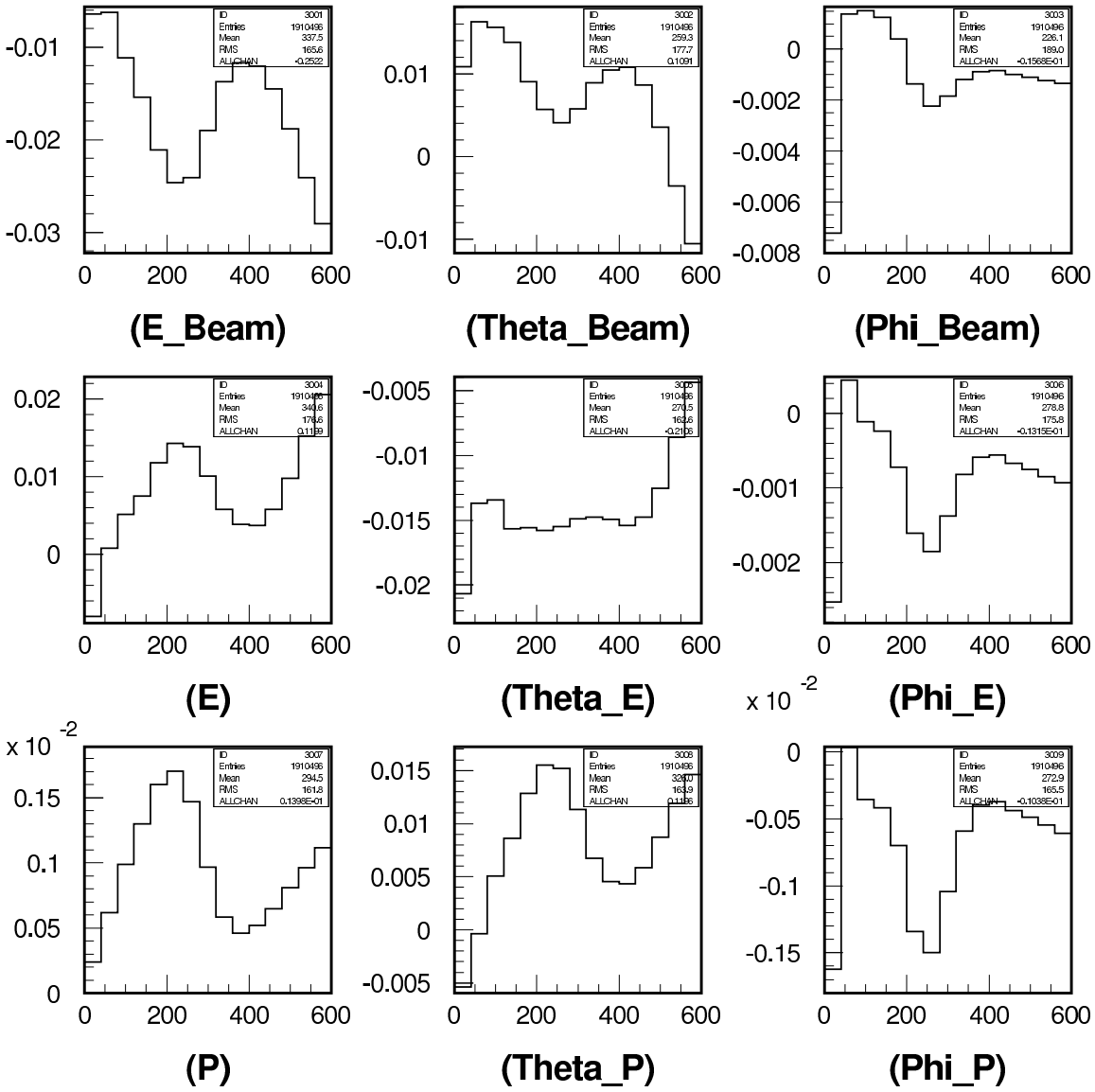

FIG. 86: Fractional shifts in the cross section (y-axis) versus the the missing momentum in MeV (x-axis). The labels in parentheses refer to the quantity which was shifted in computing the change in cross section.

TABLE XXXVIII: Kinematic systematic uncertainties for the beam and the two spectrometers. E_{Beam} is the incident electron energy, e is the scattered electron energy, p is the momentum of the proton, and θ and ϕ are the in-plane and out-of-plane angles for each particle.

Quantity	Uncertainty
δE_{Beam}	0.30×10^{-3}
θ_{Beam}	0.10 mrad
ϕ_{Beam}	0.10 mrad
δe	0.17×10^{-3}
θ_e	0.12 mrad
ϕ_e	0.23 mrad
δp	0.23×10^{-3}
θ_p	0.13 mrad
ϕ_p	0.29 mrad

TABLE XXXIX: Estimates of other systematic uncertainties. "Global" refers to kinematics independent uncertainties which are common to all kinematics settings and bins, whereas "Kinematics" refer to the kinematics dependent part.

One-third of the global uncertainties was estimated to contribute to kinematics dependent uncertainties.

Quantity	$\delta\sigma(\%)$	
	Global	Kinematics
Beam Charge	1	$\frac{1}{3}$
Computer Deadtime	1	$\frac{1}{3}$
Left Tracking Efficiency	1	$\frac{1}{3}$
Right Tracking Efficiency	1	$\frac{1}{3}$
Left Triggering Efficiency	1	$\frac{1}{3}$
Right Triggering Efficiency	1	$\frac{1}{3}$
Target Boiling Correction	2	$\frac{2}{3}$
Particle Identification	1	$\frac{1}{3}$
Radiative Corrections	1	$\frac{1}{3}$
Normalization	6	2
Sum in Quadrature	7	2.33

TABLE XL: Kinematics dependent uncertainties for the single bin scheme.

p_{miss} (MeV)	$\delta\sigma$ (%)
20	0.380
60	0.299
100	0.419
140	0.546
180	0.717
220	0.830
260	0.812
300	0.644
340	0.477
380	0.418
420	0.429
460	0.495
500	0.620
540	0.792
580	0.965

TABLE XLI: Kinematics dependent uncertainties for the multi-bin schemes.

p_{miss} (MeV)	$\delta\sigma$ (%)
50	0.321
150	0.512
250	0.814
350	0.484
450	0.472
550	0.793

protons with the Bethe-Bloch formula, with additional corrections for density and shell effects. Energy loss straggling is approximated by either Landau, Vavilov, or Gaussian distributions, depending on the ratio between the mean energy loss and maximum energy loss in a single collision. In a final stage of event simulation, the mean energy losses of electrons and protons are subtracted to allow comparison with data corrected for the mean energy losses.

In MCEEP, the spectrometer resolution is simulated by:

1. Transport of particles generated at the target to the focal plane, by application of spectrometer forward transfer functions.
2. Simulation of multiple scattering in the spectrometer exit window and air, by addition of Gaussian functions to particle transport coordinates.
3. Simulation of position resolution of VDCs.
4. Transport of particles back to target with reverse transfer functions.

The spectrometer resolution is simulated by addition of Gaussian distributions to particle coordinates reconstructed at the target, with parameters of the Gaussian chosen to match the experimentally observed spectrometer resolution. MCEEP simulates spectrometer acceptance (see Figure 87) by transport of particles to five internal spectrometer aperture cuts. On top of that, an R-function cut (see Section V.2) is used to match the acceptance distributions of the data and the simulation as shown in Figure 88. Figures 89 and 90 show more comparisons for other variables.

V.10.1 Jeschonnek PWBA

All kinematics were simulated with the Jeschonnek relativistic (unfactorized) plane wave born approximation (PWBA) calculations for ^{2}H$(e, e'p)n$ [41]. This paper deals only with the PWIA but the calculations were modified to include also the PWBA in MCEEP. Unfortunately, they do not include final state interactions (FSI), meson exchange currents (MEC) nor isobar currents (IC) because of the extensive computer processing time required. In this analysis, the Jeschonnek PWBA simulation did not include radiative or energy loss corrections, to facilitate comparison with the radiatively corrected data.

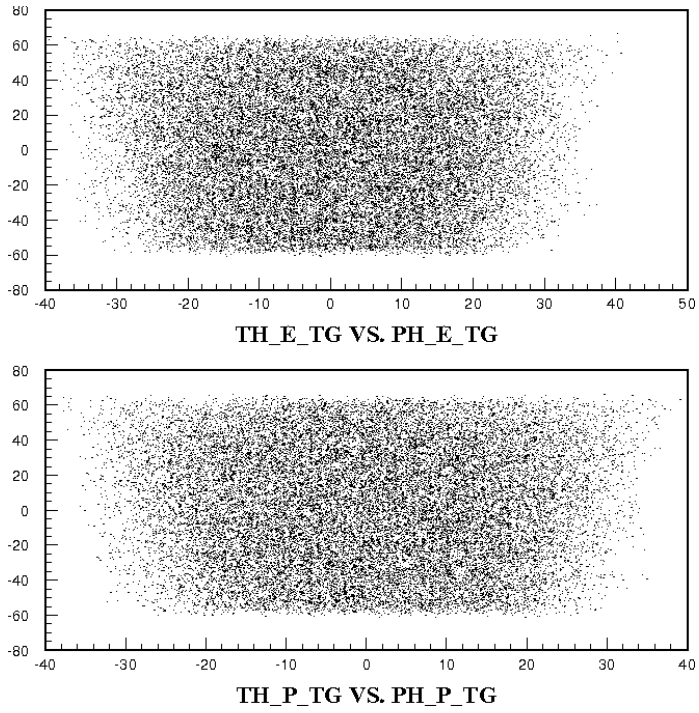

FIG. 87: Spectrometer acceptance distributions for Left (top) and Right (bottom) arm solid angles in terms of the target angles (θ_{tg}, ϕ_{tg}). Angles are in mrad.

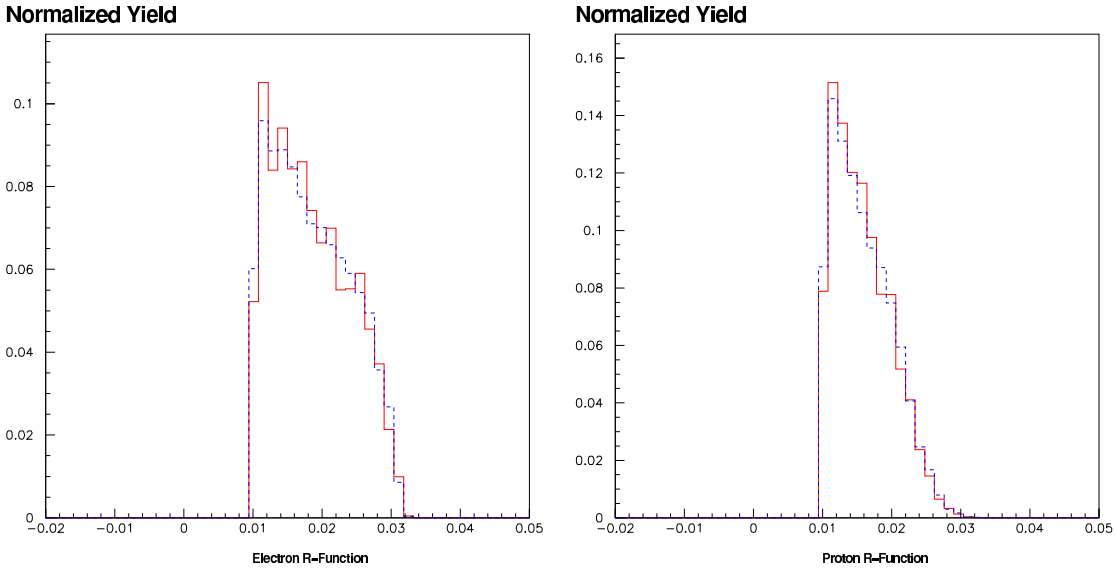

FIG. 88: Comparisons for the Left (Electron) and Right (Proton) R-Functions for the Q3_f20l ($Q^2 = 3.5$ GeV^2, $p_{miss} = 200$ MeV and $\phi_x = 0$) kinematics. Data is dashed lines and simulation is solid lines. A cut of $RFn > 0.01$ was used in the analysis. The yields are arbitrarily normalized.

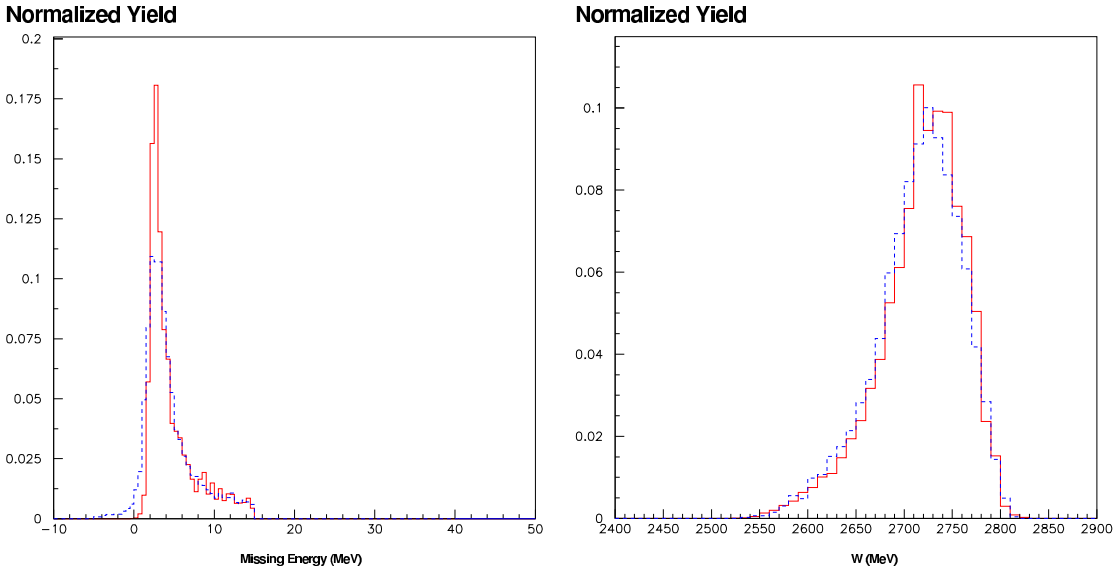

FIG. 89: Comparisons of the missing energy, E_{miss}, and invariant mass, W for the Q3_f201 ($Q^2 = 3.5$ GeV^2, $p_{miss} = 200$ MeV and $\phi_x = 0$) kinematics. Data is dashed lines and simulation is solid lines. The yields are arbitrarily normalized.

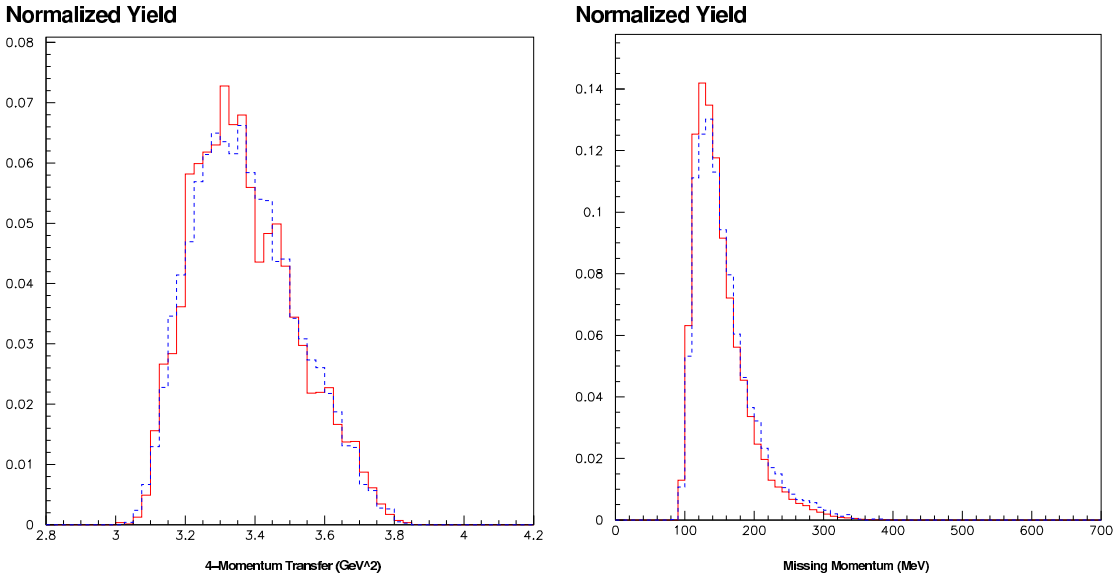

FIG. 90: Comparisons for the 4-momentum transfer, Q^2, and the missing momentum, p_{miss} for the Q3_f201 ($Q^2 = 3.5$ GeV^2, $p_{miss} = 200$ MeV and $\phi_x = 0$) kinematics. Data is dashed lines and simulation is solid lines. The yields are arbitrarily normalized.

V.10.2 Laget PWBA and PWBA+FSI

The data were also simulated using Laget's PWBA and Laget's PWBA+FSI [45] formalism. Unfortunately, MEC and IC were not available at the time of writing this dissertation. These calculations were implemented by interpolating on a set of data files generated from the calculations of Laget defined on a grid of points spanning the experimental acceptance for the unpolarized ^{2}H$(e, e'p)n$ response functions [100, 122]. In this dissertation, the Laget PWBA and PWBA+FSI simulations were calculated for the bound state, without including radiative or energy loss corrections to compare with the radiatively corrected data. Another simulation was carried out for Laget's PWBA+FSI including radiative and energy loss corrections. This simulation was compared with the unradiated one in order to correct the data for these effects (see Section V.3).

CHAPTER VI

RESULTS AND CONCLUSIONS

The final results for the cross section, the longitudinal-transverse response function, R_{LT}, and A_{LT} asymmetry are presented in this chapter for the different binning schemes in this analysis (single bin over Q^2 and W, and multi-bin over Q^2 or W). Figure 91 shows a comparison of the data without radiative corrections and the radiatively folded simulation before and after applying the final optimized cuts (discussed in Section V.2). From this comparison, one can see reasonable agreement between the data and the simulation acceptance in Q^2 and W after the application of the final cuts. Similar comparisons for ϕ_x and p_{miss} after applying the final optimized cuts are shown in Figure 92. Again, very good agreement is observed between the data and the simulation before extracting the final results. The acceptance for the missing momentum, p_{miss}, and the out of plane angle, ϕ_x, after applying the final cuts is shown in Figure 93. For $p_{miss} > 500$ MeV, $\phi_x = 0$ is not populated sufficiently to extract the R_{LT} response function nor the A_{LT} asymmetry. Figure 94 shows the three binning schemes over Q^2 and W acceptance based on the unradiated simulation, used in the final analysis to compare with the radiatively corrected data. All the data from the highest Q^2 perpendicular kinematics were combined to form an effectively larger acceptance proton spectrometer.

Four different plots were made for each bin (the data were radiatively corrected first):

- The fivefold differential cross section for the ^{2}H$(e, e'p)n$ reaction.
- The cross section ratio to the Laget PWBA+FSI calculations. The Laget FSI+PWBA calculations are shown as a horizontal line at a ratio equal to unity in the cross section ratio plots.
- The longitudinal-transverse response function, R_{LT}.
- The longitudinal-transverse asymmetry, A_{LT}.

Three theoretical calculations were used to compare with the radiatively corrected data:

- Jeschonnek PWBA (referred to as "Jeschonnek" in the plots),
- Laget PWBA, and
- Laget PWBA+FSI (referred to as "Laget FSI" in the plots).

The conventions and units used in the plots are those of Jeschonnek. As a general remark, the Jeschonnek PWBA and Laget PWBA calculations show very good agreement in almost all the plots which indicates the consistency of these two different PWBA calculations.

The Laget FSI+PWBA calculations were used to evaluate the kinematics dependent systematic uncertainty. In addition to the kinematics dependent uncertainty, there is a kinematics independent uncertainty of 7% which is not shown for the cross section, cross section ratio and R_{LT} plots. There is no kinematics independent uncertainty for the A_{LT} asymmetry by definition.

VI.1 SINGLE BIN RESULTS

In order to extract the p_{miss} dependence of the cross section, R_{LT}, and A_{LT} for a single bin over the acceptance of Q^2 and W, we needed to average both theory and data over the whole Q^2 and W acceptance.

VI.1.1 Cross Section

The fivefold differential cross section dependence on p_{miss} for central values of $Q^2 = 3.5$ GeV^2 and $W = 2650$ MeV is shown in Figure 95 and listed in Table XLII. The PWBA calculations by Jeschonnek and Laget agree very nicely for the whole range of p_{miss}. The Laget PWBA+FSI calculation agrees with the PWBA until $p_{miss} \sim 300$ MeV where the FSI effects start to increase the cross section abruptly from what the PWBA calculations predict. The data cross section dependence on p_{miss} agrees reasonably with the Laget PWBA+FSI calculation suggesting a large FSI contribution above $p_{miss} \sim 300$ MeV. A more detailed comparison of the cross sections is obtained by taking the ratio of the cross sections to the Laget PWBA+FSI calculation, shown in Figure 96 and listed in Table XLII. In this plot, the discrepancy at very low p_{miss} cast some doubt on neutron form factor measurements using the deuteron as target. The cross section ratio oscillation at $p_{miss} \sim 300$ MeV shows the need for additional ingredient in the calculations (for example, adding contributions from the MEC and IC mechanisms) to improve agreement with the data at these missing momentum values. Similar features of the ^{2}H$(e,e'p)n$ cross section ratio have been observed in a previous Hall A experiment (see Figure 11 in Chapter I) and casts some doubt on neutron form factor measurements done using ^{2}H$(e,e'p)n$ at low p_{miss} [91].

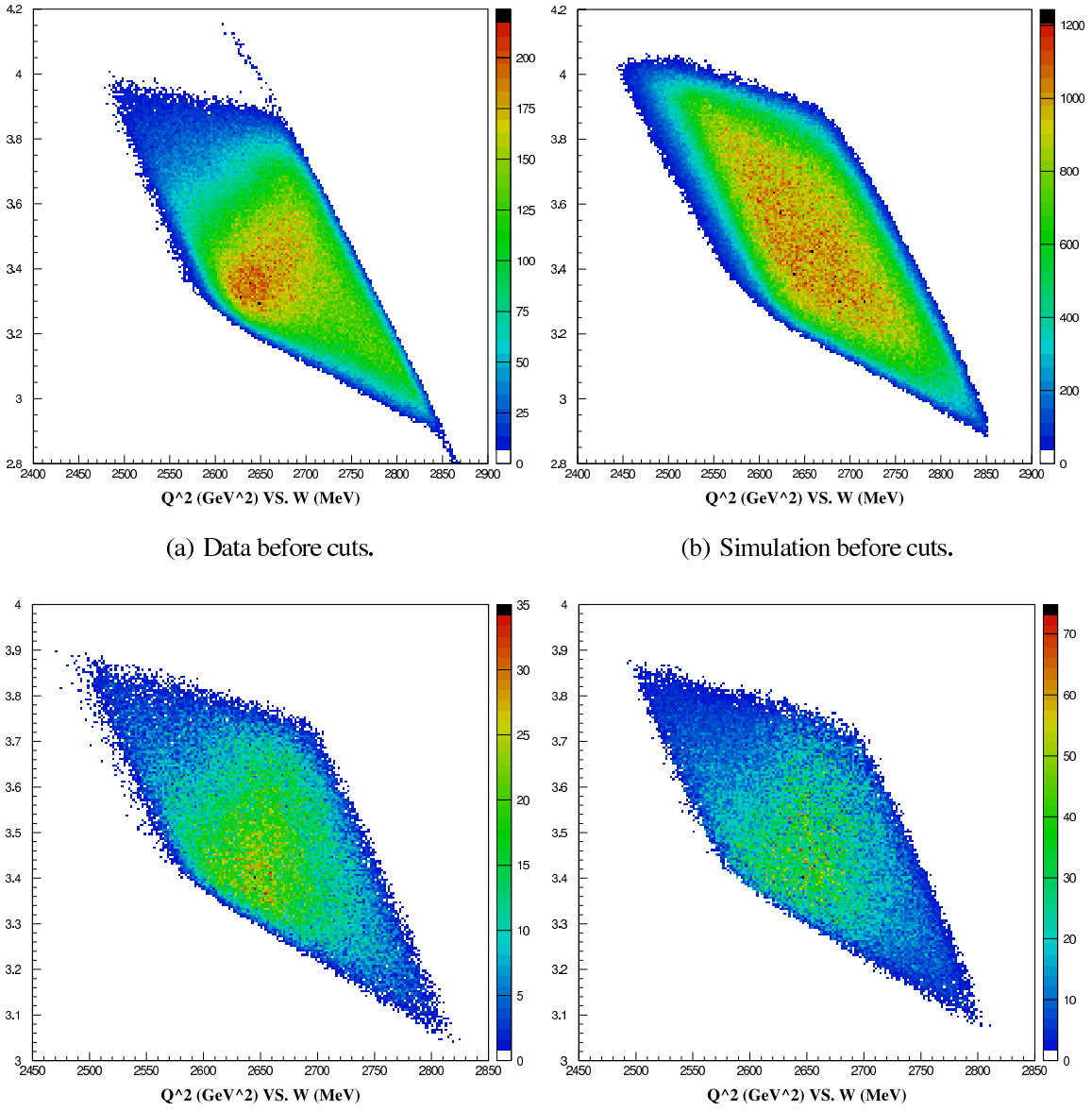

(a) Data before cuts.

(b) Simulation before cuts.

(c) Data after cuts.

(d) Simulation after cuts.

FIG. 91: Comparisons of the four-momentum transfer, Q^2, versus the invariant mass, W, for the data (Left) and the radiated simulation (right), before (Top) and after (Bottom) application of the final cuts.

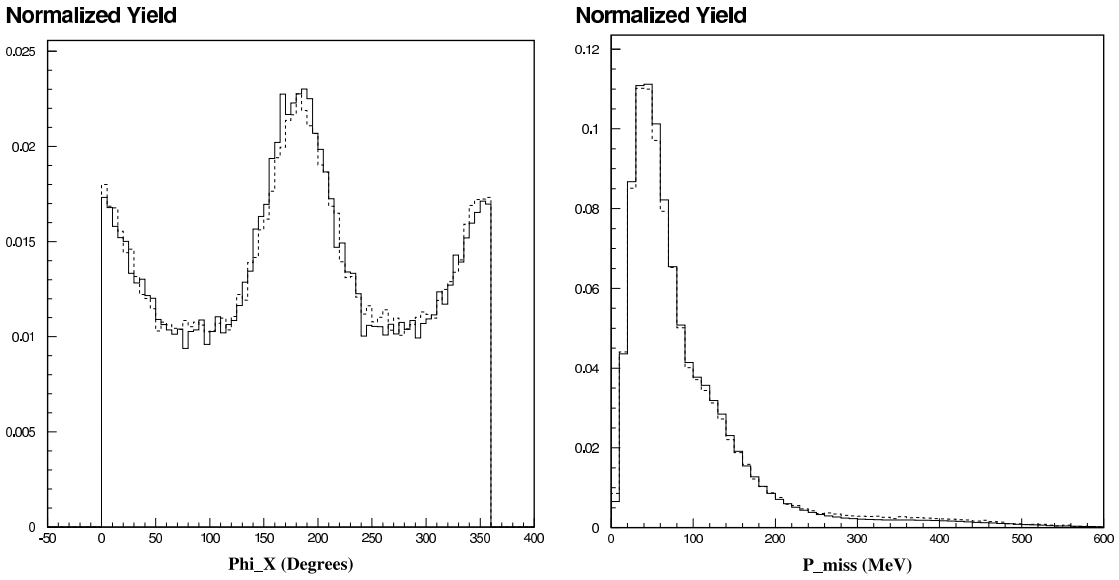

FIG. 92: Comparisons of the out of plane angle, ϕ_x, between the scattering and reaction planes, and the missing momentum, p_{miss}, for the data and simulation. Data is dashed lines and simulation is solid lines. The yields are arbitrarily normalized.

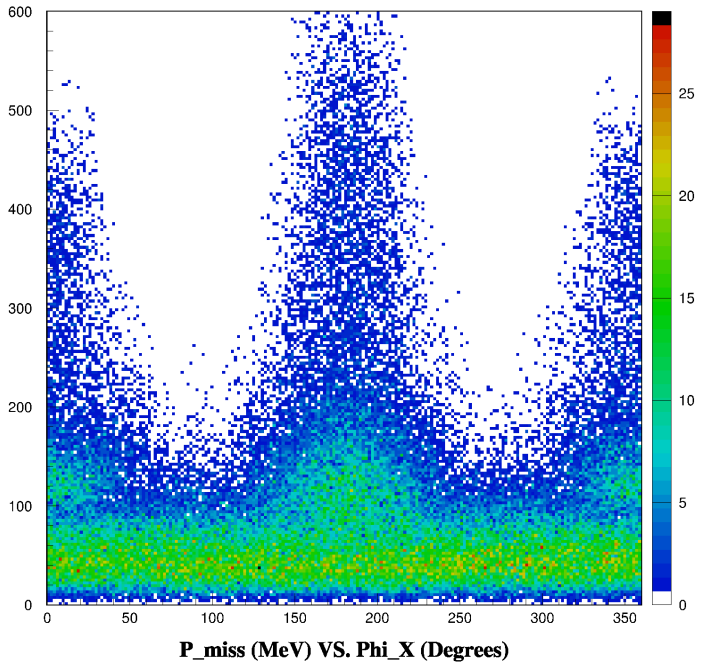

FIG. 93: The acceptance over the missing momentum, p_{miss}, and the out of plane angle, ϕ_x, after applying the final cuts. For $p_{miss} > 500$ MeV, $\phi_x = 0$ is not populated sufficiently to extract the R_{LT} response function nor the A_{LT} asymmetry.

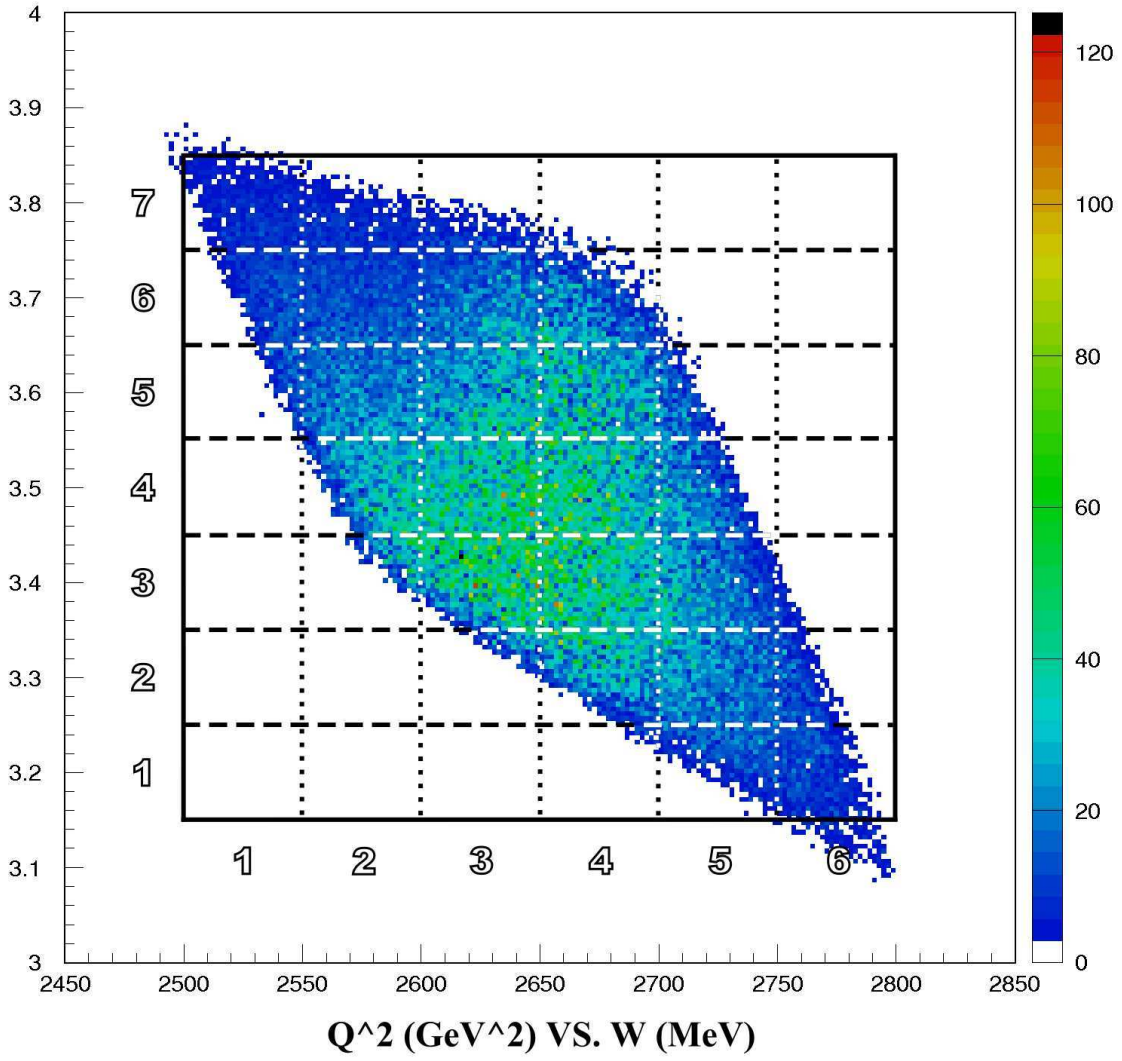

FIG. 94: Binning schemes. The "single bin" scheme over $Q^2$and W is represented by the solid square and the "multi-bin" schemes over $Q^2$and W are represented by the numbered horizontal dashed and vertical dotted rectangles respectively.

VI.1.2 R_{LT} Response Function and A_{LT} Asymmetry

The results for the longitudinal-transverse response function, R_{LT}, at central values of Q^2= 3.5 GeV^2 and W= 2650 MeV, are shown in Figures 97 and listed in Table XLII. The separated R_{LT} positive values are shown on the logarithmic plot of $-R_{LT}$ by using open circles. A blow-up of low R_{LT} values is shown on a linear scale in Figure 98. From these figures, we can see that the shape of R_{LT} is reproduced by Laget's PWIA+FSI calculation but not the magnitude. At low p_{miss} values (less than 200 MeV), the separated R_{LT} agrees reasonably well with all the theoretical calculations which means that FSI has a minor effect on R_{LT} at low p_{miss}. For $p_{miss} > 200$ MeV, the PWBA+FSI calculation under-predicts $-R_{LT}$. This again suggests the need for additional theoretical calculations.

Figure 99 shows the results for the longitudinal-transverse asymmetry, A_{LT}, for the same central values of Q^2 and W as R_{LT} in Figure 97. From this figure, we can see that the shape of A_{LT} is reproduced by Laget's PWIA+FSI calculation but not the magnitude. Again, we can see similar features for A_{LT} as we did for R_{LT}. For low p_{miss} values (less than 200 MeV), the separated A_{LT} agrees in general with all the theoretical calculations presented in this analysis. For recoil momentum higher than about 200 MeV, theoretical calculations over-predict $-A_{LT}$. Note that A_{LT} has the same sign as R_{LT} by definition. The extracted values of A_{LT} are listed in Table XLII.

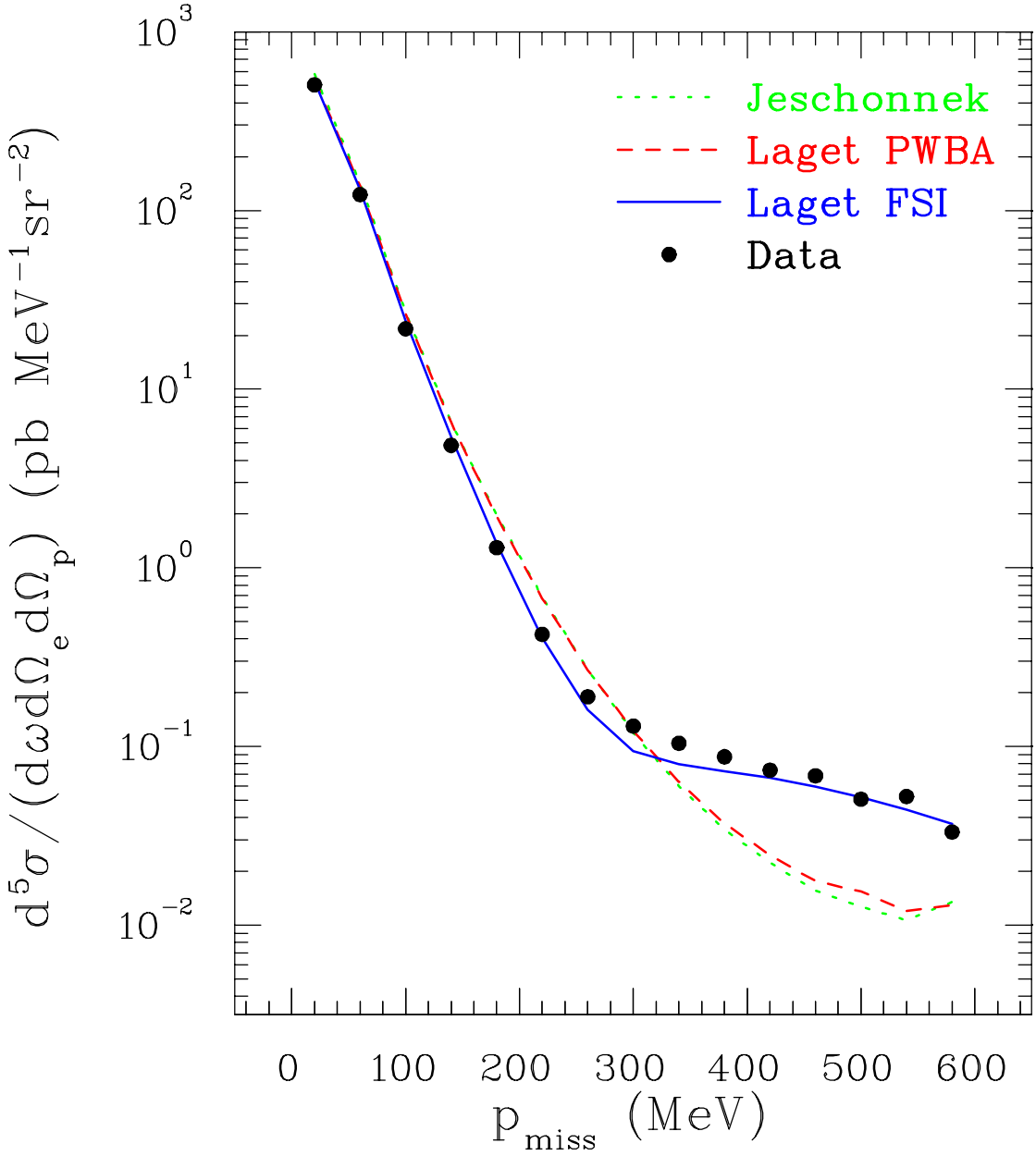

FIG. 95: Cross Section for the single bin scheme. The error bars (very small) represent the quadrature sum of the statistical uncertainty and the kinematics dependent systematic uncertainty. A kinematics independent systematic uncertainty of 7% is not shown.

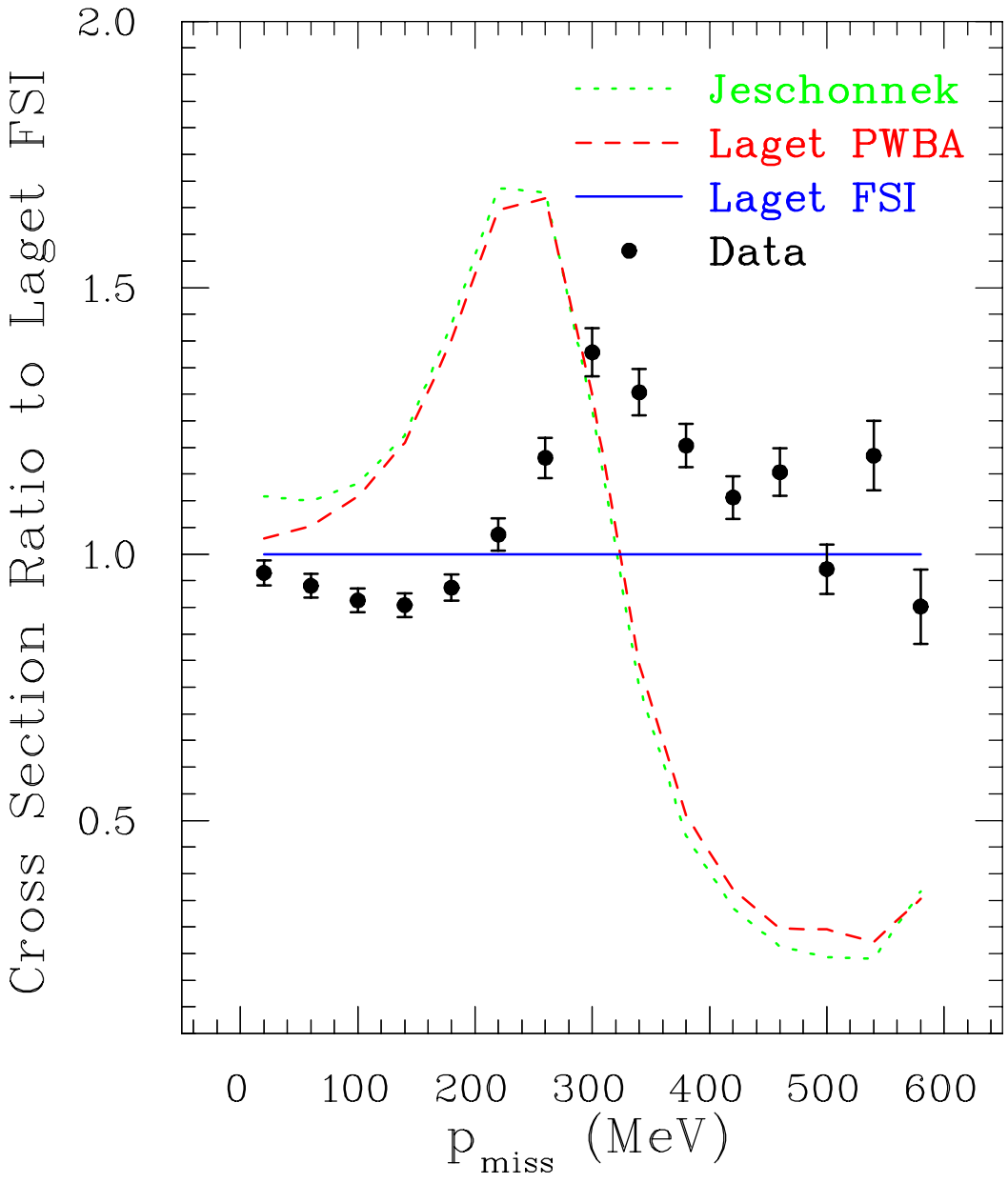

FIG. 96: Cross Section Ratio for the single bin scheme. The error bars represent the quadrature sum of the statistical uncertainty and the kinematics dependent systematic uncertainty. A kinematics independent systematic uncertainty of 7% is not shown.

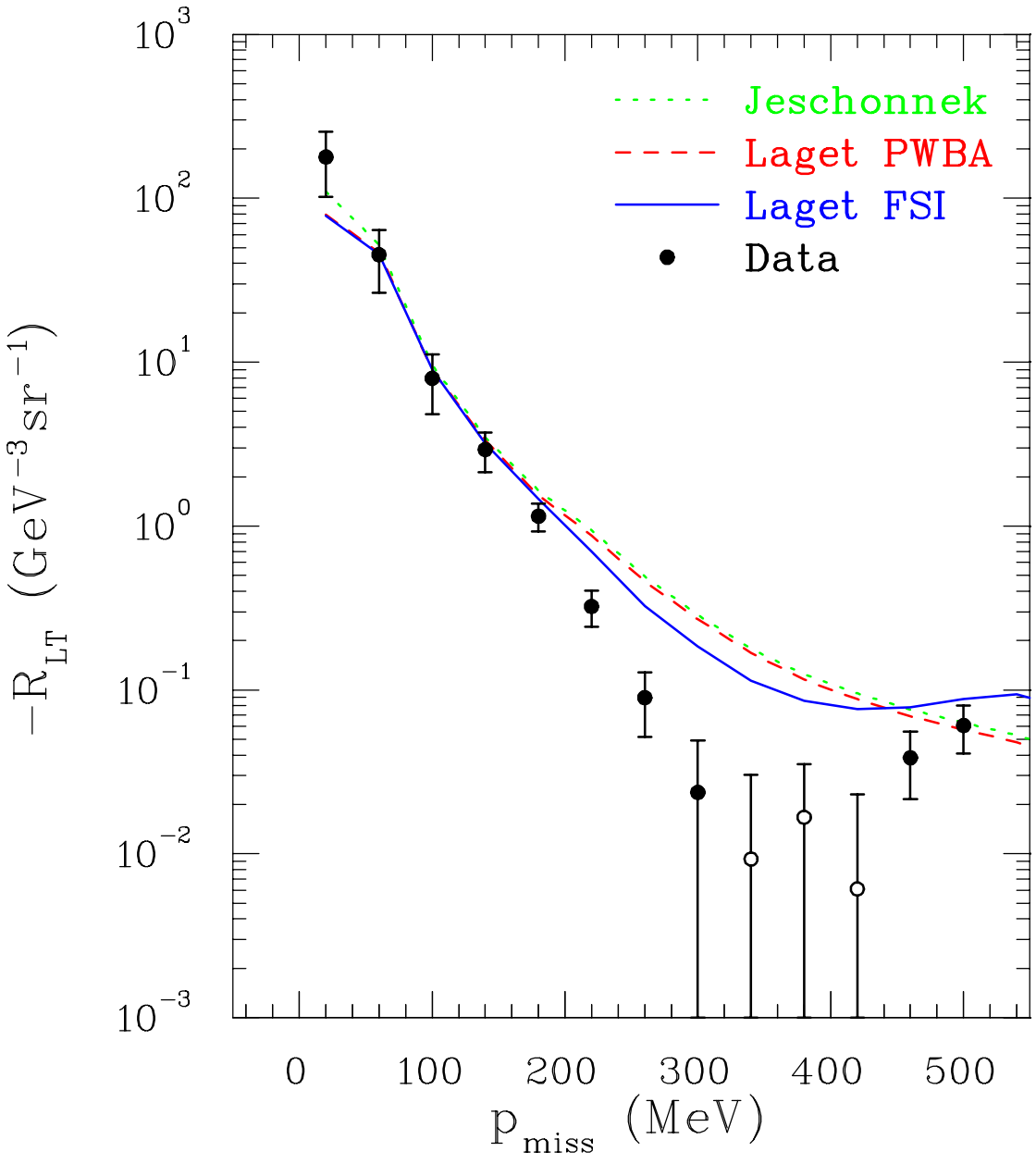

FIG. 97: Longitudinal-Transverse Response Function, R_{LT}, for the single bin scheme. Positive R_{LT} values are shown by open circles. The error bars represent the quadrature sum of the statistical uncertainty and the kinematics dependent systematic uncertainty. A kinematics independent systematic uncertainty of 7% is not shown.

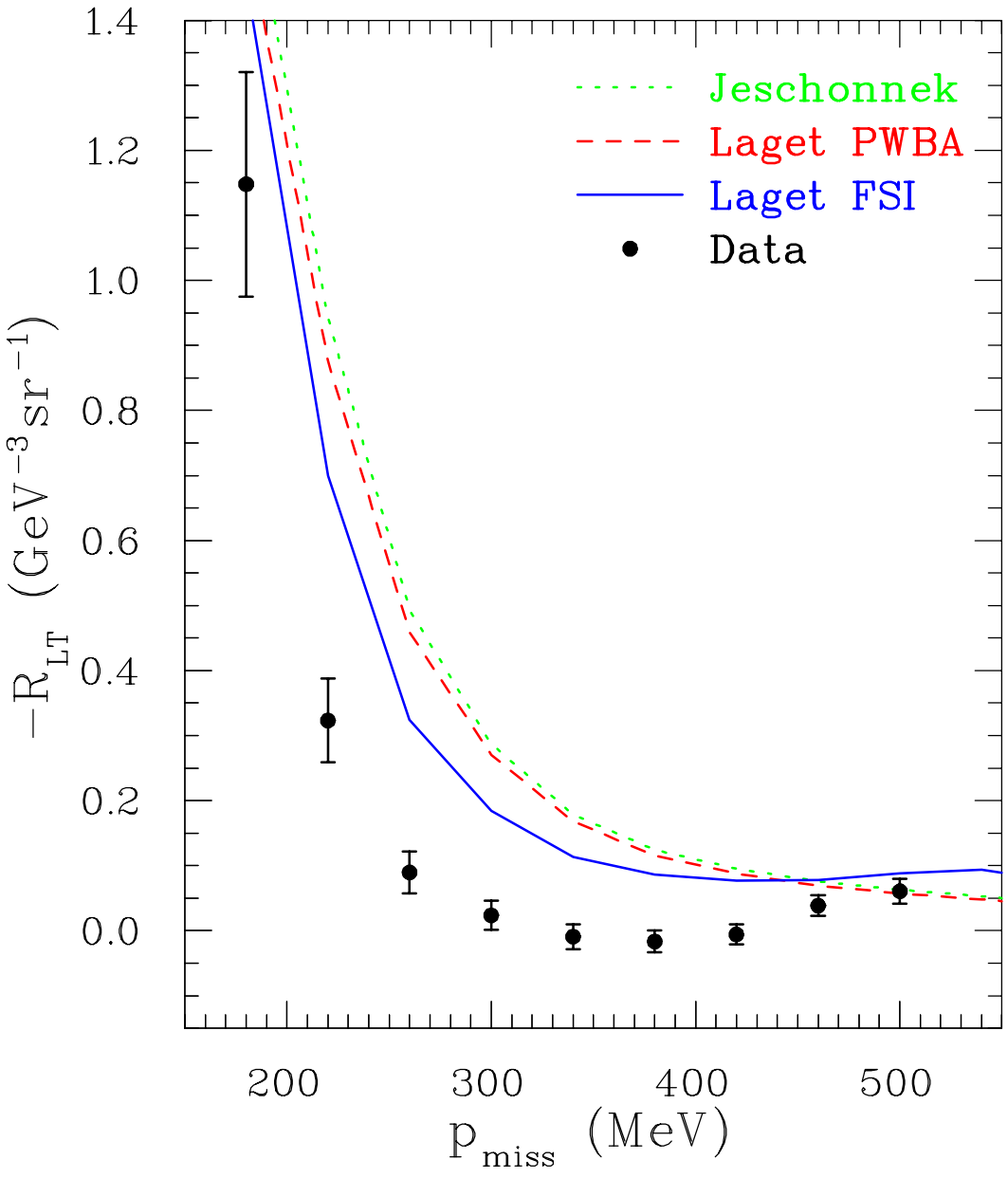

FIG. 98: The R_{LT} response function for the single bin scheme (blow-up of Figure 97). The error bars represent the quadrature sum of the statistical uncertainty and the kinematics dependent systematic uncertainty. A kinematics independent systematic uncertainty of 7% is not shown.

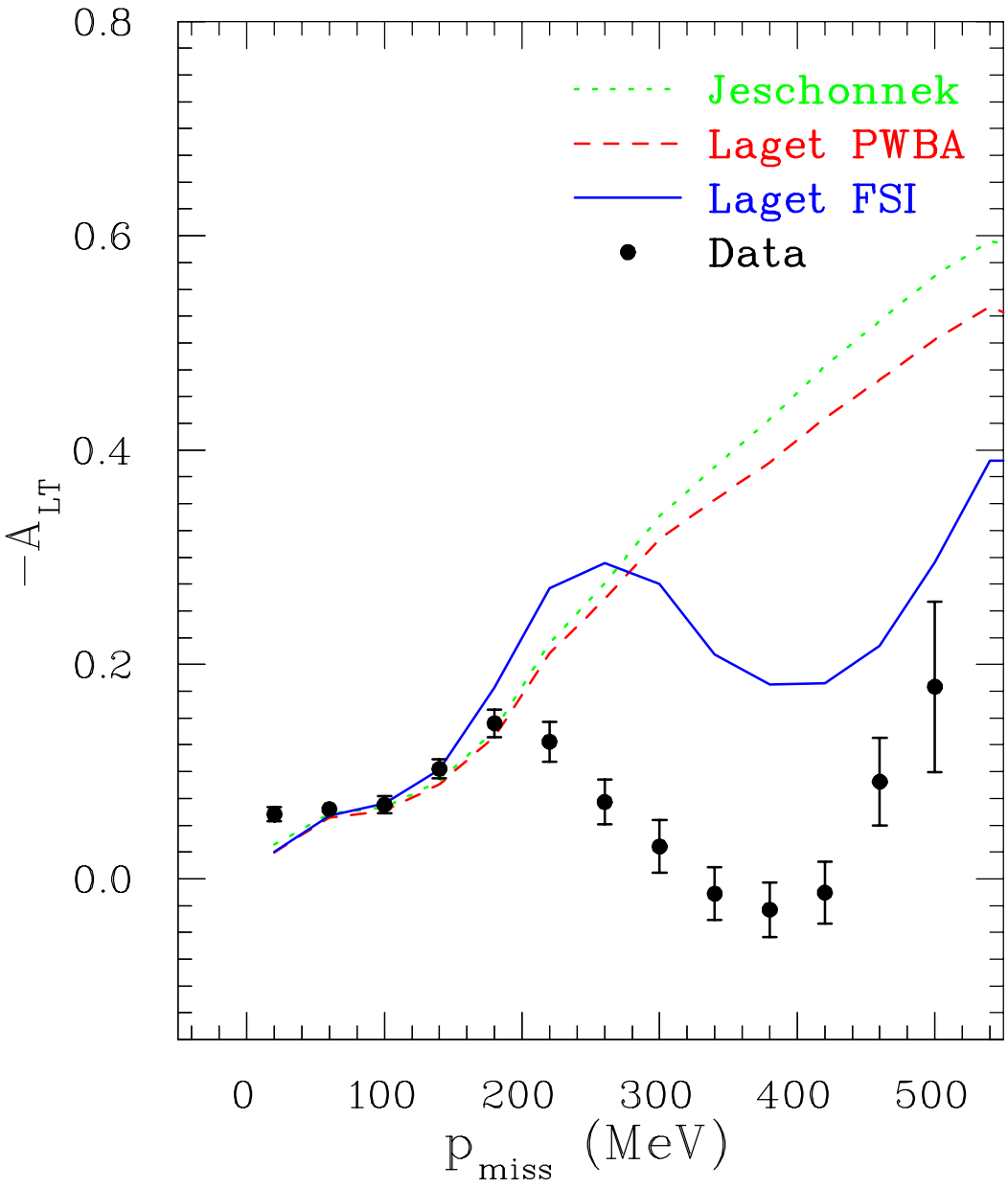

FIG. 99: Longitudinal-Transverse Asymmetry, A_{LT}, for the single bin scheme. The error bars represent the quadrature sum of the statistical uncertainty and the kinematics dependent systematic uncertainty.

TABLE XLII: Results for the single bin scheme. The quoted uncertainty is statistical.

p_{miss} (MeV)	σ (pb MeV^{-1}sr^{-2})	$\delta\sigma$	R_{LT} (GeV^{-3}sr^{-1})	δR_{LT}	A_{LT}	δA_{LT}
20	5.049E+2	2.230E+0	-1.781E+2	1.866E+1	-6.021E-2	6.324E-3
60	1.225E+2	4.594E-1	-4.517E+1	3.804E+0	-6.496E-2	5.490E-3
100	2.176E+1	1.218E-1	-7.960E+0	8.944E-1	-6.906E-2	7.802E-3
140	4.845E+0	3.544E-2	-2.926E+0	2.474E-1	-1.026E-1	8.848E-3
180	1.298E+0	1.396E-2	-1.148E+0	9.556E-2	-1.452E-1	1.269E-2
220	4.235E-1	6.585E-3	-3.230E-1	4.416E-2	-1.278E-1	1.850E-2
260	1.897E-1	3.762E-3	-8.957E-2	2.543E-2	-7.159E-2	2.079E-2
300	1.299E-1	2.892E-3	-2.367E-2	1.929E-2	-3.004E-2	2.464E-2
340	1.043E-1	2.437E-3	9.302E-3	1.640E-2	1.382E-2	2.441E-2
380	8.763E-2	2.121E-3	1.672E-2	1.467E-2	2.878E-2	2.556E-2
420	7.382E-2	1.984E-3	6.092E-3	1.367E-2	1.294E-2	2.913E-2
460	6.857E-2	2.067E-3	-3.859E-2	1.451E-2	-9.062E-2	4.105E-2
500	5.069E-2	2.073E-3	-6.062E-2	1.825E-2	-1.791E-1	7.958E-2
540	5.255E-2	2.589E-3	3.255E-1	1.517E-1	4.522E-1	2.448E-1
580	3.317E-2	2.420E-3	1.805E+1	2.133E+1	9.864E-1	1.472E+0

TABLE XLIII: Reference for the the multi-bin scheme results. p_{miss} refers to the central value for a given bin.

p_{miss}	Figure Number		Table Number	
(MeV)	σ and σ Ratio	R_{LT} and A_{LT}	Multi-bin over Q^2	Multi-bin over W
50	102	108	XLIV	L
150	103	109	XLV	LI
250	104	110	XLVI	LII
350	105	111	XLVII	LIII
450	106	112	XLVIII	LIV
550	107	–	XLIX	LV

VI.2 MULTI-BIN RESULTS

In this section a detailed look at the dependence of the results on Q^2 and W for the multi-bin schemes is provided. The dependence of the Q^2 and W acceptance on p_{miss} for the lowest p_{miss} bin (0–100 MeV) is quite interesting as shown in Figure 100. At very low p_{miss} values, the Q^2 and W acceptance shrinks to a very small region at the central values of Q^2 and W. The dependence of the average missing momentum, $\langle p_{miss} \rangle$, on Q^2 and W for the two multi-bin schemes is shown in Figure 101. From these plots, we can see clearly that the central Q^2 and W values correspond, in average, to low p_{miss}.

A handy reference for all the multi-bin scheme results (plots and tables) is listed in Table XLIII.

VI.2.1 Cross Section

The multi-bin results for the cross section and its ratio are shown in Figures 102-107. In the following paragraphs, each p_{miss} bin result will be discussed.

$p_{miss} = 50$ MeV At this low p_{miss} value, the cross section has a large peak at the center of the Q^2 and W acceptance with an upper limit of about 150 pb MeV^{-1}sr^{-2}. This peak is directly related to the minimum seen in Figure 101 and the fact that the cross section is largest at low p_{miss} (see Figure 95). The cross section ratio exhibits some systematic disagreement which increases at the lower and upper limits of the W acceptance. The cross section ratio varies slightly (0.8–1.0) over the whole Q^2 acceptance.

$\boldsymbol{p_{miss} = 150}$ **MeV** The cross section generally decreases as Q^2 increases for almost all the Q^2 acceptance as expected. The cross section ratio varies slightly (0.6–0.8) over the whole Q^2 and W acceptance.

$\boldsymbol{p_{miss} = 250}$ **MeV** The cross section has a minimum over the Q^2 and W acceptance for this p_{miss} bin. It is interesting to notice that the location of the cross section minimum value over the Q^2 and W acceptance is not predicted precisely by the Laget PWBA+FSI calculation ($\Delta Q^2 \approx 0.1$ GeV and $\Delta W \approx 50$ MeV). A wiggle in the cross section ratio can be seen over the Q^2 acceptance and less significantly over the W acceptance which suggests the need for a "full" theoretical calculation.

$\boldsymbol{p_{miss} = 350}$ **MeV** Theoretical calculations fail to predict the cross section at the high $Q^2$and low W region of the acceptance for this bin.

$\boldsymbol{p_{miss} = 450}$ **MeV** A very reasonable agreement between the data and the Laget PWBA+ FSI calculation is present for this p_{miss} bin. The cross section generally decreases as Q^2 increases and increases as W increases for almost the whole Q^2 and W acceptance. The cross section ratio varies (0.8-1.2) over the Q^2 and W acceptance which again suggests the need for a better theoretical calculation that takes into account the other reaction mechanisms such as MEC and IC.

$\boldsymbol{p_{miss} = 550}$ **MeV** There is some agreement between the data and the Laget PWBA+FSI calculation for this high p_{miss} bin, but there is no obvious theoretical prediction of the cross section variations over the Q^2 and W acceptance in this case.

VI.2.2 R_{LT} Response Function and A_{LT} Asymmetry

The multi-bin results for the R_{LT} response function and A_{LT} asymmetry are shown in Figures 108-112. In the following paragraphs, each p_{miss} bin result will be discussed.

$\boldsymbol{p_{miss} = 50}$ **MeV** Both the R_{LT} response function and A_{LT} asymmetry features are grossly reproduced by all the theoretical calculations for this p_{miss} bin. At this low p_{miss} value, R_{LT} and A_{LT} vary rapidly over the available Q^2 and W acceptance.

$\boldsymbol{p_{miss} = 150}$ **MeV** Both the R_{LT} response function and A_{LT} asymmetry variations are still reasonably predicted by all the theoretical calculations for this p_{miss} bin. In this case, R_{LT} and A_{LT} vary less rapidly over the whole Q^2 and W acceptance than they did for $p_{miss} = 50$ MeV.

$\boldsymbol{p_{miss} = 250}$ **MeV** Both the R_{LT} response function and A_{LT} asymmetry variations are reasonably predicted by the Laget PWBA+FSI calculation which indicates some FSI contribution for this p_{miss} bin. On the other hand, the values of $-R_{LT}$ and $-A_{LT}$ are underestimated by all the theoretical calculations.

$\boldsymbol{p_{miss} = 350}$ **MeV** Both the R_{LT} response function and A_{LT} asymmetry variations are predicted slightly better by the Laget PWBA+FSI calculation for this p_{miss} bin but the values are underestimated by all the theoretical calculations. In this case, R_{LT} and A_{LT} values are consistent with zero over the whole Q^2 and W acceptance.

$\boldsymbol{p_{miss} = 450}$ **MeV** All the theoretical calculations fail to predict the variations of the R_{LT} response function over the Q^2 acceptance for this p_{miss} bin. In this case also, R_{LT} and A_{LT} values are almost consistent with zero over the whole Q^2 and W acceptance.

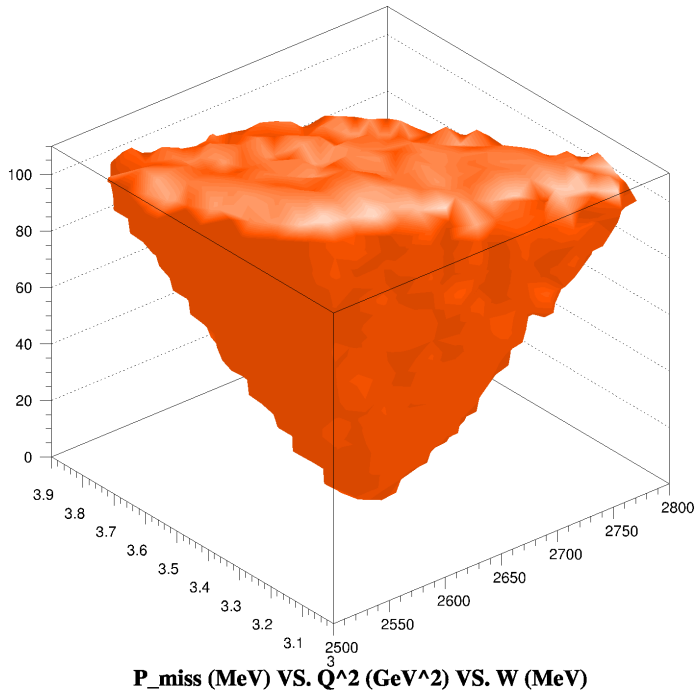

FIG. 100: The dependence of the missing momentum, p_{miss}, on Q^2 and W for the lowest p_{miss} bin ($0 < p_{miss} < 100$ MeV).

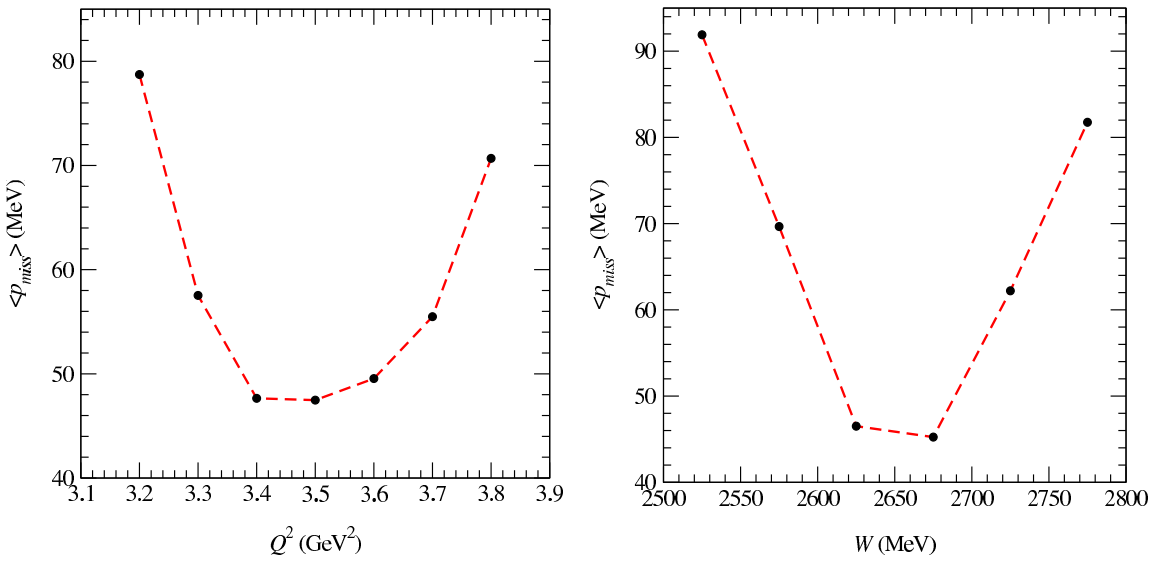

(a) Mult-bin scheme over Q^2.

(b) Mult-bin scheme over W.

FIG. 101: The dependence of the average missing momentum, $\langle p_{miss} \rangle$, on Q^2 and W for the lowest p_{miss} bin ($0 < p_{miss} < 100$ MeV).

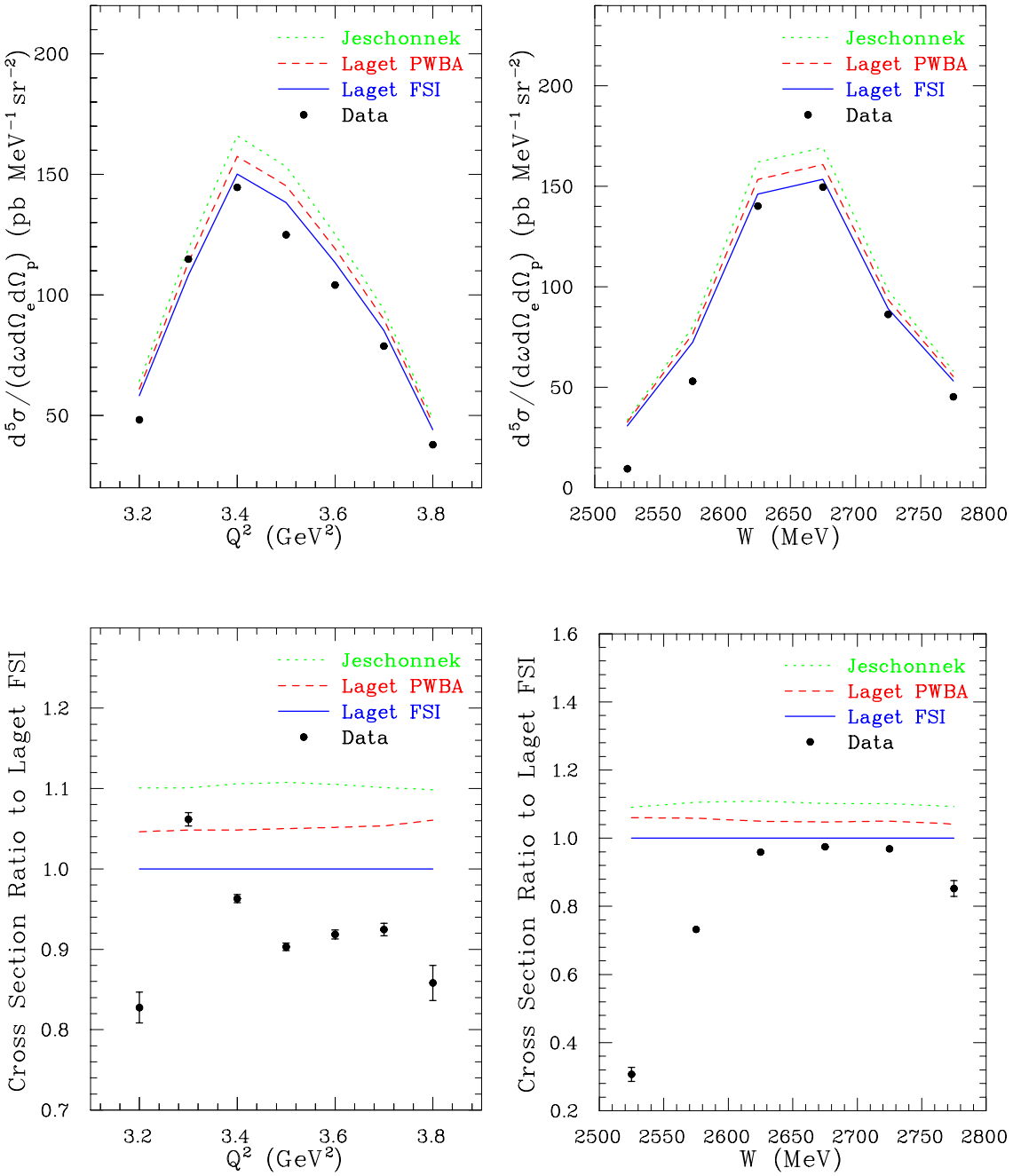

FIG. 102: Multi-bin results for the cross section and its ratio at $p_{miss} = 50$ MeV. A kinematics independent systematic uncertainty of 7% for the cross section and its ratio is not shown.

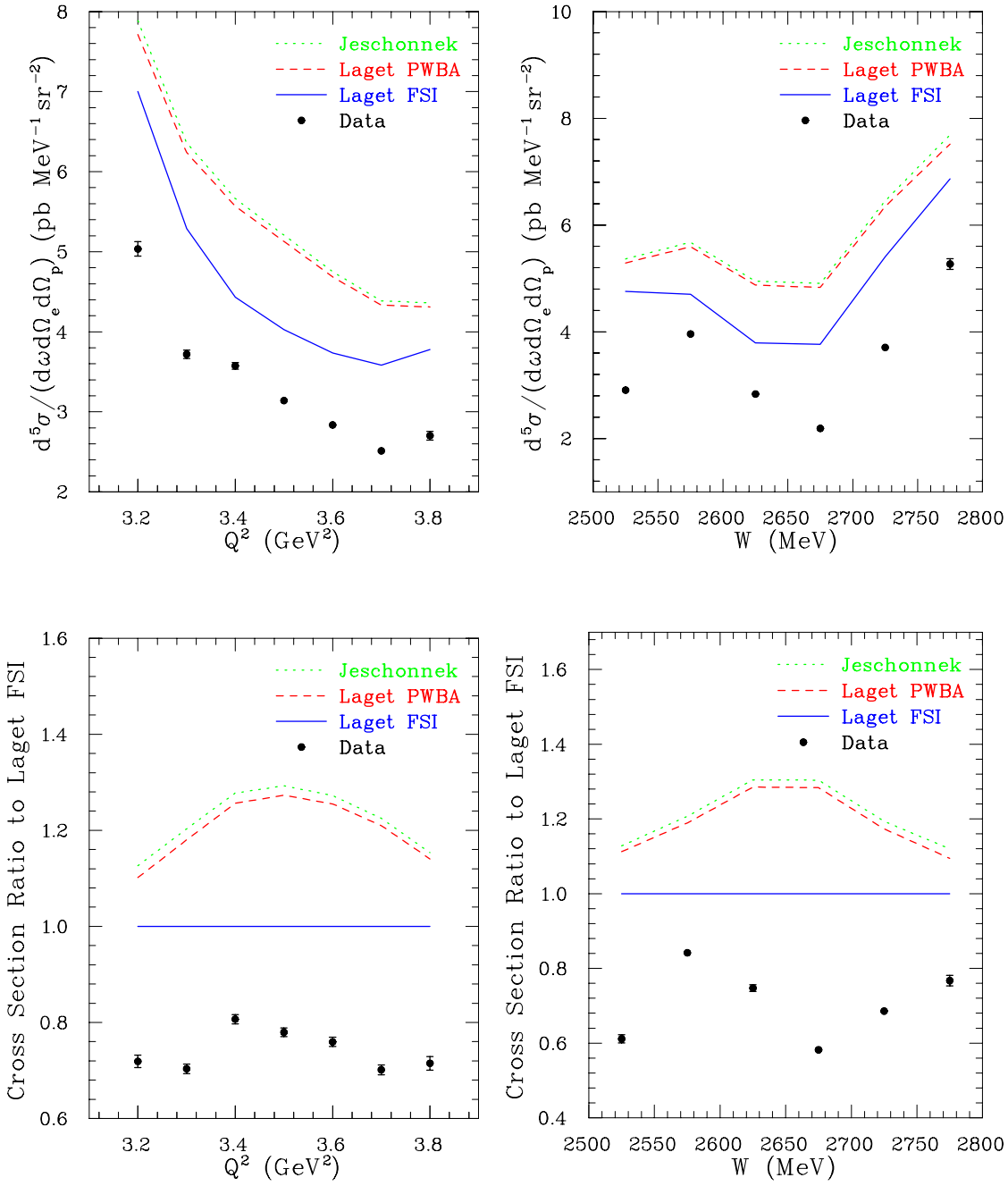

FIG. 103: Multi-bin results for the cross section and its ratio at $p_{miss} = 150$ MeV. A kinematics independent systematic uncertainty of 7% for the cross section and its ratio is not shown.

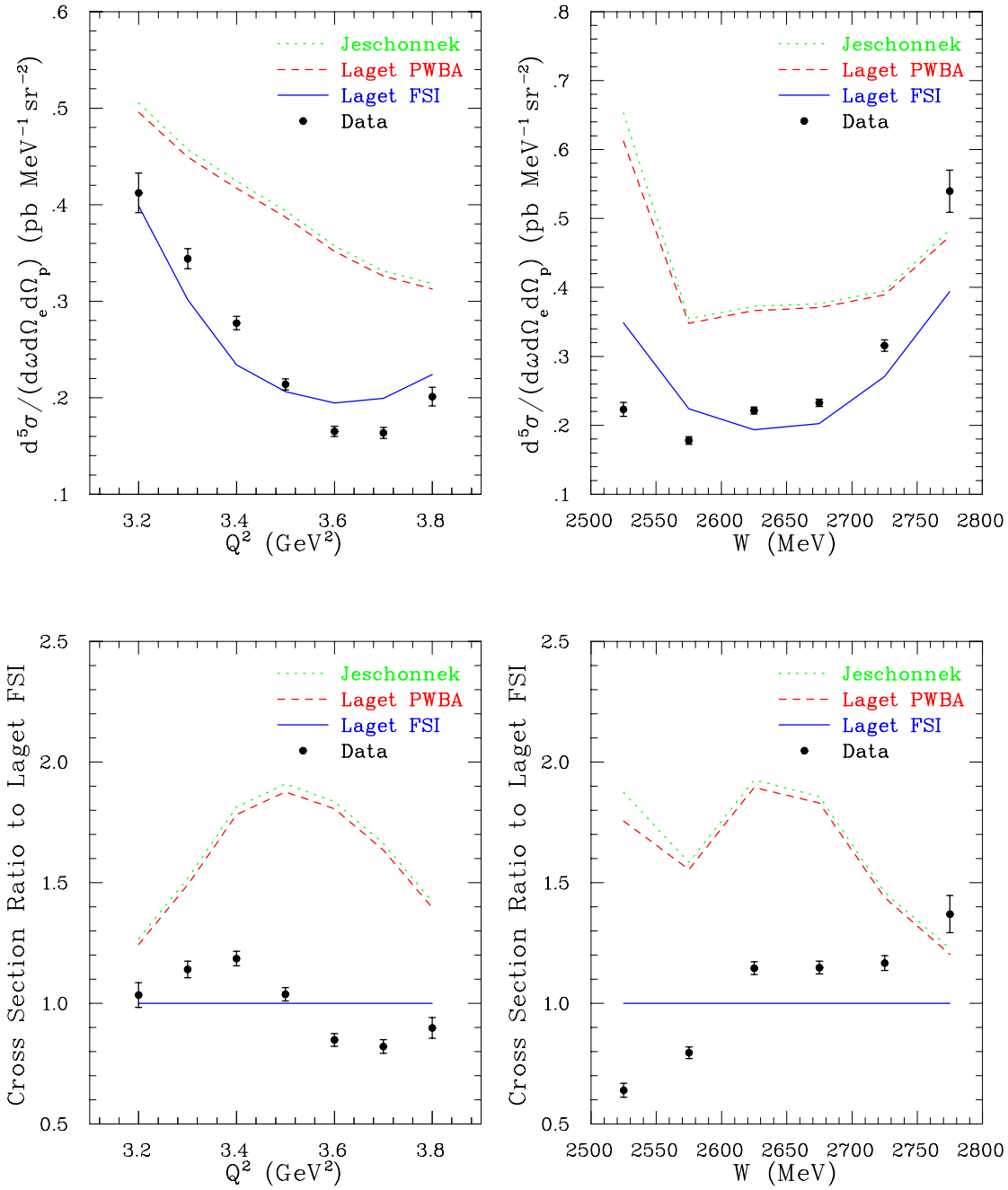

FIG. 104: Multi-bin results for the cross section and its ratio at $p_{miss} = 250$ MeV. A kinematics independent systematic uncertainty of 7% for the cross section and its ratio is not shown.

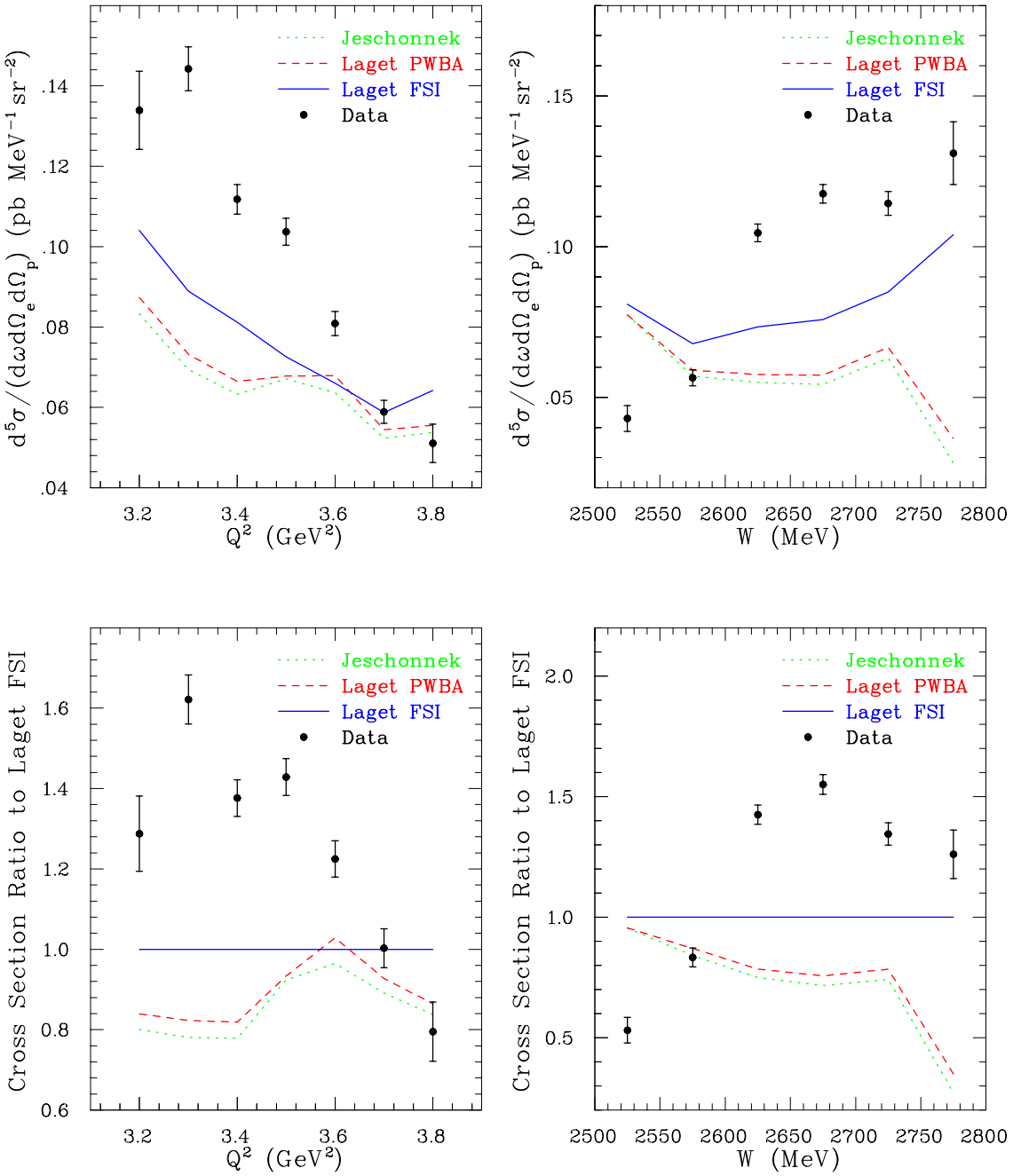

FIG. 105: Multi-bin results for the cross section and its ratio at $p_{miss} = 350$ MeV. A kinematics independent systematic uncertainty of 7% for the cross section and its ratio is not shown.

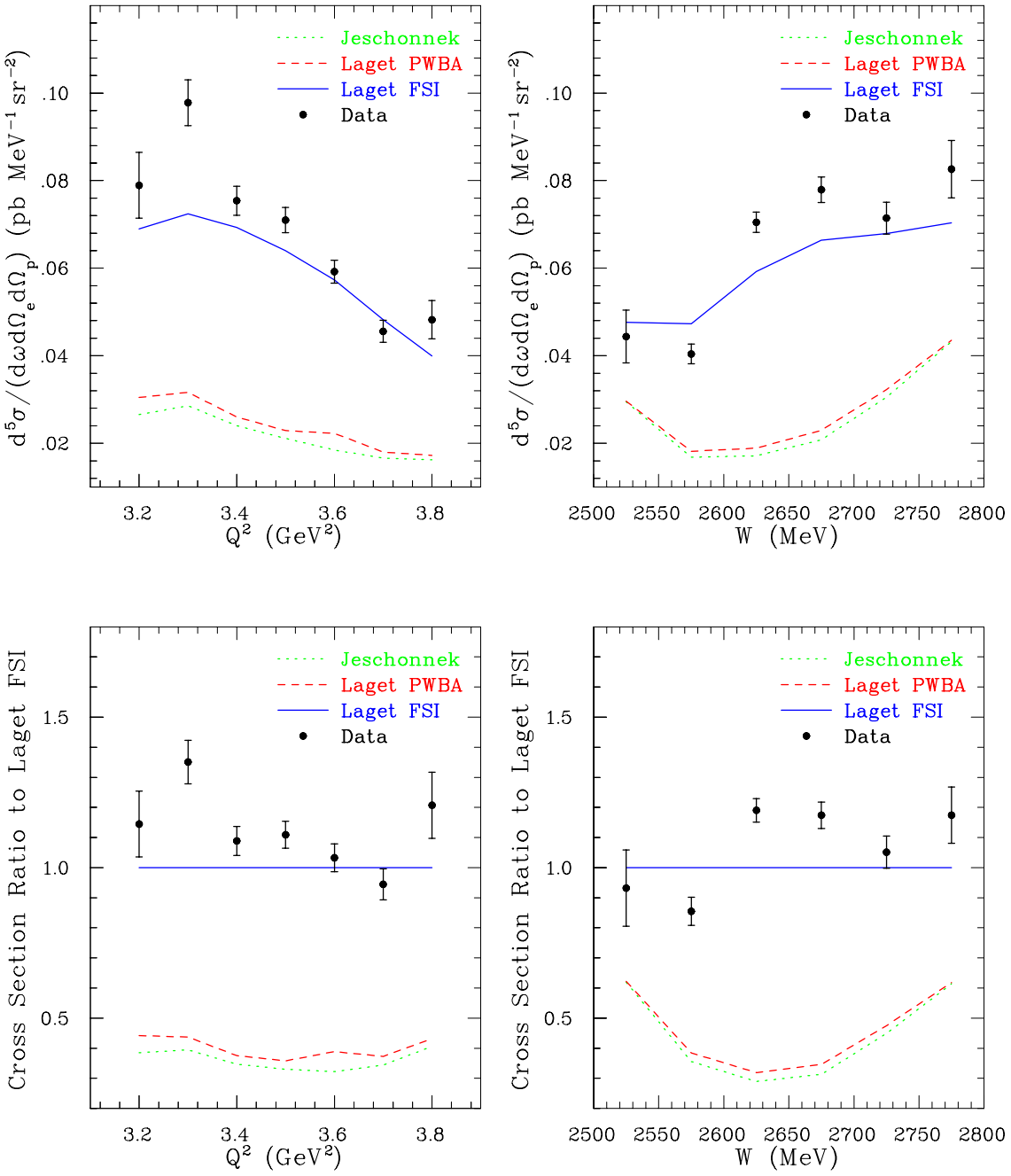

FIG. 106: Multi-bin results for the cross section and its ratio at $p_{miss} = 450$ MeV. A kinematics independent systematic uncertainty of 7% for the cross section and its ratio is not shown.

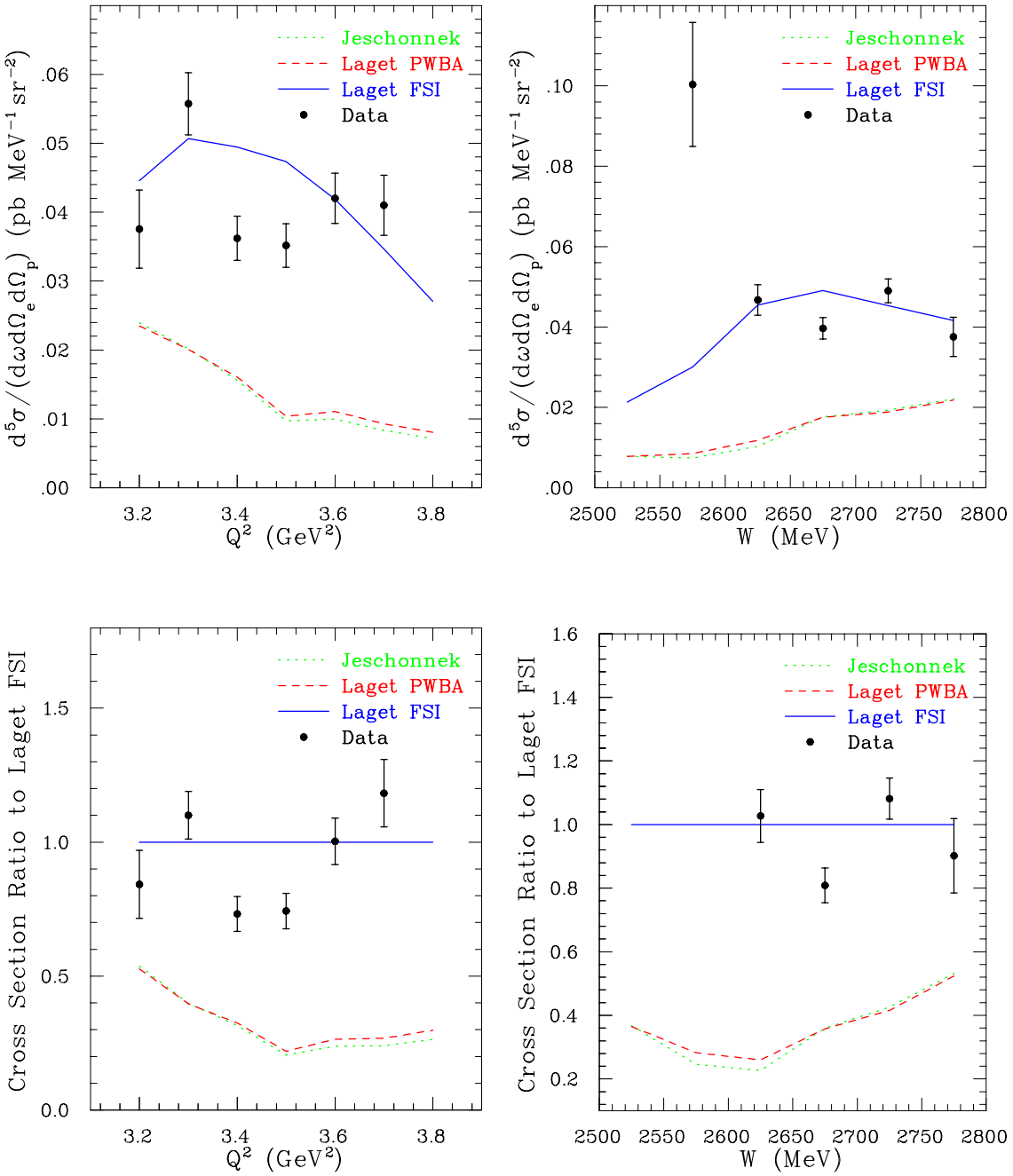

FIG. 107: Multi-bin results for the cross section and its ratio at $p_{miss} = 550$ MeV. A kinematics independent systematic uncertainty of 7% for the cross section and its ratio is not shown.

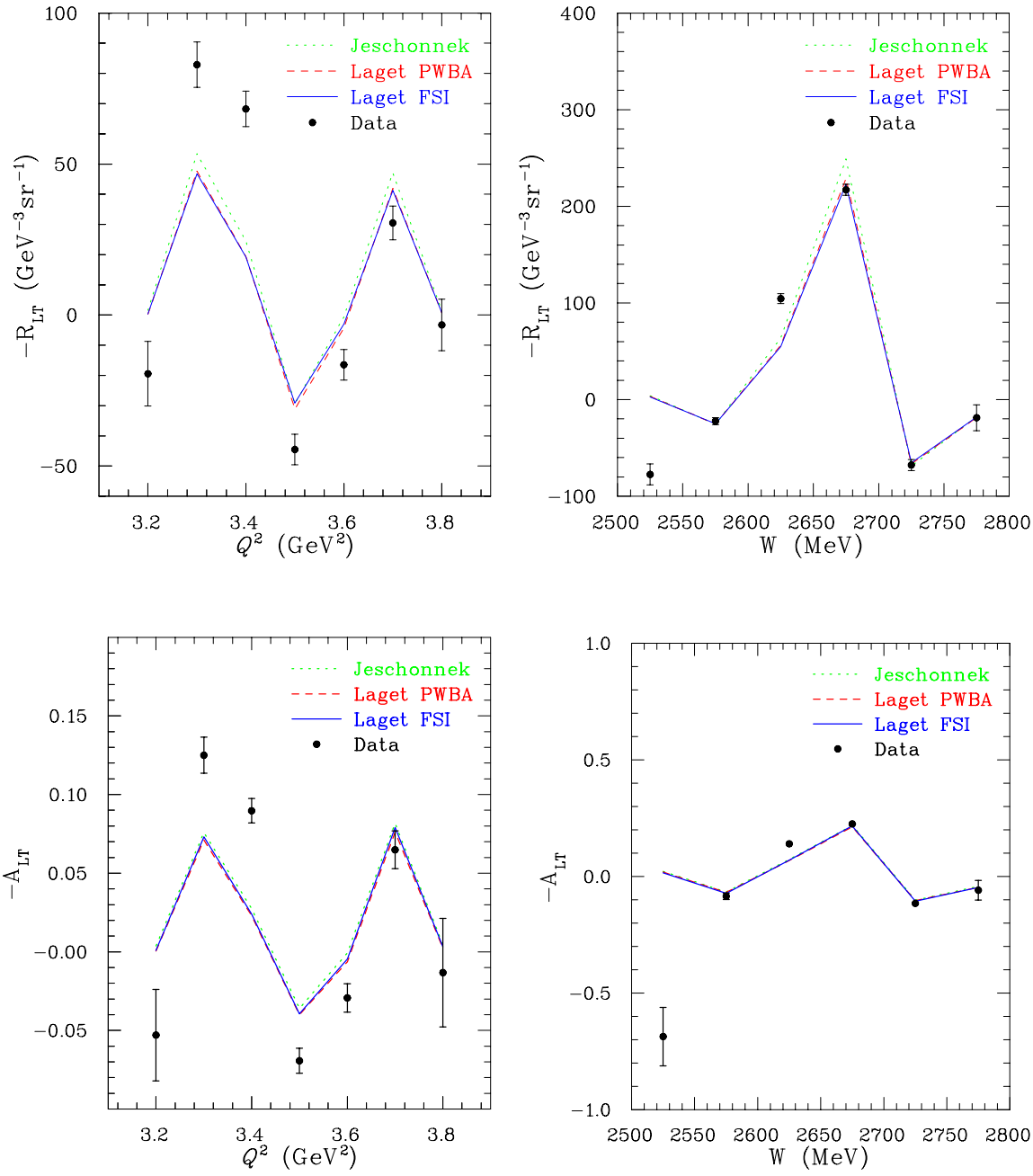

FIG. 108: Multi-bin results for the R_{LT} response function and the A_{LT} asymmetry at $p_{miss} = 50$ MeV. A total systematic uncertainty of 7% for R_{LT} is not shown.

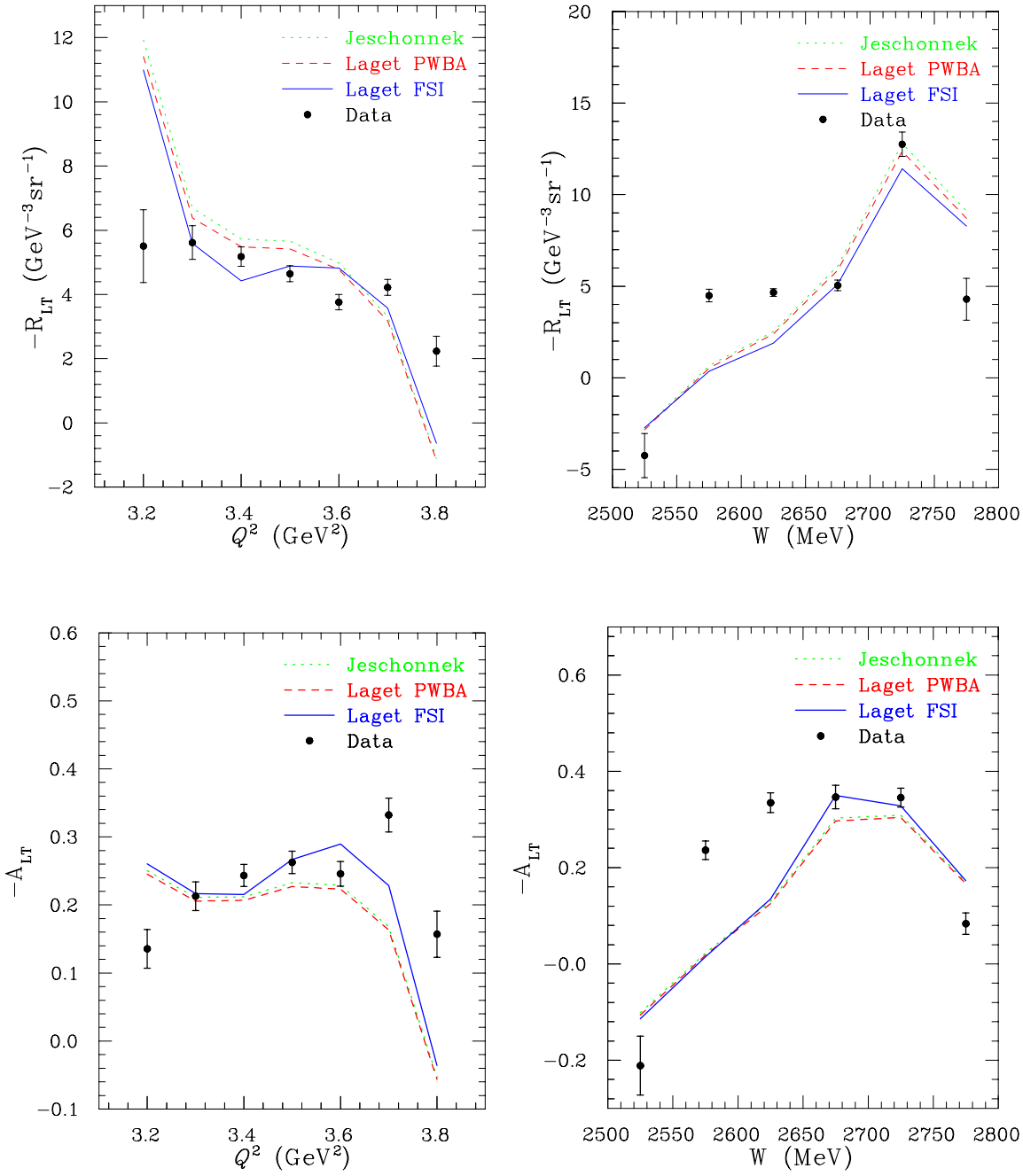

FIG. 109: Multi-bin results for the R_{LT} response function and the A_{LT} asymmetry at $p_{miss} = 150$ MeV. A kinematics independent systematic uncertainty of 7% for R_{LT} is not shown.

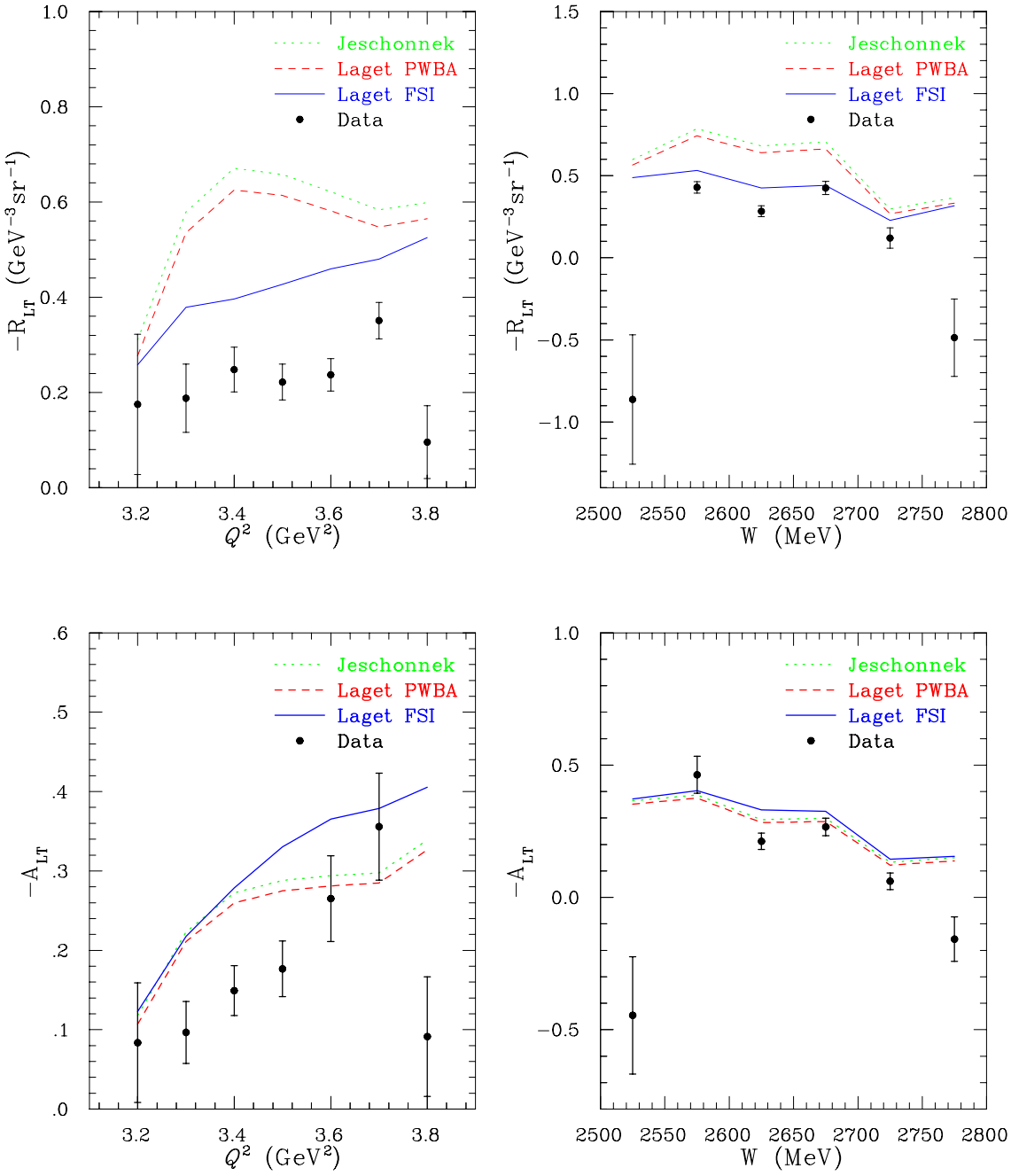

FIG. 110: Multi-bin results for the R_{LT} response function and the A_{LT} asymmetry at $p_{miss} = 250$ MeV. A kinematics independent systematic uncertainty of 7% for R_{LT} is not shown.

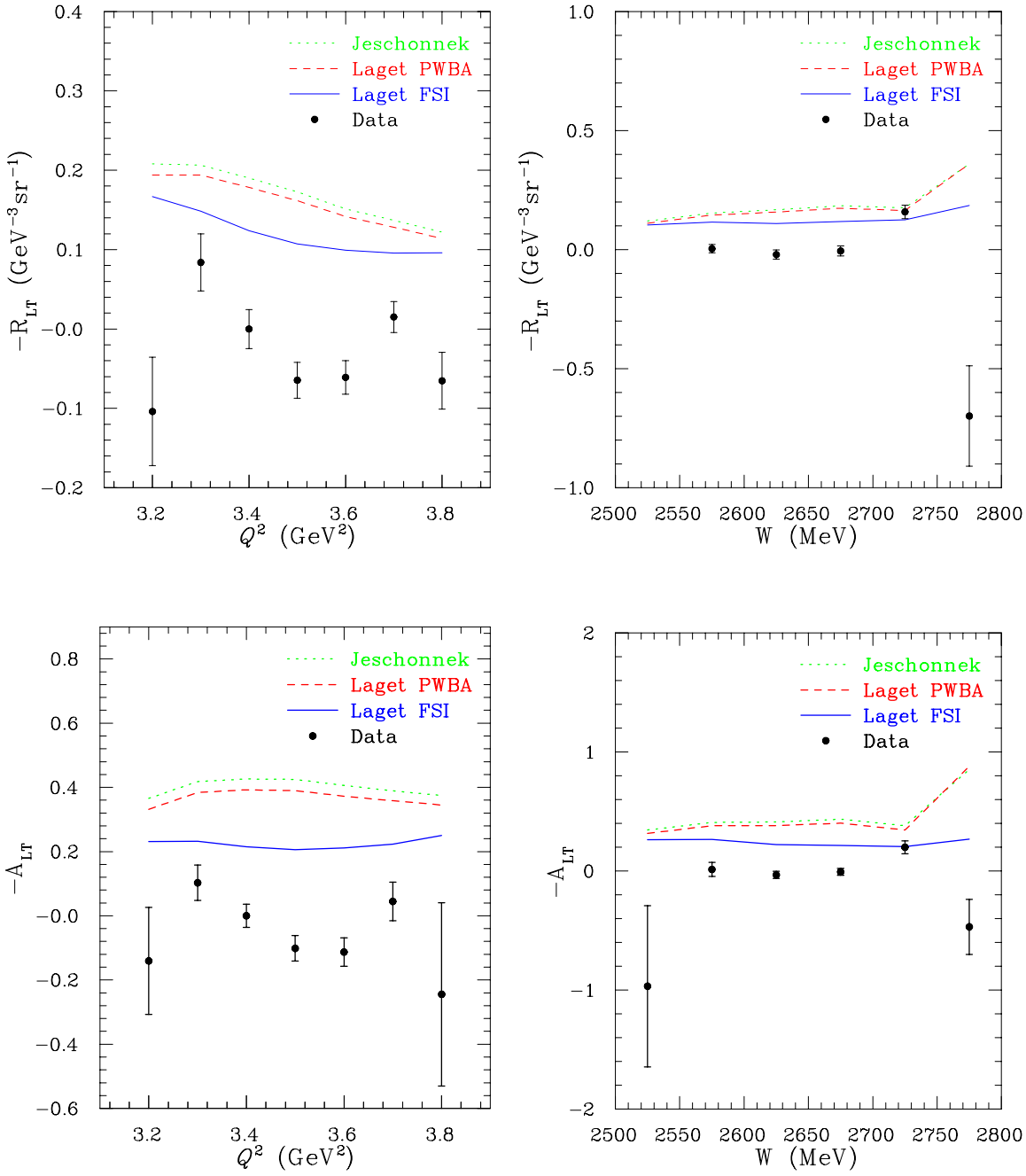

FIG. 111: Multi-bin results for the R_{LT} response function and the A_{LT} asymmetry at $p_{miss} = 350$ MeV. A kinematics independent systematic uncertainty of 7% for R_{LT} is not shown.

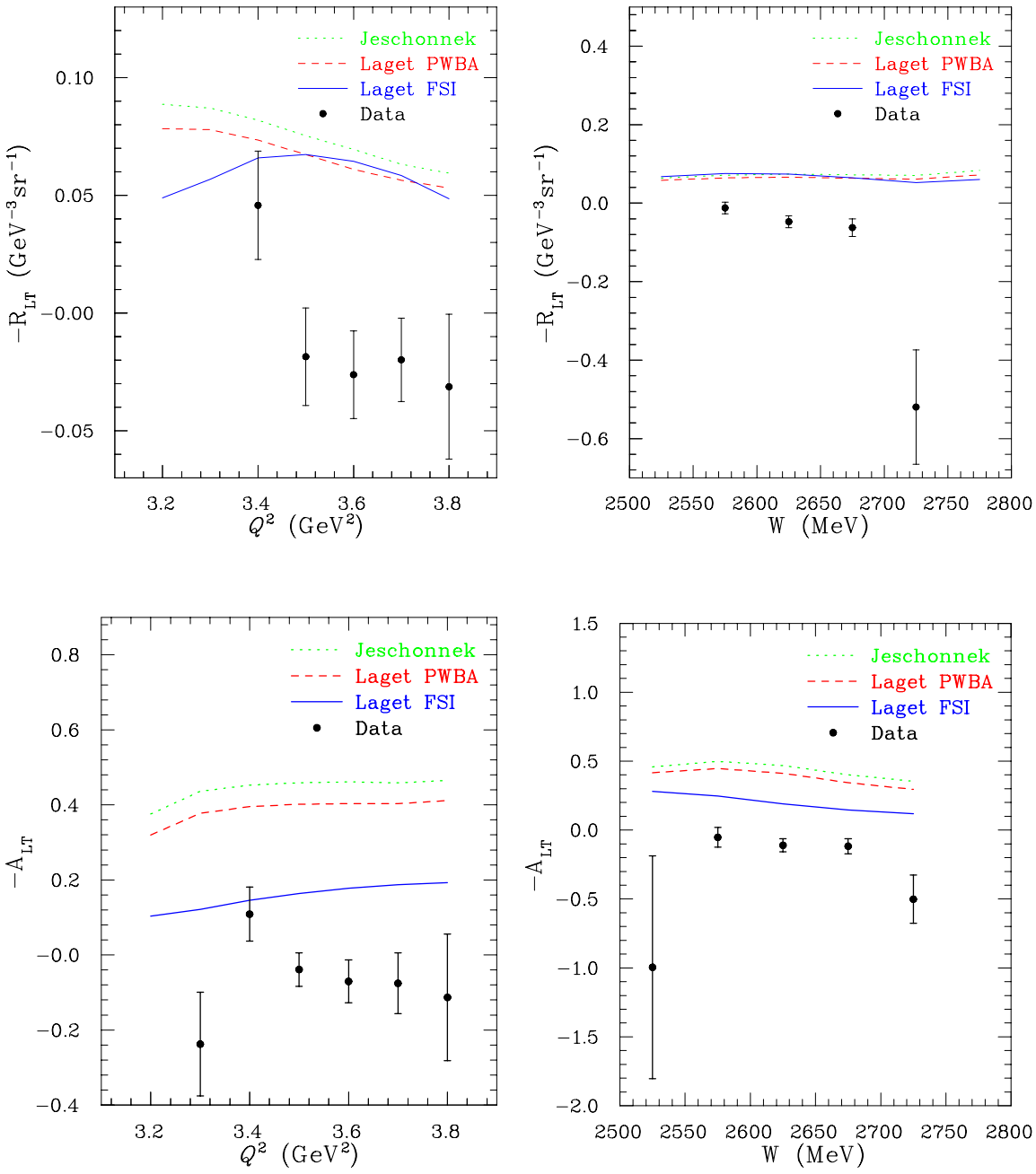

FIG. 112: Multi-bin results for the R_{LT} response function and the A_{LT} asymmetry at $p_{miss} = 450$ MeV. A kinematics independent systematic uncertainty of 7% for R_{LT}.

TABLE XLIV: Results for the multi-bin scheme over Q^2 at $p_{miss} = 50$ MeV. The quoted uncertainty is statistical.

Q^2 (GeV^2)	σ (pb MeV^{-1}sr^{-2})	$\delta\sigma$	R_{LT} (GeV^{-3}sr^{-1})	δR_{LT}	A_{LT}	δA_{LT}
3.2	4.820E+1	1.119E+0	1.943E+1	1.065E+1	5.297E-2	2.910E-2
3.3	1.148E+2	9.095E-1	-8.289E+1	7.518E+0	-1.250E-1	1.147E-2
3.4	1.446E+2	7.526E-1	-6.824E+1	5.859E+0	-8.965E-2	7.751E-3
3.5	1.249E+2	6.467E-1	4.453E+1	5.088E+0	6.932E-2	7.957E-3
3.6	1.041E+2	6.229E-1	1.647E+1	5.060E+0	2.930E-2	9.010E-3
3.7	7.877E+1	6.526E-1	-3.049E+1	5.612E+0	-6.487E-2	1.198E-2
3.8	3.789E+1	9.635E-1	3.278E+0	8.537E+0	1.326E-2	3.453E-2

TABLE XLV: Results for the multi-bin scheme over Q^2 at $p_{miss} = 150$ MeV. The quoted uncertainty is statistical.

Q^2 (GeV^2)	σ (pb MeV^{-1}sr^{-2})	$\delta\sigma$	R_{LT} (GeV^{-3}sr^{-1})	δR_{LT}	A_{LT}	δA_{LT}
3.2	5.035E+0	9.064E-2	-5.504E+0	1.133E+0	-1.355E-1	2.828E-2
3.3	3.720E+0	5.241E-2	-5.613E+0	5.235E-1	-2.129E-1	2.104E-2
3.4	3.575E+0	4.179E-2	-5.178E+0	3.021E-1	-2.432E-1	1.623E-2
3.5	3.140E+0	3.644E-2	-4.642E+0	2.476E-1	-2.626E-1	1.649E-2
3.6	2.836E+0	3.560E-2	-3.758E+0	2.410E-1	-2.458E-1	1.820E-2
3.7	2.512E+0	3.659E-2	-4.218E+0	2.487E-1	-3.322E-1	2.478E-2
3.8	2.702E+0	5.361E-2	-2.233E+0	4.666E-1	-1.570E-1	3.378E-2

TABLE XLVI: Results for the multi-bin scheme over Q^2 at $p_{miss} = 250$ MeV. The quoted uncertainty is statistical.

Q^2 (GeV^2)	σ (pb MeV^{-1}sr^{-2})	$\delta\sigma$	R_{LT} (GeV^{-3}sr^{-1})	δR_{LT}	A_{LT}	δA_{LT}
3.2	4.123E-1	2.052E-2	-1.751E-1	1.473E-1	-8.360E-2	7.531E-2
3.3	3.440E-1	1.038E-2	-1.880E-1	7.151E-2	-9.663E-2	3.901E-2
3.4	2.774E-1	7.052E-3	-2.481E-1	4.681E-2	-1.492E-1	3.152E-2
3.5	2.140E-1	5.722E-3	-2.218E-1	3.769E-2	-1.767E-1	3.516E-2
3.6	1.652E-1	5.157E-3	-2.371E-1	3.393E-2	-2.652E-1	5.394E-2
3.7	1.636E-1	5.630E-3	-3.509E-1	3.831E-2	-3.558E-1	6.722E-2
3.8	2.012E-1	9.609E-3	-9.577E-2	7.664E-2	-9.139E-2	7.538E-2

TABLE XLVII: Results for the multi-bin scheme over Q^2 at $p_{miss} = 350$ MeV. The quoted uncertainty is statistical.

Q^2 (GeV^2)	σ (pb MeV^{-1}sr^{-2})	$\delta\sigma$	R_{LT} (GeV^{-3}sr^{-1})	δR_{LT}	A_{LT}	δA_{LT}
3.2	1.339E-1	9.754E-3	1.040E-1	6.827E-2	1.406E-1	1.665E-1
3.3	1.442E-1	5.456E-3	-8.385E-2	3.594E-2	-1.029E-1	5.534E-2
3.4	1.118E-1	3.702E-3	4.587E-5	2.458E-2	6.798E-5	3.643E-2
3.5	1.037E-1	3.328E-3	6.454E-2	2.265E-2	1.014E-1	3.969E-2
3.6	8.087E-2	2.997E-3	6.096E-2	2.112E-2	1.130E-1	4.465E-2
3.7	5.890E-2	2.840E-3	-1.504E-2	1.951E-2	-4.461E-2	5.964E-2
3.8	5.107E-2	4.743E-3	6.527E-2	3.582E-2	2.446E-1	2.853E-1

TABLE XLVIII: Results for the multi-bin scheme over Q^2 at $p_{miss} = 450$ MeV. The quoted uncertainty is statistical.

Q^2 (GeV^2)	σ (pb MeV^{-1}sr^{-2})	$\delta\sigma$	R_{LT} (GeV^{-3}sr^{-1})	δR_{LT}	A_{LT}	δA_{LT}
3.2	7.893E-2	7.545E-3	9.762E+0	6.686E+0	9.564E-1	8.215E-1
3.3	9.780E-2	5.230E-3	1.719E-1	6.212E-2	2.377E-1	1.381E-1
3.4	7.542E-2	3.315E-3	-4.572E-2	2.300E-2	-1.087E-1	7.214E-2
3.5	7.096E-2	2.880E-3	1.853E-2	2.073E-2	3.869E-2	4.466E-2
3.6	5.920E-2	2.630E-3	2.619E-2	1.860E-2	7.051E-2	5.707E-2
3.7	4.557E-2	2.504E-3	1.987E-2	1.767E-2	7.551E-2	8.125E-2
3.8	4.821E-2	4.379E-3	3.128E-2	3.073E-2	1.133E-1	1.687E-1

TABLE XLIX: Results for the multi-bin scheme over Q^2 at $p_{miss} = 550$ MeV. The quoted uncertainty is statistical.

Q^2 (GeV^2)	σ (pb MeV^{-1}sr^{-2})	$\delta\sigma$
3.2	3.755E-2	5.672E-3
3.3	5.574E-2	4.500E-3
3.4	3.621E-2	3.215E-3
3.5	3.517E-2	3.151E-3
3.6	4.201E-2	3.629E-3
3.7	4.100E-2	4.367E-3
3.8	1.153E-1	2.271E-2

TABLE L: Results for the multi-bin scheme over W at $p_{miss} = 50$ MeV. The quoted uncertainty is statistical.

W (MeV)	σ (pb MeV^{-1}sr^{-2})	$\delta\sigma$	R_{LT} (GeV^{-3}sr^{-1})	δR_{LT}	A_{LT}	δA_{LT}
2525	9.472E+0	6.432E-1	7.742E+1	1.090E+1	6.863E-1	1.253E-1
2575	5.304E+1	4.800E-1	2.228E+1	3.551E+0	8.475E-2	1.361E-2
2625	1.402E+2	6.428E-1	-1.045E+2	5.204E+0	-1.399E-1	7.073E-3
2675	1.497E+2	6.345E-1	-2.170E+2	5.746E+0	-2.250E-1	6.187E-3
2725	8.626E+1	6.204E-1	6.774E+1	5.720E+0	1.153E-1	9.838E-3
2775	4.531E+1	1.238E+0	1.877E+1	1.339E+1	5.915E-2	4.227E-2

TABLE LI: Results for the multi-bin scheme over W at $p_{miss} = 150$ MeV. The quoted uncertainty is statistical.

W (MeV)	σ (pb MeV^{-1}sr^{-2})	$\delta\sigma$	R_{LT} (GeV^{-3}sr^{-1})	δR_{LT}	A_{LT}	δA_{LT}
2525	2.907E+0	5.137E-2	4.241E+0	1.203E+0	2.113E-1	6.103E-2
2575	3.958E+0	3.973E-2	-4.489E+0	3.453E-1	-2.362E-1	1.936E-2
2625	2.834E+0	3.356E-2	-4.659E+0	2.150E-1	-3.348E-1	2.067E-2
2675	2.190E+0	2.873E-2	-5.044E+0	2.880E-1	-3.463E-1	2.440E-2
2725	3.707E+0	4.191E-2	-1.275E+1	6.635E-1	-3.453E-1	1.949E-2
2775	5.269E+0	9.902E-2	-4.296E+0	1.142E+0	-8.342E-2	2.231E-2

TABLE LII: Results for the multi-bin scheme over W at $p_{miss} = 250$ MeV. The quoted uncertainty is statistical.

W (MeV)	σ (pb MeV^{-1}sr^{-2})	$\delta\sigma$	R_{LT} (GeV^{-3}sr^{-1})	δR_{LT}	A_{LT}	δA_{LT}
2525	2.231E-1	1.003E-2	8.626E-1	3.941E-1	4.457E-1	2.217E-1
2575	1.781E-1	5.418E-3	-4.290E-1	3.479E-2	-4.634E-1	6.987E-2
2625	2.215E-1	5.092E-3	-2.834E-1	3.333E-2	-2.119E-1	3.086E-2
2675	2.326E-1	5.397E-3	-4.246E-1	4.022E-2	-2.664E-1	3.329E-2
2725	3.157E-1	8.291E-3	-1.204E-1	6.175E-2	-6.089E-2	3.183E-2
2775	5.396E-1	3.042E-2	4.862E-1	2.356E-1	1.579E-1	8.405E-2

TABLE LIII: Results for the multi-bin scheme over W at $p_{miss} = 350$ MeV. The quoted uncertainty is statistical.

W (MeV)	σ (pb MeV^{-1}sr^{-2})	$\delta\sigma$	R_{LT} (GeV^{-3}sr^{-1})	δR_{LT}	A_{LT}	δA_{LT}
2525	4.301E-2	4.272E-3	5.916E+0	3.294E+0	9.682E-1	6.764E-1
2575	5.650E-2	2.666E-3	-3.693E-3	1.748E-2	-1.234E-2	5.855E-2
2625	1.045E-1	2.936E-3	2.091E-2	1.906E-2	3.323E-2	3.071E-2
2675	1.175E-1	3.109E-3	5.998E-3	2.124E-2	8.114E-3	2.876E-2
2725	1.143E-1	3.943E-3	-1.583E-1	2.830E-2	-1.985E-1	5.410E-2
2775	1.310E-1	1.040E-2	6.988E-1	2.111E-1	4.701E-1	2.307E-1

TABLE LIV: Results for the multi-bin scheme over W at $p_{miss} = 450$ MeV. The quoted uncertainty is statistical.

W (MeV)	σ (pb MeV^{-1}sr^{-2})	$\delta\sigma$	R_{LT} (GeV^{-3}sr^{-1})	δR_{LT}	A_{LT}	δA_{LT}
2525	4.438E-2	6.038E-3	5.935E+1	3.805E+1	9.956E-1	8.089E-1
2575	4.041E-2	2.227E-3	1.223E-2	1.508E-2	5.225E-2	7.143E-2
2625	7.048E-2	2.305E-3	4.724E-2	1.505E-2	1.103E-1	4.763E-2
2675	7.791E-2	2.897E-3	6.226E-2	2.244E-2	1.174E-1	5.512E-2
2725	7.142E-2	3.646E-3	5.196E-1	1.455E-1	5.014E-1	1.749E-1
2775	8.261E-2	6.585E-3	-2.902E+0	5.224E+1	1.216E+0	3.019E+1

TABLE LV: Results for the multi-bin scheme over W at $p_{miss} = 550$ MeV. The quoted uncertainty is statistical.

W (MeV)	σ (pb MeV^{-1}sr^{-2})	$\delta\sigma$
2525	4.561E-1	2.202E-1
2575	1.003E-1	1.543E-2
2625	4.673E-2	3.776E-3
2675	3.966E-2	2.687E-3
2725	4.901E-2	2.936E-3
2775	3.756E-2	4.870E-3

VI.3 CONCLUSIONS

The ^{2}H$(e,e'p)n$ reaction coincidence cross section for Q^2= 3.5 GeV^2, $x_{Bj} = 1$, and p_{miss} values between 0.0 and 0.5 GeV was extracted from the collected E01-020 data. An extraction of R_{LT} and A_{LT} was performed on the top of the quasielastic peak ($x_{Bj} = 1$) over the available range of recoil momentum to test the validity of the relativistic models used for the theoretical calculations in this work: Jeschonnek PWBA, and Laget PWBA and PWBA+FSI. Three different binning schemes were used to extract the results: the first was simply a single bin over Q^2 and W, and the other two schemes used several bins in order to examine the Q^2 or W dependence. The cross sections show clearly the effect of final state interactions (FSI) between the two final state nucleons. The gross features of our data are roughly reproduced by the Laget FSI calculation. This result and results from previous data at lower Q^2 suggest that the momentum transfer dependence of this reaction is reasonably under control. The cross section ratio to the Laget PWBA+FSI calculation has a wiggle at p_{miss} ~300 MeV. It is yet to be seen whether this is merely due to the lack of MEC and IC in the present theoretical calculation. However, a similar feature was observed in a previous Hall A experiment. Further, discrepancies at very low p_{miss} cast some doubt on neutron form factor measurements using the deuteron as target. We expect that other relativistic theoretical calculations will become available in the near future to compare with the results from this dissertation. This will allow us to distinguish between the different theoretical models.

Figure 113 shows a summary of the cross sections for the multi-bin schemes. The cross section decreases as p_{miss} increases, over the whole Q^2 and W acceptance except for high p_{miss} (represented by the stars), high Q^2, and low W values, which is an anomaly that needs to be explained. The high p_{miss} cross section is very small, allowing other processes to compete with the reaction of interest. The corresponding summary plots for the cross section ratio are shown in Figure 114.

Figure 115 shows a summary of the R_{LT} results for the multi-bin schemes. Positive R_{LT} values are represented by open symbols. As we can see from the plots in this figure, R_{LT} is nearly constant over the whole Q^2 and W acceptance for each p_{miss} bin. Other summary plots are shown in Figure 116 for the A_{LT} asymmetry.

In conclusion, the studies that have been presented in this dissertation will help to constrain the models of the deuteron structure and reaction mechanisms which will provide vital input for heavier nuclei.

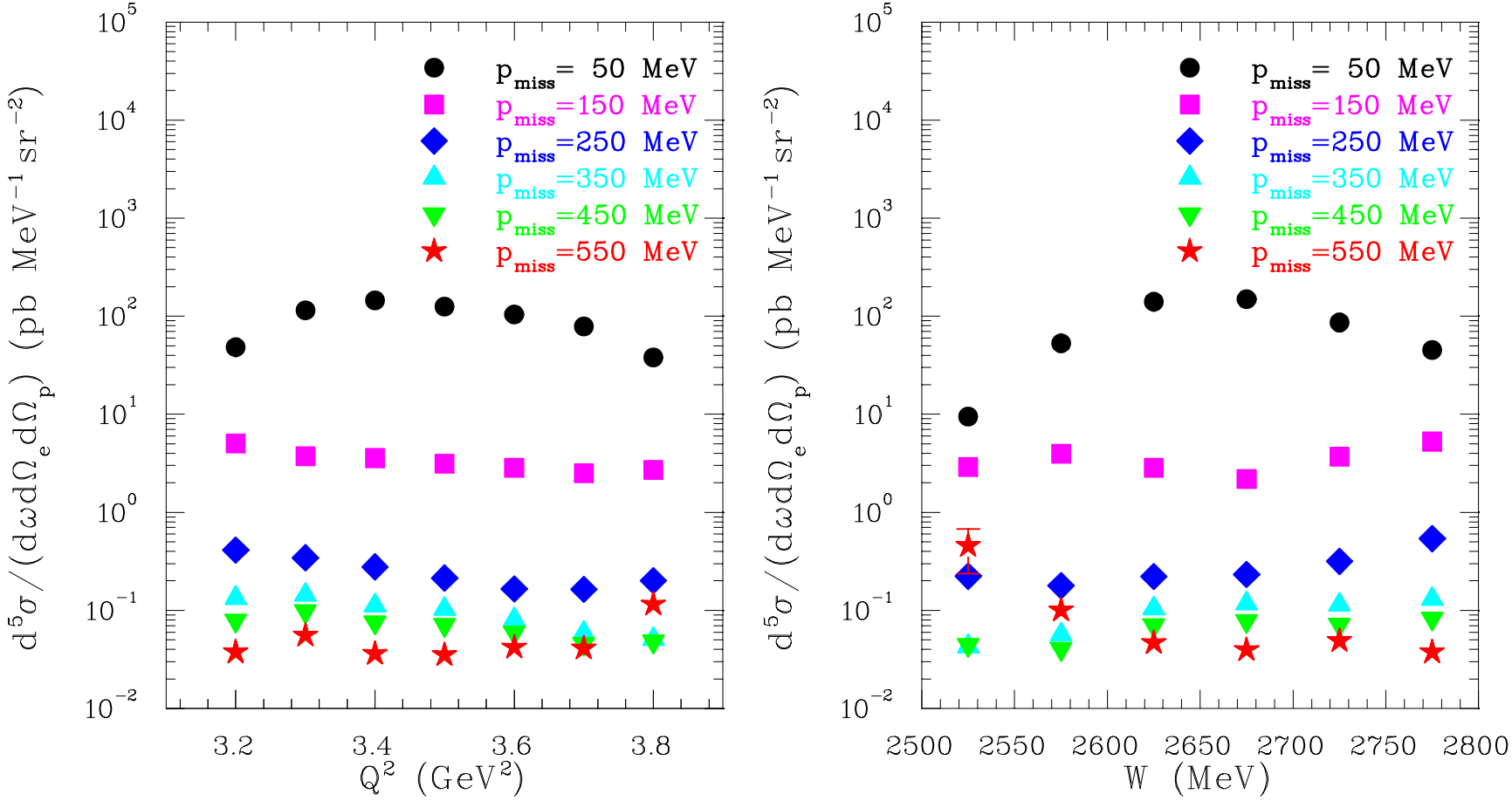

FIG. 113: Summary of cross section results for the multi-bin schemes. A kinematics independent systematic uncertainty of 7% is not shown.

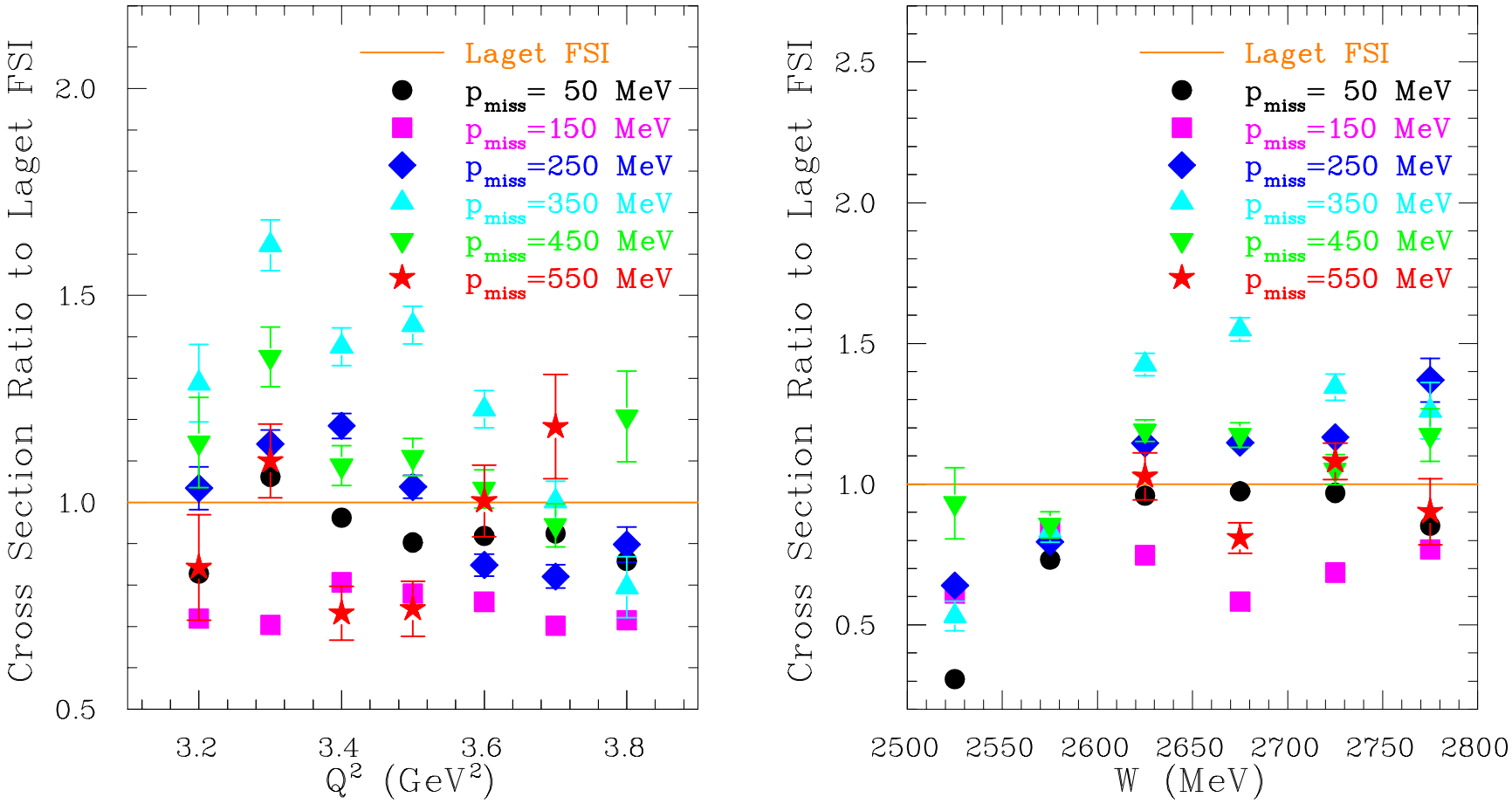

FIG. 114: Summary of the cross section ratio results for the multi-bin schemes. A kinematics independent systematic uncertainty of 7% is not shown.

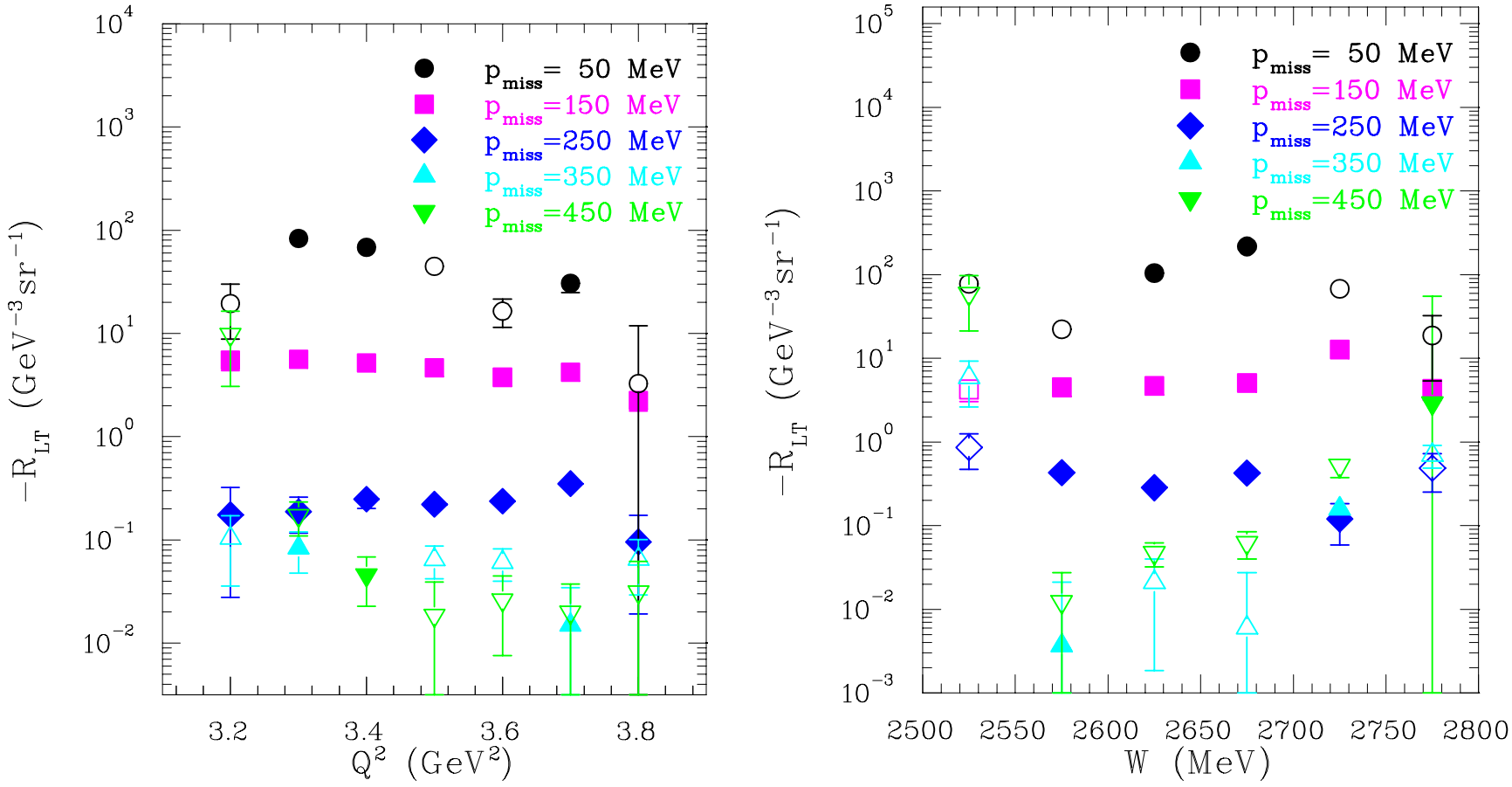

FIG. 115: Summary of R_{LT} results for the multi-bin schemes. Positive R_{LT} values are represented by open symbols. A kinematics independent systematic uncertainty of 7% is not shown.

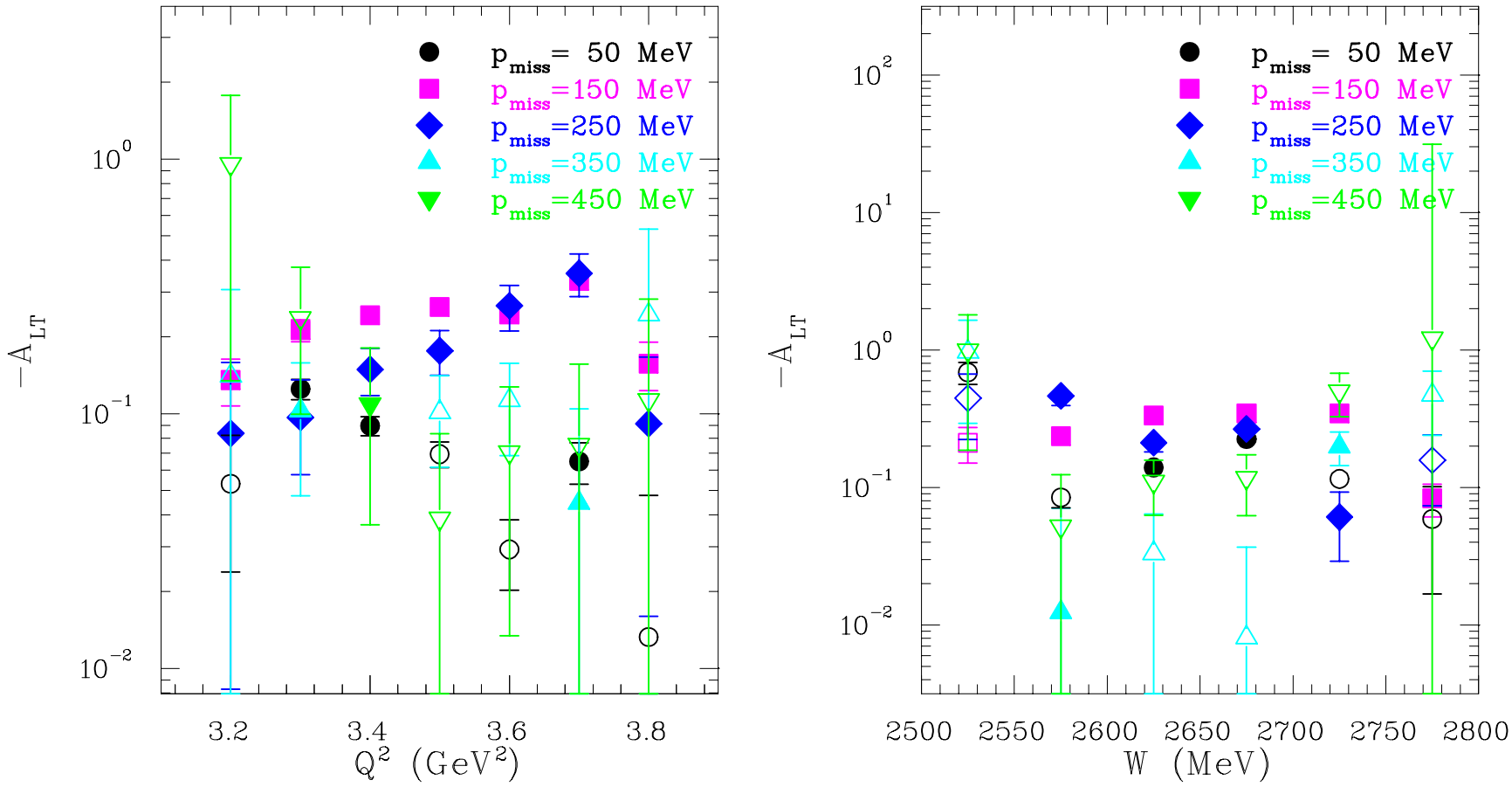

FIG. 116: Summary of A_{LT} results for the multi-bin schemes. Positive A_{LT} values are represented by open symbols.

REFERENCES

[1] M. Garçon and J. W. Van Orden, Adv. Nucl. Phys. **26**, 293 (2001).

[2] J. Carlson and R. Schiavilla, Rev. Mod. Phys. **70**, 743 (1998).

[3] S. Platchkov *et al.*, Nucl. Phys. **A510**, 740 (1990).

[4] C. Ciofi degli Atti *et al.*, Phys. Lett. **B376**, 309 (1996).

[5] C. E. Carlson, J. R. Hiller and R. J. Holt, Ann. Rev. Nucl. Part. Sci. **47**, 395 (1997).

[6] J. D. Walecka, *Electron Scattering for Nuclear and Nucleon Structure*, Cambridge, Cambridge University Press, 2001.

[7] L. C. Alexa *et al.*, Phys. Rev. Lett. **82**, 1374 (1999).

[8] L. L. Frankfurt, M. I. Strikman, D. B. Day and M. M. Sargsian, Phys. Rev. **C48**, 2451 (1993).

[9] P. E. Ulmer *et al.*, Phys. Rev. Lett. **89**, 062301-1 (2002).

[10] W. Fabian and H. Arenhövel, Nucl. Phys. **A314**, 253 (1979).

[11] S. Jeschonnek and T. W. Donnelly, Phys. Rev. **C59**, 2676 (1999).

[12] W. Boeglin, M. Jones, A. Klein, P. E. Ulmer and E. Voutier, JLab Experiment E01-020 Proposal (2001).

[13] S. Frullani and J. Mougey, Adv. Nucl. Phys. **14**, 1 (1984).

[14] S. Boffi, C. Giusti and F. D. Pacati, Phys. Rep. **226**, 1 (1993).

[15] T. W. Donnelly, Adv. Nucl. Phys. **22**, 36 (1996).

[16] J. J. Kelly, Adv. Nucl. Phys. **23**, 75 (1996).

[17] A. Picklesimer and J.W. Van Orden, Phys. Rev. **C40**, 290 (1989).

[18] A. S. Raskin and T. W. Donnelly, Ann. Phys. (N.Y.) **191**, 78 (1989).

[19] V. Dmitrasinovic and F. Gross, Phys. Rev. **C40**, 2479 (1989).

[20] G. van der Steenhoven, Few-Body Systems **17**, 79 (1994).

[21] J. A. Caballero, T. W. Donnelly, E. Moya de Guerra and J. M. Udías, Nucl. Phys. **A632**, 323 (1998).

[22] S. Jeschonnek, Phys. Rev. **C63**, 034609 (2001).

[23] J. Adam, Jr. *et al.*, Phys. Rev. **C66**, 044003 (2002).

[24] S. Jeschonnek and J. W. Van Orden, Phys. Rev. **C62**, 044613 (2000).

[25] C. Ciofi degli Atti and L. P. Kaptari, Phys. Rev. **C63**, 044601 (2001).

[26] R. J. Glauber, Phys. Rev. **100**, 242 (1955).

[27] L. L. Frankfurt, W.G. Greenberg, J.A. Miller, M.M. Sargsian and M.I. Strikman, Z. Phys. **A352**, 97 (1995).

[28] L. L. Frankfurt, M. M. Sargsian and M. I. Strikman, Phys. Rev. **C56**, 1124 (1997).

[29] D. O. Riska, Phys. Rep. **181**, 207 (1989).

[30] J. J. Aubert *et al.*, Phys. Lett. **B123**, 275 (1983) .

[31] L. L. Frankfurt and M. I. Strikman, Nucl. Phys. **B250**, 143 (1985).

[32] M. R. Frank, B. K. Jennings, G. A. Miller, Phys. Rev **C54**, 920 (1996).

[33] E. Hummel and J. A. Tjon, Phys. Rev. **C42**, 423 (1990).

[34] J. A. Tjon, Fewbody Systems Suppl. **5**, 17 (1992).

[35] E. Hummel and J. A. Tjon, Phys. Rev. **C49**, 21 (1994).

[36] B. Mosconi and P. Ricci, Nucl. Phys. **A517**, 483 (1990).

[37] B. Mosconi, J. Pauschenwein, and P. Ricci, Phys. Rev. **C48**, 332 (1993).

[38] H. Arenhövel, W. Leidemann and E. L. Tomusiak, Phys. Rev. **C46**, 455 (1992).

[39] H. Arenhövel, W. Leidemann and E. L. Tomusiak, Phys. Rev. **C52**, 1232 (1995).

[40] F. Ritz, H. Göller, T. Wilbois and H. Arenhövel, Phys. Rev. **C55**, 2214 (1997).

[41] S. Jeschonnek and T. W. Donnelly, Phys. Rev. **C57**, 2438 (1998).

[42] J. M. Laget, Phys. Rep. **69**, 1 (1981).

[43] J. M. Laget, Phys. Lett. **B199**, 493 (1987).

[44] J. M. Laget, Nucl. Phys. **A579**, 333 (1994).

[45] J. M. Laget, Phys. Lett. **B609**, 49 (2005).

[46] R. Machleidt, K. Holinde and C. Elster, Phys. Rep. **149**, 1 (1987).

[47] R. B. Wiringa, V. G. J. Stokes, and R. Schiavilla, Phys. Rev. **C51**, 38 (1995).

[48] S. Galster *et al.*, Nucl. Phys. **B32**, 221 (1971).

[49] O. Gayou *et al.*, Phys. Rev. Lett. **88**, 092301 (2002).

[50] M. Croissiaux, Phys. Rev. **127**, 613 (1962).

[51] T. Tamae *et al.*, Phys. Rev. Lett. **59**, 2919 (1987).

[52] P. von Neumann-Cosel *et al.*, Phys. Rev. Lett. **88**, 202304-1 (2002).

[53] M. van der Schaar *et al.*, Phys. Rev. Lett. **66**, 2855 (1991).

[54] M. van der Schaar *et al.*, Phys. Rev. Lett. **68**, 776 (1992).

[55] J. E. Ducret *et al.*, Phys. Rev. **C49**, 1783 (1994).

[56] F. Frommberger *et al.*, Phys. Lett. **B339**, 17 (1994).

[57] H. J. Bulten *et al.*, Phys. Rev. Lett. **74**, 4775 (1995).

[58] D. Jordan *et al.*, Phys. Rev. Lett. **76**, 1579 (1996).

[59] W-J. Kasdorp *et al.*, Phys. Lett. **B393**, 42 (1997).

[60] A. Pellegrino *et al.*, Phys. Rev. Lett. **78**, 4011 (1997).

[61] K. I. Blomqvist *et al.*, Phys. Lett. **B424**, 33 (2002).

[62] S. Gilad, Nucl. Phys. **A631**, 276c (1998).

[63] T. de Forest, Jr., Nucl. Phys. **A392**, 232 (1983).

[64] P. E. Ulmer, H. Ibrahim and N. Liyanage, JLAB-TN-00-024, 2000.

[65] H. Ibrahim, P. E. Ulmer and N. Liyanage, JLAB-TN-02-032, 2002.

[66] Jefferson Science Associates, LLC, "JLab: Thomas Jefferson National Accelerator Facility" <http://www.jlab.org> (2 December 2006).

[67] C.W. Leemann, D.R. Douglas, G.A. Krafft, Ann. Rev. Nucl. Part. Sci. **51**, 413 (2001).

[68] B.A. Mecking *et al.*, Nucl. Instr. and Meth. **A503**, 513 (2003).

[69] J. Alcorn *et al.*, Nucl. Inst. Meth. **A522**, 294 (2004).

[70] The Hall A Collaboration, "Experimantal HAll A", Jefferson Lab, <http://hallaweb.jlab.org> (2 December 2006).

[71] J. H. Mitchell, "Hall A operational manual", Experimantal HAll A, 29 Febraury 2000 <http://hallaweb.jlab.org/document/OPMAN> (2 December 2006).

[72] Dave Meekins, private communication.

[73] CONSCI, Ltd, "Merlin Microscience", Consolidated Sciences, 30 March 2006, <http://www.conscicorp.com/mms-index.htm> (2 December 2006).

[74] Atlantic Analytical Laboratory, Inc., "AAL: Atlantic Analytical Laboratory", 13 November 2006 <http://www.atlanticanalytical.com> (2 December 2006).

[75] P. Vernin *et al.*, Nucl. Inst. Meth. **A449**, 505 (2000).

[76] Nilanga Liyanage, JLAB-TN-01-049, 2002.

[77] R. Perrino *et al.*, Nucl. Inst. Meth. **A457**, 571 (2001).

[78] L. Lagamba *et al.*, Nucl. Inst. Meth. **A471**, 325 (2001).

[79] K. G. Fissum *et al.*, Nucl. Inst. Meth. **A474**, 108 (2001).

[80] M. Iodice *et al.*, Nucl. Inst. Meth. **A411**, 223 (1998).

[81] O. Hansen *et al.*, "ESPACE Coordinates and Basic Varaibles: Defination", 23 August 1999, <http://www.jlab.org/~mliang/coord_def.ps> (2 December 2006).

[82] David Abbott *et al.*, "CODA: CEBAF Online Data Acquisition", Data Acquisition at Jefferson Lab, 7 March 2005, <http://coda.jlab.org> (2 December 2006).

[83] Bill Rawnsley, “EPICS: Experimental Physics and Industrial Control System”, <http://www.epics.org> (2 December 2006).

[84] The Hall A Collaboration, “ESPACE: Event Scanning Program for Hall A Collaboration Experiments”, Experimental Hall A, 19 October 2002, <http://hallaweb.jlab.org/espace> (2 December 2006).

[85] CERN, “CERNLIB: CERN Program Library”, European Organization for Nuclear Research, 1 Febraury 2006, <http://cernlib.web.cern.ch> (2 December 2006).

[86] CERN, “PAW: Physics Analysis Workstation”, CERN Program Library, 11 July 2006 <http://paw.web.cern.ch> (2 December 2006).

[87] Rene Brun and Fons Rademakers, “ROOT: An Object-Oriented Data Analysis Framework”, The ROOT System, 14 June 2006, <http://root.cern.ch> (2 December 2006).

[88] Gilles Quemener and Eric Voutier, JLab Experiment E01-020 Run Plan (2002).

[89] Bodo Reitz, private communication.

[90] C. Hyde-Wright, JLAB-TN-01-001, 2001.

[91] Paul Ulmer, private communication.

[92] Mark Jones, private communication.

[93] P. E. Ulmer, JLAB-TN-05-064, 2005.

[94] D.S. Armstrong, B. Moffit, R. Suleiman, JLAB-TN-03-017, 2003.

[95] Luminita Coman, private communication.

[96] JLab Experiment E99-117, Jian-Ping Chen, Zein-Eddine Meziani and Paul Souder (Spokespersons).

[97] Nilanga Liyanage, JLAB-TN-02-012, 2002.

[98] Michael Kuss, private communication.

[99] H. Ibrahim, JLAB-TN-06-040, 2006.

[100] P. Ulmer, "MCEEP: Monte Carlo for $(e, e'p)$ experiments", 10 August 2006, <http://www.physics.odu.edu/~ulmer/mceep/mceep.html> (2 December 2006).

[101] Werner Boeglin, private communication.

[102] H. Ibrahim, "E01-020 Analysis", Experiment E01-020, 21 June 2006, <http://www.jlab.org/~hibrahim/e01020/analysis> (2 December 2006).

[103] MySQL AB, "MySQL Community Server", MySQL Database, 2006, <http://www.mysql.com> (2 December 2006).

[104] H. Ibrahim, "E01-020 Database", Experiment E01-020, 18 July 2006, <http://www.jlab.org/~hibrahim/e01020/database> (2 December 2006).

[105] W. R. Leo, *Techniques for Nuclear and Particle Physics Experiments*, Sprenger-Verlag, 1994.

[106] John J. LeRose, "R-functions for the HRS", Experimental Hall A, 3 August 2005 <http://www.jlab.org/~lerose/r-function.html> (2 December 2006).

[107] Jeff Lachniet, private communication.

[108] P. E. Bosted, Phys. Rev. **C51**, 409 (1995).

[109] E. J. Brash *et al.*, Phys. Rev. **C65**, 051001 (2002).

[110] P. Mergel, Ulf-G. Meißner and D. Drechsel, Nucl. Phys. **A596**, 367 (1996).

[111] M. K. Jones *et al.*, Phys. Rev. Lett. 84, 1398 (2000).

[112] O. Gayou *et al.*, Phys. Rev. **C64**, 038202 (2001).

[113] E. L. Lomon, Phys. Rev. **C64**, 035204 (2001).

[114] E. L. Lomon, Phys. Rev. **C66**, 045501 (2002).

[115] M. F. Gari and W. Krümpelmann, Phys. Lett. **B274**, 159 (1992).

[116] M. F. Gari and W. Krümpelmann, Phys. Lett. **B282**, 483 (1992).

[117] J. J. Kelly, Phys. Rev. **C70**, 068202 (2004).

[118] J. Arrington, Phys. Rev. **C68**, 034325 (2003).

[119] M. N. Rosenbluth, Phys. Rev. **79**, 615 (1950).

[120] J. Arrington, "SIMC : Monte Carlo for Hall C", Experimental Hall C, 19 July 2002, <http://www.jlab.org/~jroche/simc> (2 December 2006).

[121] Peter Monaghan, private communication.

[122] Eric Voutier, private communication.

[123] H. Ibrahim, "Stable Current Periods", E01-020 Analysis, 6 March 2006, <http://www.jlab.org/~hibrahim/e01020/analysis/current> (2 December 2006).

[124] Free Software Foundation, "GCC: The GNU Compiler Collection", The GNU project, 19 November 2006, <http://gcc.gnu.org> (2 December 2006).

APPENDIX A

ANALYZED RUNS

A complete list of the beam and kinematic settings for all the deuterium $Q^2 = 3.5$ GeV^2 and $x_{Bj} = 1$ runs is given below.

TABLE LVI: Analyzed runs.

	Kinematics			Beam		Left Arm		Right Arm	
Run	p_{miss}	ϕ_x	E_{Beam}	$Time$	I_{Beam}	P_L	θ_L	P_R	θ_R
	(MeV)		(MeV)	(sec)	(μA)	(MeV)	(°)	(MeV)	(°)
2774	0	-	5009.01	908.08	100.80	3140.89	27.29	2646.40	−32.92
2793			5008.90	1191.29	102.24	3140.87	27.29	2645.10	−32.92
2795	100	π	5009.00	1566.09	102.33	3140.84	27.29	2633.70	−35.20
2798			5008.99	2195.12	102.21	3140.91	27.29	2633.70	−30.87
2804	200	0	5009.03	2513.98	102.49	3140.92	27.29	2617.00	−28.71
2805			5009.03	2637.23	102.33	3140.85	27.29	2617.00	−28.71
2806			5008.99	2186.42	102.28	3140.91	27.29	2617.00	−28.71
2807			5009.01	2534.61	102.51	3140.92	27.29	2617.00	−28.71
2808			5009.04	2517.69	102.33	3140.93	27.29	2617.00	−28.71
2809			5009.05	2559.55	102.27	3140.88	27.29	2617.00	−28.71
2810			5009.02	2840.04	102.12	3140.88	27.29	2617.00	−28.71
2811			5009.02	2631.76	102.25	3140.91	27.29	2617.00	−28.71
2813		π	5009.01	2492.60	102.26	3140.89	27.29	2617.00	−37.36
2814			5009.02	2703.84	102.29	3140.92	27.29	2617.00	−37.36
2815			5009.02	2416.28	102.32	3140.83	27.29	2617.00	−37.36
2816			5009.02	1450.44	102.39	3140.87	27.29	2617.00	−37.36
2817			5009.00	2350.12	101.98	3140.83	27.29	2617.00	−37.36
2827			5009.04	1605.79	100.00	3140.90	27.29	2617.00	−37.36
2828			5009.03	2572.79	99.97	3140.90	27.29	2617.00	−37.36
2829			5009.01	2735.41	100.35	3140.90	27.29	2617.00	−37.36
2835	300	π	5009.01	2301.38	95.02	3140.89	27.29	2589.69	−39.51
2836			5009.00	2338.22	95.05	3140.90	27.29	2589.70	−39.51
2837			5009.02	2004.29	95.00	3140.90	27.29	2589.70	−39.51
2838			5009.01	1996.62	95.06	3140.90	27.29	2589.70	−39.51
2839			5008.99	701.19	94.92	3140.90	27.29	2589.70	−39.51

Table LVI: Analyzed runs (*Continued.*)

Run	Kinematics		Beam			Left Arm		Right Arm	
	p_{miss}	ϕ_x	E_{Beam}	$Time$	I_{Beam}	P_L	θ_L	P_R	θ_R
	(MeV)		(MeV)	(sec)	(μA)	(MeV)	(°)	(MeV)	(°)
2840			5009.01	2227.50	95.12	3140.90	27.29	2589.70	−39.51
2842			5009.00	872.56	100.13	3140.90	27.29	2589.70	−39.51
2844			5008.83	1955.74	100.65	3140.91	27.29	2589.70	−39.51
2845			5009.04	455.83	100.33	3140.90	27.29	2589.70	−39.51
2846			5009.03	1897.03	100.35	3140.90	27.29	2589.69	−39.51
2847			5009.01	1736.87	100.10	3140.91	27.29	2589.70	−39.51
2848			5008.99	1669.66	100.14	3140.91	27.29	2589.70	−39.51
2849			5009.16	2310.60	100.23	3140.91	27.29	2589.70	−39.51
2850			5009.01	2025.56	100.14	3140.91	27.29	2589.70	−39.51
2851			5009.01	605.22	100.08	3140.91	27.29	2589.69	−39.51
2852			5008.99	1952.03	100.14	3140.92	27.29	2589.70	−39.51
2853			5009.01	1907.92	100.18	3140.89	27.29	2589.70	−39.51
2854			5009.04	2062.40	100.27	3140.89	27.29	2589.70	−39.51
2855		0	5009.03	2676.27	100.25	3140.89	27.29	2589.70	−26.56
2856			5009.00	2593.83	100.80	3140.89	27.29	2589.70	−26.56
2859			5009.04	2652.04	100.58	3140.89	27.29	2589.70	−26.56
2860			5009.00	1698.30	100.64	3140.89	27.29	2589.70	−26.56
2861			5009.00	2589.09	98.74	3140.90	27.29	2589.70	−26.56
2862			5009.01	2418.60	98.36	3140.89	27.29	2589.70	−26.56
2863			5009.02	400.63	98.21	3140.89	27.29	2589.70	−26.56
2864			5009.05	2023.21	98.20	3140.89	27.29	2589.70	−26.56
2865			5009.00	1690.44	98.19	3140.89	27.29	2589.70	−26.56
2866			5009.01	2657.66	98.13	3140.90	27.29	2589.70	−26.56
2867			5009.00	2545.63	98.23	3140.89	27.29	2589.70	−26.56
2868			5009.03	2420.46	98.33	3140.90	27.29	2589.70	−26.56
2869			5009.04	2491.79	98.33	3140.90	27.29	2589.70	−26.56
2874	400	0	5008.99	2489.02	96.24	3140.90	27.29	2552.60	−24.42
2875			5009.02	2403.73	96.31	3140.90	27.29	2552.60	−24.42
2876			5009.04	1879.95	96.44	3140.90	27.29	2552.60	−24.42
2877			5009.05	2064.51	96.18	3140.90	27.29	2552.60	−24.42
2878			5008.99	2408.19	96.32	3140.90	27.29	2552.60	−24.42
2879			5009.00	2092.14	96.37	3140.90	27.29	2552.60	−24.42

Table LVI: Analyzed runs (*Continued.*)

Run	Kinematics		Beam			Left Arm		Right Arm	
	p_{miss}	ϕ_x	E_{Beam}	$Time$	I_{Beam}	P_L	θ_L	P_R	θ_R
	(MeV)		(MeV)	(sec)	(μA)	(MeV)	(°)	(MeV)	(°)
2880			5009.02	1963.14	96.31	3140.90	27.29	2552.60	−24.42
2881			5009.01	839.35	96.39	3140.90	27.29	2552.60	−24.42
2882			5009.01	2233.45	96.41	3140.89	27.29	2552.60	−24.42
2883			5009.00	2035.57	96.55	3140.89	27.29	2552.60	−24.42
2884			5008.99	2303.20	96.26	3140.89	27.29	2552.60	−24.42
2885			5009.02	2170.35	96.42	3140.89	27.29	2552.60	−24.42
2886			5009.00	1964.00	96.41	3140.89	27.29	2552.60	−24.42
2887			5009.01	2366.06	97.28	3140.89	27.29	2552.59	−24.42
2888			5009.17	1414.90	96.75	3140.89	27.29	2552.60	−24.42
2889			5009.01	2528.17	96.83	3140.89	27.29	2552.60	−24.42
2891			5009.00	2051.75	96.75	3140.89	27.29	2552.60	−24.42
2892			5009.01	1708.71	96.91	3140.89	27.29	2552.60	−24.42
2893			5009.01	2016.67	96.86	3140.90	27.29	2552.60	−24.42
2894			5009.00	2448.68	97.24	3140.90	27.29	2552.60	−24.42
2898		π	5008.98	2122.05	97.12	3140.89	27.29	2552.60	−41.64
2899			5009.03	2126.83	97.12	3140.89	27.29	2552.60	−41.64
2900			5009.01	2515.08	96.88	3140.90	27.29	2552.60	−41.64
2901			5009.01	2506.67	97.05	3140.90	27.29	2552.60	−41.64
2902			5009.00	2466.46	96.92	3140.90	27.29	2552.60	−41.64
2903			5009.00	2398.45	96.95	3140.90	27.29	2552.60	−41.64
2904			5009.01	2147.28	96.85	3140.90	27.29	2552.60	−41.64
2906			5008.99	2391.71	96.88	3140.90	27.29	2552.60	−41.64
2907			5008.97	2179.01	96.85	3140.90	27.29	2552.60	−41.64
2908			5009.01	2012.43	96.71	3140.90	27.29	2552.60	−41.64
2909			5009.67	703.75	96.61	3140.90	27.29	2552.60	−41.64
2911			5009.04	2314.43	97.04	3140.90	27.29	2552.60	−41.64
2912			5009.05	1209.83	97.56	3140.90	27.29	2552.60	−41.64
2913			5009.00	937.28	100.60	3140.89	0.00	2552.60	−41.64
2914			5009.00	297.50	100.72	3140.89	27.29	2552.60	−41.64
2916			5009.01	2542.26	100.70	3140.89	27.29	2552.60	−41.64
2920			5009.02	1679.21	100.70	3140.89	0.00	2552.60	−41.64
2921			5009.09	1645.38	100.66	3140.89	27.29	2552.60	−41.64

Table LVI: Analyzed runs (*Continued.*)

Run	Kinematics		Beam			Left Arm		Right Arm	
	p_{miss}	ϕ_x	E_{Beam}	$Time$	I_{Beam}	P_L	θ_L	P_R	θ_R
	(MeV)		(MeV)	(sec)	(μA)	(MeV)	(°)	(MeV)	(°)
2922			5008.94	1098.19	100.67	3140.89	27.29	2552.60	−41.64
2929	500	π	5008.09	2620.33	100.71	3140.89	27.29	2506.60	−43.77
2930			5008.31	576.42	100.44	3140.89	27.29	2506.60	−43.77
2931			5008.46	1746.59	100.51	3140.90	27.29	2506.60	−43.77
2932			5008.02	1989.10	100.52	3140.90	27.29	2506.60	−43.77
2933			5009.00	2148.31	100.57	3140.89	27.29	2506.60	−43.77
2934			5008.99	2329.17	89.70	3140.90	27.29	2506.60	−43.77
2935			5008.98	2665.12	86.86	3140.90	27.29	2506.60	−43.77
2936			5009.00	878.32	100.43	3140.89	27.29	2506.60	−43.77
2937			5009.01	2576.90	100.67	3140.89	27.29	2506.60	−43.77
2938			5009.00	2226.12	100.67	3140.89	27.29	2506.60	−43.77
2939			5008.96	2088.65	100.59	3140.89	27.29	2506.60	−43.77
2940			5009.20	2468.97	100.70	3140.89	27.29	2506.60	−43.77
2951			5009.03	2064.04	100.60	3140.89	27.29	2506.60	−43.77
2952			5009.01	1247.22	100.63	3140.90	27.29	2506.60	−43.77
2953			5009.00	2490.72	100.61	3140.89	27.29	2506.60	−43.77
2954			5009.00	2560.43	100.74	3140.89	27.29	2506.60	−43.77
2955			5009.00	2626.89	100.57	3140.89	27.29	2506.60	−43.77
2959			5008.99	2541.73	100.65	3140.89	27.29	2366.59	−41.39

APPENDIX B

OPTICS MATRIX ELEMENTS

In this appendix, the optimized c_i and C_i coefficients for both the left and right arms (see Section IV.8) are listed in Tables LVII-LXII.

TABLE LVII: Left arm y_{000}, t_{000} and p_{000} offsets.

Matrix	Before Optimization			After Optimization		
Elements	c_1	c_2	c_3	c_1	c_2	c_3
y_{000}	-0.00773	0.00111	0.00223	-0.00706	0.00116	0.00131
t_{000}	-1.00180	-0.33183	-0.04336	-1.00530	-0.33246	-0.04202
p_{000}	-0.00144	-0.00182	0.00125	-0.00156	-0.00163	-0.00054

TABLE LVIII: Right arm y_{000}, t_{000} and p_{000} offsets.

Matrix	Before Optimization			After Optimization		
Elements	c_1	c_2	c_3	c_1	c_2	c_3
y_{000}	-0.00423	0.00028	0.00211	-0.00471	0.00097	0.00179
t_{000}	-1.00430	-0.33505	-0.04178	-1.00230	-0.33445	-0.04198
p_{000}	-0.00127	-0.00239	0.00147	-0.00177	-0.00288	0.00315

TABLE LIX: Left arm Y_{jkl} tensor.

Matrix	Before Optimization				After Optimization			
Elements	C_1	C_2	C_3	C_4	C_1	C_2	C_3	C_4
Y_{001}	0.73283	−1.2860	−0.57211	0.04873	0.70909	−1.2746	−0.63166	0.06163
Y_{003}	9.9213	53.548	0.0	0.0	16.091	26.467	0.0	0.0
Y_{010}	−1.1694	−0.72909	0.22982	−0.05215	−1.1566	−0.7514	0.14144	−0.08853
Y_{012}	36.094	−15.544	0.0	0.0	28.853	38.086	0.0	0.0
Y_{021}	17.938	185.13	0.0	0.0	52.426	165.62	0.0	0.0
Y_{030}	74.934	−25.003	0.0	0.0	63.969	4.9473	0.0	0.0
Y_{101}	−1.7531	−5.0478	−0.59753	0.0	−1.3604	−5.0977	−4.3633	0.0
Y_{103}	97.607	0.0	0.0	0.0	308.93	0.0	0.0	0.0
Y_{110}	−12.987	0.25753	4.9306	0.0	−13.373	−1.2221	0.44632	0.0
Y_{112}	600.28	0.0	0.0	0.0	33.276	0.0	0.0	0.0
Y_{121}	−892.45	0.0	0.0	0.0	−891.77	0.0	0.0	0.0
Y_{130}	−166.32	0.0	0.0	0.0	1260.5	0.0	0.0	0.0
Y_{201}	434.58	259.89	0.0	0.0	421.85	190.05	0.0	0.0
Y_{210}	326.06	−124.38	0.0	0.0	301.90	−123.66	0.0	0.0
Y_{301}	2418.1	0.0	0.0	0.0	3549.6	0.0	0.0	0.0
Y_{310}	3585.7	0.0	0.0	0.0	3654.1	0.0	0.0	0.0

TABLE LX: Left arm T_{jkl} and P_{jkl} tensors.

Matrix	Before Optimization				After Optimization			
Elements	C_1	C_2	C_3	C_4	C_1	C_2	C_3	C_4
T_{100}	−2.3324	0.53249	0.034595	0.33158	−2.3026	0.49701	0.00895	0.29786
T_{102}	−34.909	3.8075	0.0	0.0	7.2079	38.986	0.0	0.0
T_{200}	−5.3501	3.0370	−6.9767	0.0	−5.3079	2.7459	−0.23884	0.0
T_{300}	74.753	−153.35	0.0	0.0	75.536	−169.65	0.0	0.0
P_{000}	−0.00087	0.00026	0.0	0.0	−0.00092	0.00018	0.0	0.0
P_{001}	−0.67882	−0.13161	0.22068	−0.03528	−0.67567	−0.13789	0.24818	0.03589
P_{003}	18.252	−9.6302	0.0	0.0	13.188	−17.849	0.0	0.0
P_{010}	−0.34526	0.34595	−0.05757	0.092352	−0.34997	0.34109	−0.05479	0.08348
P_{012}	−4.6563	−24.154	0.0	0.0	−11.119	−33.736	0.0	0.0
P_{021}	0.36992	−20.275	0.0	0.0	−8.2274	−21.905	0.0	0.0
P_{030}	−1.0848	−33.840	0.0	0.0	−0.07709	−33.792	0.0	0.0
P_{101}	5.6803	−0.87208	−0.79653	0.0	5.7264	0.09563	0.30631	0.0
P_{103}	41.060	−1824.2	0.0	0.0	−64.573	−1921.4	0.0	0.0
P_{110}	3.6122	0.36325	−4.9132	0.0	3.6612	1.0506	−1.9584	0.0
P_{112}	−536.69	0.0	0.0	0.0	−443.56	0.0	0.0	0.0
P_{121}	−1133.4	0.0	0.0	0.0	−618.81	0.0	0.0	0.0
P_{130}	−689.75	0.0	0.0	0.0	−645.10	0.0	0.0	0.0
P_{201}	−4.8181	−1.0121	0.0	0.0	−13.812	−96.671	0.0	0.0
P_{210}	−97.873	4.8791	0.0	0.0	−91.464	76.084	0.0	0.0
P_{301}	−642.84	0.0	0.0	0.0	−354.21	0.0	0.0	0.0
P_{310}	−2142.0	0.0	0.0	0.0	−2259.6	0.0	0.0	0.0

TABLE LXI: Right arm Y_{jkl} tensor.

Matrix	Before Optimization				After Optimization			
Elements	C_1	C_2	C_3	C_4	C_1	C_2	C_3	C_4
Y_{001}	0.80453	−1.1543	−0.54236	0.26796	0.77350	−1.1528	−0.52828	0.22798
Y_{003}	9.7965	28.032	0.0	0.0	7.9414	1.9410	0.0	0.0
Y_{010}	−1.1728	−0.74842	0.09235	0.04752	−1.1921	−0.72215	0.14117	0.06458
Y_{030}	54.594	−77.452	0.0	0.0	23.842	−41.757	0.0	0.0
Y_{100}	0.06453	−0.02041	−0.11810	−0.24877	0.07043	−0.04777	−0.16241	−0.02293
Y_{101}	−2.7136	−7.8803	−3.2253	0.0	−1.5926	−7.2740	−3.4065	0.0
Y_{103}	597.97	0.0	0.0	0.0	943.75	0.0	0.0	0.0
Y_{110}	−15.460	−1.2919	−1.9652	0.0	−14.451	−0.98949	−0.44393	0.0
Y_{112}	560.34	0.0	0.0	0.0	334.53	0.0	0.0	0.0
Y_{121}	−186.04	0.0	0.0	0.0	−252.55	0.0	0.0	0.0
Y_{130}	1360.2	0.0	0.0	0.0	665.24	0.0	0.0	0.0
Y_{201}	395.65	266.44	0.0	0.0	379.72	158.83	0.0	0.0
Y_{210}	304.14	−91.766	0.0	0.0	306.95	−109.63	0.0	0.0
Y_{301}	3636.4	0.0	0.0	0.0	3255.8	0.0	0.0	0.0
Y_{310}	5004.4	0.0	0.0	0.0	4067.0	0.0	0.0	0.0

TABLE LXII: Right arm T_{jkl} and P_{jkl} tensors.

Matrix	Before Optimization				After Optimization			
Elements	C_1	C_2	C_3	C_4	C_1	C_2	C_3	C_4
T_{002}	0.49238	0.41165	3.3959	0.0	0.07028	0.09031	0.59487	0.0
T_{020}	−0.25752	−0.53019	−0.71086	0.0	−0.00587	−0.15508	0.58537	0.0
T_{100}	−2.3048	0.50613	−0.078347	0.05656	−2.2889	0.48272	−0.05934	0.11444
T_{120}	87.612	−9.3453	0.0	0.0	−13.179	−8.9416	0.0	0.0
T_{200}	−3.5759	2.1619	0.34619	0.0	−5.0946	4.0745	0.30971	0.0
T_{202}	517.52	0.0	0.0	0.0	645.54	0.0	0.0	0.0
T_{300}	54.436	−75.934	0.0	0.0	52.231	−65.828	0.0	0.0
T_{400}	−3119.7	0.0	0.0	0.0	−2982.1	0.0	0.0	0.0
P_{001}	−0.63302	−0.16875	0.24403	0.01027	−0.63346	−0.16309	0.22789	−0.00264
P_{003}	18.181	−15.165	0.0	0.0	15.280	−15.433	0.0	0.0
P_{010}	−0.35775	0.34406	−0.03396	0.10200	−0.34857	0.32732	−0.04015	0.08167
P_{012}	−5.3417	−30.527	0.0	0.0	−8.6195	−36.012	0.0	0.0
P_{021}	−1.9213	15.377	0.0	0.0	−7.7586	30.154	0.0	0.0
P_{030}	12.530	−32.319	0.0	0.0	12.652	−15.239	0.0	0.0
P_{100}	−0.02702	0.02481	−0.03244	−0.16188	−0.03034	0.002302	0.01696	−0.06203
P_{101}	5.1427	−1.0670	2.2678	0.0	5.1451	−0.95311	0.67278	0.0
P_{103}	399.53	0.0	0.0	0.0	312.12	0.0	0.0	0.0
P_{110}	3.8215	0.33985	−1.5177	0.0	3.4648	0.30508	−1.6104	0.0
P_{112}	−177.05	0.0	0.0	0.0	−269.34	0.0	0.0	0.0
P_{121}	−1276.4	0.0	0.0	0.0	−703.78	0.0	0.0	0.0
P_{130}	−466.99	0.0	0.0	0.0	269.78	0.0	0.0	0.0
P_{201}	−6.4186	−75.807	0.0	0.0	−14.838	−67.141	0.0	0.0
P_{210}	−85.821	64.207	0.0	0.0	−92.358	66.579	0.0	0.0
P_{301}	−868.81	0.0	0.0	0.0	−919.23	0.0	0.0	0.0
P_{310}	−1711.7	0.0	0.0	0.0	−1592.3	0.0	0.0	0.0

APPENDIX C

HALL A SURVEY SIGN CONVENTIONS

The sign convention of various Hall A surveys [70] is explained in this Appendix.

C.1 SPECTROMETER SURVEYS:

To get the $x_\circ$, $y_\circ$ and $z_\circ$ spectrometer offsets in Hall A coordinate system for ESPACE header files, use the following conventions:
Left arm central angle,$\theta_\circ$ is always positive.
Right arm central angle,$\theta_\circ$ is always negative.
$y_\circ$ is the spectrometer vertical offset (positive $\equiv$ up).
$h_\circ$ is the spectrometer horizontal offset. The sign of $h_\circ$ is determined from Table LXIII.

TABLE LXIII: Sign of the spectrometer horizontal offset,$h_\circ$.

Arm	Left		Right	
Object Location	Downstream	Upstream	Downstream	Upstream
$h_\circ$ Sign	negative	positive	positive	negative

$x_\circ$ and $z_\circ$ are obtained from the following equations:

$$x_\circ = h_\circ \cos\theta_\circ, \tag{159}$$

$$z_\circ = -h_\circ \sin\theta_\circ, \tag{160}$$

For the optimization files we take:
sp_v_off $\equiv y_\circ$,
sp_h_off $\equiv h_\circ$.

C.2 COLLIMATOR SURVEYS:

To get the sieve central hole coordinates, x_sieve_4 (positive $\equiv$ down) and y_sieve_4 (positive $\equiv$ left), for the optimization files, we use the following relations:
x_sieve_4 $\equiv -\Delta$Y,
y_sieve_4 $\equiv +\Delta$X.

C.3 TARGET SURVEYS:

To get the x_t, y_t and z_t target offsets in Hall A coordinate system for ESPACE header files, we use the following relations:

$x_t \equiv -\Delta$X,

$y_t \equiv -\Delta$Y,

$z_t \equiv -\Delta$Z.

For the optimization files, we take the optics target central foil z-position as zreact_5 $\equiv z_t$.

APPENDIX D

STABLE CURRENT PROGRAM

The stable current program files can be downloaded from this web page:

http://www.jlab.org/~hibrahim/e01020/analysis/current

The stable current program is written in C++ and is compiled by the G++ compiler which is part of the GNU Compiler Collection (GCC) [124].

```
////////////////////// stable_current.cpp //////////////////////
// Purpose: Stable Current Finder
// Author: Hassan Ibrahim, 2005
// Compile: g++ -o stable_current stable_current.cpp
// Use: ./stable_current
//  or  ./stable_current [kinematics input_file output_file]

# include <cstdlib>
# include <cmath>
# include <string>
# include <iostream>
# include <fstream>
# include <iomanip>

using namespace std

double bcmcur(string k, double u, double d, double t);

const double curerr = 5.0;
const double edgetime = 30.0;
const double goodcur = 5.0;
const double goodtime = 30.0;

const double uconst[2] = {4092.4, 4101.6};
const double dconst[2] = {4188.5, 4165.65};
const double uoff[2] = {163.8, 163.8};
const double doff[2] = {110.0, 110.0};

const int nscal = 13;

main(int argc, char* argv[])
{
```

```
double ref[nscal];
double tmp[nscal];
double low[nscal];
double pre[nscal];
double high[nscal];

double refcur;
double tmpcur;
double lowcur;
double ctime;
double cbcmu3;
double cbcmd3;
double avecur;
double avechar;

double ct1;
double ct3;
double ct5;
double ce1;
double ce3;
double ce5;

int n = 0;
int s = 0;

bool lowset = false;
bool highset = false;

string dummy;

char* kin = new char [20];        // kinematics
char* infile  = new char [20];    // input filename string variable
char* outfile = new char [20];    // output filename string variable

fstream fin;     // define fin as a file input object
fstream fout;    // define fout as a file output object

cout << '\n';
cout << " ----------------------\n";
cout << "| Stable Current Finder |\n";
cout << " ----------------------\n";
```

```
cout << '\n';

// ------------- Inputs -------------

if (argc == 4)
  {
    kin = argv[1];
    infile = argv[2];
    outfile = argv[3];
  }
else
  {
    cout << "Kinematics (q1,q2,q3) : "; cin >> kin;
    cout << "Input Filename        : "; cin >> infile;
    cout << "Output Filename       : "; cin >> outfile;
    cout << '\n';
  }

//------------- Calculations ------------------

fin.open(infile, ios_base::in); // open the input file

if ( !fin )
  {
    cerr << ">>> Error opening input file!\n\n";
    exit(1);
  }

getline(fin, dummy); // event,ctime,time,cbcmu3,bcmu3,cbcmd3,bcmd3

for (int i=0, i<nscal, i++) fin >> ref[i];

refcur = bcmcur(kin, ref[4], ref[6], ref[2]);

for (int i=0, i<nscal, i++) fin >> tmp[i];

fout.open(outfile, ios_base::out);       // open the output file

fout.precision(10);
fout.setf(ios_base::left);
```

```
  fout << setw(24) << "From (Event) To"  << setw(12) << "Time (s)"
<< setw(12) << "Q (uC)" << setw(12) << "I (uA)" << setw(12) << "T1"
<< setw(12) << "T3" << setw(12) << "T5" << setw(12) << "E1"
<< setw(12) << "E3" << setw(12) << "E5" << '\n';

  while (!fin.eof())
    {

      n++;

      tmpcur = bcmcur(kin, tmp[4], tmp[6], tmp[2]);

      if (!lowset)
        {
          if (tmpcur > goodcur)
            {
              if (abs(refcur - tmpcur) < curerr)
                {
                  if ((tmp[1] - ref[1]) / 1024 > edgetime)
                    {
                      for (int i=0, i<nscal, i++) low[i] = tmp[i];
                      for (int i=0, i<nscal, i++) pre[i] = tmp[i];
                      lowcur = tmpcur;
                      lowset = true;
                    }
                }
              else
                {
                  for (int i=0, i<nscal, i++) ref[i] = tmp[i];
                  refcur = bcmcur(kin, ref[4], ref[6], ref[2]);
                }
            }
        }
      else
        {
          if (abs(lowcur - tmpcur) > curerr)
            {
              for (int i=0, i<nscal, i++) high[i] = pre[i];
              highset = true;
            }
          else
```

```
            {
              for (int i=0, i<nscal, i++) pre[i] = tmp[i];
            }
        }

      for (int i=0, i<nscal, i++) fin >> tmp[i];

      if (lowset && (highset || fin.eof()))
        {
          if (fin.eof())
            {
              for (int i=0, i<nscal, i++) high[i] = pre[i];
            }
          ctime = high[1] - low[1];
          if (ctime / 1024 > goodtime)
            {
              s++;

              cbcmu3 = high[3] - low[3];
              cbcmd3 = high[5] - low[5];
              avecur = bcmcur(kin, cbcmu3, cbcmd3, ctime);
              avechar = avecur * ctime / 1024;

              ct1 = high[7] - low[7];
              ct3 = high[8] - low[8];
              ct5 = high[9] - low[9];
              ce1 = high[10] - low[10];
              ce3 = high[11] - low[11];
              ce5 = high[12] - low[12];

              fout << setw(12) << low[0] << setw(12) << high[0]
<< setw(12) << ctime / 1024 << setw(12) << avechar << setw(12)
<< avecur << setw(12) << ct1 << setw(12) << ct3 << setw(12)
<< ct5 << setw(12) << ce1 << setw(12) << ce3 << setw(12) << ce5 << '\n';
            }
          lowset = false;
          highset = false;
        }
    }

  fin.close();     // close the input file
```

```
  fout.close();    // close the output file

  cout << "The input file " <<infile <<" includes "<< n <<" lines.\n";
  cout << "Number of stable current periods is " << s << ".\n";
  cout << "The output file " << outfile << " was saved.\n\n";
}

// Function bcmcur

double bcmcur(string k, double u, double d, double t)
{

  double c;
  double uc;
  double dc;
  int m;

  m = (k == "q3") ? 1 : 0;

  uc = (u / t * 1024 - uoff[m]) / uconst[m];
  dc = (d / t * 1024 - doff[m]) / dconst[m];

  c = ( uc + dc ) / 2.0;

  return c;

}
```

APPENDIX E

DERIVATIVES OF KINEMATICAL OFFSETS

$$\frac{\partial W}{\partial \delta_e} = -E, \tag{161}$$

$$\frac{\partial W}{\partial \theta_e} = -\frac{EE'}{M_p}\sin\theta_e\cos\phi_e, \tag{162}$$

$$\frac{\partial W}{\partial \phi_e} = -\frac{EE'}{M_p}\cos\theta_e\sin\phi_e, \tag{163}$$

$$\frac{\partial W}{\partial \delta_p} = \frac{\partial W}{\partial \theta_p} = \frac{\partial W}{\partial \phi_p} = 0, \tag{164}$$

$$\frac{\partial E_{miss}}{\partial \delta_e} = -E', \tag{165}$$

$$\frac{\partial E_{miss}}{\partial \delta_p} = -\frac{p^2}{E_p}, \tag{166}$$

$$\frac{\partial E_{miss}}{\partial \theta_e} = \frac{\partial E_{miss}}{\partial \theta_p} = \frac{\partial E_{miss}}{\partial \phi_e} = \frac{\partial E_{miss}}{\partial \phi_p} = 0, \tag{167}$$

$$\frac{\partial p_{missx}}{\partial \delta_e} = -E'\sin\theta_e\cos\phi_e, \tag{168}$$

$$\frac{\partial p_{missx}}{\partial \delta_p} = -p\sin\theta_p\cos\phi_p, \tag{169}$$

$$\frac{\partial p_{missx}}{\partial \theta_e} = -E'\cos\theta_e\cos\phi_e, \tag{170}$$

$$\frac{\partial p_{missx}}{\partial \theta_p} = -p\cos\theta_p\cos\phi_p, \tag{171}$$

$$\frac{\partial p_{missx}}{\partial \phi_e} = E'\sin\theta_e\sin\phi_e, \tag{172}$$

$$\frac{\partial p_{missx}}{\partial \phi_p} = p\sin\theta_p\sin\phi_p, \tag{173}$$

$$\frac{\partial p_{missy}}{\partial \delta_e} = -E'\sin\phi_e, \tag{174}$$

$$\frac{\partial p_{missy}}{\partial \delta_p} = -p\sin\phi_p, \tag{175}$$

$$\frac{\partial p_{missy}}{\partial \theta_e} = \frac{\partial p_{missy}}{\partial \theta_p} = 0, \tag{176}$$

$$\frac{\partial p_{missy}}{\partial \phi_e} = -E'\cos\phi_e, \tag{177}$$

$$\frac{\partial p_{missy}}{\partial \phi_p} = -p\cos\phi_p, \tag{178}$$

$$\frac{\partial p_{missz}}{\partial \delta_e} = -E' \cos\theta_e \cos\phi_e, \quad (179)$$

$$\frac{\partial p_{missz}}{\partial \delta_p} = -p \cos\theta_p \cos\phi_p, \quad (180)$$

$$\frac{\partial p_{missz}}{\partial \theta_e} = E' \sin\theta_e \cos\phi_e, \quad (181)$$

$$\frac{\partial p_{missz}}{\partial \theta_p} = p \sin\theta_p \cos\phi_p, \quad (182)$$

$$\frac{\partial p_{missz}}{\partial \phi_e} = E' \cos\theta_e \sin\phi_e, \quad (183)$$

$$\frac{\partial p_{missz}}{\partial \phi_p} = p \cos\theta_p \sin\phi_p. \quad (184)$$

APPENDIX F

FITTING FILES FOR THE KINEMATICS CALIBRATION

The fitting computer files for the kinematics calibration can be downloaded from this web page:

http://www.jlab.org/~hibrahim/e01020/analysis/kincal

F.1 THE INPUT FILE (KINCAL.INP)

The input file used by the fitting program is listed below:

```
-----------------------------------------------------------------
sig_dele   sig_delp    sig_thee   sig_thep    sig_phie    sig_phip
-----------------------------------------------------------------
10.0E-5,    10.0E-5,     8.0E-5,    8.0E-5,     8.0E-5,     8.0E-5
-------------------------------------------------------------------------------------------------------------------
run     ebeam    moml      momr      thel       ther      del_w   del_em   del_pmx  del_pmy   del_pmz
-------------------------------------------------------------------------------------------------------------------
2594, 5008.460, 2918.582, 2877.317, 30.474322,-30.483480,  9.9660, 2.23926, 3.22058, 0.846959, 0.863014
2596, 5008.480, 3159.311, 2617.491, 26.980713,-33.300646, 10.858, 2.34749, 4.00829, 0.840967, 1.00067
2599, 5008.480, 3425.225, 2338.965, 23.979249,-36.578624, 10.771, 2.56341, 4.21446,-0.393876, 1.35824
2600, 5008.480, 3695.414, 2044.664, 20.979818,-40.397981,  8.799, 1.83452, 3.94423,-0.978451, 0.696069
2632, 5008.490, 3140.307, 2648.076, 27.264631,-32.916592,  9.836, 2.32254, 3.59949, 0.606018, 1.29037
2672, 5008.510, 3140.334, 2648.073, 27.264631,-32.916592,  9.902, 2.0589,  3.82971, 0.346928, 0.963902
2792, 5008.520, 3140.253, 2648.073, 27.264420,-32.926764, 11.061, 2.52528, 4.09572, 0.553575, 1.30005
```

F.2 THE FITTING PROGRAM (KINCAL.FOR)

The fitting program is written in Fortran 77 and is compiled by the G77 compiler which is part of the GNU Compiler Collection (GCC) [124].

```
c     Program: kincal.for
c     Purpose: Kinematics Calibration
c     Author : Hassan Ibrahim (2006)
c     Compile: g77 kincal.for -o kincal
c     Usage  : ./kincal
      implicit none
c     Declare Variables
      integer nx,ny,nzmax
      parameter (nx=6)
      parameter (ny=5)
      parameter (nzmax=20)       ! Set this >= number of runs
      double precision pi,mp
      parameter (pi=3.14159265359)
```

```
      parameter (mp=938.272)
      integer i,j,k,l,n,nz,lun,dof
      integer run(nzmax)
      double precision chisq,chisqpdof,chisqmin,chisqminpdof
      double precision e0(nzmax),pe0(nzmax),pp0(nzmax)
      double precision the0(nzmax),thp0(nzmax)
      double precision e,pe,pp,ep
      double precision sthe,cthe,sthp,cthp
      double precision sphe,cphe,sphp,cphp
      double precision sigx(nx),delx(nx),sigdelx(nx)
      double precision dely(ny,nzmax),delysum(ny),delyave(ny)
      double precision delynew(ny,nzmax)
      double precision delymin(ny,nzmax),delyminsum(ny),delyminave(ny)
      double precision sigy2(ny,nzmax)
      double precision dy_dx(nx,ny,nzmax)
      double precision mat(nx,nx),mat_inv(nx,nx)
      double precision vec(nx),vec_out(nx)
      character*80 dummy
c     Read initial offsets and nominal uncertainites
      open(unit=2,name='kincal.inp',status='old',form='formatted')
      read(2,*) dummy
      read(2,*) dummy
      read(2,*) dummy
      read(2,*) (sigx(i), i = 1, nx)
      read(2,*) dummy
      read(2,*) dummy
      read(2,*) dummy
      k = 1
 100  read(2,*,end=999) run(k),e0(k),pe0(k),pp0(k),the0(k),thp0(k),
     #        (dely(j,k), j = 1, ny)
      k = k + 1
      goto 100
 999  close(unit=2)
      nz = k - 1
c     Initialization
      chisq = 0.0
      do i = 1, nx
         do j = 1, ny
            do k = 1, nz
               dy_dx(i,j,k) = 0.0
            enddo
```

```
         enddo
      enddo
      do j = 1, ny
         do k = 1, nz
            sigy2(j,k) = 0.0
            delynew(j,k) = 0.0
         enddo
      enddo
      do i = 1, nx
         vec(i) = 0.0
      enddo
      do i = 1, nx
         do l = 1, nx
            mat(i,l) = 0.0
         enddo
      enddo
      do j = 1, ny
         delysum(j) =0.0
      enddo
c     Start the main loop over kinematic settings
      do k = 1, nz
         e = e0(k)
         pe = pe0(k)
         pp = pp0(k)
         sthe = sin(the0(k) * pi / 180.0)
         cthe = cos(the0(k) * pi / 180.0)
         sthp = sin(thp0(k) * pi / 180.0)
         cthp = cos(thp0(k) * pi / 180.0)
         sphe = 0.0
         cphe = 1.0
         sphp = 0.0
         cphp = 1.0
         ep = sqrt(pp**2 + mp**2)
         dy_dx(1,1,k) = -e                      ! dw_ddele
         dy_dx(3,1,k) = -e*pe/mp*sthe*cphe      ! dw_dthe
         dy_dx(5,1,k) = -e*pe/mp*cthe*sphe      ! dw_dphe
         dy_dx(1,2,k) = -pe                     ! dem_ddele
         dy_dx(2,2,k) = -pp**2/ep               ! dem_ddelp
         dy_dx(1,3,k) = -pe*sthe*cphe           ! dpmx_ddele
         dy_dx(2,3,k) = -pp*sthp*cphp           ! dpmx_ddelp
         dy_dx(3,3,k) = -pe*cthe*cphe           ! dpmx_dthe
```

```
            dy_dx(4,3,k) = -pp*cthp*cphp           ! dpmx_dthp
            dy_dx(5,3,k) = +pe*sthe*sphe           ! dpmx_dphe
            dy_dx(6,3,k) = +pp*sthp*sphp           ! dpmx_dphp
            dy_dx(1,4,k) = -pe*sphe                ! dpmy_ddele
            dy_dx(2,4,k) = -pp*sphp                ! dpmy_ddelp
            dy_dx(5,4,k) = -pe*cphe                ! dpmy_dphe
            dy_dx(6,4,k) = -pp*cphp                ! dpmy_dphp
            dy_dx(1,5,k) = -pe*cthe*cphe           ! dpmz_ddele
            dy_dx(2,5,k) = -pp*cthp*cphp           ! dpmz_ddelp
            dy_dx(3,5,k) = +pe*sthe*cphe           ! dpmz_dthe
            dy_dx(4,5,k) = +pp*sthp*cphp           ! dpmz_dthp
            dy_dx(5,5,k) = +pe*cthe*sphe           ! dpmz_dphe
            dy_dx(6,5,k) = +pp*cthp*sphp           ! dpmz_dphp
            do i = 1, nx
               do j = 1, ny
                  sigy2(j,k) = sigy2(j,k) + dy_dx(i,j,k)**2 * sigx(i)**2
               enddo
            enddo
            do i = 1, nx
               do j = 1, ny
                  vec(i) = vec(i) + dely(j,k) * dy_dx(i,j,k) / sigy2(j,k)
                  do l = 1, nx
                     mat(i,l) = mat(i,l) + dy_dx(i,j,k) * dy_dx(l,j,k) /
     #                    sigy2(j,k)
                  enddo
               enddo
            enddo
         enddo
c        End of the main loop over kinematic settings
         dof = (ny - 1) * (nz - 1)
c        Initial Chi-Square
         do j = 1, ny
            do k = 1, nz
               chisq = chisq +(dely(j,k))**2/sigy2(j,k)
            enddo
         enddo
         chisqpdof = chisq / dof
         do j = 1, ny
            do k = 1, nz
               delysum(j) = delysum(j) + dely(j,k)
            enddo
```

```
         delyave(j) = delysum(j) / nz
      enddo
c     Chi-Square Minimization
      call matinv(mat,mat_inv,nx)
      call mat_mult(nx,nx,1,mat_inv,vec,vec_out)
      do i = 1, nx
         delx(i) = vec_out(i)
         sigdelx(i) = sqrt(mat_inv(i,i))
      enddo
c     Minimized Chi-Square
      do j = 1, ny
         do k = 1, nz
            do i = 1, nx
               delynew(j,k) = delynew(j,k) + dy_dx(i,j,k) * delx(i)
            enddo
            delymin(j,k) = dely(j,k)-delynew(j,k)
            chisqmin = chisqmin +delymin(j,k)**2/sigy2(j,k)
         enddo
      enddo
      chisqminpdof = chisqmin / dof
      do j = 1, ny
         do k = 1, nz
            delyminsum(j) = delyminsum(j) + delymin(j,k)
         enddo
         delyminave(j) = delyminsum(j) / nz
      enddo
c     Write out the results
      do n = 1, 2
         if (n .eq. 1) then
            lun = 1
            open(unit=lun,name='kincal.out',status='unknown')
         else
            lun = 6
         endif
         write(lun,*)
         write(lun,*) "Kinematics Calibration"
         write(lun,*) "----------------------"
         write(lun,*)
         write(lun,*) "Nominal Spectrometer Uncertainties:"
         write(lun,*)
         write(lun,10) "DelE","DelP","TheE (rad)","TheP (rad)",
```

```
#        "PhiE (rad)","PhiP (rad)"
      write(lun,*)
      write(lun,20) (sigx(i), i = 1, nx)
      write(lun,*)
      write(lun,*) "Number of Runs =",nz
      write(lun,*)
      write(lun,*) "Initial Kinematical Offsets:"
      write(lun,*)
      write(lun,30) "Run", "W (MeV)","Em (MeV)","Pmx (MeV)",
#        "Pmy (MeV)", "Pmz (MeV)"
      write(lun,*)
      do k = 1, nz
         write(lun,40) run(k), (dely(j,k), j = 1, ny)
      enddo
      write(lun,*)
      write(lun,50) "AVG", (delyave(j),j=1,ny)
      write(lun,*)
      write(lun,*) "Initial Chi-Square per Degree of Freedom =",
#        chisqpdof
      write(lun,*)
      write(lun,*) "----------------------------------------"
      write(lun,*)
      write(lun,*) "Fit Results:"
      write(lun,*)
      write(lun,*) "Spectrometer Offsets:"
      write(lun,*)
      write(lun,10) "DelE","DelP","TheE (rad)","TheP (rad)",
#        "PhiE (rad)","PhiP (rad)"
      write(lun,20) (delx(i), i = 1, nx)
      write(lun,*)
      write(lun,*) "Spectrometer Uncertainties:"
      write(lun,*)
      write(lun,20) (sigdelx(i), i = 1, nx)
      write(lun,*)
      write(lun,*) "----------------------------------------"
      write(lun,*)
      write(lun,*) "Minimized Kinematical Offsets:"
      write(lun,*)
      write(lun,30) "Run", "W (MeV)","Em (MeV)","Pmx (MeV)",
#        "Pmy (MeV)", "Pmz (MeV)"
      write(lun,*)
```

```
         do k = 1, nz
            write(lun,40) run(k), (delymin(j,k),j=1,ny)
         enddo
         write(lun,*)
         write(lun,50) "AVG", (delyminave(j),j=1,ny)
         write(lun,*)
         write(lun,*) "Minimized Chi-Square per Degree of Freedom =",
     #        chisqminpdof
         write(lun,*)
         close(unit=lun)
 10      format(6(a10,2x))
 20      format(6(f10.6,2x))
 30      format(a4,6(2x,a10))
 40      format(i4,5(2x,f10.6))
 50      format(a4,5(2x,f10.6))
      enddo
c
      stop
      end
C
C     ------------------------------------------------------------
C     ------------------------------------------------------------
C     SUBROUTINE MATINV
C
C     Purpose:
C     Invert a symmetric matrix
C
C     Usage:
C     CALL MATINV( ARRAY, ARRAY_INV, NORDER )
C
C     Description of parameters:
C     ARRAY     - input matrix
C     ARRAY_INV - inverse matrix
C     NORDER    - degree of matrix
C
C     Subroutines and function subprograms required:
C     none
C
C     Based on routine of Bevington.
C
C     ------------------------------------------------------------
```

```
C
      SUBROUTINE MATINV (ARRAY, ARRAY_INV, NORDER  )
C
      IMPLICIT DOUBLE PRECISION (A-H,O-Z)
      DOUBLE PRECISION ARRAY(NORDER,NORDER),ARRAY_INV(NORDER,NORDER)
      INTEGER IK(20), JK(20)
C
      DO I=1,NORDER
         DO J=1,NORDER
            ARRAY_INV(I,J) = ARRAY(I,J)
         ENDDO
      ENDDO
C
      DO K=1,NORDER
C
C     FIND LARGEST ELEMENT ARRAY(I,J) IN REST OF MATRIX
C
         AMAX = 0.D0
 21      DO I=K,NORDER
            DO J=K, NORDER
               IF(  ABS(AMAX) -  ABS(ARRAY_INV(I,J) ) ) 24,24,30
 24            AMAX = ARRAY_INV( I,J )
               IK(K) = I
               JK(K) = J
 30         ENDDO
         ENDDO
C
C     INTERCHANGE ROWS AND COLUMNS TO PUT AMAX IN ARRAY_INV(K,K)
C
         IF( AMAX ) 41,140, 41
 41      I=IK(K)
         IF( I-K) 21,51,43
C
 43      DO J=1,NORDER
            SAVE = ARRAY_INV( K,J)
            ARRAY_INV(K,J) = ARRAY_INV(I,J)
            ARRAY_INV(I,J) = -SAVE
         ENDDO
C
 51      J = JK(K)
         IF(J-K) 21,61,53
```

```
C
 53      DO I=1,NORDER
            SAVE = ARRAY_INV(I,K)
            ARRAY_INV(I,K) = ARRAY_INV(I,J)
            ARRAY_INV(I,J) = -SAVE
         ENDDO
C
C     ACCUMULATE ELEMENTS OF INVERSE MATRIX
C
 61      DO I=1,NORDER
            IF(I-K) 63,70,63
 63         ARRAY_INV(I,K) = -ARRAY_INV(I,K)/AMAX
 70      ENDDO
C
 71      DO I=1,NORDER
            DO J=1,NORDER
               IF( I-K) 74,80,74
 74            IF( J-K) 75,80,75
 75            ARRAY_INV(I,J) = ARRAY_INV(I,J)
     #              + ARRAY_INV(I,K)*ARRAY_INV(K,J)
 80         ENDDO
         ENDDO
C
 81      DO J=1,NORDER
            IF(J-K) 83,90,83
 83         ARRAY_INV(K,J) = ARRAY_INV(K,J)/AMAX
 90      ENDDO
C
         ARRAY_INV(K,K) = 1./AMAX
      ENDDO
C
C     RESTORE ORDERING OF MATRIX
C
 101  DO L=1, NORDER
         K = NORDER-L+1
         J = IK(K)
         IF(J-K) 111,111,105
C
 105     DO I=1,NORDER
            SAVE = ARRAY_INV(I,K)
            ARRAY_INV(I,K) = -ARRAY_INV(I,J)
```

```
            ARRAY_INV(I,J) = SAVE
         ENDDO
C
 111     I = JK(K)
         IF(I-K) 130,130,113
C
 113     DO J=1,NORDER
            SAVE = ARRAY_INV(K,J)
            ARRAY_INV(K,J) = -ARRAY_INV(I,J)
            ARRAY_INV(I,J) = SAVE
         ENDDO
 130  ENDDO
 140  RETURN
      END
C
C     ---------------------------------------------------------------
C
C     SUBROUTINE MAT_MULT
C     AUTHOR:   M. Nozar
C     DATE:     19-JUL-1991
C     PURPOSE:
C     Computes product of any two matrices:
C     matprod(mxp) = matrix1(mxn) * matrix2(nxp)
C     ---------------------------------------------------------------
C
      SUBROUTINE MAT_MULT(m,n,p,MATRIX1,MATRIX2,MATPROD)
      IMPLICIT NONE
C
      INTEGER            m,n,p,I,J,K
      DIMENSION          MATRIX1(m,n),MATRIX2(n,p),MATPROD(m,p)
      DOUBLE PRECISION   MATRIX1, MATRIX2, MATPROD
C
C     ---------------------------------------------------------------
C     Multiply two matrices
C     ---------------------------------------------------------------
C
      DO I = 1,m
         DO J = 1,p
            MATPROD(I,J) = 0.D0
            DO K = 1,n
               MATPROD(I,J) = MATPROD(I,J)+MATRIX1(I,K)*MATRIX2(K,J)
```

```
            ENDDO
          ENDDO
        ENDDO
C
        RETURN
        END
```

F.3 THE OUTPUT FILE (KINCAL.OUT)

The output file of the fitting program is listed below:

```
Kinematics Calibration
 ----------------------
 Nominal Spectrometer Uncertainties:
      DelE        DelP  TheE (rad)  TheP (rad)  PhiE (rad)  PhiP (rad)
  0.000100    0.000100    0.000080    0.000080    0.000080    0.000080
 Number of Runs = 7
 Initial Kinematical Offsets:
 Run     W (MeV)    Em (MeV)   Pmx (MeV)   Pmy (MeV)   Pmz (MeV)
2594    9.966000    2.239260    3.220580    0.846959    0.863014
2596   10.858000    2.347490    4.008290    0.840967    1.000670
2599   10.771000    2.563410    4.214460   -0.393876    1.358240
2600    8.799000    1.834520    3.944230   -0.978451    0.696069
2632    9.836000    2.322540    3.599490    0.606018    1.290370
2672    9.902000    2.058900    3.829710    0.346928    0.963902
2792   11.061000    2.525280    4.095720    0.553575    1.300050
 AVG   10.170429    2.270200    3.844640    0.260303    1.067474
 Initial Chi-Square per Degree of Freedom =  96.8894019
 ------------------------------------------------
 Fit Results:
 Spectrometer Offsets:
      DelE        DelP  TheE (rad)  TheP (rad)  PhiE (rad)  PhiP (rad)
 -0.000287   -0.000574   -0.001146   -0.000448    0.001054   -0.001440
 Spectrometer Uncertainties:
  0.000173    0.000232    0.000117    0.000132    0.000230    0.000291
 ------------------------------------------------
 Minimized Kinematical Offsets:
 Run     W (MeV)    Em (MeV)   Pmx (MeV)   Pmy (MeV)   Pmz (MeV)
2594   -0.525909   -0.168267   -0.359236   -0.220371   -0.239125
2596    0.652439    0.026755    0.215791    0.401371   -0.063593
2599    0.818201    0.334625    0.187507   -0.152278    0.353427
```

2600	-0.732136	-0.292455	-0.326278	-0.028443	-0.264716
2632	-0.401563	-0.011140	-0.181652	0.102363	0.217896
2672	-0.335679	-0.274786	0.048537	-0.156694	-0.108562
2792	0.823590	0.191617	0.314978	0.049868	0.227521
AVG	0.042706	-0.027664	-0.014336	-0.000598	0.017550

Minimized Chi-Square per Degree of Freedom = 0.735985483

VITA

Hassan F. Ibrahim
Department of PHYSICS
Old Dominion University
Norfolk, VA 23529

Hassan F. Ibrahim was born in Giza, Egypt on December 21, 1969. He received a B.S. in physics with "Distinction" from Cairo University in 1991. He was appointed later as a Demonstrator at the Physics Department, Cairo University in the same year, and in 1997 he became an Assistant Teacher at the same department after he received a Master degree in physics. In 1999, he was offered an assistantship from Old Dominion University, Virginia, USA, to join the graduate physics program. In 2004, Hassan received another Master degree in physics from Old Dominion University and, finally, he was awarded a Ph.D. in physics from the same university in December 2006.

List of selected publications:

1. A. Acha *et al.*, "Precision Measurements of the Nucleon Strange Form Factors at $Q^2 \sim 0.1$ GeV^2", arXiv:nucl-ex/0609002.
2. C. Munoz-Camacho *et al.*, "Scaling Tests of the Cross Section for Deeply Virtual Compton Scattering", arXiv:nucl-ex/0607029, Phys. Rev. Lett. (to be published).
3. K. A. Aniol *et al.*, "Parity-violating electron scattering from He-4 and the strange electric form factor of the nucleon", Phys. Rev. Lett. **96**, 022003 (2006).
4. K. A. Aniol *et al.*, "Constraints on the nucleon strange form factors at $Q^2 \sim 0.1$ GeV^2", Phys. Lett. **B635**, 275 (2006).
5. J. J. Kelly *et al.*, "Recoil polarization measurements for neutral pion electroproduction at $Q^2 = 1$ (GeV/c)^2 near the Delta resonance", arXiv:nucl-ex/0509004.
6. J. J. Kelly *et al.*, "Recoil Polarization for Delta Excitation in Pion Electroproduction", Phys. Rev. Lett. **95**, 102001 (2005).
7. I. A. Qattan *et al.*, "Precision Rosenbluth measurement of the proton elastic form factors", Phys. Rev. Lett. **94**, 142301 (2005).
8. J. Alcorn *et al.*, "Basic Instrumentation For Hall A At Jefferson Lab", Nucl. Inst. Meth. **A522**, 294 (2004).

Typeset using LaTeX.